Evaluating Ice Microphysics in NWP Models with Satellite Observations

Inaugural-Dissertation
zur
Erlangung des Doktorgrades
der Mathematisch-Naturwissenschaftlichen Fakultät
der Universität zu Köln

vorgelegt von

Sonja Reitter

aus Rotenburg/Wümme

Köln 2013

1. Berichterstatter: Prof. Dr. S. Crewell
2. Berichterstatter: Prof. Dr. R. Neggers

Tag der mündlichen Prüfung: 24. Oktober 2013

Abstract

Ice clouds are an important part of the Earth's atmospheric water cycle and have a large impact on the global radiation budget. Yet ice clouds are still poorly understood and their correct representation remains a major challenge for state-of-the-art atmospheric models. Also, the evaluation of the models' performance with respect to ice clouds is not straightforward; remote sensing instruments, for example, measure other quantities than the models predict. Therefore, two basic evaluation approaches exist: observation-to-model (commonly termed retrieval) and model-to-observation (commonly termed forward operator). Both approaches introduce errors into the comparison of models and observations because of the necessary intrinsic assumptions. The common practice in model evaluation of choosing either the one or the other of these approaches might give an incomplete picture.

The present study evaluates the ice microphysics of two numerical weather prediction (NWP) models currently operational at the German weather service (Deutscher Wetterdienst, DWD): the global model GME and the regional model COSMO-DE (an application of the Consortium for Small-scale Modelling, COSMO). In doing so, this study contributes significantly to ongoing model development at DWD. Both case studies and long-term evaluations are carried out. Cloud Satellite (CloudSat) Cloud Profiling Radar (CPR) observations are heavily relied on; the CPR is the first and — up to date — only cloud radar in space and is able to vertically resolve even optically thick clouds. This study focuses on one specific question raised for each of the respective models and while doing so applies both approaches; the standard CloudSat radar reflectivity factor–ice water content (IWC) retrieval for the observation-to-model approach and the forward operator QuickBeam for the model-to-observation approach. This enables for one, to profit from the full informational content, and for the other, to compare both approaches directly to each other and evaluate them.

For the global model GME, two precipitation schemes, a diagnostic and a prognostic one, are compared and evaluated. The focus is on the question whether the new prognostic scheme is capable of capturing ice clouds more realistically than the old diagnostic scheme. The prognostic scheme is shown to exhibit improved performance in comparison to the diagnostic scheme in terms of IWC magnitude. In both models snow is found to dominate over cloud ice in total IWC, emphasizing the need for including snow in the model's radiation budget in the future. Furthermore, one reason for the remaining difference between the prognostic scheme and the observations — the unrealistic fall speed of snow — is identified. As a consequence, the new prognostic scheme with an adapted parameterization for snow fall speed was successfully introduced into operational service at DWD.

In the regional NWP model COSMO-DE, a long-known bias between brightness temperatures simulated from COSMO-DE forecasts and those observed by Meteosat Second Generation (MSG) Spinning Enhanced Visible and Infrared Imager (SEVIRI) is investigated. The pivotal question is whether a novel two-moment cloud ice scheme exhibits improved performance with respect to this bias and, if that is so, why. It is shown that the novel two-moment cloud ice scheme does indeed reduce this bias and can therefore be considered an improvement in comparison to two standard schemes, the two-category ice scheme and the currently operational three-category ice scheme. The improvement in simulated brightness temperatures is due to a vertical redistribution of cloud ice to lower model levels. Furthermore, sensitivity studies identify two of the four changes introduced, which are responsible for most of the improved performance: the change to a different heterogeneous nucleation scheme and the inclusion of cloud ice sedimentation. Enhanced vertical level number and modifications in aerosol number concentrations reveal comparatively little effect. As a consequence, cloud ice sedimention will be included per se in DWD's future NWP model, the Icosahedral non-hydrostatic (ICON) model, currently still under development.

Concerning the two evaluation approaches conducted, the present study finds the general features in the two evaluations to be captured by both approaches. Some details are captured merely by the one or the other approach, in which case both approaches together give the more complete picture. However, the model-to-observation approach appears to be easier to interpret; its uncertainties are easier to assess than those of the observation-to-model approach and it ensures a better control over the comparison.

Zusammenfassung

Eiswolken sind ein wichtiger Bestandteil des atmosphärischen Wasserkreislaufs der Erde und haben einen großen Einfluss auf den globalen Strahlungshaushalt. Dennoch sind Eiswolken bisher nicht vollständig verstanden. Dies führt unter anderem dazu, dass ihre korrekte Darstellung in aktuellen atmosphärischen Modellen weiterhin eine große Herausforderung darstellt. Die Evaluierung dieser Modelle hinsichtlich ihrer Fähigkeit Eiswolken vorherzusagen ist nicht trivial: Beobachtungsdaten von Eiswolken, zum Beispiel von Fernerkundungsinstrumenten, liefern andere Größen als die, die Modelle vorhersagen. Aus diesem Grund existieren zwei wesentliche Evaluierungsansätze: Beobachtung-zu-Modell (üblicherweise als Retrieval bezeichnet) und Modell-zu-Beobachtung (üblicherweise als Vorwärtsoperator bezeichnet). In beiden Ansätzen müssen Annahmen gemacht werden, die zu Unsicherheiten im Evaluierungsprozess führen. Zumeist wird nur einer der beiden Ansätze verfolgt, was zu einem unvollständigen Bild führen kann.

In der vorliegenden Arbeit wird die Eismikrophysik zweier numerischer Wettervorhersagemodelle (NWP-Modelle) evaluiert, die beim Deutschen Wetterdienst (DWD) aktuell operationell im Einsatz sind: das globale Modell GME und das regionale Modell COSMO-DE (einer Anwendung des Consortium for Small-scale Modelling, COSMO). Damit liefert diese Arbeit einen wichtigen Beitrag zur fortlaufenden Modellentwicklung beim DWD. Es werden sowohl Fallstudien als auch Langzeitevaluierungen durchgeführt. Dazu werden die Beobachtungen des Cloud Satellite (CloudSat) Cloud Profiling Radar (CPR), des ersten und bisher einzigen Wolkenradars im All, extensiv genutzt. Der Vorteil des CPR ist, dass es selbst optisch dicke Wolken vertikal auflösen kann. Die Studie konzentriert sich auf jeweils eine spezifische Frage pro Modell und verfolgt bei der Evaluierung von GME und COSMO-DE beide möglichen Ansätze: das Standard-Eiswassergehalt (IWC)-Retrieval aus den CloudSat Radarreflektivitäten für den Beobachtung-zu-Modell-Ansatz und den Vorwärtsoperator

QuickBeam für den Modell-zu-Beobachtung-Ansatz. Dies ermöglicht es zum einen den gesamten Informationsgehalt auszuschöpfen und zum anderen die beiden Ansätze direkt miteinander zu vergleichen und zu bewerten.

Für das globale NWP-Modell GME werden zwei Niederschlagsschemata, ein diagnostisches und ein prognostisches, miteinander verglichen und bewertet. Zentrale Frage ist, ob das neue prognostische Niederschlagsschema in der Lage ist, Eiswolken realistischer darzustellen, als das alte diagnostische Niederschlagsschema. Es wird gezeigt, dass das prognostische Schema eine realistischere Größenordnung des IWC wiedergibt, als das diagnostische Schema. In beiden Modellen dominiert Schnee gegenüber Wolkeneis im Gesamt-IWC. Dies unterstreicht die Notwendigkeit, Schnee im Strahlungsschema des Modells zukünftig mit zu berücksichtigen. Desweiteren wird ein Grund für den verbleibenden Unterschied zwischen dem prognostischen Schema und den Beobachtungen, nämlich die unrealistische Fallgeschwindigkeit von Schnee, identifiziert. Infolgedessen wurden das neue prognostische Schema mit einer angepassten Fallgeschwindigkeit von Schnee erfolgreich in den operationellen Betrieb des DWD eingeführt.

Im regionalen NWP-Modell COSMO-DE wird ein bereits lang bekannter Bias zwischen den aus COSMO-DE Vorhersagen simulierten Helligkeitstemperaturen und den von Meteosat Second Generation (MSG) Spinning Enhanced Visible and Infrared Imager (SEVIRI) beobachteten untersucht. Zentrale Fragestellung ist, ob das neue Zwei-Momenten-Wolkeneisschema bezüglich dieses Bias besser abschneidet, und wenn ja, warum. Es zeigt sich, dass das neue Zwei-Momenten-Wolkeneisschema diesen Bias tatsächlich reduziert und somit eine Verbesserung zu zwei Standard-Eisschemata, dem Zwei-Kategorie-Eisschema und dem momentan operationellen Drei-Kategorie-Eisschema, darstellt. Die Verbesserung in den simulierten Helligkeitstemperaturen beruht auf einer vertikalen Umverteilung des Wolkeneises in tiefer liegende Modellschichten. Sensitivitätsstudien zeigen zudem, dass zwei der insgesamt vier eingeführten Änderungen für einen Großteil der verbesserten Darstellung verantwortlich sind: der Wechsel zu einem anderen heterogenen Eisnukleationsschema und das Einführen der Sedimentation von Wolkeneis. Eine erhöhte vertikale Schichtzahl und Änderungen der Aerosolanzahldichten haben einen vergleichsweise geringen Effekt. Infolgedessen wird Wolkeneissedimentation im zukünftigen NWP-Modell des DWD, dem Icosahedral non-hydrostatic (ICON) Modell, standardmäßig implementiert.

Bezüglich der zwei verfolgten Ansätze zeigt die vorliegende Arbeit, dass die Grundaussagen der Evaluierungen von beiden Ansätzen wiedergegeben werden. Manche Details sind allerdings nur mit dem einen oder dem anderen Ansatz identifizierbar. Beide Ansätze zusammen liefern demzufolge das umfassendste Bild. Der Modell-zu-Beobachtung-Ansatz scheint jedoch in der Interpretation eingängiger zu sein: die hier auftretenden Unsicherheiten sind leichter abzuschätzen als beim Beobachtung-zu-Modell-Ansatz und ermöglichen eine bessere Kontrolle über den Vergleich.

Contents

1 Introduction

1.1 Motivation

Ice clouds have a large impact on the Earth's climate system due to their role in the atmospheric water cycle and their effects on the global radiation budget. Of the various parts in the complex chain of processes of the atmospheric water cycle, ice clouds are one of the least well-understood parts and therefore add to the uncertainty in precipitation forecast. Concerning their radiative impact, ice clouds contribute to the radiation budget through shortwave albedo and longwave greenhouse effects (*Chen et al., 2011*). The Intergovernmental Panel on Climate Change (IPCC) states in its 4th assessment report that clouds in general and their radiative effect in particular are not yet well understood (*IPCC, 2007*). The annual mean ice water path (IWP)* of the global climate models (GCMs) contributing to this report varies by two orders of magnitude (*Waliser et al., 2009*; cf. Fig. 1.1). *Waliser et al. (2011)* investigate the impact of frozen phase precipitation on the global radiation balance and find its neglection to lead to an overestimation of up to 10 % of integrated column cooling. *Li et al. (2013)* attribute the persistence of a systematic bias in top of atmosphere radiative fluxes in the Coupled Model Intercomparison Project Phase 3 (CMIP3) and Phase 5 (CMIP5) simulations partly to the neglection of the radiative effects of precipitating frozen phase. This illustrates the fact that a good description of ice clouds is still a major challenge for both GCMs and numerical weather prediction (NWP) models. Furthermore, it emphasizes the importance of including not only realistic ice clouds but also frozen phase precipitation in the radiation schemes of atmospheric models in order to obtain a realistic radiation balance. However, the consideration of frozen phase precipitation in radiation schemes is currently not standard in NWP models. Before this becomes reason-

*Throughout the present study the term ice water path (IWP) refers to the sum of all columnar integrated atmospheric frozen phase water, regardless of its habit.

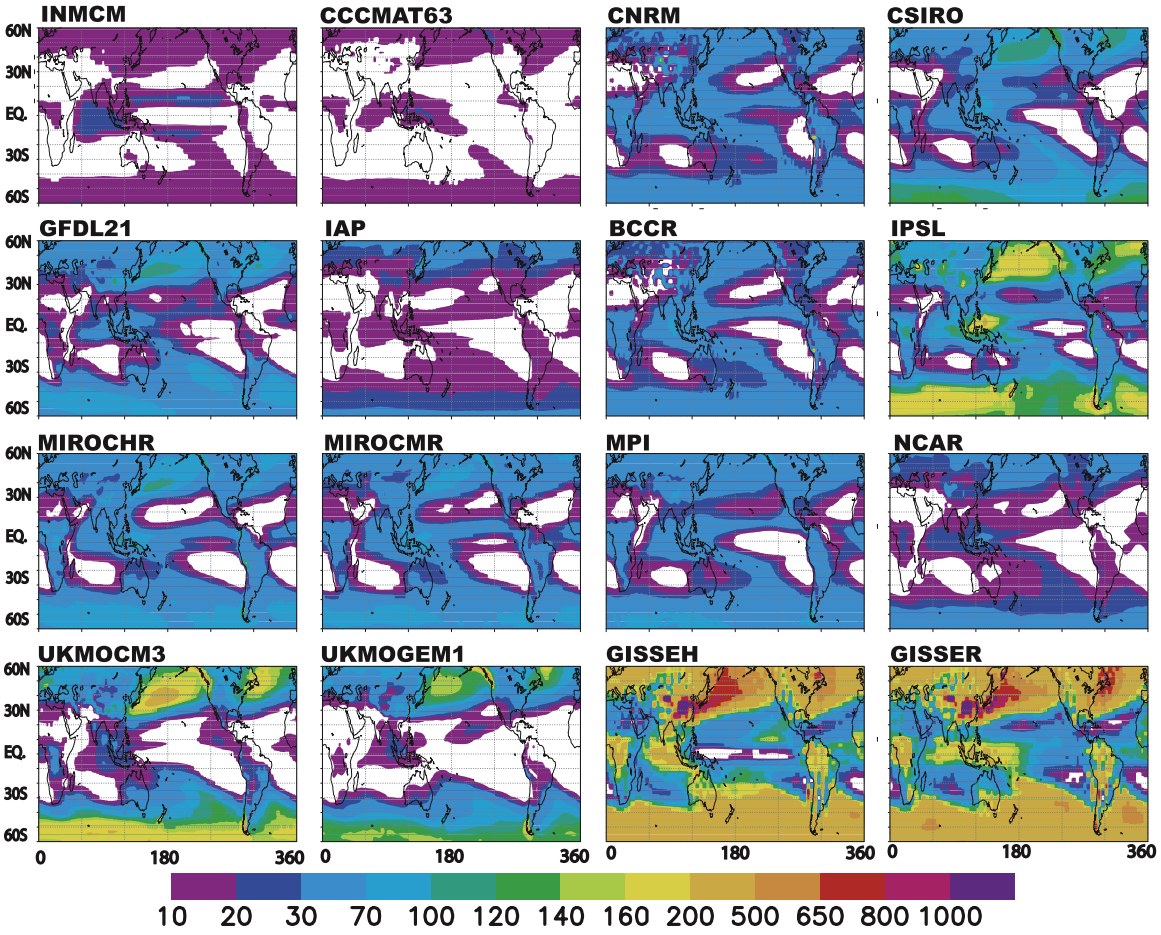

Figure 1.1: Annual mean values of IWP in $\mathrm{g\,m^{-2}}$ from the 1970-1994 period of the twentieth century GCM simulations contributing to the IPCC 4th Assessment Report (20c3m scenario). Note that the colour scale is not linear. From *Waliser et al. (2009)*.

able, the representation of ice cloud microphysics in models needs to be improved. Also, due to increased available computational power, the general trend in model development is heading towards increased model resolution on the one hand and attempts to describe frozen phase in more detail on the other hand. Especially the latter is noted by *Avramov and Harrington (2010)* who investigate the influence of different particle habits on model results. With all this, the importance of good ice cloud microphysical schemes increases.

At the German weather service (Deutscher Wetterdienst, DWD), efforts are in progress to develop an efficient cloud microphysical scheme which is both physically consistent and computationally efficient. Before entering operational forecast service, new schemes are first corrected for potential numerical issues and code errors. Subsequently, they are internally verified at DWD to ensure that their performance with regard to certain standardized skill scores (e. g. for surface precipitation) is better than that of the former scheme. The former scheme could potentially produce better results even though it might be physically less reasonable, because it is already tuned towards best results. Therefore, new schemes

are run in parallel routine for some time and only become operational once they actually perform better than the former scheme. In addition to this internal routine verification, further evaluation outside DWD is desirable, since it ensures the comparison with more special observational data. At operational weather forecast centers, these data might either not be available, or the time for more detailed evaluation might be lacking. The comparison of model and observation data is a challenging task. Instruments, retrievals, and forward operators can exhibit strong sensitivities to factors such as particle size, and the microphysical schemes of the models vary greatly in configuration and complexity.

Both the development and the evaluation of such a cloud microphysical scheme require suitable observational data. Small ice crystals remain one of the most difficult objects to be observed. In situ measurements with aircrafts are affected by crystal shattering on probe tip or inlet shroud and overestimate small ice crystal concentrations by a factor of two (*McFarquhar et al., 2007*). More recent campaigns try to reduce these errors with improved measurement techniques (*Zhang et al., 2013*). Remote sensing in general has to cope with instrument sensitivity limits. Ground-based remote sensing additionally suffers from attenuation losses when having to penetrate thick clouds. This leaves space-based or airborne remote sensing as the best contemporary measurement technique for obtaining information from cloud top in the atmosphere. The Cloud Satellite (CloudSat) Cloud Profiling Radar (CPR; *Stephens et al., 2002*) is the first and — up to date — only cloud radar in space. It offers the unique opportunity to vertically resolve even thick ice clouds from space — in contrast to the numerous passive satellite-based sensors as, for example, Meteosat Second Generation (MSG) Spinning Enhanced Visible and Infrared Imager (SEVIRI). Due to its high resolution and the near-global coverage (compared to ground-based radars) the CloudSat CPR is predestined for the evaluation of models in general and global models in particular because it is able to penetrate clouds and to assess the occurrence of multi-level clouds (*Mace et al., 2009*). It has evolved as the state-of-the-art choice for cloud observation. However, CloudSat has some limitations since it is less sensitive to smaller frozen particles. These can be detected well by the Cloud Aerosol Lidar and Infrared Pathfinder Satellite Observation (CALIPSO) Cloud-Aerosol Lidar with Orthogonal Polarization (CALIOP) which flies in formation with CloudSat (*Winker et al., 2007*). However, the instrument's wavelength limits its use to optically thin clouds.

In addition to the requirement of suitable observational data, model evaluation also calls for suitable methodologies. The problem with all remote sensing observations is, that the instruments measure different quantities than the models predict. For example, a radar such as the CloudSat CPR measures a radar reflectivity factor, whereas a model predicts specific atmospheric water contents. One variable needs to be converted into the other to enable a direct comparison. Two basic approaches exist: observation-to-model and model-to-observation. The first is commonly termed retrieval, the latter forward operator or instrument simulator. Both exist in a large variety, they range from very basic to highly complex and both introduce errors into the comparison of models and observations because of the necessary intrinsic assumptions. Retrievals suffer from instrument sensitivity limitations,

from domination of the observed signal by a certain particle type, and from assumptions based on incorrect field measurements. Forward operators on the other hand suffer from simplified assumptions made in the scattering properties of the particles.

Model evaluation studies usually concentrate on one or the other approach. *Delanoë et al. (2011)* apply the observation-to-model approach to evaluate the ice cloud microphysical schemes of the global versions of the European Centre for Medium-Range Weather Forecasts' (ECMWF) Integrated Forecast System (IFS) and the UK Met Office's Unified Model (MetUM) with CloudSat and CALIPSO data. They use data from the combined CloudSat-CALIPSO ice water content (IWC)[†] retrieval of *Delanoë and Hogan (2010)* to evaluate IWC and cloud fraction of the models. The interpretation of cloud fraction differences between model and observation is difficult, since cloud fraction is an ambiguous and unphysical variable dependent on its individual definition in the respective models and observations. *Li et al. (2012)* use results from three different combined CloudSat-CALIPSO IWC retrievals to evaluate the CMIP5 GCMs' IWCs and IWPs. They find annual mean IWP to differ by a factor of 2–10 between observations and models for several regions. The authors aim to reduce the uncertainties that the observation-to-model approach introduces by including three different retrievals and by excluding certain problematic regimes in their comparison. Though a range of retrievals enables to increase the confidence in the results, the errors introduced by the retrievals are not removed. Instrument sensitivity limits and retrieval assumptions still remain an issue.

On the other hand, *Marchand et al. (2009)* apply the model-to-observation approach and make use of the radar simulator QuickBeam (*Haynes et al., 2007*; see also Chap. 5.2) to evaluate the radar reflectivity factors obtained from the Multiscale Modelling Framework (MMF). Though overall model performance is good, they discover several shortcomings, one being the model's tendency to produce too many hydrometeors in convectively active regions. Including these regions in the comparison is problematic, since the CloudSat CPR suffers from multiple scattering in regimes with strong rain (Battaglia *et al.*, 2008b). The authors assume these multiple scattering effects to be negligible. *Bodas-Salcedo et al. (2008)* evaluate the MetUM global forecast model at 40 km horizontal resolution using a radar simulator. They are able to identify an inconsistency in the parameterization of ice cloud fraction of their model. Subgrid variability is accounted for with the Subgrid Cloud Overlap Profile Sampler (SCOPS). Though results are improved with SCOPS, it does not include overlap algorithms for precipitation. The authors apply a simple precipitation overlap algorithm and emphasize the need for a more sophisticated one. *Nam and Quaas (2012)* apply the Cloud Feedback Model Intercomparison Project (CFMIP) Observational Simulator Package (COSP) for cloud and precipitation evaluation of the European Centre/Hamburg Model version 5 (ECHAM5) GCM. They find that the radiative balance of the model is only obtained by compensating errors in the model's microphysics. *Satoh et al. (2010)* utilize COSP not only for evaluation but also for sensitivity studies with cloud microphysical

[†]Throughout the present study the term ice water content (IWC) refers to the sum of all atmospheric frozen phase water content, regardless of its habit.

schemes in the Nonhydrostatic Icosahedral Atmospheric Model (NICAM). They find that with decreasing horizontal model resolution, cloud ice and snow decrease in upper layers and rain and snow increase in the lower layers because reduced maximum upward velocity in convective cores results in water vapour accumulation in lower layers in their model. Similarly, *Inoue et al. (2010)* also focus on COSP output such as simulated lidar backscatter coefficients, though they do include retrieved parameters such as a satellite-derived cloud classification in their study of the representation of high-level clouds in NICAM. Following this line, the present study utilizes both approaches, observation-to-model and model-to-observation, in order to profit from their complementarity.

1.2 Objectives

In order to support ongoing model development at DWD, the present study aims at evaluating novel ice microphysical schemes for two operational NWP models with state-of-the-art satellite observations. In doing so, both possible approaches available when comparing model to satellite data are persued. This enables them to be extensively compared and their advantages and disadvantages discussed.

In the first part of the study, the operational global NWP model of DWD, GME (*Majewski et al., 2002*), is evaluated with special focus on the performance of a diagnostic versus a prognostic precipitation scheme. A prognostic variable is a variable, which is directly predicted by the model. It is available at every model time step and therefore increases the demand for computational power. In contrast, a diagnostic variable is calculated from the prognostic variables only at the time of forecast. It is diagnosed. No memory of it exists for the next time step. The change from the diagnostic to the prognostic precipitation scheme is deemed necessary at DWD, firstly because of the development towards increased model resolution and secondly because of the efforts in progress to adjust the microphysical parameterizations of all three models in DWD's currently operational NWP model chain. The present study evaluates the representation of grid-scale frozen phase in the two model versions with CloudSat CPR data and analyzes the individual contributions of cloud ice and snow to total frozen phase. Within the evaluation, both possible approaches — observation-to-model and model-to-observation — are undertaken, in order to exploit their complementarity. For the first approach, the standard CloudSat IWC retrieval is applied. For the second approach, the well-known radar simulator QuickBeam is utilized and is developed further to meet the requirements of the model's new microphysical scheme.

The second part of the study is concerned with COSMO-DE (*Baldauf et al., 2011*), an application of the Consortium for Small-scale Modelling (COSMO) and the operational regional NWP model of DWD. A specific long-known problem, namely a bias between simulated and observed MSG SEVIRI brightness temperatures identified amongst others by *Böhme et al. (2011)*, is addressed. A statistical approach is undertaken first to determine

whether a recently developed more sophisticated cloud ice microphysical scheme (*Köhler, 2013*) performs better than the operational scheme with respect to this problem. This new scheme was originally developed to improve the representation of ice nucleation processes in COSMO-DE. In contrast to the operational version of COSMO-DE, it is a two-moment cloud ice scheme, predicting both specific contents and number concentrations of atmospheric particles (see Chap.3.2.5 for details). Currently, this scheme is for research only, since the number of prognostic variables is increased by a two-moment scheme. As in the first part, the present study utilizes CloudSat CPR data, now complemented by CALIPSO CALIOP data. In the subsequent case study, the cloud vertical structure is investigated in detail to determine how and why exactly the novel scheme performs differently. To this end, sensitivity studies with varying model settings are performed. The first set of model runs performed tests the various configurations implemented in the new scheme independently in order to assess which change in the microphysial scheme has the largest effect. A second set of model runs is performed with the new microphysical scheme, to test its sensitivity to the number of vertical model levels and the aerosol number concentrations which serve as ice nuclei (IN).

Within the scope of the model evaluations performed in the present study, both evaluation approaches (observation-to-model and model-to-observation) are undertaken. The assumptions made in both approaches are summarized and reviewed. Notably the case study and the statistical approach undertaken for GME evaluation enable a comprehensive analysis of the benefits and downsides of the respective tools and the direct comparison of the two approaches.

1.3 Overview

The study is organized as follows. An introductory overview of cloud microphysics is given in Chap. 2, with an extra section dedicated to the representation of cloud microphysics in NWP models. In Chap. 3, the models evaluated in the present study are introduced. General aspects are given, but special focus is laid on the description of the cloud microphysical parameterizations in the various model versions. Subsequently, the satellite data utilized for evaluating the models and their various versions are introduced in Chap. 4. The measurement techniques and error sources of the satellites are explained. Chapter 5 is dedicated to the tools used in the present study: the retrievals and forward operators which are applied to the observed and modelled data are described. The two following chapters contain the actual model evaluations. Firstly, in Chap. 6, the global NWP model GME is evaluated. The exact question of interest is formulated, before the matching procedure of model and satellite data is explained. A case study is presented first in order to understand the tools utilized, before a statistical approach is undertaken, in order to obtain robust results. The chapter ends with a summary of the GME-specific results. Secondly, in Chap. 7, the regional NWP model COSMO-DE is evaluated. Again, the question of interest is posed, after

which the matching between model and satellite data is explained. This is done somewhat different than for GME in the previous chapter. In contrast to GME, for COSMO-DE a statistical approach is undertaken first, before looking into the details of a case study as to why exactly the results of the statistical approach are as observed. Analogous to the GME chapter, the COSMO-DE chapter ends with a summary of the COSMO-DE-specific results. Finally, in Chap. 8, the presented results are summarized and reviewed. Additionally, results of a more general nature are given and suggestions for further research are proposed.

The evaluation of GME presented in Chap. 6 has recently been published:

Reitter, S., K. Fröhlich, A. Seifert, S. Crewell, and M. Mech (2011) Evaluation of ice and snow content in the global numerical weather predicition model GME with CloudSat, *Geosci. Model Dev., 4*, 579-589.

2 Cloud microphysics

In order to understand the treatment of clouds in NWP models, this chapter gives an introductory overview of cloud microphysics in general, with special focus on ice cloud microphysics and their representation in NWP models. Far from being comprehensive, its aim is rather to communicate the basic processes involved and to provide a look-up chapter for later chapters, in which the processes parameterized in the evaluated models are listed, but no more explained. For a more extensive insight into cloud microphysics, see *Rogers and Yau (1989)*, *Lamb and Verlinde (2012)*, *Pruppacher and Klett (1997)*, and *Wallace and Hobbs (1977)*, from which the following process descriptions are taken, if not stated otherwise. The chapter ends with a description of how cloud microphysics are represented in atmospheric models.

2.1 Cloud microphysics in nature

Cloud physics, the science of clouds in the atmosphere, is commonly divided into two branches: cloud dynamics on the one hand, which are concerned with processes that take place on a scale from tens of meters to hundreds of kilometers, and cloud microphysics on the other hand, which deal with processes on a scale from micrometers to centimeters (*Rogers and Yau, 1989*). Though amount, phase, and habit of produced precipitation also depend on large-scale phenomena such as air motion and moisture supply, and in that respect belong to cloud dynamics, the processes governing the production, growth, destruction, and the interaction between cloud and precipitation particles belong to cloud microphysics. Turbulence, which is also strongly linked to cloud composition, is highly variable in scale, and as such can belong either to cloud dynamics or to cloud microphysics.

Hydrometeors

Atmospheric air is a mixture of dry air and water vapour and contains suspended particles such as aerosols and so-called hydrometeors. Hydrometeors comprise all condensated or frozen atmospheric water particles, whether suspended in the air or falling towards the Earth's surface. Examples are cloud droplets, cloud ice, and fog for suspended hydrometeors, and drizzle, rain, snow, graupel, hail, and virga for precipitating hydrometeors (*Glickman and American Meteorological Society, 2000*). A wide variety of shapes and sizes of hydrometeors exist; from simple spheres in case of cloud droplets, to complex aggregates in case of snow, and from diameters around 1 μm in case of cloud droplets, to several centimeters in case of hailstones. This broad range of appearance is due to the various processes involved in shaping the hydrometeors themselves and their particle size distributions (PSDs). These processes are described in the following.

Phase changes

The phase changes of water are the most basic cloud microphysical processes: condensation of vapour to liquid and evaporation of liquid to vapour, freezing of liquid to solid and melting of solid to liquid, and (direct) deposition of vapour to solid and sublimation of solid to vapour. The process of initiating a new phase from water vapour or liquid water in an environment supersaturated with respect to liquid or frozen phase is called nucleation for droplets and ice nucleation for ice crystals. Condensation, freezing, and deposition are all (ice) nucleation processes (*Glickman and American Meteorological Society, 2000*). Since after nucleation or ice nucleation the new phase is of smaller entropy than the original phase water vapour or liquid water, a free energy barrier has to be overcome to enter the new, more stable phase. The nucleation (ice nucleation) rate is the rate at which droplets (ice crystals) cross this free energy barrier and form from critical embryonic droplets (ice crystals).

Nucleation and ice nucleation

In theory, the formation of embryonic droplets or ice crystals can proceed in two ways: homogeneously from a stochastic event in the presence of supersaturation with respect to liquid or frozen phase (i. e. the excess of relative humidity over the equilibrium value of 100 %) alone, or heterogeneously on suitable insoluble or partially soluble hygroscopic aerosol particles* called cloud condensation nuclei (CCN)† or ice nuclei (IN). Note that, though often assumed otherwise, homogeneous ice nucleation does not imply that it is homomolecular.

A solution droplet can be in equilibrium with its environment at much lower supersaturation rates than a pure water droplet of the same size. The same applies to a larger droplet in contrast to a smaller droplet due to the weaker curvature. The interaction of the change in

*These are mostly expected to be particulates, but high-molecular-weight organic compounds on droplets are receiving increased attention for IN (*Cantrell and Heymsfield, 2005*).

†CCN are those condensation nuclei (CN), which are 'activated' at a given supersaturation and enter the cloud forming process (*Rogers and Yau, 1989*).

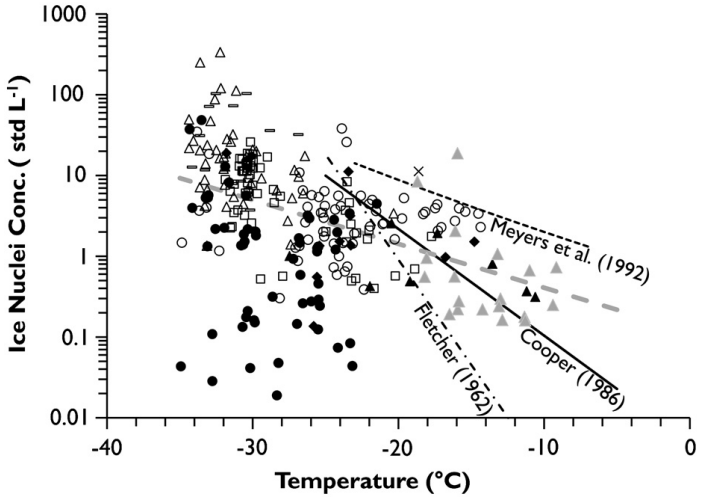

Figure 2.1: IN number concentrations active at saturations with respect to liquid or above versus temperature (from *DeMott et al., 2010*). Included are measurements from eight campaigns in various regions and spanning in total 12 years (symbols). Also included are common simplified parameterizations (see Chap. 2.2 for a definition) for IN number concentration as a function of temperature from three studies (black lines). The dashed grey line depicts a temperature-dependent fit to all data.

saturation vapour pressure due to the amount of solute dissolved (Raoult's Law) and due to the curvature of the droplet (Kelvin effect) is described by Köhler theory (*Pruppacher and Klett, 1997*). Since usually a sufficient number of CCN[‡] is available in the atmosphere, high supersaturation rates with respect to liquid phase only very rarely occur in nature, and homogeneous nucleation therefore does not play a role. Rather, heterogeneous nucleation dominates.

For ice nucleation, this is different. Only few particles suitable as IN exist in the atmosphere, so that supercooled droplets are common. *Rogers et al. (1998)* state that only 1 in 10^5 ambient particles are suitable as IN. *Lamb and Verlinde (2012)* give $1\,l^{-1}$ as a typical IN concentration at $-20\,°C$; for approximately every 4 °C decrease in temperature, IN concentration increases by a factor of ten (*Fletcher, 1962*). The number of IN activated at a specific temperature varies greatly with location and time (*DeMott et al., 2010*), as demonstrated in Fig. 2.1.

For pure water droplets, homogeneous ice nucleation does not occur down to a temperature of approximately $-40\,°C$. For solution droplets (liquid aerosols), homogeneous ice nucleation occurs at warmer temperatures, because the solute depresses the freezing point of the liquid. Liquid aerosols especially suitable for homogeneous ice nucleation are sulfates, sulfates internally mixed with organics, and potassium (*DeMott et al., 2003*), though their homogeneous ice nucleation ability changes with solution droplet size and water accomodation coefficient of the solute (*Kärcher and Koop, 2005*). Throughout the present study, the two types of homogeneous nucleation (of pure water droplet and of liquid aerosols)

[‡]CCN concentrations in the atmosphere vary with supersaturation with respect to liquid phase, air mass origin, height, and time of day and range from 10 to $10^3\,cm^{-3}$ (*Wallace and Hobbs, 1977*).

will be termed homogeneous nucleation and homogeneous nucleation of liquid aerosols. Homogeneous ice nucleation through direct deposition does not occur in nature, since the required supersaturations with respect to frozen phase are never achieved.

In contrast to homogeneous ice nucleation, given the presence of suitable IN, heterogeneous ice nucleation already occurs at a few degrees below zero. Aerosols especially suitable as IN for heterogeneous ice nucleation are to current understanding mineral dust, fly ash, metalls, sulfates, and organics (*DeMott et al., 2003*). *Rogers and Yau (1989)* distinguish between four heterogeneous ice nucleation mechanisms:

- heterogeneous deposition (i. e. water vapour deposits directly onto an IN),
- condensation freezing (i. e. heterogeneous nucleation of a droplet followed by freezing),
- contact freezing (i. e. a supercooled droplet freezes spontaneously on contact with an IN), and
- immersion freezing (i. e. a supercooled droplet freezes after embedding an IN).

The latter two long prooved hard to distinguish since in both mechanisms an internal mixture of aerosol is required (*Fornea et al., 2009*). Heterogeneous deposition and contact freezing are to current understanding unimportant in cirrus formation, whereas immersion freezing is considered to be the most efficient heterogeneous ice nucleation mechanism in cirrus (*Gierens, 2003*). Apart from these classic heterogeneous ice nucleation mechnisms, others have been proposed which are still subject of controversy (*Hoose and Möhler, 2012*).

In nature, both homogeneous and heterogeneous ice nucleation occur. Notable homogeneous ice nucleation requires low temperatures and strong updrafts and produces comparatively small but numerous ice crystals. Notable heterogeneous ice nucleation already occurs at much higher temperatures and in weaker updrafts and produces larger but fewer ice crystals. However, for some combination of ambient air temperature, vertical velocity, and available IN, both ice nucleation processes can occur simultaneously and they then compete for the available water vapour (*Ren and MacKenzie, 2005*).

Ice formation in general is a complex process and the chemical and physical principles underlying it are still poorly understood (*Cantrell and Heymsfield, 2005*). Besides, ice formation also depends on macrophysical parameters such as cloud temperature, cloud type, cloud age, and radiation.

Growth processes and precipitation formation

Once a stable droplet or ice crystal is generated, various processes can lead to further growth and finally precipitation production. In general, precipitation forms when a usually stable cloud environment becomes unstable, that is when some droplets or ice crystals grow at the expense of others. It is commonly distinguished between the warm rain process, in which

liquid water particles interact with water vapour and other liquid water particles, and cold rain processes, where frozen water particles are involved in the interaction. Generally, the probability for precipitation increases with cloud age, temperature, and vertical extent.

Warm rain process

In the warm rain process, droplet growth can occur in two ways. Firstly, by ongoing diffusional growth from water vapour. This process is very slow and does not lead to drop formation in realistic time. Secondly, droplets can grow through the classical collision-coalescence mechanism. In this mechanism, precipitation is formed by collision of droplets with each other and subsequent coalescence (i. e. sticking together/merging), resulting in fewer but larger droplets. This basic particle growth mechanism exists in many varieties. In the warm rain process, three basic processes lead to the production of large drops. First, autoconversion[§], the initial stage of the collision-coalescence process, leads to the formation of larger droplets (diameter $\sim 40\,\mu$m) and eventually drizzle drops (diameter ~ 0.1 mm) through the collision and coalescence of small droplets (diameter $\sim 20\,\mu$m). Second, once the drops are larger and have already begun to fall (i. e. have become drizzle drops), accretion commences: falling drops grow after collision and coalescence with non-precipitating droplets. Third, once enough large drops are available, large hydrometeor self-collection rapidly adds to large drop production. However, drop size is limited, since at diameters larger than approximately 6 mm the drops become unstable und drop break-up occurs, producing new small droplets.

For falling drops to actually become precipitation, their sedimentation rate (i. e. fall of hydrometeor relative to ambient air) has to exceed their evaporation rate, enabling them to reach the ground before evaporating completely. The fall velocity of liquid precipitation varies with particle size and ranges from $0.2\,\mathrm{m\,s^{-1}}$ to nearly $10\,\mathrm{m\,s^{-1}}$ (*Khvorostyanow and Curry, 2001*). The warm rain process dominates in the tropics, but also plays a role in mid-latitudinal mixed phase clouds.

Cold rain processes

Compared to the warm rain process, cold rain processes are far more complex and diverse. The initial cold rain process is depositional (diffusional) growth of ice crystals. If droplets exist, then the diffusional growth occurs at the expense of these droplets. The reason is the smaller equilibrium vapour pressure over frozen water in comparison to over liquid water. In such an environment, ice crystals will grow by diffusion of water vapour and supercooled droplets will evaporate to compensate for this. This process is referred to as the Bergeron-Findeisen process[¶] (*Korolev, 2006*). In contrast to diffusional growth of droplets in the warm rain process, the diffusional growth of ice crystals in the cold rain processes is faster and can alone account for precipitation formation.

[§]Note that the term autoconversion is sometimes also applied to drops or even ice crystals rather than merely droplets.

[¶]The Bergeron-Findeisen process is sometimes also referred to as the Wegener-Bergeron-Findeisen, Bergeron-Findeisen-Wegener, or simply ice phase process or theory.

When the ice crystals become larger, various other processes (apart from ongoing depositional growth) add to their further growth. Collision with supercooled droplets followed by rapid freezing is called riming and results in the production of rimed ice crystals, then graupel, and eventually (in case of a slow freezing pace and strong updrafts) hail. Collision of ice crystals with other ice crystals followed by sticking together is called aggregation and results in the formation of snowflakes (aggregates). Aggregation is especially important near the melting layer, where the sticking efficiency is higher due to the liquid coating of the melting ice crystals.

Once a frozen particle has grown large enough for its fall velocity to exceed the upward velocity of the ambient air, sedimentation begins. As in the warm rain process, accretion may occur: falling snowflakes grow after collision with non-precipitating ice crystals. Should the frozen particle fall below the 0 °C level, melting occurs. Dependent on ambient air temperature and particle diameter, the particle may either reach the ground before thoroughly melting and fall as frozen precipitation (e. g. snow, graupel, hail) or it may have melted completely and fall as rain. For melting hailstones and graupel, depending on the thickness of their liquid coating and their fall speed, shedding may occur: the liquid coating is shed off as raindrops. The fall velocity of frozen precipitation varies greatly with particle size and habit and ranges from $0.2\,\mathrm{m\,s^{-1}}$ for small needles to several tens of $\mathrm{m\,s^{-1}}$ for large hailstones.

Ice enhancement

So far, all introduced processes were based on the so-called primary ice production mechanisms, on homogeneous and heterogeneous ice nucleation. However, observational studies show that in nature, the development of an ice crystal population in a cloud occurs at much higher speeds than these processes alone would enable and that the concentration of ice crystals exceeds the concentration of IN by orders of magnitude. This suggests additional mechanisms, which act as multipliers of the ice crystals produced by the primary ice production mechanisms and are hence referred to as secondary ice production mechanisms or ice enhancement mechanisms. These are not yet fully understood and a topic of ongoing research (e. g. *Fridlind et al., 2007*). So far, several theories have been suggested and are deemed more or less likely and effective in nature (*Cantrell and Heymsfield, 2005*). Some proposed mechanisms are: fracture of ice crystals after collision, fragmentation of ice crystals during evaporation, shattering of large drops during freezing, and splintering of ice crystals during riming, also referred to as rime-splintering or Hallett-Mossop process (*Hallett and Mossop, 1974*; *Saunders and Hosseini, 2001*).

An overview of all described cloud microphysical processes is depicted in Fig. 2.2. Though for a single particle the above mentioned microphysical processes occur successively, in the life cycle of a natural cloud, consisting of a whole particle population (up to $800\,\mathrm{cm^{-3}}$ for continental storm clouds; *Rogers and Yau, 1989*), several or all of these processes occur simultaneously. Furthermore, the processes compete for available water vapour. Therefore, these processes are difficult or impossible to discriminate in the model world. For example,

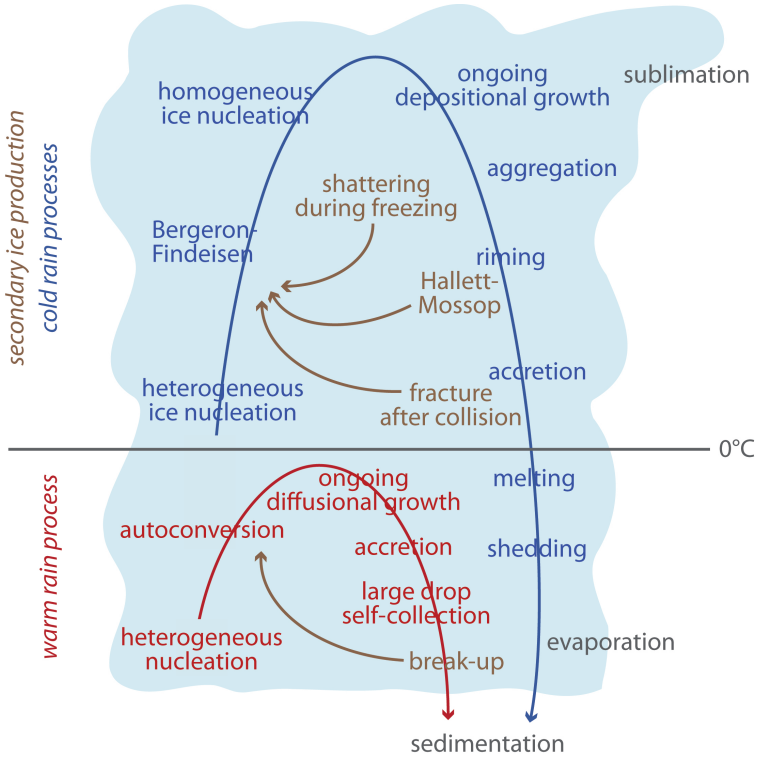

Figure 2.2: Schematic to illustrate the various cloud microphysical processes (based on *Lamb and Verlinde, 2012*).

when shedding occurs, the falling liquid-coated particle will also collect droplets during its fall, thereby thickening its liquid coating. This additional liquid water is shedd off as drops, too. These drops in turn, are re-collected by other falling liquid-coated particles. How atmospheric models can nevertheless handle this multitude of intertwined processes, or at least approximate them, is described in the following section.

2.2 Cloud microphysics in NWP models

The complex nature of cloud microphysics cannot be fully captured by NWP models, for two reasons. Firstly, the understanding of all processes involved is still incomplete (*Heintzenberg and Carlson, 2009*), as demonstrated in the previous section. Secondly, even the known processes cannot all be implemented into the models. Due to limited computational power, models have a far coarser resolution (several km) than would be necessary to resolve cloud microphysical processes explicitely (a few μm). In relation to the model grid, cloud microphysical processes occur at subgrid-scale and need to be parameterized. A parameterization is the description of a subgrid-scale process with the predicted grid-scale parameters of a model, and the determination of the temporal changes of these grid-scale parameters due to the subgrid-scale process. In short, it is the formulation of the ensemble

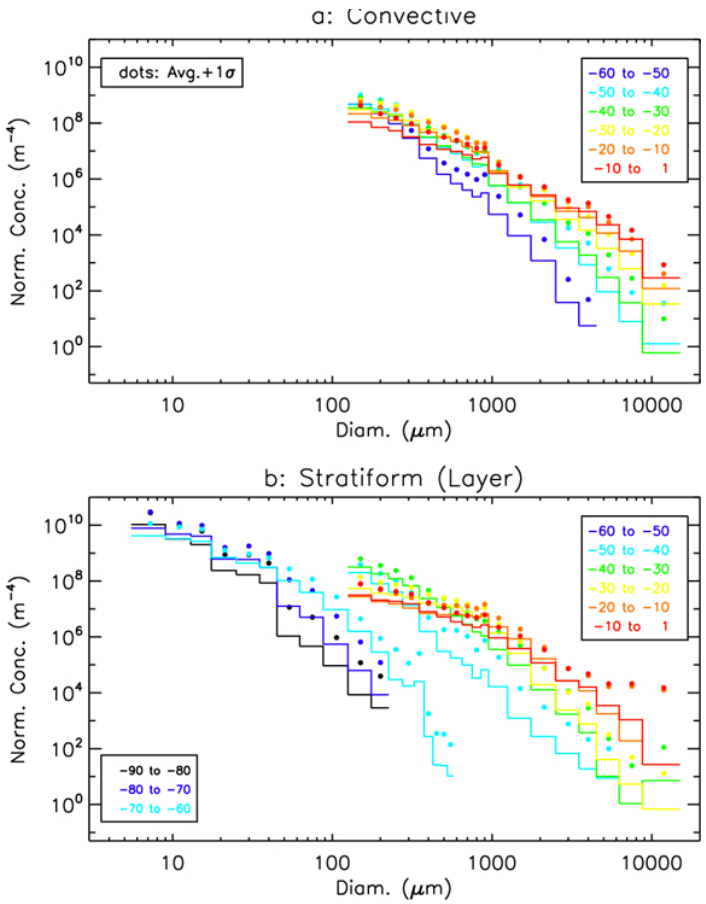

Figure 2.3: Average PSDs plotted in 10 °C temperature increments. The dots show one standard deviation above average value/bin. From *Heymsfield et al. (2013)*.

effect of subgrid-scale processes on the resolved grid-scale variables (*Doms et al., 2011*).

Since it is the ensemble effect rather than the effect of a single particle that is of interest for model cloud microphysics, the first and most basic assumption made in a model is to group the multitude of various hydrometeors into a few distinct hydrometeor classes. The more hydrometeor classes, the more complex the scheme. Second, the model needs to describe the members of such a hydrometeor class. Most microphysical processes depend very much on particle shape and size, that is the PSD has a strong impact on the overall evolution of the cloud as a whole. The description of the members of the hydrometeor classes is commonly done through the choice of a characteristic mass-size relation which gives the mass m as a function of diameter D (Eq. 2.1) and an appropriate PSD, which gives the number density N of particles as a function of diameter D (Eq. 2.2). The chosen PSD is usually based on observed PSDs and could, for example, be monodisperse, exponential, gamma, or any other reasonable mathematical function $f(D)$. Finding a good fit to observed PSDs is a challenging task, since observed PSDs exhibit a large spread. Exemplarily, PSDs for convective and stratiform cloud situations from 10 field campaigns are depicted in Fig. 2.3 from *Heymsfield et al. (2013)*. How the fit of different mathematical functions to an observed PSD varies

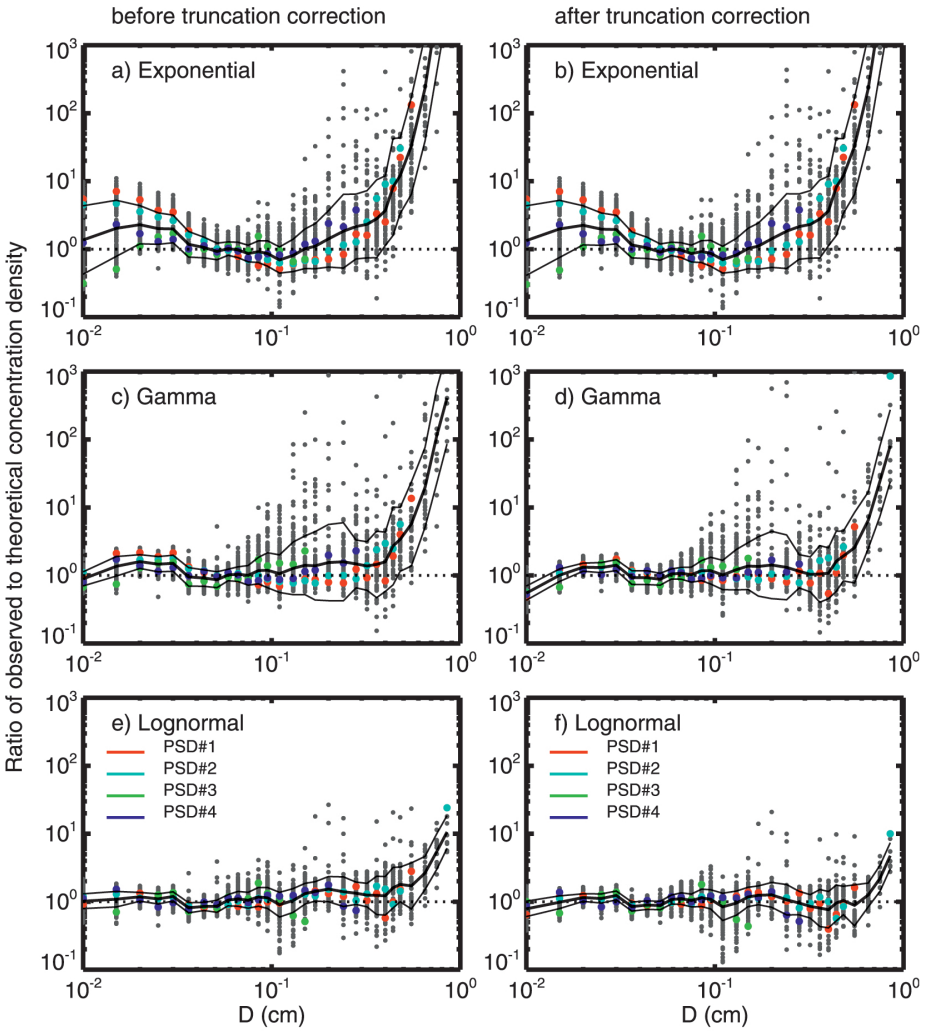

Figure 2.4: Ratio of observed to theoretical number concentration for three distribution types on 31 July 2007. Before (left) and after truncation correction (right). Thick black line: geometric mean. Thin black lines: one standard deviation above and below mean. From *Tian et al. (2010)*.

is depicted for one case study in Fig. 2.4 from *Tian et al. (2010)*. For cirrus clouds, the authors find the lognormal function to provide the best fit to observed PSDs. Exactly which hydrometeor classes and which corresponding PSDs the models evaluated in the present study use, is described in detail in Chap. 3.

$$m_x(D) = \alpha_x \cdot D^{\beta_x} \tag{2.1}$$

$$N_x(D) = f_x(D), \tag{2.2}$$

where α (in $\mathrm{kg\,m^{-\beta}}$) and β (dimensionless) are coefficients dependent on hydrometeor class x.

Total water mass remains the same, though the water mass of one hydrometeor class may increase (decrease) at the expense (in favour) of another. The water mass in each hydrometeor

class is mathematically described by budget equations, taken together commonly referred to as the water-continuity model. Basically, two approaches exist to implement this into a NWP model: spectral water-continuity models and bulk water-continuity models.

Spectral water-continuity models are the most direct approach for representing cloud microphysics in a NWP model. Each hydrometeor class is subdivided according to particle size. The number of particles per size bin (the particle number concentration) $N_x(D)$ is predicted using budget equations. The total number density of a hydrometeor class N_x is then calculated by integrating over the whole PSD. The total mass fraction (or specific content) q_x of a hydrometeor class x is calculated by integrating over the mass of the particles in each size bin. Thus, spectral water-continuity models directly predict the PSD, and from this diagnose the total number density N_x and total mass fraction q_x. These are simply proportional to the zeroth $\mathcal{M}_0$ and third moment $\mathcal{M}_3$ of the PSD (Eq. 2.3-2.5).

$$\mathcal{M}_n = \int_0^\infty D^n \cdot N(D)\, dD \tag{2.3}$$

$$N_x = \int_0^\infty N_x(D)\, dD \qquad \sim \mathcal{M}_0 \tag{2.4}$$

$$q_x = \frac{1}{\rho} \cdot \int_0^\infty m_x(D) \cdot N_x(D)\, dD \qquad \sim \mathcal{M}_3, \tag{2.5}$$

where n is the order of moment $\mathcal{M}$ and ρ is the ambient air density. Since the accuracy of spectral water-continuity models depends on a sufficiently large number of bins per hydrometeor class, these models quickly become complicated and computationally expensive. Therefore, though being very detailed, they are not suitable for NWP model application.

Bulk water continuity-models aim at minimizing the number of equations by reducing the number of hydrometeor classes to a minimum and by predicting their respective total mass fraction directly. For this, assumptions on particle shape and PSD are needed. In contrast to the spectral water-continuity models, the moments (or rather parameters proportional to the moments, e. g. total mass fraction q_x) are predicted with budget equations and the shape of the PSD is diagnosed from these. This requires the assumption, that the evolution of a PSD can be approximated by varying the free parameters of the mathematical function $f(D)$ assumed for the PSD. These free parameters are related to the moments of the PSD. Standard bulk water-continuity models for NWP application are one-moment schemes, which, as the name suggests, merely predict one moment, usually the total mass fraction q_x (Eq. 2.5). A two-moment scheme additionally predicts another moment, usually the total number concentration N_x (Eq. 2.2). Though multi-moment schemes are possible, they are currently only used in research (e. g. *Lim and Hong, 2010*; *Thompson et al., 2008*; *Seifert and Beheng, 2006*), since doubling the predicted moments means doubling the number of included prognostic variables, which increases computational costs drastically.

As stated above, the microphysical processes and their feedbacks are represented by budget equations, with which the respective parameters are predicted. For a one-moment bulk

water-continuity model the budget equation for the total mass fraction q_x in advection form is

$$\frac{\partial q_x}{\partial t} + \vec{v} \cdot \nabla q_x - \frac{1}{\rho} \frac{\partial P_x}{\partial z} = S^x - \frac{1}{\rho} \nabla \cdot \vec{F}_x, \tag{2.6}$$

with the three-dimensional wind vector $\vec{v}$ and the density of moist air ρ. The budget equation consists of five terms: the temporal evolution of the total mass fraction q_x plus the advection of q_x and the vertical divergence of the precipitation fluxes P_x equal the cloud microphysical sources and sinks (or transfer rates) S^x and the turbulent fluxes $\vec{F}_x$. The precipitation fluxes depend on the terminal fall speed of the particle, which in turn depends on q_x. For non-precipitating hydrometeor classes, terminal fall speed is negligible and the precipitation flux term is commonly set to zero and neglected. For precipitating hydrometeor classes, the turbulent flux term is commonly neglected, since it is small in comparison to the precipitation flux term.

In the following chapter, the cloud microphysical schemes currently in use at DWD are reviewed. The cloud microphysical schemes of the model versions evaluated in the present study are described in the respective model chapters.

3 Model data

The operational NWP system at DWD currently consists of a chain of three models nested into each other: the global model GME and the regional models COSMO-EU and COSMO-DE. Within the process of model development, model versions which actually enter operational service receive an official release version number. Prior to becoming operational, new model versions undergo extensive tests. Once these new versions are close to becoming operational, the runs performed with them are stored in DWD's database under a unique experiment number, enabling their discrimination.

The present study evaluates two models of DWD's model chain, GME and COSMO-DE. The models themselves and the experimental versions of them are introduced in the following sections.

3.1 GME

In the following, the GME model with its general aspects and particularly its microphysics is described. Since the present study compares two versions of the model, emphasis is laid on describing the differences between the two versions. At the end of the chapter, Table 3.3 summarizes the most important microphysical parameters of the model versions. For a more comprehensive introduction to GME see *Majewski et al. (2002)* and *Schulz and Schättler (2011)*. For details on the cloud microphysical parameterizations see *Doms et al. (2011)*.

3.1.1 General aspects

GME (*Majewski et al., 2002*) is the global NWP model of DWD. Operational since 1 December 1999, it is a hydrostatic model of the atmosphere and delivers the boundary conditions for the regional scale models COSMO-EU and COSMO-DE. The primitive equations are solved using a finite-difference method on a hexagonal icosahedral A-grid (cf. Fig. 3.1). GME uses terrain-following coordinates in the vertical, which are defined via the time-dependent surface pressure and are smoothed out towards the stratosphere (hybrid coordinates). Thus, level thickness varies with time. The GME versions evaluated in this study all have a mean horizontal grid size of 40 km* and 40 hybrid levels in the vertical. Level thickness ranges approximately from 25 m at the Earth's surface, 550 m in 5 km height, to 750 m in 10 km height. Forecasts are available in hourly resolution and the model is initialized four times a day (at 0, 6, 12, and 18 UTC). The model is initialized using a three-dimensional variational data assimilation system. GME assimilates observations of geopotential, horizontal wind vector, temperature, sea surface temperature, relative humidity, snow cover, snow depth, fraction of fresh snow, sea ice cover, and ozone mixing ratio. The observations stem from synoptic stations, drifting buoy, radiosondes, polar-orbiting and geostationary satellites, and aircrafts (*Wergen and Buchhold, 2002*; *Majewski et al., 2002*) .

In addition to resolved (i. e. grid-scale) clouds which are parameterized by microphysical schemes, GME also provides information from within a grid-box (i. e. subgrid-scale) for several applications (e. g. cloud fraction) and as input for other parts of the model (e. g. radiation scheme). In the following, the grid-scale cloud scheme, that is the microphysical parameterization of the model, is explained in detail.

*The to-date operational version has an increased horizontal resolution of 30 km.

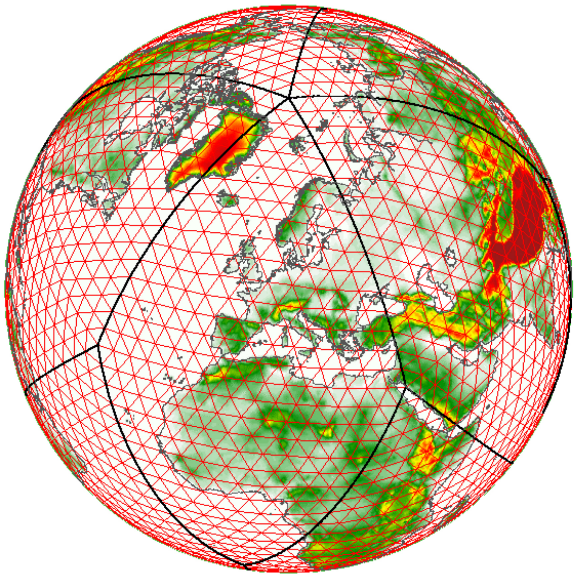

Figure 3.1: Model domain and horizontal grid structure of GME (from *Majewski et al., 2004*).

3.1.2 Cloud microphysics: Two-category ice scheme

Grid-scale precipitation in GME and the associated cloud microphysical interactions are formulated as a bulk scheme (see Chap. 2.2 for a general introduction to bulk schemes). GME distinguishes between precipitating and non-precipitating hydrometeor classes, featuring in total four hydrometeor classes: First, cloud water (index $x = c$), which is defined as droplets suspended in the air, with diameters smaller than 100 μm and no remarkable motion relative to the air flow. Second, cloud ice (index $x = i$), defined similar to cloud water, but for frozen phase. Third, rain (index $x = r$), which consists of comparably large drops, with diameters ranging from 100 to 8000 μm and size-dependent fall speed relative to the ambient air flow. Fourth, snow (index $x = s$), treated as large, slightly rimed ice crystals and aggregates of ice crystals, also with size-dependent fall speed relative to the ambient air flow. Owing to the number of frozen phase hydrometeor classes, this scheme is commonly referred to as the two-category ice scheme.

The particles in these four hydrometeor classes interact through various cloud microphysical processes which are formulated as a function of the specific contents q_x of the hydrometeor classes. Figure 3.2 gives a schematic overview of the hydrometeor classes and the

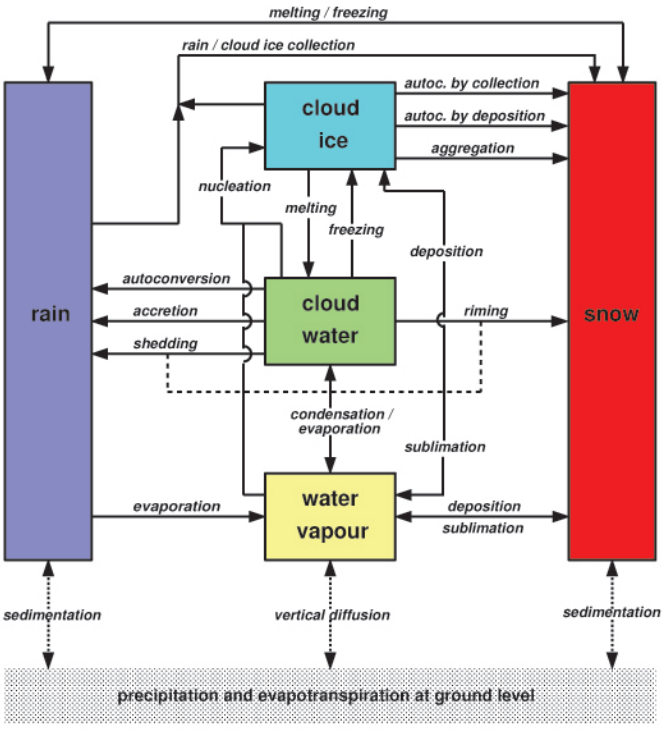

Figure 3.2: Microphysical processes of cloud and precipitation generation in the two-category ice scheme of DWD (from *Schulz and Schättler, 2011*). All conversion terms are defined positive, with the exception of the condensation and evaporation of cloud water S_c and the depositional growth and sublimation of snow S^s_{dep}, which are positive for condensation/deposition and negative for evaporation/sublimation.

Table 3.1: Sources and sinks in the two-category ice scheme of DWD and their dependency on predicted model variables.

term	process	function of
S_c	condensation and evaporation of cloud water	q_v
S^c_{au}	autoconversion of cloud water, producing rain	q_c
S^c_{ac}	accretion of cloud water by rain	q_c, q_r
S_{ev}	evaporation of rain	q_r, q_v
S_{nuc}	heterogeneous ice nucleation	T, q_v, q_i
S^c_{frz}	homogeneous ice nucleation	T, q_c
S^i_{dep}	deposition growth and sublimation of cloud ice	T, q_v, q_i
S^i_{melt}	melting of cloud ice	T, q_i
S^i_{au}	autoconversion of cloud ice, producing snow	q_i
S_{aud}	ongoing depositional growth of cloud ice, producing snow	T, q_i
S_{agg}	aggregation of snow (collection of cloud ice)	q_i, q_s
S_{rim}	riming of snow	T, q_c, q_s
S_{shed}	collection and shedding of cloud water by wet snow, producing rain	T, q_c, q_s
S^i_{cri}	collection of cloud ice by rain, producing snow	q_i, q_r
S^r_{cri}	freezing of rain due to collection of cloud ice by rain, producing snow	q_i, q_r, m_i
S^s_{dep}	depositional growth and sublimation of snow	q_s, q_v
S^r_{frz}	freezing of rain due to heterogeneous ice nucleation, producing snow	T, q_r
S^s_{melt}	melting of snow, producing rain	T, q_v, q_s

interaction processes as parameterized in DWD's two-category ice scheme, which is implemented in GME. As stated in Chap. 2.2, though undergoing changes regarding a particular hydrometeor class, in total, water mass remains constant. Table 3.1 lists all parameterized sources and sinks S, and additionally gives the model parameters of which they are dependent. Equations 3.1–3.5 show how conservation of total mass is ensured, and how the source and sink terms add to the water mass of each hydrometeor class. All conversion terms are defined positive, with exception of the condensation and evaporation of cloud water S_c and the depositional growth and sublimation of snow S^s_{dep}, which are positive for condensation/deposition and negative for evaporation/sublimation.

$$S^v = -S_c + S_{ev} - S^i_{dep} - S^s_{dep} - S_{nuc} \tag{3.1}$$

$$S^c = S_c - S^c_{au} - S^c_{ac} - S^c_{frz} + S^i_{melt} - S_{rim} - S_{shed} \tag{3.2}$$

$$S^i = S_{nuc} + S^c_{frz} + S^i_{dep} - S^i_{melt} - S^i_{au} - S_{aud} - S_{agg} - S^i_{cri} \tag{3.3}$$

$$S^r = S^c_{au} + S^c_{ac} - S_{ev} + S_{shed} - S^r_{cri} - S^r_{frz} + S^s_{melt} \tag{3.4}$$

$$S^s = S^i_{au} + S_{aud} + S_{agg} + S_{rim} + S^s_{dep} + S^i_{cri} + S^r_{cri} + S^r_{frz} - S^s_{melt} \tag{3.5}$$

The transfer rate for condensation and evaporation S_c is obtained by saturation adjustment:

it is assumed that in case of supersaturation with respect to liquid phase a sufficient number of CCN is always present, enabling the formation of cloud droplets. Heterogeneous ice nucleation through heterogeneous deposition S_{nuc} is parameterized by a simple temperature-dependent relation following *Fletcher (1962)*. For temperatures below $-25\,°C$, supersaturation with respect to frozen phase is sufficient for heterogeneous deposition to occur. For temperatures between $-25\,°C$ and $-6\,°C$, supersaturation with respect to liquid phase is required, too. In both cases, no cloud ice is yet allowed to be present ($q_i = 0$). Exemplarily, the source and sink term for heterogeneous ice nucleation S_{nuc} is given in Eq. 3.6. For the exact formulations of all other source and sink terms it is referred to the model documentation (*Doms et al., 2011*).

$$S_{nuc} = \rho^{-1} \cdot m_i^0 \cdot \Delta t^{-1} N_i(T) \tag{3.6}$$

Homogeneous ice nucleation S^c_{frz} of all cloud water instantaneously sets in for temperatures below $-37\,°C$. Note that homogeneous freezing in this scheme refers to freezing of pure water only and does not include homogeneous ice nucleation of liquid aerosols.

Once pristine ice crystals exist, they can continue to grow (or shrink away) by water vapour deposition (cloud ice sublimation) S^i_{dep}, which sets in for supersaturation (subsaturation) with respect to frozen phase. This depends on the number concentration of cloud ice particles $N_i(T)$ which in turn is temperature dependent (how the number concentrations N_x are parameterized is explained in detail in the respective sections of the model versions). To avoid unnaturally large ice crystals, their size is limited to a maximum diameter of $\sim 200\,\mu m$.

Rain production through autoconversion of cloud water S^c_{au} is parameterized as a function of the specific content of cloud water q_c without any autoconversion thresholds. Snow production through autoconversion of cloud ice S^i_{au} is parameterized in similar manner. Snow production through further depositional growth of cloud ice S_{aud} is dependent on the time scale for cloud ice to grow to snow of initial snow mass $3 \times 10^{-9}\,kg$ (corresponding to a minimum snowflake diameter of $\sim 300\,\mu m$). Further mass increase of rain by accretion S^c_{ac} and further mass increase of snow by aggregation S_{agg} is included. For temperatures below (above) freezing level riming of snow (shedding) S_{rim} (S_{shed}) occurs. Note that in the cloud microphysical scheme of the model, the term shedding is not used in the sense of liquid-coated frozen particles shedding the liquid layer off as rain, as introduced in Chap. 2.1. Rather, it is the collection of cloud water by falling, melting snow and the subsequent shedding off of this liquid coating as rain. The collision of supercooled rain with cloud ice leads to instantaneous freezing of the rain which is from then on considered to be snow. This snow production process involves two sinks since it firstly decreases cloud ice S^i_{cri} and secondly decreases rain S^r_{cri}. Two diffusional growth processes are parameterized: evaporation of rain S_{ev} and deposition/sublimation of snow S^s_{dep}. The latter is defined positive for deposition. Melting of cloud ice S^i_{melt} occurs instantaneously when temperature rises above $0\,°C$. Melting of snow S^s_{melt} occurs gradually when temperature rises above $0\,°C$.

The heterogeneous ice nucleation mechanisms contact and immersion freezing of rain to form snow are combined to one transfer term S^r_{frz} and occur below a temperature threshold of $-2\,°C$. For all included sources and sinks, if not stated otherwise, all conversion rate coefficients, collection (sticking) efficiencies, or similar, are set to constant numerical values based on empirical studies. For the exact numbers it is referred to the model documentation (*Doms et al., 2011*).

In the following sections, the exact microphysical parameterizations, in particular the mass-size relations and the PSDs of the different hydrometeor classes, are given separately for the various model versions.

3.1.3 GMEdiag

Model development is an ongoing and rapid process. Therefore, the GME version serving as a control run for the experiment (described in the following Chap. 3.1.4) in the present study varies throughout the study. Release version GME 2.19 is the basis for GME6864 which was run for a period of eleven days, from 2 August 2008 to 12 August 2008, and during this period, serves as control run. This is the period the presented case study (see Chap. 6.3) is taken from. For the statistical approach (see Chap. 6.4), the GME version operational up to 1 February 2010 serves as control run. The only difference to GME6864 is, that it is based on a more recent release version, namely GME 2.20. The two release versions GME 2.19 and GME 2.20 merely differ with respect to the implemented aerosol climatology, which has no impact on the investigations performed in the present study. Therefore, GME6864 and the more recently operational GME version can be considered to be identical. In the following, the control run is always referred to as GMEdiag, whether it is the one or the other version. The reason for this naming will become clear in the following.

GMEdiag features a two-category ice scheme as described in Chap. 3.1.2. The non-precipitating hydrometeor classes cloud water and cloud ice are treated prognostically. The precipitating hydrometeor classes rain and snow are treated diagnostically, that is the full budget equation (Eq. 2.6) is reduced to a diagnostic relation by neglecting horizontal advection and prescribing stationarity and horizontal homogenity for total mass fraction q_x.

$$-\frac{1}{\rho}\frac{\partial P_x}{\partial z} = S^x \tag{3.7}$$

For hydrostatic models with coarse resolution this is applicable, since the characteristic timescale for horizontal transport is long compared to the time a precipitating particle needs to reach the ground. Consequently, particles will reach the ground before entering an adjacent column. Since the precipitation fluxes P_x are a function of the total mass fraction q_x (see Chap. 2.2), they replace the total mass fraction q_x in the formulation of the sources

and sinks S^x and become the dependent variable. For each time step, the diagnostic budget equation (Eq. 3.7) is integrated from top to bottom, yielding the precipitation rates at the surface.

In the following, the assumptions on mass-size relations and PSDs of the hydrometeor classes made in GMEdiag, as required for bulk water-continuity models, are described. For both non-precipitating hydrometeor classes, that is cloud water (index $x = c$) and cloud ice (index $x = i$), a monodisperse PSD is assumed. That is, all particles in the population are of the same size:

$$N_x = N_{0_x} \tag{3.8}$$

$$D_x = D_{0_x} \tag{3.9}$$

For cloud water, the diameter D_c is fixed to a constant $D_{0_c} = 20\,\mu$m. Cloud water is assumed to consist of spherical droplets. The indices of the mass-size relation (Eq. 2.1) for cloud water are given in Table 3.3. For cloud ice, the number concentration N_i is fixed to a value $N_{0_i}(T)$ dependent on temperature T (in °C) to implicitely take ice enhancement (see Chap. 2.1) into account.

$$N_i(T) = N_{0_i}(T) = 100\,m^{-3} \cdot e^{-0.2 \cdot T} \tag{3.10}$$

Cloud ice is assumed to consist of hexagonal plates. The density of cloud ice is fixed to $\rho_i = 5 \times 10^{-2}\,\mathrm{kg\,m^{-3}}$, resulting in the indices of the mass-size relation (Eq. 2.1) for cloud ice as given in Table 3.3. However, ice crystal size is limited to a maximum of diameter $D_{i_{max}} = 200\,\mu$m.

For both precipitating hydrometeor classes, that is rain (index $x = r$) and snow (index $x = s$), an exponential PSD is assumed:

$$N_x(D) = N_{0_x} \cdot e^{-\lambda_x D}, \tag{3.11}$$

with intercept parameter N_{0_x} in $\mathrm{m^{-4}}$ and slope parameter λ_x in $\mathrm{m^{-1}}$. Rain is assumed to consist of spherical drops. A Marshall-Palmer distribution is assumed for rain, so that the intercept parameter for rain is set to an empirical value of $N_{0_r} = 8 \times 10^6\,\mathrm{m^{-4}}$. The indices of the mass-size relation (Eq. 2.1) for rain are given in Table 3.3. Snow is assumed to consist of densily rimed aggregates of dendrites with a maximum linear dimension D_s. The intercept parameter for snow is set to an empirical value of $N_{0_s} = 8 \times 10^5\,\mathrm{m^{-4}}$. The indices of the mass-size relation (Eq. 2.1) for snow are given in Table 3.3.

The terminal fall speeds of the precipitating hydrometeor classes v_T^x are size-dependent:

$$v_T^r = 130\,\mathrm{m^{1/2}\,s^{-1}} \cdot D^{1/2} \tag{3.12}$$

$$v_T^s = 15\,\mathrm{m^{1/2}\,s^{-1}} \cdot D^{1/2}. \tag{3.13}$$

3.1.4 GMEprog

On 2 February 2010, a novel version of GME went operational. Prior to being introduced into operational service, it was extensively tested. Firstly as GME6831, for a period of eleven days, from 2 August 2008 to 12 August 2008. Secondly as GME1007, for a four-month period from 1 July 2009 to 31 October 2009. As with the control run GMEdiag, the only difference between these two versions is the release version they are based on (GME6831 on GME 1.19 and GME1007 on GME 2.20) and no implications for the present study are expected. Therefore, this new GME version is in the following referred to as GMEprog, whether it is the one or the other version. The reason for this naming will become clear in the following. Note that the original experiment numbers might still be contained in some figures.

As the corresponding control run GMEdiag, GMEprog features a two-category ice scheme (see Chap. 3.1.2), but three major changes are introduced. Firstly, with general model development going towards resolution enhancement, the assumptions underlying diagnostic schemes are no longer valid. Especially for processes where horizontal transport is of importance, like for example lee-side precipitation, higher resolution models with diagnostic precipitation schemes will deliver erroneous results. Also, since GME delivers the boundary conditions for the regional models COSMO-EU and COSMO-DE, efforts are in progress at DWD to adjust the parameterizations of GME to those of COSMO-EU. Therefore, in support of ongoing model development, a prognostic precipitation scheme is introduced in GMEprog and replaces the diagnostic one in GMEdiag. This new prognostic precipitation scheme is based on the full prognostic budget equations (Eq. 2.6), however, advection is not yet implemented.

$$\frac{\partial q_x}{\partial t} - \frac{1}{\rho}\frac{\partial P_x}{\partial z} = S^x - \frac{1}{\rho}\nabla \cdot \vec{F}_x \tag{3.14}$$

Table 3.2: Coefficients and exponents of moment (from *Field et al., 2005*).

x	a_x	b_x
1	5.065339	0.476221
2	-0.062659	-0.015896
3	-3.032362	0.165977
4	0.029469	0.007468
5	-0.000285	-0.000141
6	0.312550	0.060366
7	0.000204	0.000079
8	0.003199	0.000594
9	0.000000	0.000000
10	-0.015952	-0.003577

The scheme follows *Rutledge and Hobbs (1983)*, *Lin et al. (1983)*, and *Doms et al. (2011)*. In contrast to the diagnostic scheme, where the precipitation fluxes P_x are the dependent variable (see Chap. 3.1.3), the sources and sinks S^x are now formulated in terms of total mass fraction q_x. Numerically, the prognostic budget equations cannot be solved in one step. Instead, preliminary values for the prognostic variables (i. e. specific contents q_x) are first calculated. With these, the sources and sinks and the sedimentation are obtained. In a third and final step, these values are used to update the values for the prognostic variables.

A second difference between GMEprog and GMEdiag is the treatment of snow. Based on aircraft measurements by *Field et al. (2005)*, a parameterization of the intercept parameter N_{0_s} of the exponential snow size distribution (Eq. 3.11) is introduced in GMEprog. The intercept parameter N_{0_s} is now proportional to the number concentration of snowflakes and is described as a function of temperature T and specific content of snow q_s.

$$N_{0_s} = \frac{27}{2}\, a(3,T)^{-3} \left(\frac{q_s}{0.069}\right)^{4-3b(3,T)} = 13.5 \cdot \frac{\mathcal{M}_2^4}{\mathcal{M}_3^3} \tag{3.15}$$

The functions $a(3,T)$ and $b(3,T)$ are given in Table 3.2 (Table 2 of *Field et al., 2005*), with

$$\begin{aligned} \log_{10} a(3,T) = {} & a_1 + a_2 \cdot T_m + 3 \cdot a_3 + 3 \cdot a_4 \cdot T_m + a_5 \cdot T_m^2 + 3^2 \cdot a_6 \\ & + 3 \cdot a_7 \cdot T_m^2 + 3^2 \cdot a_8 \cdot T_m + a_9 \cdot tm^3 + 3^3 \cdot a_{10} \end{aligned} \tag{3.16}$$

$$\begin{aligned} b(3,T) = {} & b_1 + b_2 \cdot T_m + 3 \cdot b_3 + 3 \cdot b_4 \cdot T_m + b_5 \cdot T_m^2 + 3^2 \cdot b_6 \\ & + 3 \cdot b_7 \cdot T_m^2 + 3^2 \cdot b_8 \cdot T_m + b_9 \cdot tm^3 + 3^3 \cdot b_{10}. \end{aligned} \tag{3.17}$$

$\mathcal{M}_{2,3}$ are second and third moments (Eq. 2.3), specific content of snow q_S is in $\mathrm{kg\,kg^{-1}}$, and mean temperature T_m in °C (but between −40 °C and 0 °C). Furthermore, the intercept parameter N_{0_s} is in two ways constrained, ensuring that

$$38.1375 \cdot 10^5 \cdot \exp(-0.107 \cdot T_m) \leq \exp(-0.107 \cdot T_m) \leq 7.6275 \cdot 10^8 \cdot \exp(-0.107 \cdot T_m) \tag{3.18}$$

and

$$10^6 m^{-4} \leq N_{0_s} \leq 10^9 m^{-4}. \tag{3.19}$$

The third and final difference between GMEdiag and GMEprog is the treatment of the autoconversion of cloud ice S_{au}^i and aggregation S_{agg}. The constant numerical value is replaced by a temperature-dependent sticking efficiency $e_i(T)$ similar to *Lin et al. (1983)*:

$$e_i(T) = \max(0.2, \min\{\exp[0.09(T - T_0)], 1.0\}), \tag{3.20}$$

with $T_0 = 273.15\,\mathrm{K}$ and T in K.

Table 3.3: Coefficients of mass-size relations and PSDs as implemented in the evaluated GME versions.

model version	hydrometeor type	diagnostic (d) or prognostic (p)	distribution type	α	β	D_0	N_0
GMEdiag	cloud water	p	monodisperse	524	3	20	
	cloud ice	p	monodisperse	130	3		cf. Eq. 3.10
	rain	d	exponential	524	3		8×10^6
	snow	d	exponential	0.038	2		8×10^5
GMEprog	cloud water	p	monodisperse	524	3	20	
	cloud ice	p	monodisperse	130	3		cf. Eq. 3.10
	rain	p	exponential	524	3		8×10^6
	snow	p	exponential	0.069	2		cf. Eq. 3.15

3.2 COSMO-DE

COSMO-DE is an application of the COSMO model (Consortium for Small-scale Modelling; `http://www.cosmo-model.org`) and in operational forecast service at DWD. In the following, general aspects of COSMO-DE, its microphysics, and in particular differences between the various model versions evaluated in the present study, are described. For a more comprehensive introduction to COSMO-DE see *Baldauf et al. (2011)*. For details on the cloud microphysical parameterizations see *Doms et al. (2011)* and *Köhler (2013)*. For details on the preprocessing to obtain the lateral boundary conditions see *Schättler (2012)*.

3.2.1 General aspects

COSMO-DE (*Baldauf et al., 2011*) is the cloud-resolving regional NWP model at DWD. Operational since 16 April 2007, it is a non-hydrostatic, fully compressible limited-area model of the atmosphere, covering Germany and its neighbouring countries, as depicted in Fig. 3.3. The primitive thermo-hydrodynamical equations describing compressible flow in a moist atmosphere are solved using a finite-difference method on an Arakawa-C grid. COSMO-DE uses rotated latitude/longitude coordinates in the horizontal and time-indepen dent, generalized terrain-following coordinates in the vertical. The model versions utilized in this study have a horizontal resolution of 2.8 km and, if not stated otherwise in the respective chapters, 50 hybrid levels in the vertical. Level thickness ranges approximately from 20 m at the Earth's surface, 400 m in 5 km height, to 1000 m in 20 km height. Operationally, forecasts are initialized every three hours (at 0, 3, 6, 9, 12, 15, 18, and 21 UTC) and are available in hourly resolution. The model can be initialized using interpolated data from various coarse-grid models, such as GME and COSMO-EU, both operated by DWD itself, or IFS, operated by ECMWF. The interpolation of the coarser grid model data to initial and/or boundary data on COSMO-DE grid resolution is performed by the program

INT2LM (*Schättler, 2012*). Operationally, the closest COSMO-EU forecasts (1-, 2-, and 3-hour old) are used. These first guesses are updated through continuous four-dimensional data assimilation based on observation nudging (nudgecast). COSMO-DE currently assimilates observations of temperature, pressure, relative humidity, two-dimensional horizontal wind vector, geopotential, and precipitation rate from synoptic stations, drifting buoy, radiosondes, aircrafts, ground-based wind profilers, and the German radar network (*Schraff and Hess, 2012*).

As GME, COSMO-DE provides grid-scale and subgrid-scale (stratiform and convective) cloud information. No feedback between the three cloud types occurs, except for the dependency on changes in water vapour and temperature, and when convective precipitation falls out. In the following, the grid-scale cloud scheme, that is the microphysical parameterization of the model is explained in detail.

In the present study, all COSMO-DE runs are based on release version COSMO-DE 4.18, because this is the release version which was operational from 26 May 2011 to 1 August 2011, the time *Köhler (2013)* began with the development of the new two-moment cloud ice scheme. For computational cost reasons, the initial conditions of all COSMO-DE runs are obtained from existing analyses of a COSMO-EU experiment (COSMO-EU8273), initialized at 0, 6, and 12 UTC. These boundary conditions are interpolated hourly to the COSMO-DE grid with INT2LM v1.18 (*Schättler, 2012*).

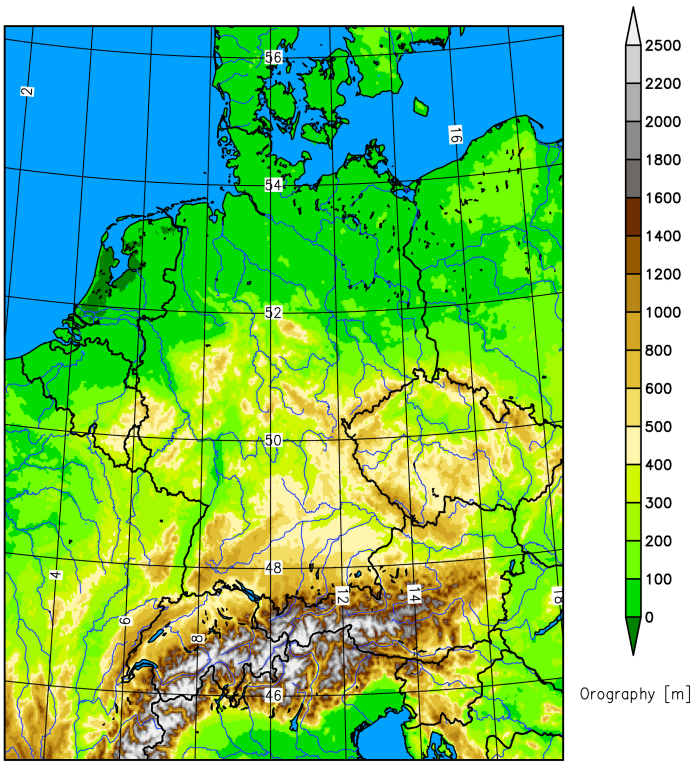

Figure 3.3: Model domain of COSMO-DE (from *Doms et al., 2011*).

3.2.2 Cloud microphysics: Three-category ice scheme

As in GME, grid-scale precipitation in COSMO-DE and the associated cloud microphysical interactions are formulated as a bulk scheme. However, the currently operational cloud microphysical scheme of COSMO-DE includes a fifth hydrometeor class: graupel (index $x = g$), which is defined similar to snow, but due to its production processes features a higher density and fall speed. The introduction of graupel improves the model's performance in synoptic situations with strong updrafts, that is in more convective situations, since in these situations graupel-like particles are likely to occur. Owing to the number of frozen phase hydrometeor classes, this scheme is commonly referred to as the three-category ice scheme (*Reinhardt and Seifert, 2006*).

Figure 3.4 gives a schematic overview of the hydrometeor classes and the interaction processes as parameterized in DWD's three-category ice scheme, which is implemented in the currently operational version of COSMO-DE. Table 3.4 lists all parameterized sources and sinks S, and additionally gives the model parameters of which they are dependent. Equations 3.21–3.26 show how conservation of total mass is ensured, and how the source and

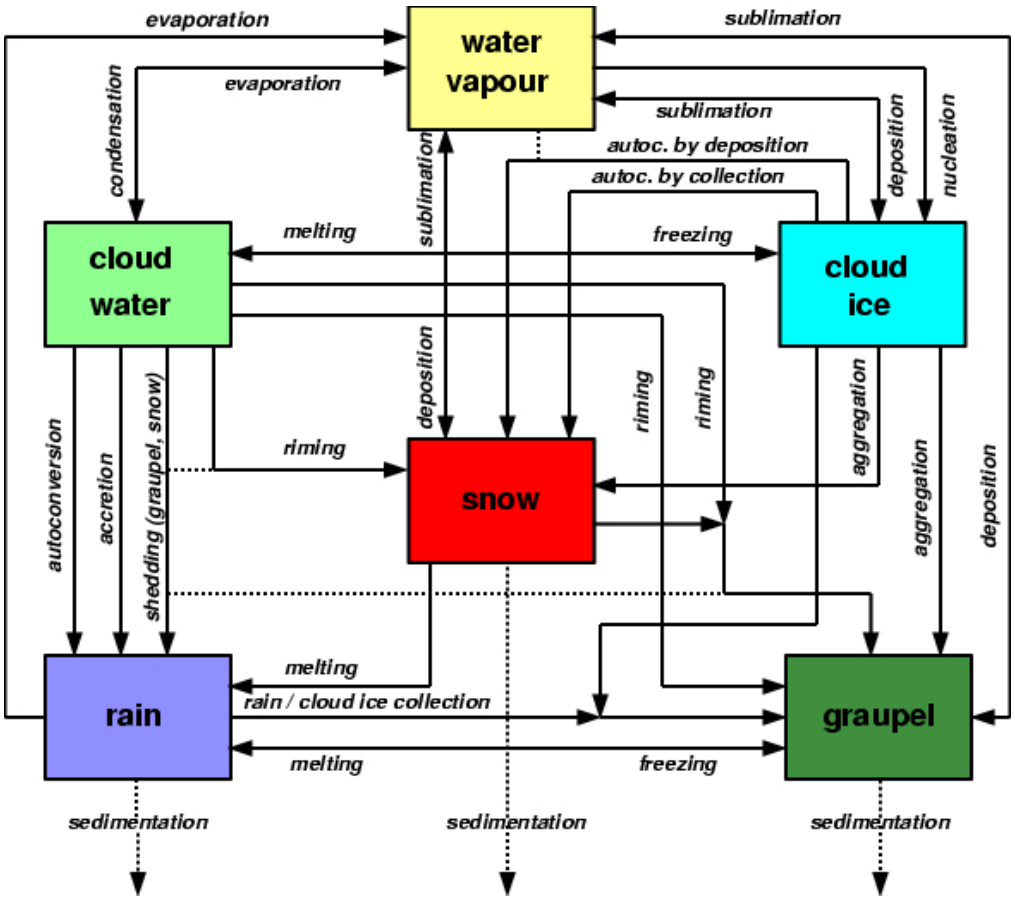

Figure 3.4: Microphysical processes of cloud and precipitation generation in the three-category ice scheme of DWD (from *Doms et al., 2004*).

sink terms add to the water mass of each hydrometeor class.

$$S^v = -S_c + S_{ev} - S^i_{dep} - S^s_{dep} - S^g_{dep} - S_{nuc} - S_{conr} \tag{3.21}$$

$$S^c = S_c - S^c_{au} - S^c_{ac} - S^c_{frz} + S^i_{melt} - S_{rim} - S_{shed} - S_{rim2} \tag{3.22}$$

$$S^i = S_{nuc} + S^c_{frz} + S^i_{dep} - S^i_{melt} - S^i_{au} - S_{aud} - S_{agg} - S^i_{cri} - S_{agg2} \tag{3.23}$$

$$S^r = S^c_{au} + S^c_{ac} - S_{ev} + S_{shed} - S^r_{cri} - S^r_{frz} + S^s_{melt} + S^g_{melt} + S_{conr} \tag{3.24}$$

$$S^s = S^i_{au} + S_{aud} + S_{agg} + S_{rim} + S^s_{dep} - S^s_{melt} - S_{consg} \tag{3.25}$$

$$S^g = S_{agg2} + S_{rim2} + S^g_{dep} - S^g_{melt} + S_{consg} + S^r_{frz} + S^i_{cri} + S^r_{cri} \tag{3.26}$$

Table 3.4: Sources and sinks in the three-category ice scheme of DWD and their dependency on predicted model variables. The horizontal lines separate between sources and sinks whoes parameterization is as in the two-category ice scheme (top), whoes parameterizations have changed in comparison to the two-category ice scheme (middle), or that are not included at all in the two-category ice scheme (bottom). All conversion terms are defined positive, with exception of the condensation and evaporation of cloud water S_c and the depositional growth and sublimation of snow S^s_{dep} and S^g_{dep}, which are positive for condensation/deposition and negative for evaporation/sublimation.

term	process	function of
S_c	condensation and evaporation of cloud water	q_v
S^c_{ac}	accretion of cloud water by rain	q_c, q_r
S_{ev}	evaporation of rain	q_v, q_r
S_{nuc}	heterogeneous ice nucleation	T, q_v, q_i
S^c_{frz}	homogeneous ice nucleation	T, q_c
S^i_{dep}	deposition growth and sublimation of cloud ice	T, q_v, q_i
S^i_{melt}	melting of cloud ice	T, q_i
S^i_{au}	autoconversion of cloud ice, producing snow	q_i
S_{aud}	ongoing depositional growth of cloud ice, producing snow	T, q_i
S_{agg}	aggregation of snow (collection of cloud ice)	q_i, q_s
S_{rim}	riming of snow	T, q_c, q_s
S^s_{dep}	deposition growth and sublimation of snow	q_v, q_s
S^s_{melt}	melting of snow, producing rain	T, q_v, q_s
S^c_{au}	autoconversion of cloud water, producing rain	q_c
S_{shed}	collection and shedding of cloud water by wet snow and graupel, producing rain	T, q_c, q_s, q_g
S^i_{cri}	collection of cloud ice by rain, producing graupel	q_i, q_r
S^r_{cri}	freezing of rain due to collection of cloud ice by rain, producing graupel	q_i, q_r, m_i
S^r_{frz}	freezing of rain due to heterogeneous ice nucleation, producing graupel	T, q_r
S_{conr}	condensation on melting snow and graupel, producing rain	q_v, q_s, q_g
S_{consg}	conversion from snow to graupel due to riming	q_c, q_s
S_{agg2}	aggregation of graupel	q_i, q_g
S_{rim2}	riming of graupel	T, q_c, q_g
S^g_{dep}	deposition growth and sublimation of graupel	q_v, q_g
S^g_{melt}	melting of graupel, producing rain	T, q_v, q_g

The following sources and sinks are parameterized exactly as in the two-category ice scheme (see Chap. 3.1.2): condensation and evaporation of cloud water S_c, accretion of cloud water by rain S^c_{ac}, evaporation of rain S_{ev}, heterogeneous ice nucleation S_{nuc}, homogeneous ice nucleation S^c_{frz}, depositional growth and sublimation of cloud ice S^i_{dep}, melting of cloud ice S^i_{melt}, autoconversion of cloud ice S^i_{au}, ongoing depositional growth of cloud ice S_{aud}, aggregation of snow S_{agg}, riming of snow S_{rim}, depositional growth and sublimation of snow S^s_{dep}, and melting of snow S^s_{melt}.

Due to the introduction of a further hydrometeor class, graupel, some transfer rates change: Cloud ice collection by rain, S^i_{cri} and S^r_{cri}, now leeds to the production of graupel rather than snow. The same applies for the homogeneous freezing of rain S^r_{frz} below $-37\,°\mathrm{C}$. Besides, the tranfer rate S^r_{frz} now also includes a formulation for heterogeneous freezing of rain to form graupel, for temperatures above $-37\,°\mathrm{C}$. Rain production through collection and shedding of cloud water S_{shed} now occurs from wet snow and wet graupel. Finally, a threshold value of $0.2\,\mathrm{g\,kg^{-1}}$ for specific cloud water content q_c is introduced for autoconversion of cloud water S^c_{au}.

Additionally, due to the introduction of graupel, some completely new sources and sinks arise. Rain production can occur through condensation on melting snow and graupel S_{conr}. Snow is converted into graupel by riming S_{consg} if the amount of collected supercooled cloud water by snow exceeds 12 % of the volume of the snowflake. This process is active for specific cloud water contents above $0.2\,\mathrm{g\,kg^{-1}}$. For temperatures below freezing level, further mass increase of graupel can occur by aggregation S_{agg2} and riming S_{rim2}, both parameterized analogously to snow. As a diffusional growth process, depositional growth and sublimation of graupel S^g_{dep} are included. S^g_{dep} is positive (negative) for deposition (sublimation). Finally, melting of graupel S^g_{melt} occurs gradually when temperature rises above $0\,°\mathrm{C}$.

For all included sources and sinks, if not stated otherwise, all conversion rate coefficients, collection (sticking) efficiencies, or similar, are set to constant numerical values based on empirical studies. For the exact numbers it is referred to the model documentation (*Doms et al., 2011*).

3.2.3 COSMO-DE9009 (three-category ice scheme)

COSMO-DE9009 serves as control run for the COSMO-DE experiments conducted within the present study. Like the currently operational COSMO-DE version, COSMO-DE9009 features a three-category ice scheme as described in Chap. 3.2.2. All hydrometeor classes are treated prognostically. The full budget equations (Eq. 2.6) are used. In contrast to the prognostic scheme implemented in GMEprog, this scheme allows for advection.

In the following, the assumptions on mass-size relations and PSDs of the hydrometeor

classes made in COSMO-DE9009 are described. The hydrometeor classes cloud water, cloud ice, and snow are treated exactly as in GMEprog (see Chap. 3.1.4), that is, exactly the same PSDs and mass-size relations are used. For rain, a gamma-shaped PSD is assumed:

$$N_r(D) = N_{0_r} \cdot D^{\mu} \cdot e^{-\lambda_r D}, \tag{3.27}$$

with $\mu = 0.5$ and N_{0_r} =$3.96 \times 10^7\,\mathrm{m}^{-4}$. The assumptions on the mass-size relation of rain remain the same as for GMEprog (see Chap. 3.1.4) and are given in Table 3.6. For graupel (index $x = g$), an exponential PSD is assumed (Eq. 3.11). Graupel is assumed to consist of frozen spheroids with a higher density than snow. The indices of the mass-size relation (Eq. 2.1) for graupel are given in Table 3.6. The terminal fall speed of graupel is size-dependent, analogous to rain and snow:

$$v_T^g = 442\,\mathrm{m}^{1/2}\,\mathrm{s}^{-1} \cdot D^{0.89} \tag{3.28}$$

COSMO-DE9009 was run as a nudgecast for 24 h for a period of one month, from 1 June 2010 to 30 June 2010.

3.2.4 COSMO-DE8819 (two-category ice scheme)

Since the actual experiment investigated in the present study, COSMO-DE8822 (introduced in Chap. 3.2.5), is based on a two-category ice scheme (in contrast to a three-category ice scheme as the operational COSMO-DE version), a second control run is performed within the present study: COSMO-DE8819. COSMO-DE8819 features a two-category ice scheme as described in Chap. 3.1.2, but in contrast to GME it does account for advection and assumes a gamma distribtion for rain, as described in Chap. 3.2.2 and Chap. 3.2.3. The indices of the mass-size relations and the PSDs are summarized in Table 3.6. COSMO-DE8819 was run as a nudgecast for 24 h for a period of one month, from 1 June 2010 to 30 June 2010.

3.2.5 COSMO-DE8822 (two-moment cloud ice scheme)

Since cirrus clouds are still a major challenge in atmospheric modelling, efforts are in progress at DWD to develop an efficient ice nucleation scheme which is both physically consistent and computationally efficient. A novel cloud microphysical scheme was developed and implemented into COSMO-DE by *Köhler (2013)*. The model runs conducted with it in the present study are in the following referred to as COSMO-DE8822.

COSMO-DE8822 is based on DWD's two-category ice scheme as introduced in Chap. 3.2.2. The two-category ice scheme was chosen instead of COSMO-DE's standard three-category ice scheme, since the new scheme was originally designed for GME, for which a three-

category ice scheme is not reasonable, due to its coarse resolution. In COSMO-DE8822, the hydrometeor classes cloud water, rain, and snow are treated exactly as in COSMO-DE8819 (see Chap. 3.2.4). For cloud ice, a two-moment parameterization is introduced. That is, not only the specific hydrometeor content of cloud ice q_i as in the one-moment schemes, but also the number concentration for cloud ice $N_i(D)$ is predicted. This is physically more reasonable than the one-moment treatment, but computationally not so demanding as the complete two-moment scheme of *Seifert and Beheng (2006)*.

Additionally, cloud ice is split into two modes according to its formation: homogeneous and heterogeneous ice nucleation. Hence, this scheme is commonly referred to as the two-moment two-mode cloud ice scheme. However, COSMO-DE8822 as investigated in the present study uses a computationally more efficient version of the original *Köhler (2013)* scheme: Though both homogeneous and heterogeneous ice nucleation are included, both processes contribute to one q_i and $N_i(D)$. This way, instead of having three additional prognostic variables, only one additional prognostic variable (the number concentration of cloud ice $N_i(D)$) has to be computed in comparison to the two-category ice scheme. Therefore, the scheme used in the present study in COSMO-DE8822 is referred to as the two-moment cloud ice scheme. Table 3.5 lists all parameterized sources and sinks S, and additionally gives the model parameters of which they are dependent. Equations 3.29–3.33 show how conservation of total mass is ensured, and how the source and sink terms add to the water mass of each hydrometeor class.

$$S^v = -S_c + S_{ev} - S^i_{dep} - S^s_{dep} - S_{nuc} - S_{nuc2} \tag{3.29}$$

$$S^c = S_c - S^c_{au} - S^c_{ac} - S^c_{frz} + S^i_{melt} - S_{rim} - S_{shed} \tag{3.30}$$

$$S^i = S_{nuc} + S_{nuc2} + S^c_{frz} + S^i_{dep} - S^i_{melt} - S^i_{au} - S_{aud} - S_{agg} - S^i_{cri} \tag{3.31}$$

$$S^r = S^c_{au} + S^c_{ac} - S_{ev} + S_{shed} - S^r_{cri} - S^r_{frz} + S^s_{melt} \tag{3.32}$$

$$S^s = S^i_{au} + S_{agg} + S_{rim} + S^s_{dep} + S^i_{cri} + S^r_{cri} + S^r_{frz} - S^s_{melt} \tag{3.33}$$

All conversion terms are defined positive, with exception of S_c and S^s_{dep}, which are positive for condensation/deposition and negative for evaporation/sublimation.

Apart from the two-moment treatment for cloud ice, several other changes to the ice nucleation processes are introduced in COSMO-DE8822. Firstly, the old heterogeneous ice nucleation scheme partly following *Fletcher (1962)* (therefore referred to as modified *Fletcher (1962)* scheme) is replaced by a new one based on *Phillips et al. (2008)*. The old heterogeneous ice nucleation scheme was meant to incorporate both heterogeneous ice nucleation itself and homogeneous ice nucleation of liquid aerosols in one source and sink term S_{nuc} ((pure) homogeneous ice nucleation is treated in S^c_{frz}). However, the empirical formulation of the modified *Fletcher (1962)* scheme represents heterogeneous ice nucleation far better than homogeneous ice nucleation of liquid aerosols. Also, heterogeneous ice nucleation is parameterized merely as a function of temperature in this scheme. Contrary, the new two-moment cloud ice scheme now accounts for heterogeneous ice nucleation S_{nuc} (*Phillips*

Table 3.5: Sources and sinks in the two-moment cloud ice scheme of DWD and their dependency on predicted model variables.

term	process	function of
S_c	condensation and evaporation of cloud water	q_v
S^c_{au}	autoconversion of cloud water, producing rain	q_c
S^c_{ac}	accretion of cloud water by rain	q_c, q_r
S_{ev}	evaporation of rain	q_r, q_v
S_{nuc}	homogeneous ice nucleation of supercooled liquid aerosols	T, q_v
S_{nuc2}	heterogeneous ice nucleation	T, q_v
S^c_{frz}	homogeneous ice nucleation	T, q_c
S^i_{dep}	deposition growth and sublimation of cloud ice	T, q_v
S^i_{melt}	melting of cloud ice	T, q_i
S^i_{au}	autoconversion of cloud ice, producing snow	q_i
S_{aud}	ongoing depositional growth of cloud ice, producing snow	T, q_i
S_{agg}	aggregation of snow (collection of cloud ice)	q_i, q_s
S_{rim}	riming of snow	T, q_c, q_s
S_{shed}	collection and shedding of cloud water by wet snow, producing rain	T, q_c, q_s
S^i_{cri}	collection of cloud ice by rain, producing snow	q_i, q_r
S^r_{cri}	freezing of rain due to collection of cloud ice by rain, producing snow	q_i, q_r, m_i
S^s_{dep}	depositional growth and sublimation of snow	q_v, q_s
S^r_{frz}	freezing of rain due to heterogeneous nucleation, producing snow	T, q_r
S^s_{melt}	melting of snow, producing rain	T, q_v, q_s

et al., 2008) and homogeneous ice nucleation of liquid aerosols S_{nuc2} (*Kärcher et al., 2006*) separately. Heterogeneous ice nucleation is now dependent on aerosol PSDs (which can serve as IN) in addition to temperature. Three classes of background aerosols are included: inorganic black carbon (soot), insoluable organic carbon, and dust/metals. The initial IN number densities are obtained empirically from flow diffusion chamber measurements and are set to $162\,000\,\mathrm{cm}^{-3}$ for dust, $15\,\mathrm{cm}^{-3}$ for soot, and $1.77\,\mathrm{cm}^{-3}$ for organics. How many of these available IN are actually activated depends on temperature and supersaturation with respect to frozen phase. Organics dominate in case of deposition freezing, whereas soot dominates in case of condensation/immersion freezing.

Secondly, a tracking variable for activated IN is introduced. This was deemed necessary, because the *Phillips et al. (2008)* scheme favours heterogeneous ice nucleation by assuming a constant number of IN available for ice nucleation. If cloud ice is transformed into snow, these IN are lost and the model assumes it can produce new ones. This results in an overestimation of cloud ice produced by heterogeneous ice nucleation. With the new tracking variable, IN are only available after a mixing timescale of 2 h. The tracking variable constitutes a further prognostic variable which enhances the computational cost of the scheme. Also, heterogeneous ice nucleation is only triggered, if a maximum number of IN of $50\,\mathrm{l}^{-1}$

available for heterogeneous freezing is not exceeded.

Thirdly, the treatment of depositional growth of cloud ice S^i_{dep} is adjusted. Rather than merely being limited by supersaturation with respect to frozen phase, a more physical so-called relaxation approach with an exponential approximation to supersaturation with respect to frozen phase is chosen. Since the two cloud ice modes and snow all compete for available water vapour, their growth timescales are coupled. Though cloud water and rain also deplete water vapour through diffusion, these hydrometeor classes are neglected since their relaxation times are considered to be comparatively short.

Finally, as opposed to the operational COSMO-DE, cloud ice is considered as a precipitating hydrometeor class in the two-moment cloud ice scheme, thereby modifying its budget equation (Eq. 2.6) accordingly. The reason is that cloud ice sedimentation plays an important role in the life cycle of a cirrus cloud. The high supersaturation rates with respect to frozen phase observed in cirrus clouds are thought to be a result of the larger ice crystals falling out before having completely depleted supersaturation with respect to frozen phase. Therefore, the larger ice crystals become, the more important their sedimentation becomes. Also, the larger an ice crystal is, the larger its terminal fall velocity increases with increasing altitude (where ambient air density is lower). Consequently, the introduced terminal fall velocity for cloud ice incorporates two factors A and B (given in *Köhler, 2013*) which account for this difference in terminal fall velocity resulting from the ice crystal size difference.

$$v^i_T = A \cdot D^B \tag{3.34}$$

Table 3.6: Coefficients of mass-size relations and PSDs as implemented in the evaluated COSMO-DE versions.

model version	hydrometeor type	distribution type	α	β	D_0	N_0
COSMO-DE9009	cloud water	monodisperse	524	3	20	
	cloud ice	monodisperse	130	3		cf. Eq. 3.10
	rain	gamma	524	3		3.96×10^7
	snow	exponential	0.038	2		cf. Eq. 3.15
	graupel	exponential	169.6	3.1		4×10^6
COSMO-DE8819	cloud water	monodisperse	524	3	20	
	cloud ice	monodisperse	130	3		cf. Eq. 3.10
	rain	gamma	524	3		3.96×10^7
	snow	exponential	0.038	2		cf. Eq. 3.15
COSMO-DE8822	cloud water	monodisperse	524	3	20	
	cloud ice	monodisperse	130	3		prognostic
	rain	gamma	524	3		3.96×10^7
	snow	exponential	0.038	2		cf. Eq. 3.15

This formulation is similar to that of the terminal fall velocities described previously for the precipitating hydrometeors rain, snow, and graupel, except that the factors A and B are not fixed but variable in Eq. 3.34.

For all included sources and sinks, if not stated otherwise, all conversion rate coefficients, collection (sticking) efficiencies, or similar, are set to constant numerical values. For the exact numbers it is referred to the model documentation (*Doms et al., 2011*) and the description of the two-moment cloud ice scheme (*Köhler, 2013*). For details on the cloud microphysial parameterizations of the two-moment cloud ice scheme see *Köhler (2013)*. COSMO-DE8822 was run as a nudgecast for 24 h for a period of one month, from 1 June 2010 to 30 June 2010.

4 Satellite observations

Remote sensing in general looks back at a history of more than 60 years and today, a great variety of measurements is available. Concerning the measurement platform, three basic possibilities exist: ground-based, airborne, and satellite-based. The advantage of conventional ground-based measurements lies in the possibility of easily locating several instruments at the same site so that they view the same atmospheric volume. This allows for more sophisticated retrievals of atmospheric properties by fully exploiting sensor synergy (e. g. *Löhnert et al., 2008*). Furthermore, ground-based measurements are available at a high temporal resolution, and by now some comparatively long time series exist. The downside is that ground-based measurements are unevenly distributed over the Earth and especially sparse over the ocean and in developing countries. Though they are irreplacable, for example, as a testbed for future satellite missions or for retrieval development, they are not suitable for global climate monitoring or for evaluating an atmospheric model on its full domain, the task of the present study. Airborne measurements (based on aircrafts or balloons) again are only available on campaign basis (e. g. Tropical Warm Pool–International Cloud Experiment (TWP-ICE), *May et al., 2008*) or along specific flight routes. For the time and domain covered, campaign data deliver a comprehensive data set suitable and very much needed, for example, for parameterization development. But since neither long time series are available, nor a continuously high temporal and spatial coverage is provided, airborne measurements are not suitable for continuous model evaluation. In contrast, satellite-based measurements offer a global or near-global coverage. Also, the time series are the longest available. For these reasons, satellite data are exceptionally well-suited for model evaluation, in particular for global models. Meteorological satellites are devided into two basic types according to their orbits *Kidder and Haar (1995)*: geostationary orbits (GEO) and low Earth orbits (LEO). Both have their benefits (and downsides). GEO satellites provide a continuous time series over a specific region but owing to their high altitude at a coarse

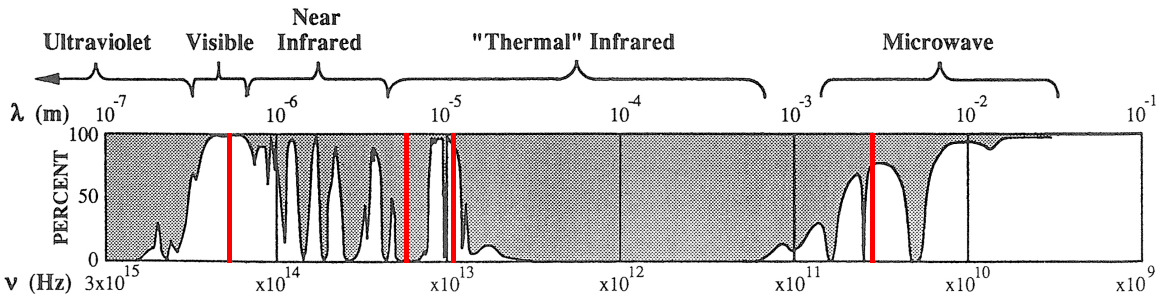

Figure 4.1: Spectrum of transmittance from microwave to visible wavelengths for standard atmosphere without hydrometeors (from *Grody, 1993*). Red: channels of instruments used in the present study.

resolution. LEO satellites have a much higher resolution but are forced to circle the Earth. Therefore, they do not pass the same spot on Earth very often but they deliver data on a near-global scale. If they are on sun-synchronous orbits, they are not suitable for observing the diurnal cycle, as is often the case with polar-orbiting satellites. The various available satellite observations enable to profit from their complementarity.

With respect to the remote sensing technique, two basic possibilities exist: active and passive measurements. Active instruments are essential for validating cloud microphysics, since they alone are able to deliver height-resolved information from the interior of a cloud. Passive instruments can aid, but they merely give column integrals. Focussing on cloud ice microphysics, active satellite-based (and airborne) measurements have an advantage compared to ground-based measurements: signals of active satellite-based instruments in the frozen part of the cloud are not so strongly affected by attenuation be atmospheric gases and hydrometeors, since they do not have to travel through lower humid/warm parts to reach the upper cold part of the cloud.

In general, remote sensing instruments differ in the range of frequency (or wavelength) of the electromagnetic spectrum in which they receive and/or emit radiation. At each frequency, the atmosphere is more or less transparent and information on different components can be obtained. Figure 4.1 depicts the spectrum of transmittance* for a clear atmosphere.

The present study utilizes data from three (two active and one passive) satellite-based sensors which measure in the visible, the infrared (IR), and the microwave range. These instruments are introduced in the following sections.

*Transmittance (also referred to as transmissivity) is the fraction of electromagnetic radiation which is not attenuated (through either scattering or absorption) and actually reaches the receiver (*Petty, 2006*).

4.1 CloudSat CPR

Launched on 28 April 2006, Cloud Satellite (CloudSat) is part of the so-called A-Train (or Afternoon Train; *Stephens et al., 2002*), which is a constellation of polar-orbiting, sun-synchronous satellites flying in an equatorial altitude of approximately 705 km in close succession to one another. This enables the satellites to sample the same column of air nearly at the same time. The A-Train satellites have an orbiting time of 1.5 h, with a constant local solar time overpass at a given latitude band. Maximum latitude covered is 82.5 °N/S. The orbit tracks of the A-Train satellites repeat every 16 days.

The payload of CloudSat is the Cloud Profiling Radar[†] (CPR; *Tanelli et al., 2008*), which is the first and to date only cloud radar in space. It is in operational mode since 2 June 2006 and was originally scheduled to operate for three years. However, with the exception of a longer breakdown in 2011 since which it is operating in daylight-only operations mode[‡], the CloudSat CPR has been operating without further disturbances to this day. It is maintained in cooperation between the Jet Propulsion Laboratory (JPL) of the National Aeronautics and Space Administration (NASA) and the Cooperative Institute for Research in the Atmosphere (CIRA) of Colorado State University. The CPR is a near-nadir-viewing[§] 94 GHz (W-band) radar measuring the power backscattered from the Earth's surface and from particles in the atmospheric column as a function of time (or range; time is converted into range using the speed of light in vacuum). The integration time step for one profile of 0.16 s results in a horizontal along-track resolution of 1.09±0.01 km. The integration leads to a footprint size of 1.3–1.4 km across track and 1.7–1.8 km along track. Vertically, the CPR's pulses sample a volume of 485 m and the data are digitized into 125 bins, each of approximately 240 m height, resulting in an oversampling of the data by a factor of two.

The radar equation for volume scattering (Eq. 4.1; *Rinehart, 1991*) relates transmitted and received powers P_t and P_r to the radar reflectivity η.

$$P_r = P_t \cdot \frac{\eta}{R^2} \cdot L^2 \cdot const. \tag{4.1}$$

R is the range and L^2 the two-way atmospheric attenuation. The constant is determined by instrument-specific factors as, for example, wave- and pulse length (see *Tanelli et al., 2008* for details). The radar reflectivity η is the integral over all (spherical) particles with diameter D (For non-spherical particles, depending on the context, this might be the diameter of a sphere with the same volume or surface area). The radar reflectivity is defined as a function of the respective backscatter cross section $\sigma(D)$ and the particle number concentration

[†]Radio detection and ranging.
[‡]On 17 April 2011 a battery anomaly forced CloudSat to leave the A-Train formation. From 27 October 2011 on data-collection was resumed in daylight-only. CloudSat returned to the A-Train on 15 Mai 2012 and since a manoevre on 18 July 2012 its footprint overlaps that from CALIPSO again.
[§]0.16 ° off-geodetic nadir since 15 August 2006 (*Tanelli et al., 2008*).

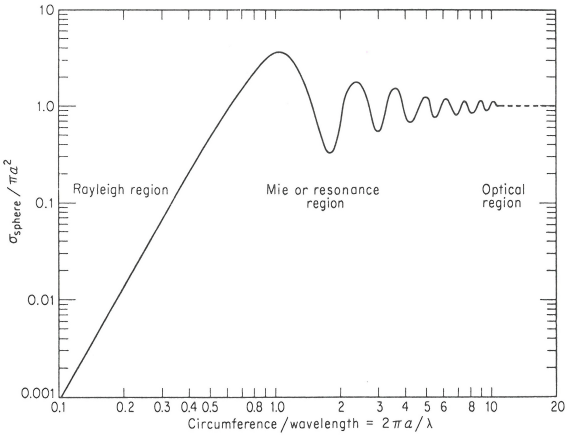

Figure 4.2: Normalized backscatter cross section σ of a sphere as a function of circumference normalized by wavelength λ (from *Rinehart, 1991*). a is the radius, in the present study depicted by r.

$N(D,R)$ (*Petty, 2006*):

$$\eta = \int_0^\infty \sigma(D) \cdot N(D,R) dD \tag{4.2}$$

For particles that are large in comparison to wavelength ($2\pi r/\lambda > 10$), the backscatter cross section σ is equal to the particle's geometric area ($\sigma = \pi \cdot r^2$; *Rinehart, 1991*). This is referred to as the optical region. For particles that are small in comparison to wavelength ($2\pi r/\lambda < 0.1$), the backscatter cross section is proportional to the sixth power of the particle radius ($\sigma = \pi^5 \cdot \lambda^{-4} \cdot |K|^2 \cdot D^6$; *Rinehart, 1991*). This is referred to as the Rayleigh region where the actual shape of the particle is not so relevant and can be treated as a sphere of equivalent volume. Figure 4.2 illustrates this effect. Inbetween ($0.1 < 2\pi r/\lambda < 10$), the backscatter cross section can also decrease with increasing particle size. This is the so-called Mie or resonance region (*Rinehart, 1991*), where shape plays a major role. Assuming Rayleigh scattering, the radar reflectivity η reformulates to

$$\eta_{Ray} = \frac{\pi^5}{\lambda^4} \cdot |K|^2 \cdot \int_0^\infty N(D,R) \cdot D^6 dD \tag{4.3}$$

However, it should be kept in mind that at the CloudSat CPR wavelength λ =3.2 mm, though the Rayleigh assumption is valid for small particles, larger particles violate the Rayleigh criterion. For example, a particle diameter of D =3 mm results in $D/\lambda = 0.94 \sim 1$). In these cases, the Rayleigh assumption leads to an overestimation of the radar reflectivity.

The dielectric factor of water K in Eq. 4.3 depends on the refractive index of water, which varies with frequency, but also with phase and temperature. The integral in Eq. 4.3 is defined as the so-called radar reflectivity factor z, which is equal to the sixth moment of the PSD $\mathcal{M}_6$. Therefore, the radar reflectivity factor z is very sensitive to particle size and the largest

particles in a population dominate it.

$$z_{Ray} = \int_0^\infty N(D) \cdot D^6 dD = \mathcal{M}_6 \tag{4.4}$$

In the data processing of the CloudSat CPR, the dielectric constant for liquid water K_{liq} is used to convert the radar reflectivity η_{Ray} into the equivalent[¶] (attenuated) radar reflectivity factor z_e. $|K_{liq}|^2$ is set to 0.75, which is representative for water at 10 °C in the W-band, a conventional procedure for remote sensing radars (*Austin et al., 2009*).

$$z_e = \eta_{Ray} \cdot \frac{\lambda^4}{\pi^5} \cdot \frac{1}{|K_{liq}|^2} \cdot 10^{18} \tag{4.5}$$

The multiplication with 10^{18} results in the common unit of $\mathrm{mm^6\,m^{-3}}$. Due to the large range in $\mathrm{mm^6\,m^{-3}}$ units, it is often preferred to give the equivalent radar reflectivity factor z_e in dBz (decibels relative to equivalent radar reflectivity factor z_e) and then capitalize the notation for distinction.

$$Z_e = 10 \cdot log_{10}\left(\frac{z_e}{1\,\mathrm{mm^6\,m^{-3}}}\right) \tag{4.6}$$

This is the parameter provided in the level 2B products of the CloudSat data processing center which are utilized in the present study. For more on the standard CloudSat products refer to the CloudSat handbook (*CIRA, 2008*).

The CloudSat CPR features a detection limit of approximately -27 dBz with a dynamic range up to $+29$ dBz and an accuracy of about 1 dBz (*Protat et al., 2009*). The CPR is designed so that its signal is dominated by cloud particles. The downside of the high frequency is that the signal is quickly attenuated by larger particles. Large rain drops can attenuate the signal completely. However, previous studies find smaller signal losses from attenuation than expected from single scattering effects alone. Apparently, the expected attenuation losses are partially compensated for by multiple scattering effects which enhance the signal to values above detection limit (e. g. *Battaglia et al., 2007*). In fact, attenuation and multiple scattering can be regarded as two different forms of appearance of multiple interactions of emitted radiation within the radar field of view (*Battaglia et al., 2011*). *Battaglia et al. (2008a)* identify three scattering regimes. In the first the single scattering assumption is valid. *Battaglia et al. (2008b)* only find significant multiple scattering effects for surface rain rates exceeding $3\,\mathrm{mm\,h^{-1}}$. In all other cases, the single scattering assumption is valid.

The quality of the equivalent radar reflectivity factor measured by the CloudSat CPR has been comprehensively validated by means of worldwide distributed ground-based as well as airborne cloud radar instruments. Validations with ground-based data allow statistical comparisons of long time series but either assume homogeneous conditions between satellite pixel and ground location or constrain measurements to match a certain time and space

[¶]The equivalent radar reflectivity factor is often also referred to as effective radar reflectivity factor.

window. Validations with airborne data enable a more direct comparison along a certain cross section but on a limited number of samples (*Protat et al., 2009*). According to *Protat et al. (2009)*, the quality of CloudSat's equivalent radar reflectivity factor measurements of cloud ice in comparison to ground-based sites is very good, with the weighted mean difference $Z_{e,CloudSat} - Z_{e,ground}$ ranging from -0.35 dBz to $+0.5$ dBz for a ± 1 h time lag around the overpass[‖].

4.2 CALIPSO CALIOP

The Aerosol Lidar[**] and Infrared Pathfinder Satellite Observation (CALIPSO) was launched together with CloudSat and lags it by 15 s in the A-Train (with the exception of the period when CloudSat changed orbit, see Chap. 4.1). CALIPSO carries a payload of three instruments, one of which is the Cloud-Aerosol Lidar with Orthogonal Polarization (CALIOP; *Hunt et al., 2009*), operational since 13 June 2006 and originally designed for an expected lifetime of three years. It is maintained by NASA and is the first polarization-sensitive lidar in space (*Winker et al., 2009*).

CALIOP is a near-nadir viewing[††] elastic-backscatter lidar, generating optical pulses at 1065 and 532 nm. The 532 nm-pulses are linearly polarized. At the Earth's surface, its beam diameter is 70 m and its receiver footprint diameter is 90 m. The laser pulse repetition frequency of CALIOP results in an along-track resolution of 335 m. Its receiver electrical bandwidth results in a fundamental vertical resolution of 30 m. Since spatial scales of atmospheric variability tend to increase with altitude, a vertically and horizontally varying on-board averaging scheme is employed to reduce downlinked data volume: with increasing altitude, data are increasingly vertically and horizontally averaged. The downside of this averaging scheme is that it potentially results in a spatial smearing of broken cirrus clouds (*York et al., 2011*). The resulting resolution ranges from 30 to 300 m in the vertical and from 0.335 to 5.025 km in the horizontal. Table 4 in *Hunt et al. (2009)* gives the exact spatial resolutions of the downlinked CALIPSO CALIOP data in the five altitude ranges.

The lidar equation (*Weitkamp, 2005*) relates transmitted and received powers P_t and $P_r(R)$

[‖]Ground-based radars selected for statistical comparison: Darwin, Australia (35 GHz), Niamey, Niger (94 GHz), Lindenberg, Germany (36 GHz), COPS site, Germany (95 GHz), and Palaiseau, France (95 GHz). The reflectivities measured by those radars with frequencies other than 94 GHz were converted into pseudo-94 GHz observations in order to retrieve $Z_{e,ground}$ (cf. *Protat et al., 2009*).

[**]Light detection and ranging.

[††]An off-geodetic nadir angle of first 0.3 ° and later 3.0 ° was chosen in order to prevent direct reflection from smooth water surfaces and domination of the backscatter signal by reflections from horizontally orientated ice crystals (*Hunt et al., 2009*).

to the backscatter coefficient $\beta(R)$:

$$P_r(R) = P_t \cdot \frac{\beta(R)}{R^2} \cdot \mathcal{T}^2(R) \cdot const. \tag{4.7}$$

R is the range and $\mathcal{T}^2(R)$ is the two-way atmospheric transmittance. The constant is determined by instrument-specific factors such as, for example, wavelength, average power of a single laser pulse, temporal pulse length, receiver area, and electronic amplifier gain. The backscatter coefficient $\beta(R)$ is defined as a function of the differential backscatter cross section $d\sigma_j/d\Omega$ at angle Ω and number concentration $N_j(R)$ of scattering particles of kind j. It describes how much light is scattered towards the lidar receiver.

$$\beta(R) = \sum_j \frac{d\sigma_j}{d\Omega} \cdot N_j(R) \tag{4.8}$$

The backscatter coefficient $\beta(R)$ is determined by the contributions from particles (aerosols and hydrometeors) $\beta_p(R)$ and from the molecular atmosphere $\beta_m(R)$ (Eq. 4.9). Multiplied by the two-way atmospheric transmittance $\mathcal{T}^2(R)$, it is termed attenuated backscatter coefficient $\beta'(R)$ (Eq. 4.10).

$$\beta(R) = \beta_p(R) + \beta_m(R) \tag{4.9}$$

$$\beta'(R) = \beta(R) \cdot \mathcal{T}^2(R) \tag{4.10}$$

This is the parameter provided in the CALIPSO Lidar Level 1B product by the Atmospheric Science Data Center (ASDC) at NASA (*Hostetler et al., 2006*), utilized in the present study.

The two-way atmospheric transmittance $\mathcal{T}^2(R)$ is represented by particulate $\mathcal{T}_p^2(R)$, molecular $\mathcal{T}_m^2(R)$, and ozone $\mathcal{T}_{O_3}^2(R)$ contributions (Eq. 4.11; *Vaughan et al., 2004*). These are each (index x) a function of optical depth $\tau(R)$ which is the path integral over the respective extinction coefficient $\alpha(R)$ (Eq. 4.12).

$$\mathcal{T}^2(R) = \mathcal{T}_p^2(R) + \mathcal{T}_m^2(R) + \mathcal{T}_{O_3}^2(R) \tag{4.11}$$

$$\mathcal{T}_x^2(R) = exp[-2 \cdot \tau_x(R)] = exp[-2 \cdot \int_0^R \alpha_x(R) dR] \tag{4.12}$$

The extinction coefficient α is a measure of how strongly radiation is attenuated by absorption and scattering (*Weitkamp, 2005*). At a given wavelength, it is proportional to total particle mass and particle number concentration (*Petty, 2006*).

As opposed to the radar, the lidar signal is less dominated by particle size, but much more particle number concentration (see definition of backscatter coefficient, Eq. 4.8). This enables it to detect optically thin clouds better than the radar (which is not sensitive enough) or passive instruments (which often have difficulties detecting the correct cloud top height (CTH)). The lidar is able to penetrate optically thin cirrus clouds and profile large fractions

of the atmosphere. However, the lidar signal is also quickly attenuated in optically thicker clouds, making the radar indispensable.

The accuracy with which a lidar measures attenuated backscatter depends on its signal-to-noise ratio (SNR). Because of its large distance to the target (cloud and aerosol particles), the SNR of CALIOP is lower than that of ground-based or airborne instruments. Generally, the SNR is lower during day- than during nighttime, due to solar background. CALIOP's SNR is improved by the spatial averaging described above. The minimum detectable backscatter (MDB) is dependent on altitude, scattering target, wavelength, and vertical and horizontal averaging. Instrument specifications claim a MDB at 532 nm for subvisible cirrus at 15 km height at 60 m vertical and 5 km horizontal resolution to be $7.0 \times 10^{-7}\,\mathrm{m^{-1}\,sr^{-1}}$ during nighttime and $\sim 1.1 \times 10^{-6}\,\mathrm{m^{-1}\,sr^{-1}}$ during daytime. Within the CALIPSO-CloudSat Validation Experiment (CC-VEX), where numerous aircraft underflights were performed, *McGill et al. (2007)* find good agreement with these values.

The attenuated backscatter provided by CALIPSO CALIOP has undergone extensive validation with both ground-based (*Mona et al., 2009*; *Mamouri et al., 2009*; *Kim et al., 2008*) and airborne (*Winker et al., 2007*; *McGill et al., 2007*; *Rogers et al., 2011*) instruments. Within the CC-VEX campaign, *McGill et al. (2007)* find a qualitatively good agreement with airborne lidar data, but they only investigate a few profiles. *York et al. (2011)* find the CALIOP to be affected by multiple scattering. In case of multiple scattering, the lidar signal seemingly penetrates deeper into the cloud and detects a lower cloud base than there actually is. The more extensive and also more independent comparison with airborne lidar observations by *Rogers et al. (2011)* finds an agreement within 2.7 %±2.1 % in clean air at nighttime and within 2.9 %±3.9 % at daytime. They find no obvious latitudinal or seasonal dependence.

4.3 MSG SEVIRI

Meteosat Second Generation (MSG; *Schmetz et al., 2002a*) is a European series of geostationary satellites maintained by the European Organisation for the Exploitation of Meteorological Satellites (EUMETSAT), the first of which was launched on 28 August 2002. MSG is to be continued until 2018, when it is supposed to be replaced by Meteosat Third Generation (MTG). As a whole, the Meteosat program is now running for 30 years, ensuring a high continuity. Currently, MSG-10 is the main satellite; it is positioned at 0 °N, 0 °E in approximately 36 000 km height. Its predecessor MSG-9 provides the rapid scanning service since 9 April 2013 covering only parts of Europe and Africa. (see `http://www.eumetsat.int/website/home/Satellites/CurrentSatellites/Meteosat/index.html`). The payload of the MSG satellites consists of two instruments, one of them being the Spinning Enhanced Visible and Infrared Imager (SEVIRI).

SEVIRI is a passive multi-spectral radiometer measuring the upwelling radiation from the Earth and the atmosphere. It scans the Earth from south to north line by line from east to west, delivering images of the full disc. One scan takes approximately 12 min, another 3 min is required for calibrating and returning back to initial scanning position. This results in an imaging-repeat cycle of 15 min. The maximum horizontal resolution of 3×3 km (1×1 km for the high-resolution visible (HRV) channel which covers only half of the full disc) is achieved at nadir; for Central Europe, due to increased off-nadir viewing angle, the horizontal resolution is approximately 3×5 km. SEVIRI features 12 channels: three channels are in the visible (HRV (broadband 0.4 to 1.1 μm), 0.6 μm, and 0.8 μm), one in the near IR (1.6 μm), and eight in the thermal IR (3.9 μm, 6.2 μm, 7.3 μm, 8.7 μm, 9.7 μm, 10.8 μm, 12.0 μm, and 13.4 μm). This channel selection provides information on the Earth's surface, water vapour, clouds, and ozone.

As a passive instrument, SEVIRI measures the spectral radiance[‡‡] I_λ emitted or scattered from Earth and atmosphere. Radiance is the rate per unit solid angle at which energy travels in a particular direction through a unit area normal to that direction (*Petty, 2006*). Its SI-unit is therefore $\mathrm{W\,m^{-2}\,sr^{-1}}$. The spectral radiance is the radiance per unit wavelength, then accordingly with SI-units of $\mathrm{W\,m^{-2}\,sr^{-1}\,m^{-1}}$ (*Glickman and American Meteorological Society, 2000*).

For a perfect absorber, a so-called blackbody, the Planck function describes the dependence between the emitted spectral radiance $B_\lambda(T)$ and the blackbody's temperature T:

$$I_\lambda = B_\lambda(T) = \frac{2 \cdot h \cdot c^2}{\lambda^5 \cdot (e^{(h \cdot c)/(k_B \cdot \lambda \cdot T)} - 1)} \tag{4.13}$$

with speed of light in vacuum $c = 2.998 \times 10^8\,\mathrm{m\,s^{-1}}$, Planck's constant $h = 6.626 \times 10^{-34}\,\mathrm{J\,s^{-1}}$, and Boltzmann's constant $k_B = 1.381 \times 10^{23}\,\mathrm{J\,K^{-1}}$. Per definition the blackbody radiance is the maximum radiance a body can possibly emit. The Planck function gives a unique relation between spectral radiance and temperature of a blackbody in thermodynamic equilibrium. With it, any spectral radiance, regardless of its source, can be converted to an equivalent blackbody temperature (*Petty, 2006*). The equivalent blackbody temperature is commonly referred to as brightness temperature T_B.

$$T_B(\lambda) \equiv B_\lambda^{-1}(I_\lambda) \tag{4.14}$$

where $B_\lambda^{-1}(I_\lambda)$ is the inverted Planck function solved for temperature T as a function of spectral radiance I_λ.

For the observed MSG SEVIRI radiances provided by EUMETSAT in their level-1.5 data and utilized in the present study, this is different. Rather than giving spectral radiances which are defined at a certain wavelength as described above, they give effective radiances

[‡‡]Radiance is often also referred to as radiant intensity or simply intensity.

which represent the integral over the spectral band around a central wavelength λ_0. *Schmetz et al. (2002b)* and *EUMETSAT (2007)* give details on the historical reasons and the procedure as such. The effective radiances are provided in $\mathrm{mW\,m^{-2}\,sr^{-1}\,cm^{-1}}$ and are to be converted to brightness temperatures with λ_0 given in μm (so that $10^4/\lambda_0$ is the wavenumber in $\mathrm{cm^{-1}}$) via the following equation:

$$T_B(\lambda) = \frac{h \cdot c \cdot 10^4}{k_B \cdot \lambda_0 \cdot log_e(1 + \frac{2 \cdot h \cdot c^2}{I_\lambda} \cdot (\frac{10^4}{\lambda_0})^3)} \tag{4.15}$$

Depending on the emissivity of a target at a certain wavelength, the brightness temperature can be very close to the target's actual temperature. And even if it is not, it is still directly proportional to the spectral radiance and remains convenient to use (*Petty, 2006*).

The accuracy of the brightness temperatures observed with SEVIRI is well assessed. The Global Space-based Inter-Calibration System (GSICS) coordinates EUMETSAT's inter-calibration activities. For SEVIRI, *Schmetz et al. (2002a)* give a general accuracy better than 1 K for the brightness temperatures. Inter-calibration with the Infrared Atmospheric Sounding Interferometer (IASI) on board of the Meteorological Operational satellite-A (MetOp-A) shows a cold bias of 1 K in the 13.4 μm channel for warm scenes (*Hewison and Müller, 2013*). *Roebeling et al. (2006)* find SEVIRI calibrated reflectances in the 0.6 μm and the 1.6 μm channel to be 6 and 26 % higher than those obtained from Advanced Very High Resolution Radiometer (AVHRR) on board the National Oceanic and Atmospheric Administration (NOAA) satellites. *Roebeling et al. (2004)* find SEVIRI 3.9 μm channel brightness temperatures to be colder than the corresponding ones from the Moderate Resolution Imaging Spectroradiometer (MODIS) and Geostationary Operational Environmental Satellite (GOES)-12 (by 6.7 and 3.3 K respectively) and the 11.7 μm channel to be approximately 1.5 K warmer.

The present study utilizes MSG SEVIRI observations from two thermal IR channels, 6.2 μm and 10.8 μm. The 10.8 μm channel is a window channel where absorption by atmospheric gases is weak. Thus, this channel is very much suitable for cloud detection since its weighting function peaks at the Earth's surface. Clouds are observed as cold with regard to the background of the comparably warm surface of the Earth. Brightness temperatures at this channel are proportional to the surface temperature in clear-sky situations or the cloud top temperature (CTT) in overcast situations. From CTT a good approximation of CTH is often possible (*Naud et al., 2005*). At 6.2 μm absorption by water vapour is strong so that the weighting function peaks in the upper troposphere (300 hPa). Thus, dependent on the humidity content in the upper troposphere, the measured brightness temperatures at this channel stem from higher or lower layers and are then accordingly lower or higher.

5 Retrievals and forward operators

The evaluation of the performance of atmospheric models is not straightforward since remote sensing instruments measure other quantities (with other units) than the models predict. The variables predicted by the models need to be converted into variables as observed, or vice versa. The present study applies both existing approaches, model-to-observation and observation-to-model, and in doing so is able to compare and discuss their advantages and disadvantages. On the observation-to-model side the CloudSat IWC retrieval (Chap. 5.1) is utilized and on the model-to-observation side the forward operators QuickBeam (Chap. 5.2) and Radiative Transfer for TOVS (RTTOV; Chap. 5.3). The pros and cons of the approaches are discussed in the respective sections below. Other issues which arise when comparing satellite and model data, such as temporal and spatial matching, are addressed in the respective evaluation chapters, since the treatment of the data varies between the different model versions.

5.1 CloudSat IWC retrieval

The determination of IWC from equivalent radar reflectivity factor Z_e is not trivial as it depends on hydrometeor size, shape, and PSD, with the largest particles dominating the equivalent radar reflectivity factor. The present study utilizes data from CloudSat's version 5.1 IWC retrieval (contained in release R04 of the level 2B products), which is based on the optimal estimation approach by *Rodgers (1976)*. The retrieval is briefly introduced in the following, for details refer to the CloudSat process description document (*Austin, 2007*) and to *Austin et al. (2009)*.

The CloudSat CPR is not able to determine the cloud phase in a given radar profile. Therefore, both a liquid and a frozen phase retrieval are run on the entire radar profile, assuming liquid-only and frozen-phase-only conditions. Afterwards, these two profiles are combined using a temperature-based scheme: regions colder than $-20\,°C$ are assumed to be pure frozen phase, regions warmer than $0\,°C$ to be pure liquid. Inbetween, the frozen phase and liquid solutions are scaled linearly with temperature, resulting in a final profile transitioning smoothly from all frozen phase to all liquid. The temperature information is provided by ECMWF model output and interpolated to the CloudSat grid. Note that these assumptions do not account for potential supercooled liquid water layers at or near cloud top at very cold temperatures. However, *Noh et al. (2011)* compares CloudSat data to aircraft data and find the amount of liquid water at or near cloud top, that is at very low temperatures, to be significant.

In the following, the retrieval for frozen phase is introduced. The retrieval for liquid runs analogously. The following equation relates measurement vector $\vec{y}$ to state vector $\vec{x}$ that is to be retrieved.

$$\vec{y} = \vec{F}(\vec{x}) + \vec{\varepsilon}_y \tag{5.1}$$

with forward model $\vec{F}(\vec{x})$ and measurement errors $\vec{\varepsilon}_y$. The individual terms are explained below.

Measurement vector

The measurement vector $\vec{y}$ contains the measured equivalent radar reflectivity factor Z_e for each height h, with p elements corresponding to the number of cloudy radar resolution bins.

State vector

The state vector $\vec{x}$ contains the unknowns, in this case the three parameters determining the PSD (i. e. particle number concentration N_T, geometric mean diameter D_g, and width parameter ω) for each height. It therefore consists of $3\times p$ elements. The state vector $\vec{x}$ is obtained by iteration, with a priori values used as initial values (see below).

A priori data

The a priori vector $\vec{x}_a$ has as many elements as the state vector $\vec{x}$, that is $3\times p$ elements. It helps to prevent outliers and constrains the solution. It consists of likely values of the state vector. Geometric mean diameter D_g and width parameter ω are obtained from empirically-derived temperature-dependent relationships.

$$\omega = 0.694 + 0.0065 \cdot T_{[°C]} \tag{5.2}$$

$$log(D_{g_{[mm]}}) = -0.684 + 0.0093 \cdot T_{[°C]} \tag{5.3}$$

Both Geometric mean diameter D_g and width parameter ω are used in addition to temperature T and equivalent radar reflectivity factor Z_e to determine the number concentration N_T

with a $Z_e - IWC$ relationship from *Liu and Illingworth (2000)*:

$$N_T = \frac{(IWC)^2 \cdot f_{Mie}(D_g, \omega) \cdot \frac{|K_{ice}|^2}{|K_{liq}|^2} \cdot exp(9\omega^2)}{(\frac{\rho\pi}{6})^2 \cdot 10^{-6} \cdot Z_e} \tag{5.4}$$

The a priori uncertainties (contained in the a priori error covariance matrix $\overleftrightarrow{S}_a$, see below) are set to the standard deviations of linear least-square fits of measurements of the three PSD parameters versus temperature.

Forward model

The forward model $\vec{F}(\vec{x})$ relates state vector $\vec{x}$ to measurement vector $\vec{y}$. Therefore, it has the same number of elements as the measurement vector $\vec{y}$.

$$\vec{F}(\vec{x}) = [Z_{FM}(h_i)] \qquad \text{with } i = 1, ..., p \tag{5.5}$$

How the individual elements $Z_{FM}(h_i)$ of the forward model are defined is derived in the following.

In releases R01* and R02 of the CloudSat CPR data, frozen phase particles are represented by a modified gamma distribution. However, for releases R03 and R04 it was decided to switch to the assumption of a lognormal PSD for frozen phase particles, since this exhibits a better behaviour in the small-particle limit (cf. *Austin et al., 2009*). The lognormal PSD for frozen phase particles is given by Eq. 5.6:

$$N(D) = \frac{N_T}{\sqrt{2\pi} \cdot \omega \cdot D} \cdot \exp\left(\frac{-log_e^2\left(\frac{D}{D_g}\right)}{2\omega^2}\right) \tag{5.6}$$

with D being the diameter of an equivalent mass sphere (either liquid or frozen phase). Using the size distribution from Eq. 5.6 and using D_g in mm, Eq. 4.4 becomes:

$$z_{Ray} = N_T \cdot D_g^6 \cdot \exp(18\omega^2) \tag{5.7}$$

At the CloudSat CPR wavelength, the cloud ice particles of thin ice clouds are sufficiently small to be modelled as Rayleigh scatterers. However, as stated above, an error may be introduced by larger particles that violate the Rayleigh criterion. This is accounted for in the forward model by introducing a correction function $f_{Mie}(D_g, \omega)$ (*Benedetti et al., 2003*).

Furthermore, as described in Chap. 4.1, the CloudSat CPR doesn't provide the radar reflectivity factor z — which is defined with respect to frozen phase — but the equivalent radar reflectivity factor z_e — which is defined with respect to liquid. Within the retrieval for frozen phase this is accounted for with a further correction term containing the ratio of the

*`http://www.cloudsat.cira.colostate.edu/dataConfig.php`.

dielectric factors K, with $|K_{ice}|^2 = 0.174$ and $|K_{liq}|^2 = 0.75$.

Introducing these two correction terms into Eq. 5.7 results in the following formulation for the measured equivalent radar reflectivity factor z_e:

$$z_e = z_{Ray} \cdot f_{Mie}(D_g, \omega) \cdot \frac{|K_{ice}|^2}{|K_{liq}|^2} \tag{5.8}$$

Combining Eq. 5.8 and Eq. 5.7 and using Eq. 4.6 to obtain dBz units, the individual elements of the forward model result.

$$Z_{FM}(h_i) = 10 \cdot log_{10}\left(N_{T,i} \cdot D_{g,i}^6 \cdot \exp(18\omega_i^2) \cdot f_{Mie}(D_{g,i}, \omega_i) \cdot \frac{|K_{ice}|^2}{|K_{liq}|^2}\right) \tag{5.9}$$

Optimal estimation technique

In the utilized optimal-estimation technique from *Rodgers (1976)*, the a priori profiles serve as virtual measurements and thereby constrain the retrieval. The optimal solution is obtained by maximizing the a posteriori probability, which is equivalent to minimizing a cost function that represents a weighted sum of state vector-a priori difference and the measurement vector-forward model difference. The solution is then obtained iteratively:

$$\vec{x}_{i+1} = \left(\overleftrightarrow{S}_a^{-1} + \overleftrightarrow{K}_i^T \overleftrightarrow{S}_\varepsilon^{-1} \overleftrightarrow{K}_i\right)^{-1} \cdot \left(\overleftrightarrow{S}_a^{-1}\vec{x}_a + \overleftrightarrow{K}_i^T \overleftrightarrow{S}_\varepsilon^{-1}\left[\vec{y} - \vec{F}(\vec{x}_i) + \overleftrightarrow{K}_i\vec{x}_i\right]\right) \tag{5.10}$$

with iteration number i, a priori error covariance matrix $\overleftrightarrow{S}_a$ (representing the variability or uncertainty of the a priori profile; information on correlations among the a priori profile values are not available), measurement error covariance matrix $\overleftrightarrow{S}_\varepsilon$ (representing the uncertainty in the measurement vector; the errors of the individual elements are assumed to be independent), and $\overleftrightarrow{K}$ matrix ($\overleftrightarrow{K} = \partial\vec{F}/\partial\vec{x}$).

Convergence is determined with a test from *Marks and Rodgers (1993)* given in Eq. 5.11, where $\overleftrightarrow{S}_x$ is the state vector error covariance matrix given in Eq. 5.12.

$$\Delta\vec{x}^T \overleftrightarrow{S}_x^{-1} \Delta\vec{x} < 0.01 \cdot 3p \tag{5.11}$$

$$\overleftrightarrow{S}_x = (\overleftrightarrow{S}_a^{-1} + \overleftrightarrow{K}^T \overleftrightarrow{S}_\varepsilon^{-1} \overleftrightarrow{K})^{-1} \tag{5.12}$$

Z_e-IWC relation

Now that the three parameters describing the PSD are retrieved, what does the actual Z_e-IWC relation look like?

IWC is defined as the sum over all frozen particles in a unit volume. For spherical particles,

IWC takes the following form:

$$IWC = \frac{1}{V}\sum_i m_i = \int_0^\infty \frac{\rho_{ice}\cdot\pi}{6} N(D) D^3 dD \sim D^3 \sim \mathcal{M}_3 \tag{5.13}$$

with density of ice ρ_{ice}. In contrast to the equivalent radar reflectivity factor Z_e which is proportional to the sixth moment $\mathcal{M}_6$, IWC is proportional to the third moment $\mathcal{M}_3$ of the PSD. Applying the lognormal PSD (Eq. 5.6) assumed by the CloudSat Z_e-IWC retrieval and using D_g in mm, Eq. 5.13 becomes

$$IWC = \frac{\rho_{ice}\cdot\pi}{6}\cdot N_T \cdot D_g^3 \cdot \exp\left(\frac{9}{2}\omega^2\right)\cdot 10^3 \tag{5.14}$$

Though several observational studies find the density of frozen phase particles to vary with particle size (e. g. *Brown and Francis, 1995*), the density of ice is fixed to a constant ρ_{ice} =917 kg m^{-3} in the CloudSat IWC retrieval. *Woods et al. (2008)* assess the sensitivity of the CloudSat IWC retrieval to frozen phase particle properties such as particle density, mass-diameter relation, and PSD. They find a better performance in case of dominating cloud ice. In case of a mixture of cloud ice and snow the CloudSat IWC retrieval exhibits a strong positive bias.

Combining Eqs. 5.7, 5.14, and 5.8, the following Z_e-IWC relationship evolves for CloudSat:

$$IWC = \left(\frac{z_e \cdot \left(\frac{\rho_{ice}\cdot\pi}{6}\right)^2 \cdot N_T \cdot 10^6}{f_{Mie}(D_g,\omega)\cdot\frac{|K_{ice}|^2}{|K_{liq}|^2}\cdot\exp(9\omega^2)}\right)^{0.5} \tag{5.15}$$

With Eq. 5.15 the detection limit of -27 dBz results in an estimated minimum detectable IWC of 0.001 g m^{-3} for the CloudSat CPR.

Since N_T, D_g, and ω in Eq. 5.15 are all variable, the Z_e-IWC relation cannot be written in the form of a simple power law. However, a scatter plot is suitable for illustrating the Z_e-IWC relationship. For one granule it is given in Figure 5.1.

Since the CloudSat CPR is not Doppler-capable and therefore cannot distinguish between precipitating and non-precipitating frozen particles, throughout the present study, the term IWC refers to the mass of total frozen phase in a unit volume; it is the sum of cloud ice water content (CIWC), snow water content (SWC), and if predicted graupel water content (GWP). The corresponding column integrated variable IWP is analogously composed of cloud ice water path (CIWP), snow water path (SWP), and graupel water path (GWP).

A short note on retrieving snow from CloudSat measurements: Several attempts have been made to retrieve snow from CloudSat observations in order to enhance the comparability with model output. If interested in surface snowfall rate alone, studies assess the probability of snow or rain reaching the ground at a certain air temperature from multiyear station data

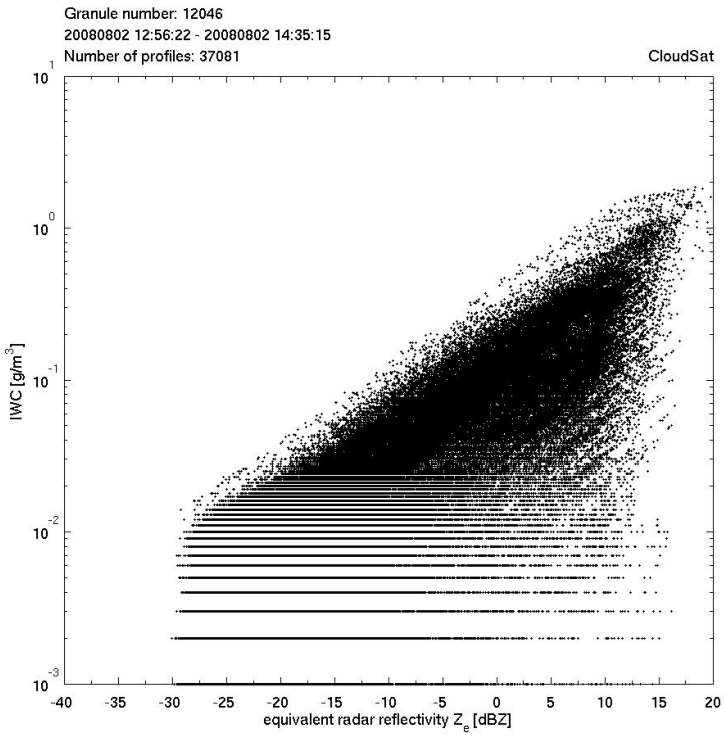

Figure 5.1: CloudSat CPR Z_e-IWC relationship from granule 12046 on 2 August 2008.

and then run a snowfall rate retrieval based on a simple power law relationship on the near-surface radar reflectivity factors of the respective profiles (e. g. *Liu, 2008*; *Hiley et al., 2011*). If upper-level SWCs are of interest, studies apply a critical diameter for partitioning the particle distribution function (PDF) into two parts (e. g. *Chen et al., 2011*). Particles with a diameter smaller than this critical diameter are considered to be cloud ice and add to CIWC, particles with a diameter larger than the critical diameter are considered to be snow and add to SWC. However, all CloudSat SWC retrievals have in common that even more assumptions are made than in the CloudSat IWC retrieval and that these assumptions lead to a very large uncertainty of SWC. Therefore, the present study does not utilize these retrieval products.

Performance

The quality of the equivalent radar reflectivity factor measured by the CloudSat CPR and the retrieved IWC have been comprehensively validated by several studies (e. g. *Protat et al., 2009*; *Austin et al., 2009*) with various approaches: Firstly, tests of the algorithm on simulated radar data, secondly, statistical comparisons of the retrieved IWC to retrievals by other instruments (ground-based, airborne, and spaceborne), and thirdly, comparisons of the algorithm output to outputs of other algorithm versions obtained with the same CloudSat data. The first approach shows a good performance of the R04 retrieval algorithm; IWC bias errors are estimated to be less than 40 %. The second approach delivers mixed results. *Protat et al. (2009)* find a good performance in comparison to ground-based measurements,

with the weighted mean difference ranging from -0.35 dBz to $+0.5$ dBz for a ± 1 h time lag around the overpass. The third approach concludes: at altitudes below 12 km and for $IWC < 1\,\mathrm{g\,m^{-3}}$ the R04 results agree well with those of other retrievals. However, above 12 km height and for higher IWCs, the results of the R04 retrieval either exceed other retrievals or fall within a spread of retrieval values. *Austin et al. (2009)* find IWCs above $1\,\mathrm{g\,m^{-3}}$ not to be trustworthy, however, suitable reference data for IWC validation is still lacking. For an extensive overview on the performance tests see *Austin et al. (2009)*.

A short note on combined CloudSat IWC retrievals: Combined retrievals aim at bridging the sensitivity limits individual instruments suffer from (see respective chapters) and combine them to gain an improved IWC retrieval. CALIPSO CALIOP is an obvious choice for combination, since it flies in close succession to CloudSat and is sensitive to the small particles the CloudSat CPR might miss. This is the so-called radar-lidar IWC retrieval (*Donovan and van Lammeren, 2001*). However, some complications exist in relating the observed backscatter coefficient of CALIPSO to IWC. In particular, in situ aircraft measurements (*McFarquhar et al., 2007*) indicate that past measurements overestimate small ice crystal concentrations by a factor of two, resulting in questionable PSDs on which all observations, the radar-lidar retrieval included, are based. Radar-lidar-radiometer IWC retrievals (*Delanoë and Hogan, 2008*) seek to further improve the retrieval results by including data from a third instrument. However, this very sophisticated retrieval requires ancillary information (in addition to the state vector) about the state of the atmosphere and surface, and instrument properties. Therefore, the present study does not utilize data from combined IWC retrievals. Then again, concerning IWP, *Delanoë et al. (2011)* state that it is dominated by larger IWC values, which is why the radar-only retrieval should provide a good enough estimate of IWP.

5.2 QuickBeam

QuickBeam is a radar simulator package developed by *Haynes et al. (2007)* and designed for a fast coupling with dynamic atmospheric models. It is freely available for the scientific community at `http://cloudsat.atmos.colostate.edu/radarsim`. In the present study, version v1.1a is utilized.

QuickBeam is a forward operator which simulates profiles of equivalent radar reflectivity factor at any given microwave frequency. It simulates what a radar system — either ground- or satellite-based — would observe given an atmospheric state. As input, QuickBeam requires the specific contents of the hydrometeors as well as profiles of pressure, temperature, and relative humidity. Additionally, the PSDs and mass-size relations of the hydrometeor classes have to be specified. Up to 50 different hydrometeor classes are allowed, and five preset PSDs can be chosen from. That is, modified gamma, exponential, power law, monodisperse, and lognormal. Hydrometeor mass may be specified as a con-

stant value or as a function of diameter. Both Rayleigh and Mie scattering are simulated. Mie scattering can either be obtained from pre-compiled scattering tables or calculated on the fly. Additionally, gaseous and hydrometeor attenuation are accounted for.

To give a small insight into the simulator, the basic procedure of QuickBeam is briefly described in the following. First, for each profile, each layer, and each hydrometeor class, the PSD is computed from given hydrometeor diameter and number concentration. Depending on the chosen hydrometeor distribution shape, the given diameter is only preliminary and is recalculated within this procedure (see introduced change 2 below). Second, the effective particle density is determined from the now finally determined diameter. Third, with both diameter and density, the electromagnetic properties of the volume are calculated. Fourth, the unattenuated equivalent reflectivity factor of the volume is computed and then summed up for all hydrometeor classes. In a final step, the attenuation due to gases and hydrometeors is computed.

Several assumptions are made within QuickBeam. First, within QuickBeam, assumptions are made concerning the shape of the modelled hydrometeors. Ice crystals are modelled as so-called soft spheres (*Haynes et al., 2007*). A soft sphere is a sphere with a diameter corresponding to the maximum diameter of the ice crystal and with an effective density and index of refraction reduced so as to represent a mixture of ice and air. Though this is a computationally efficient approximation, *Liu (2004)* finds this to be a questionable approximation for the actual particle habit, in this case of the investigated NWP models. Efforts are in progress to reduce these errors by building up a discrete-dipole approximation lookup table for particles of arbitrary shape for QuickBeam, however, this is currently not yet available.

Second, multiple scattering effects are not accounted for. Multiple scattering increases the observed radar reflectivity factor below regions with large attenuation. Especially at higher frequencies, like the 94 GHz of the CloudSat CPR, this may lead to errors (see Chap. 4.1). In these cases, the radar reflectivity factors simulated with QuickBeam are smaller than those CloudSat would actually observe. As it is shown in the following chapters, the models anyhow tend to overestimate radar reflectivity factors.

Third, QuickBeam is not capable of simulating the bright band and its associated physics (see Chap.2.1), since it allows only for hydrometeors which are either frozen phase or liquid but not a composite particle in transition from frozen phase to liquid. It is planned (*Haynes et al., 2007*) to provide a simple melting particle model which modifies the cloud microphysics, meaning that the simulated equivalent reflectivity factor profiles no longer truly represent the input cloud microphysics, but rather a mixture of the input cloud microphysics and the melting layer model modifications. However, to date this melting particle model has not yet been implemented and is therefore not contained in the current version QuickBeam v1.1a, utilized in the present study.

The accuracy of the equivalent radar reflectivity factor simulated with QuickBeam has been

validated against results from a full electromagnetic solver by *Sato and Okamoto (2006)*. They find the maximum differences to be less than 1.2 dBz for particles with $r_e < 100\,\mu$m and 4 dBz for particles with $100 < r_e < 600\,\mu$m. Due to its good performance and broad acceptance in the community QuickBeam is included in COSP (*Bodas-Salcedo et al., 2011*).

Within the present study, modifications are made to the official version of QuickBeam described above in order to meet the demands of the models QuickBeam is applied to, that is GME and COSMO-DE. In detail, three adjustments to the implemented PSDs are undertaken:

1. The predefined exponential PSD function is extended to enable the temperature- and specific water content-dependency of N_0 after *Field et al. (2005)*, as described in Chap. 3.1.4.

2. The predefined monodisperse PSD function is extended to support not only a given constant diameter D_0 from which the number concentration N_0 is then calculated, but also a given constant number concentration N_0, from which the diameter D_0 is then calculated. A temperature-dependency of this given number concentration is allowed for. This is implemented because the two-moment cloud ice scheme (*Köhler, 2013*) actually predicts the number concentrations of cloud ice.

   Since DWD's two- and three-category ice schemes (see Chap. 3.1.2 and 3.2.3) specify a maximum diameter of $D_{max} = 200\,\mu$m for monodispersly distributed cloud ice (index i), a size restriction is additionally implemented into QuickBeam: should the maximum diameter be exceeded (after being calculated from the given number concentration N_0), the number concentration N_0 is re-calculated with the diameter D_0 set to the maximum diameter $D_{0_{max}}$.

   $$D_0 = D_{0_{max}} \tag{5.16}$$

   $$N_{0,i} = \frac{q_i}{\alpha_i \cdot D_{0,i_{max}}^{\beta_i}} \tag{5.17}$$

   This approach is preferable to simply cutting off the part of the distribution which exceeds the maximum diameter, since in this way no cloud ice mass is lost.

3. The monodisperse PSD function is yet further extended, to enable the input of number concentations N_0 directly from model output. This is necessary for cloud ice in the two-moment cloud ice scheme in COSMO-DE8822 (see Chap. 3.2.5), since it explicitely prognoses these.

The effect of the change from a fixed number concentration for snow to a temperature- and specific content-dependent number concentration is in the following demonstrated for a randomly chosen GMEprog profile that contains all four hydrometeor classes. Temperature, pressure, and the distribution of the specific contents of the hydrometeors of the chosen profile are depicted in Fig. 5.2. The original fixed number concentration for snow

(N_{0_s} =8×10^5 mm^{-4}) and the new temperature- and specific content-dependent parameterization ($N_{0_s}(T, q_s)$ following *Field et al., 2005*) are displayed in the left panel in Fig. 5.3. For comparison, the constant number concentrations N_{0_s} =5×10^8 mm^{-4} (assumed for cloud water in GME) and N_{0_s} =8×10^6 mm^{-4} (assumed for rain in GME) are also tested. The corresponding intercept parameters for snow λ_s exhibit peak values ranging from 3 to 29 mm (right panel in Fig. 5.3). For three altitudes, the resulting snow PSDs are given in the bottom panel in Fig. 5.3; they feature distinctly different slopes and intercepts. Concerning the resulting simulated radar reflectivity factors, the total simulated equivalent radar reflectivity factor is dominated by snow (upper left panel in Fig. 5.4). The intercept parameter λ_s for $N_{0_s}(T, q_s)$ is much higher at higher altitudes than for the former N_{0_s} =8×10^5 mm^{-4} (right panel in Fig. 5.3). It resembles that for N_{0_s} =5×10^8 mm^{-4} very much, except for at lower altitudes (warmer temperatures), where it is smaller. The shape of the equivalent radar reflectivity factor profile for snow only (bottom left panel in Fig. 5.4) is flattened for $N_{0_s}(T, q_s)$ in comparison to the constant parameterizations for N_{0_s}, with smaller values at high and higher values at low altitudes. The maximum is shifted to lower altitudes. Two-way atmospheric attenuation due to snow only $L^2_{h,s}$ (dotted lines in bottom right panel in Fig. 5.4) is reduced for $N_{0_s}(T, q_s)$ in comparison to N_{0_s} =8×10^5 mm^{-4} (bottom right panel in Fig. 5.4). Exactly how the GME model data are matched to the CloudSat profile is irrelevant at this point, but is explained in detail in Chap. 6.2.

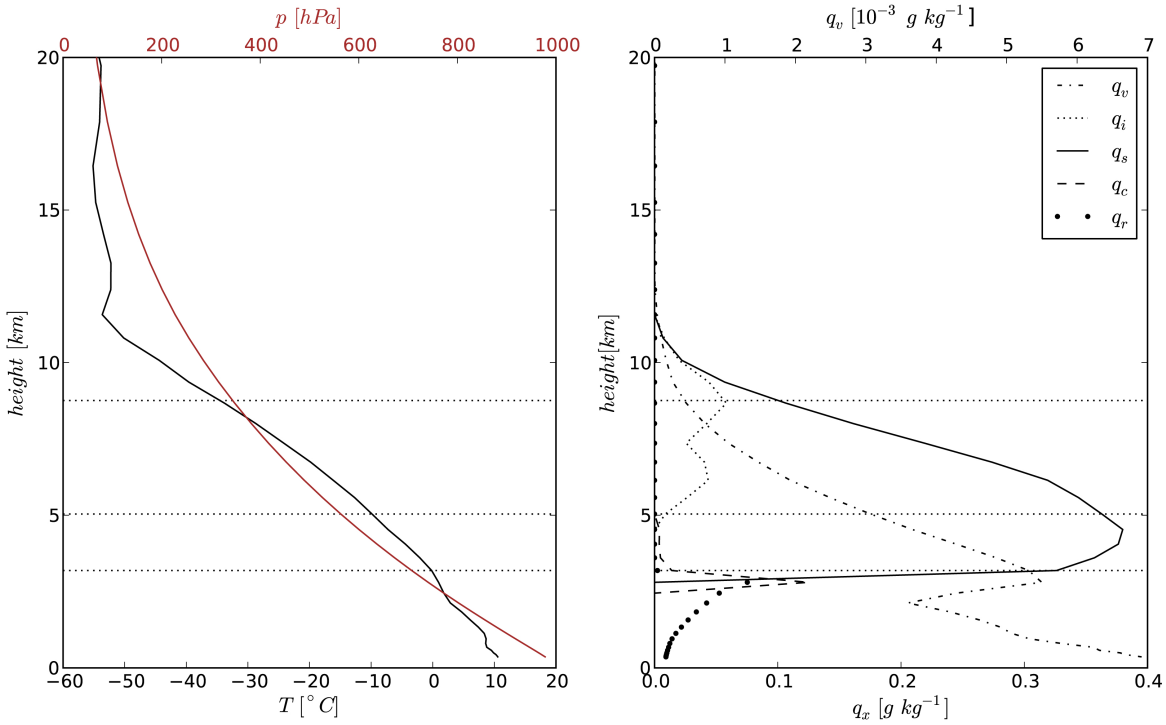

Figure 5.2: GMEprog model output corresponding to profile 30701 in granule 18000 (15 September 2009) of CloudSat CPR data. **Left**: temperature and pressure. **Right**: specific contents of hydrometeors and water vapour. The dotted horizontal lines in the panels correspond to the three altitudes depicted in the bottom panel in Fig. 5.3.

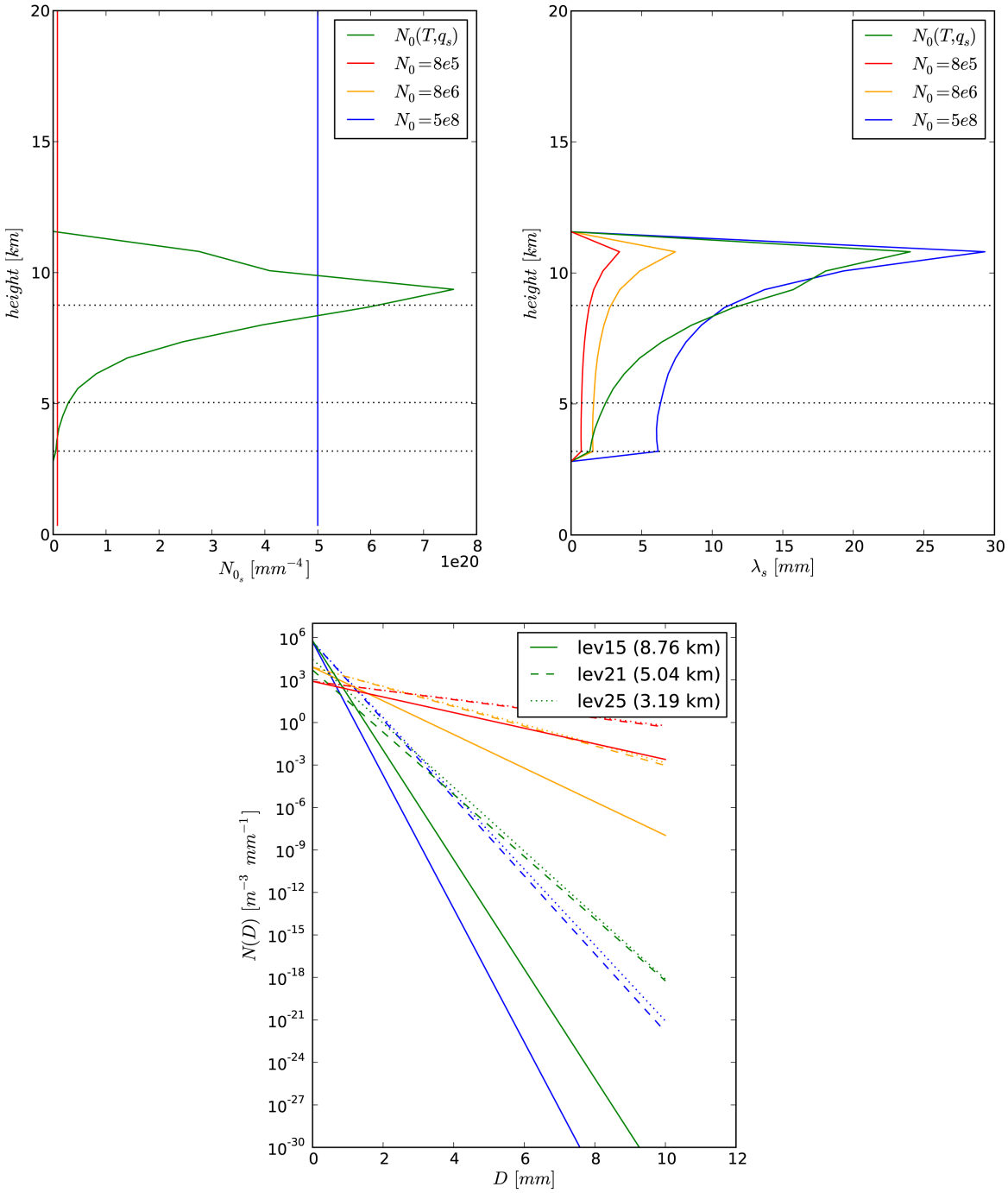

Figure 5.3: GMEprog model output corresponding to profile 30701 in granule 18000 (15 September 2009) of CloudSat CPR data. **Left**: four tested particle number concentrations for snow N_{0_s}. Red, yellow, and blue depict constant values, green the parameterization following *Field et al. (2005)*. **Right**: corresponding intercept parameters for the varying N_{0_s}. **Bottom**: corresponding PSDs for the varying N_{0_s} (colours) in three different heights (line style). The dotted horizontal lines in the two top panels correspond to the three altitudes depicted in the bottom panel.

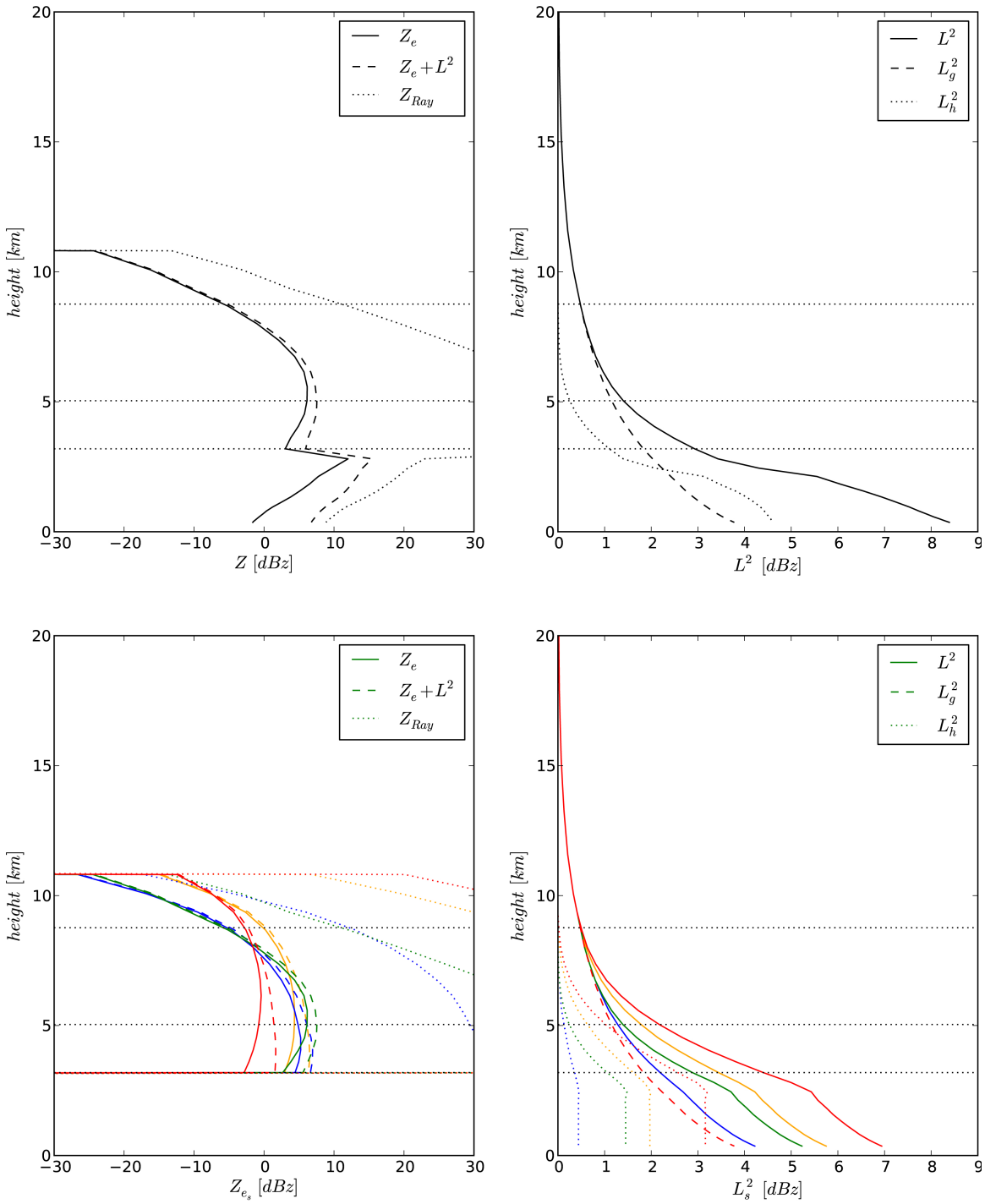

Figure 5.4: GMEprog model output corresponding to profile 30701 in granule 18000 (15 September 2009) of CloudSat CPR data. **Top left**: simulated radar reflectivity factors including all hydrometeors with snow parameterization following *Field et al. (2005)*. **Top right**: simulated two-way atmospheric attenuation including all hydrometeors with snow parameterization following *Field et al. (2005)*. Line style refers to attenuation components by hydrometeors L_h^2 (dotted), by gases L_g^2 (dashed), and the sum of both (solid). **Bottom left**: simulated snow-only radar reflectivity factors for varying N_{0_s} (colours; defined as in Fig. 5.3). **Bottom right**: simulated snow-only two-way atmospheric attenuation for varying N_{0_s} (colours; defined as in Fig. 5.3). The dotted horizontal lines in the panels correspond to the three altitudes depicted in the bottom panel of Fig. 5.3.

The Z-IWC relationship derived with QuickBeam differs from that derived through the CloudSat IWC retrieval (cf. Fig. 5.5). As a reference, the commonly used Z-IWC relationship from *Hogan et al. (2006)* is included for two temperatures. The slopes of the two approaches match well. However, the model relationship is expectedly tighter than the observational relationship, because it contains no noise. With increasing temperature (bottom row), the Z-IWC relationship is shifted towards higher reflectivity factors. Note that while the Z-IWC relationships from both approaches aggree in their general behaviour, differences exist in particular concerning large IWCs and cold temperatures. Note also that the Z-IWC relationships from CloudSat CPR and GMEprog in Fig. 5.5 are based on near-global data.

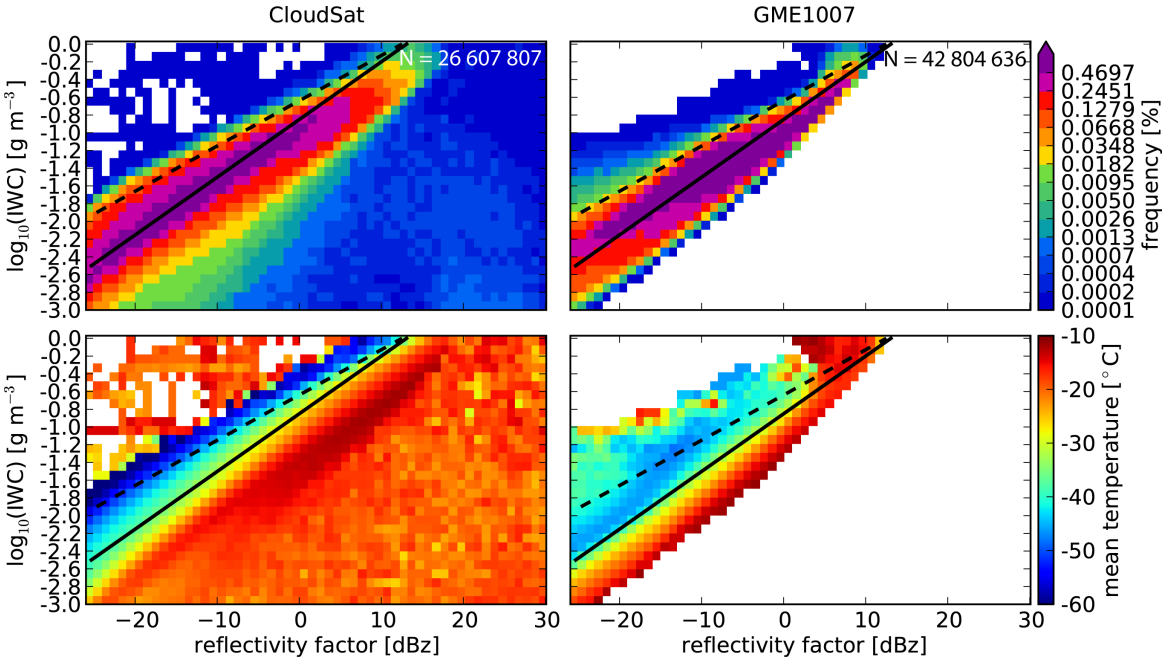

Figure 5.5: Z-IWC relationship for CloudSat (left) and GMEprog (right) for 1 July 2009 to 31 October 2009. **Top row**: frequency distribution. **Bottom row**: mean bin-temperatures. Frequency distributions are normalized with number N of included pixels. Black lines: Z-IWC relationship from *Hogan et al. (2006)* for $T = -20\,°C$ (solid) and $T = -50\,°C$ (dashed).

5.3 RTTOV and SynSat

Radiative Transfer for TOVS (RTTOV) is a fast radiative transfer model first developed to simulate radiances for (Advanced) Television Infrared Observation Satellite (TIROS) Operational Vertical Sounder ((A)TOVS). Originally developed at ECMWF (*Eyre, 1991*; *Saunders et al., 1999*), it is more recently maintained within EUMETSAT's NWP Satellite Application Facility (SAF). The forward operator is capable of simulating top of the atmosphere radiances for the channels of most satellite-based nadir-scanning radiometers and interfer-

ometers (currently or formerly operational) in the IR and the microwave range. For details on RTTOV visit EUMETSAT's NWP SAF website (`http://research.metoffice.gov.uk/research/interproj/nwpsaf/rtm/`).

Synthetic Satellite imagery (SynSat) is a diagnostic tool implemented into COSMO-DE, which couples RTTOV to COSMO-DE output (*Keil et al., 2006*). SynSat was developed in cooperation with Deutsches Zentrum für Luft- und Raumfahrt (DLR) and is now maintained at DWD. Currently, RTTOV-10 is coupled to COSMO-DE *(Faulwetter, personal communication)*. However, the older RTTOV-9.3 (*Saunders et al., 2010*) is coupled to the COSMO-DE version used in the present study (see Chap. 3.2). In the following description of SynSat, all information refers to RTTOV-9.3 and is not necessarily valid for other release versions.

The spectral range of RTTOV covers $3-20\,\mu$m in the IR and $10-200\,$GHz in the microwave range. The line-by-line models on which RTTOV is based are the general line-by-line atmospheric transmittance and radiance model (GENLN2; *Edwards, 1992*) or kCarta (*Strow et al., 1998*) or the line-by-line radiative transfer model (LBLRTM; *Clough et al., 2005*) for the IR and the millimeter-wave propagation model (MPM; *Liebe, 1989*) for the microwave range. For cloud-affected IR channels, a new multiple scattering radiance code is included which parameterizes multiple scattering in the IR but does not treat it explicitely. For the rain- and cloud-affected microwave channels, RTTOV-SCATT provides an explicit approach to compute multiple scattering (*Joseph et al., 1976*). The reflected solar component can be included, if the required additional parameters are provided, but only for the shortwave IR channels of two instruments (not for SEVIRI). In contrast to previous RTTOV versions, input profiles on any set of pressure levels are accepted.

As input, RTTOV requires profiles of temperature, the specific contents of atmospheric gases and water contents, cloud cover, and surface properties. For certain settings (e. g. if the reflected solar component is to be included), additional variables such as solar zenith and azimuth angles, satellite azimuth angle, information on water type, etc. may be required.

Concerning the atmospheric gases, water vapour, ozone, carbon dioxide, nitrous oxide, methane, and carbon monoxide can be variable. But with exception of water vapour which is mandatory, all others can be set to constant values. This is the case within SynSat, because COSMO-DE does not predict atmospheric constituents other than water vapour.

As mentioned above, RTTOV requires information on cloud cover and atmospheric water content as input. It distinguishes between 6 cloud types: (1) stratus continental, (2) stratus maritime, (3) cumulus continental clean, (4) cumulus continental polluted, (5) cumulus maritime, and (6) cirrus. The first five cloud types are pure liquid, and differ through their distinct PSDs, for which the optical parameters are avilable. The sixth cloud type is the only frozen phase cloud type. Here, the optical parameters are parameterized as a function of the effective diameter of the PSD and are available for two ice crystal shapes (hexagonal or aggregates). The user specifies firstly, ice crystal shape and secondly, on which assumptions

this parameterization of effective diameter as a function of IWC is based (four methods are possible, see *Saunders et al., 2010*). At each level, either clear-sky (0) or one (and only one) cloud type have to be specified, and all water contents have to be assigned to this cloud type. Additionally, the fractional cloud cover, ranging from 0 for clear sky to 1 for overcast, for each level has to be provided. How the standard COSMO-DE output is assigned to this format is described in the following.

COSMO-DE has three types of cloud cover. Grid-scale, subgrid-scale stratiform, and convective cloud cover. If the sum of the specific contents of snow and graupel exceeds $10^{-7}\,\mathrm{kg\,kg^{-1}}$, cloud cover for RTTOV is set to 1 . If it is smaller, cloud cover for RTTOV is set to the value of subgrid-scale cloud cover. Or else, if the specific content of convective cloud water is not zero, cloud cover is set to the subgrid-scale cloud cover plus an adjusted convective cloud cover. Finally, cloud cover is constricted to be greater equal zero and smaller equal one. For clarification, in pseudocode this looks as given below.

```
if QS + QG greater equal 1.0e-7
   cloud cover = 1
else
   cloud cover = subgrid-scale cloud cover
   if convective QC not equal 0
      cloud cover = cloud cover //
      // + convective cloud cover * (1 - subgrid-scale cloud cover)
cloud cover = min(cloud cover,1)
cloud cover = max(0,cloud cover)
```

Concerning the specific contents of hydrometeors RTTOV requires as input, the coupling is more complex. First of all, rain is not considered. Second, the user can specify whether subgrid scale cloud water should be considered or not. For the model runs performed within the present study, it is. Contrary, subgrid-scale IWC is not considered. Third, the specific contents of snow and graupel (if COSMO-DE is run with the three-category ice scheme) are added to the specific content of cloud ice so that the sum of all frozen hydrometeors enters the calculation. Note that, assuming a given mass concentration, the emissivity of snow is smaller than that of ice crystals, because snow is larger. Consequently, the consideration of snow leads to an overestimation of emissivity in the presence of snow (*Keil et al., 2006*). Cloud ice is considered, if its specific content is greater than $10^{-7}\,\mathrm{kg\,kg^{-1}}$. The total sum of specific content from frozen hydrometeors is restricted to a maximum of $10\,\mathrm{g\,m^{-3}}$, since larger values are firstly considered unphysical and secondly might cause numerical problems within RTTOV.

Now these water contents need to be assigned to one of RTTOV's six known cloud types. If no cloud water is present (only frozen phase), then cloud type (6) cirrus is chosen and assigned the previously determined frozen phase water content. The ice crystal shape is set to hexagonal plates and the parameterization of effective diameter as a function of IWC is

set to no. 4, which is based on *McFarquhar et al. (2003)*. If no cloud water plus frozen phase is present (only convective cloud water), then cloud type (3) cumulus continental clean is chosen and assigned the previously determined cloud water content. Finally, in all other cases, cloud type (1) stratus continental is chosen and assigned all previously determined cloud water content.

All COSMO-DE variables which enter RTTOV are listed in Table 5.1.

Though RTTOV's general performance is good, it is poor concerning the simulation of very broad channels, with biases of $1-2$ K (*Saunders et al., 2010*). However, this does not affect the present study since none of these channels are used.

Table 5.1: COSMO-DE input to RTTOV.

variable	name	units	dimension
temperature	T	K	3
pressure	P	Pa	3
specific humidity	q_v	$\mathrm{kg\,kg^{-1}}$	3
specific cloud water content	q_c	$\mathrm{kg\,kg^{-1}}$	3
specific cloud ice content	q_i	$\mathrm{kg\,kg^{-1}}$	3
specific snow content	q_s	$\mathrm{kg\,kg^{-1}}$	3
specific graupel content	q_g	$\mathrm{kg\,kg^{-1}}$	3
specific convective cloud water content	CLW_CON	$\mathrm{kg\,kg^{-1}}$	3
subgrid-scale cloud cover	CLC_SGS	-	3
convective cloud cover	CLC_CON	-	3
surface pressure	PS	Pa	2
2-meter temperature	T_2M	K	2
2-meter specific humidity	$RELHUM\_2M$	$\mathrm{kg\,kg^{-1}}$	2
land-sea mask	FR_LAND	-	2
surface height	$HSURF$	m	2
water type	$LSEAICE$	-	2
soil type	$SOILTYP$	-	2
10-m zonal wind component	U_10M	$\mathrm{m\,s^{-1}}$	2
10-m meridional wind component	V_10M	$\mathrm{m\,s^{-1}}$	2
sun elevation angle	SUN_EL	$^\circ$	2
sun azimuth angle	SUN_AZI	$^\circ$	2

6 Evaluation of GME

In the following chapter, the effect of the microphysics of two GME versions, GMEdiag with a diagnostic precipitation scheme (Chap. 3.1.3) and GMEprog with a prognostic precipitation scheme (Chap. 3.1.4), are compared to each other and evaluated with CloudSat CPR observations (Chap. 4.1). After introducing the question which is to be investigated (Chap. 6.1), it is described how exactly the temporal and spatial matching between model and satellite data is achieved (Chap. 6.2). The different resolutions and also sensitivities of instrument and model have to be considered; conclusions can only be drawn for ranges resolved by both (*Woods et al., 2008*). As for the analysis, a case study is presented first (Chap. 6.3) in order to introduce the applied metrics and to point out the differences between the two approaches — forward operator QuickBeam (Chap. 5.2) versus CloudSat IWC retrieval (Chap. 5.1). Second, to enable a conclusive statement concerning the differences between the two GME versions, a statistical approach is undertaken (Chap. 6.4). Since conclusions can only be drawn for ranges resolved by both models and observations (*Woods et al., 2008*), the different sensitivities of instruments and models have to be considered and criteria are developed to enhance the comparability between models and observations. At the end of this chapter, a summary of the findings is given and the GME-specific conclusions are presented (Chap. 6.5). More general conclusions are left for the overall conclusions and outlook in Chap. 8.

6.1 Posing the question

Routine precipitation verification for the new GMEprog at the mid-latitudes, where most precipitation is generated via the ice phase, was undertaken at DWD. Both frequency bias

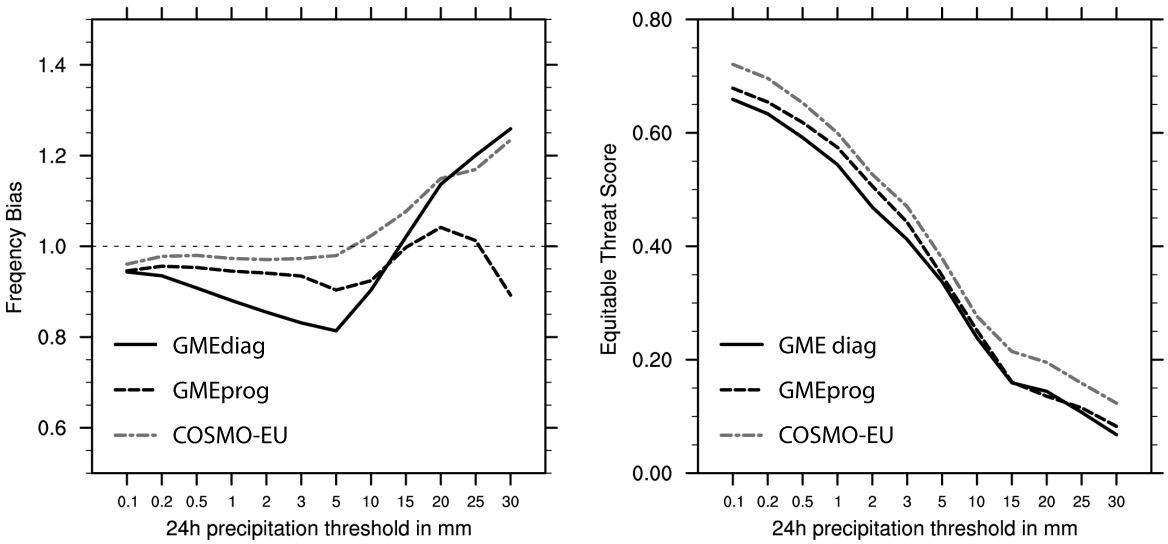

Figure 6.1: Frequency bias (left) and equitable threatscore (right) of 24 h accumulated precipitation as a function of precipitation threshold. Model results are verified against a gridded precipitation data set for Germany based on more than 600 rain gauges from 1 July 2009 to 31 October 2009. Here, GMEdiag is GME6864 and GMEprog is GME6831.

(FBI) and equitable threat score (ETS) were calculated. The FBI (Eq. 6.1) is the ratio of the frequency of forecasted to the frequency of observed events. It indicates whether the model over- or underestimates precipitation events. The ETS (Eq. 6.2) is the fraction of hits adjusted for hits expected by chance. It indicates how well forecasted events correspond to observed events.

$$FBI = (a+b)\cdot(a+c)^{-1} \tag{6.1}$$

$$ETS = (a-a_r)\cdot(a+b+c-a_r)^{-1} \tag{6.2}$$

with hits a, false alarms b, misses c, correct negatives d, and hits expected by chance $a_r = (a+b)\cdot(a+c)\cdot(a+b+c+d)^{-1}$. See also Table 6.1 for clarification.

Table 6.1: Contingency table.

		observed	
		yes	no
forecasted	yes	a	b
	no	c	d

Figure 6.1 shows an improvement in FBI for GMEprog relative to GMEdiag. For lower thresholds, GMEprog is very close to the even better results of the regional COSMO-EU, which shares the same cloud microphysical scheme. Also in terms of ETS, GMEprog shows a clear improvement compared to GME for precipitation events up to 5 mm in 24 h

and almost reaches the skill of COSMO-EU. Whether this improvement in terms of surface precipitation is connected with improved representation of grid-scale cloud ice, is investigated in the following.

6.2 Matching GME and CloudSat CPR – Part I

Temporally, for each CloudSat orbit, from the model run initialized at 0 UTC, the output of that hour which is closest to the mean time of the CloudSat orbit is chosen. Thus, forecast age varies between 1 and 24 h. Since GME resolution is hourly (see Chap. 3.1) and the length of one CloudSat orbit is approximately 1.5 h (see Chap. 4.1), the maximum time mismatch between model and satellite profile is 1.25 h. If, for example, the mean time of a CloudSat granule is 13:31 UTC, the nearest model hour is 14:00 UTC. For the first profile of the CloudSat granule, at 12:46 UTC, this would result in a time mismatch of 74 min.

To match the spatial domain of GME and CloudSat, the GME data are horizontally interpolated onto the CloudSat track with the nearest neighbour technique. Due to the coarser resolution of the model, one model profile is assigned to several adjacent CloudSat profiles. This way, no information contained in the high-resolution CloudSat data is lost.

For the frequency distributions, as an intermediate choice, both data sets are vertically linearly interpolated onto regular bins with 500 m height each. IWC, SWC, and CIWC are vertically redistributed onto the new bins, with regard to the conservation of the respective water path. This is deemed necessary, because the uneven vertical distribution of model layers in GME (see Chap. 3.1) would result in certain water contents occurring more often than others.

6.3 Case study

CloudSat passed over a cold front situated over France (cf. Fig. 6.2) on 10 August 2008 at approximately 13 UTC. The general western European weather situation present at this overflight was dominated by a series of three shortwave troughs embedded into the polar front (cf. Fig. 6.3). The corresponding surface pressure lows were situated off the coast of Norway, to the north-west of Scotland, and over the central North Atlantic (cf. Fig. 6.2). At the leading edge of the trough over Scotland, warm and moist subtropical air was led north-eastward (cf. Fig. 6.4). The associated extratropical cyclone was already well-defined and its surface front partly occluded (cf. Fig. 6.2.1). The cold front stretched from the north-western tipp of Spain across France to north-western Germany. Though the cyclogenesis of this extratropical cyclone was still in progress and the air masses were still propagating north-eastward after the CloudSat overpass, the position of the cold front over France was

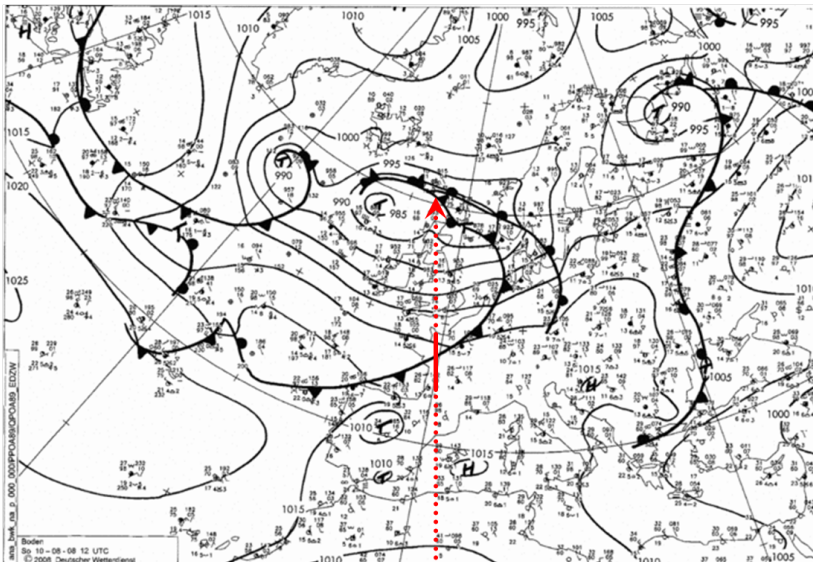

6.2.1: 10 August 2008 12 UTC.

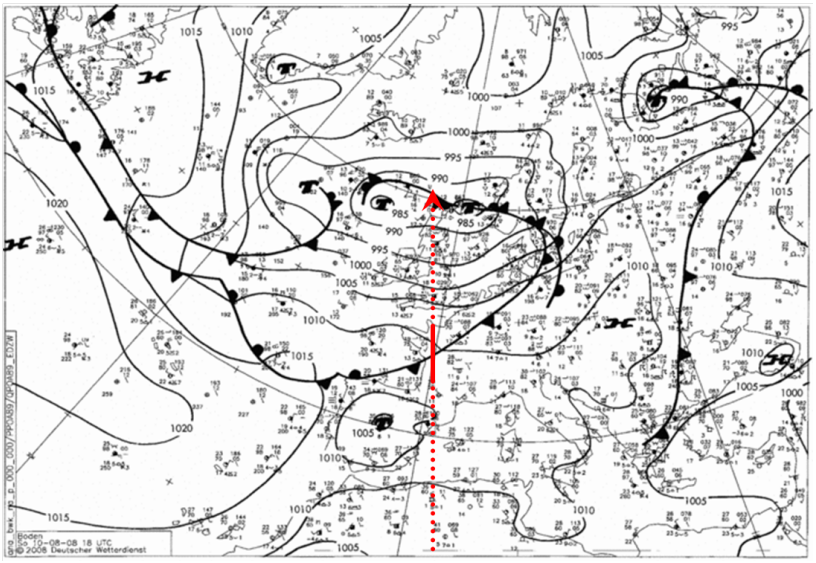

6.2.2: 10 August 2008 18 UTC.

Figure 6.2: DWD surface analysis charts for 10 August 2008 (source: `www.wetter3.de`). The red-dotted line denotes the approximate CloudSat track and direction of overpass; the solid red part of the line corresponds to the investigated 495 km cross section.

almost stationary (cf. Figs. 6.2.1-6.2.2). This fact makes the chosen case especially suitable for comparing satellite to model data, because the time mismatch does not play a major role.

According to the CloudSat CPR observations (upper panel in Fig. 6.5), the cold front is associated with a cumulonimbus-shaped cloud dominated by an area of deep convection (approximately 80 km wide). This main uplifting region is succeeded by an anvil of cirrocumuls and cirrostratus which is in total approximately 200 km wide. Below this anvil,

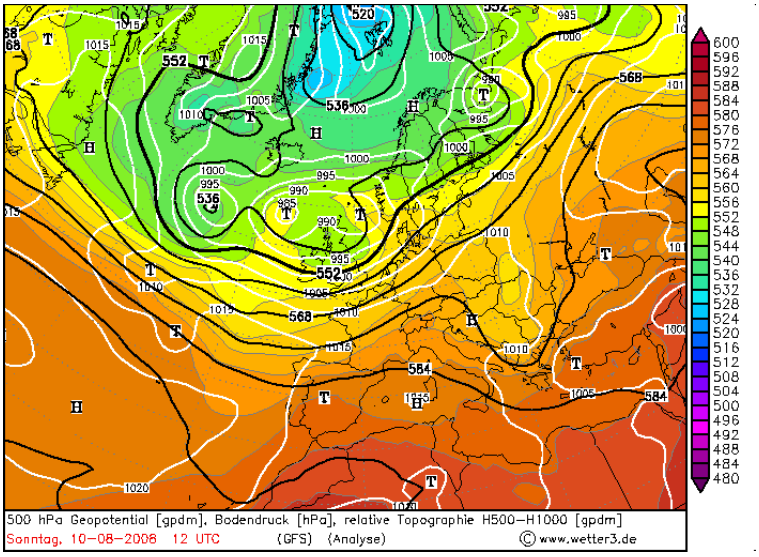

Figure 6.3: GFS analyses 500 hPa geopotential height (black contour lines), surface pressure (white contour lines), and relative topography (coloured) for 10 August 2008 12 UTC (source: `www.wetter3.de`).

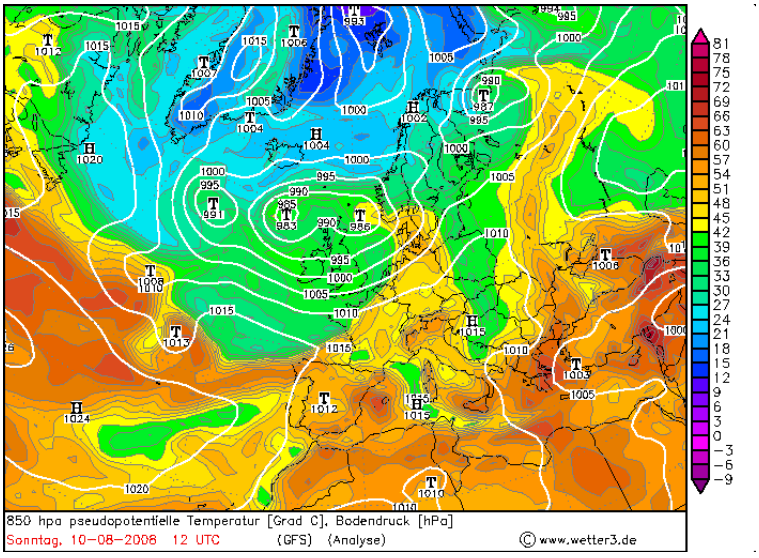

Figure 6.4: GFS analyses 850 hPa pseudopotential temperature (coloured) and surface pressure (white contour lines) for 10 August 2008 12 UTC (source: `www.wetter3.de`).

scattered shallow convective clouds indicate weak instability caused by uplifting. CTH of the cloud system as a whole is at approximately 11 km.

Both model versions, GMEdiag and GMEprog, capture the frontal cloud system (cf. middle and bottom panels in Fig. 6.5). The GMEdiag attenuated radar reflectivity factors simulated with QuickBeam (cf. middle panel in Fig. 6.5) are generally far too low in comparison to the observed CloudSat CPR reflectivity factors; the maximum values differ by roughly 50 dBz (note the different scaling of the colour bar in the middle panel). The majority of

values lies below the CloudSat CPR detection limit. Though no large spatial and temporal missmatch is observable, the vertical extension of the cloud is not well captured: CTH is at approximately 12.5 versus 11 km. This may partly be caused by the coarser vertical resolution of the model. In the region of deep convection, only a small region of notable radar reflectivity factors is simulated in approximately 2 km height, splitting the cloud into two layers. These radar reflectivity factors exceeding -40 dBz are caused by cloud water; GMEdiag predicts no rain (and no snow) for the presented case (cf. Fig. 6.7).

The magnitude of the simulated GMEprog attenuated radar reflectivity factors (cf. Fig. 6.5, lower panel) fits far better to the CloudSat CPR reflectivity factors than those of GMEdiag. In the centre of deep convection, two radar reflectivity factor maxima occur in GMEprog. This may be due to the fact that in the upper region large amounts of snow are predicted and in the lower parts rain plus cloud water (cf. Fig. 6.8). In between however, the melting layer is not simulated because the melting particle model is not yet implemented in QuickBeam (see Chap. 5.2). The splitting of the maximum radar reflectivity factors into two regions is even more extreme when regarding the unattenuated reflectivity factors (not shown). In the presented case study, attenuation of the simulated GMEprog radar reflectivity factor by hydrometeors and gases is around 10 dBz in the lower liquid cloud. As for the upper frozen cloud, the effect is lower than 2 dBz. In general, the extension of the cloud is reflected better in GMEprog than in GMEdiag, with exception of CTH; in the GMEprog CTH is also higher (approximately at 12.5 km) than observed by the CloudSat CPR.

The cross sections of retrieved and modelled IWCs (cf. Fig. 6.6) show that both GME versions determine too small IWC values in comparison to the CloudSat CPR. Mean IWCs* are $0.0853\,\mathrm{g\,m^{-3}}$ for CloudSat, $0.0038\,\mathrm{g\,m^{-3}}$ (4 %) for GMEdiag, and $0.0382\,\mathrm{g\,m^{-3}}$ (45 %) for GMEprog. Note that the mean IWC is subject to averaging effects; the choice of horizontal and vertical resolution of the data influences the mean IWC. Running means, too, have an impact on the mean. Though this is not of importance for this case study, it should be kept in mind for later chapters, specifically for Chap. 6.4 where the results of the statistical approach are presented and further measures for matching are applied.

Also, the extensions of the cloud and its core with maximum IWC values are not well reproduced by both versions. Maximum IWCs are $0.5900\,\mathrm{g\,m^{-3}}$ for CloudSat, $0.0094\,\mathrm{g\,m^{-3}}$ for GMEdiag, and $0.1707\,\mathrm{g\,m^{-3}}$ for GMEprog. However, GMEprog shows a distinct improvement in comparison to GMEdiag. CloudSat gives higher peak IWC values because its resolution (1.1 km) is far higher than that of GME (40 km). The global model is unable to capture these water content variations. In the statistical approach presented in the following Chap. 6.4, this is attempted to accounted for by horizontal smoothing.

A more direct comparison of the observed and simulated attenuated radar reflectivity factors is shown in the scatterplots in Fig. 6.9. Though a large scatter can be expected due to temporal and spatial shifts in the cloud forecasts, this offers a way to look at systematic

*Only IWCs $\geq 0.001\,\mathrm{g\,m^{-3}}$ (the CloudSat CPR detection limit) are taken into account.

effects. A negative overall bias [†] (cf. Eq. 6.3) can be seen for both GME versions, but the bias is far smaller for GMEprog than for GMEdiag (4.61 dBz versus −36.05 dBz). The percent difference (PD, cf. Eq. 6.4), too, is smaller for GMEprog: 0.02 % versus −28.44 %. However, it should be noted that in case of GMEdiag only 20 data pairs enter the calculations; all other data pairs lie below the CloudSat CPR detection limit (and are therefore not included in the comparison).

$$Avg.bias = \frac{1}{N} \cdot \sum_i (Z_{GME_i} - Z_{CloudSat_i}) \tag{6.3}$$

$$PD = 100 \cdot \frac{\frac{1}{N} \cdot \sum_i (Z_{GME_i} - Z_{CloudSat_i})}{\frac{1}{N} \sum_i Z_{CloudSat_i}} \tag{6.4}$$

The frequency distribution for the CloudSat CPR reflectivity factors reveals that the detection range of the CloudSat CPR is nearly completely covered and that each dBz-bin occurs more or less similarly often. The larger occurrence of CloudSat CPR reflectivity factors between −27.5 dBz and −30 dBz is due to noise at the lower detection limit of the CloudSat CPR and can be ignored. In contrast to the CloudSat frequency distribution, the GMEdiag frequency distribution of the reflectivity factors is narrow and askew: approximately 50 % lie in the range −35 dBz to −45 dBz. Approximately 30 % lie outside the limits of the figure, i. e. below −50 dBz. As for the GMEprog frequency distribution of the reflectivity factors, it is even more askew than that of GMEdiag. More than 80 % lie at the upper end of the range, between 2.5 dBz and 12.5 dBz. This lopsided frequency distribution is even better discernible in the joint CloudSat-GME frequency distributions in Fig. 6.10 . All in all, these distributions appear rather similar for both model versions; they are simply shifted towards higher dBz-values for GMEprog (cf. Fig. 6.10).

Just how large the difference in the observed and predicted IWCs is becomes clearer when regarding the column integrated IWPs (cf. Fig. 6.11). Whereas CloudSat observes IWPs of maximal 1600 g m^{-2}, the maximum values of GMEprog are only half of that (800 g m^{-2}) and those of GMEdiag are negligible (approximately 20 g m^{-2}). The separation of IWP into CIWP and SWP reveals that the majority is denoted by snow. Since this is missing in GMEdiag, the small IWP values are not surprising.

Finally, in Fig. 6.12 the distribution of IWC with height is displayed. According to the CloudSat CPR radar-only algorithm, the maximum IWC values (0.6 g m^{-3}) occur in approximately 7 km height. In GMEdiag the maximum (0.01 g m^{-3}) lies in 9 km height, and in GMEprog the maximum (0.18 g m^{-3}) lies in 5–5.5 km height. GMEprog is able to reproduce the higher frequencies of occurrence along the upper right edge of the particle size distribution very well. Generally speaking, although the magnitude of the IWC values is still too small and the height of maximum IWC is not predicted accurately, GMEprog appears to reproduce the CloudSat frequency distribution distinctly better than GMEdiag.

[†]Only radar reflectivity factors ≥ -30 dBz are taken into account. Therefore, the number of data pairs N included in the calculations can even be zero in extreme cases.

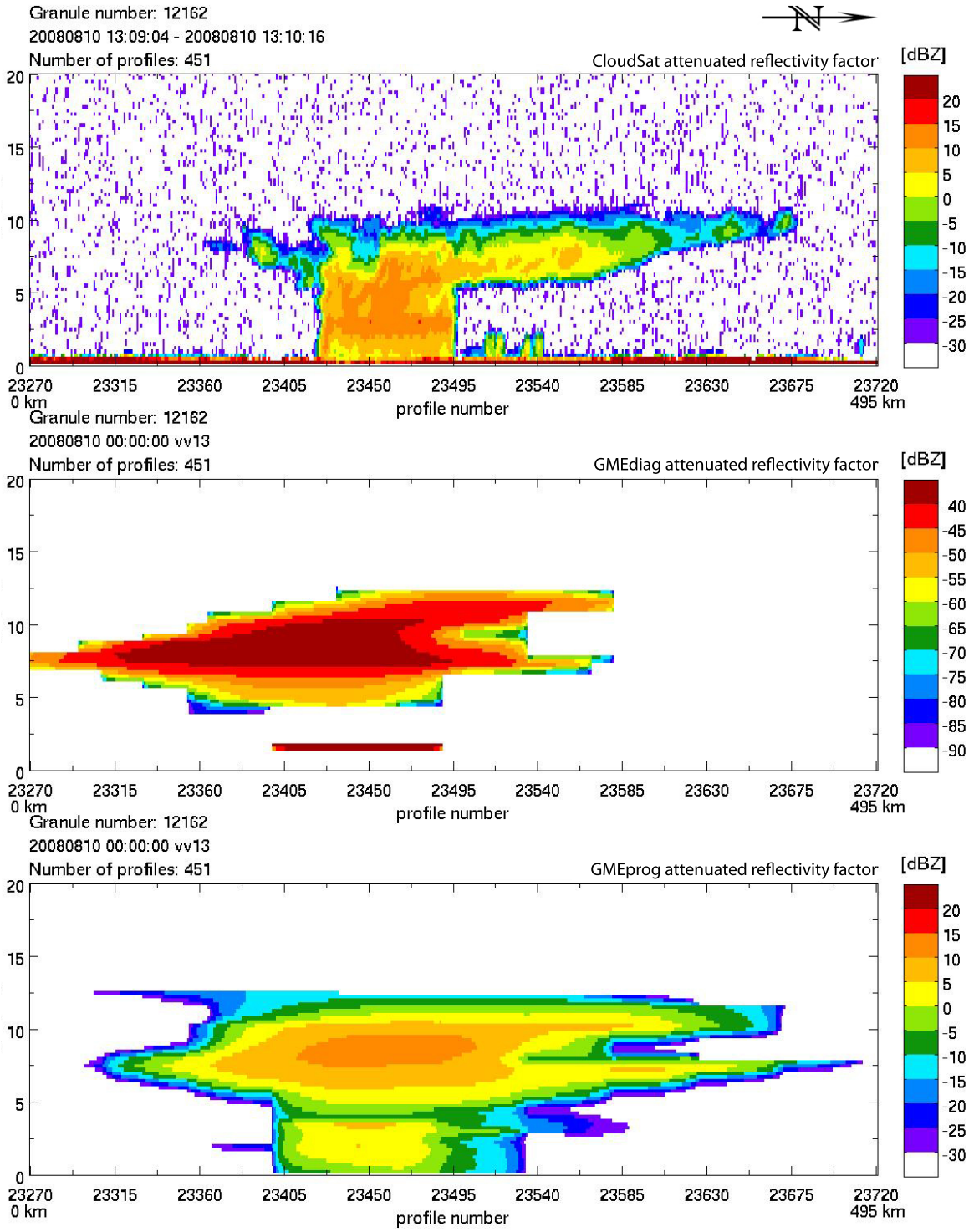

Figure 6.5: Along-track cross sections of observed CloudSat (upper panel), simulated GMEdiag (middle panel), and simulated GMEprog (lower panel) attenuated radar reflectivity factors for a part of granule 12162 on 10 August 2008 around 1310 UTC. Here, GMEdiag is GME6864 and GMEprog is GME6831. Note the different scaling of the colour bar in the middle panel.

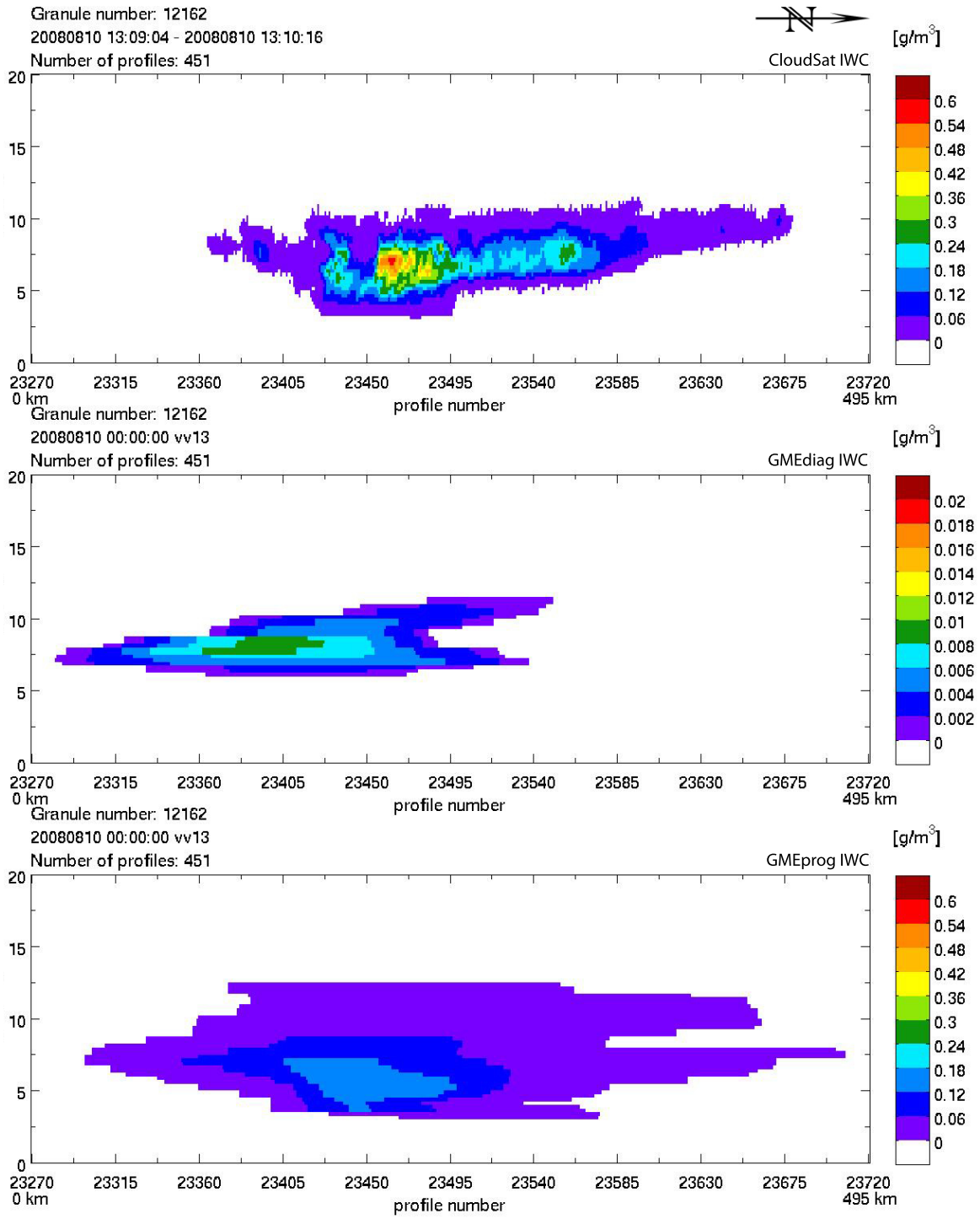

Figure 6.6: Along-track cross sections of retrieved CloudSat (upper panel), forecasted GMEdiag (middle panel), and GMEprog (lower panel) IWC for a part of granule 12162 on 10 August 2008 around 1310 UTC. Here, GMEdiag is GME6864 and GMEprog is GME6831. Note the different scaling of the colour bar in the middle panel.

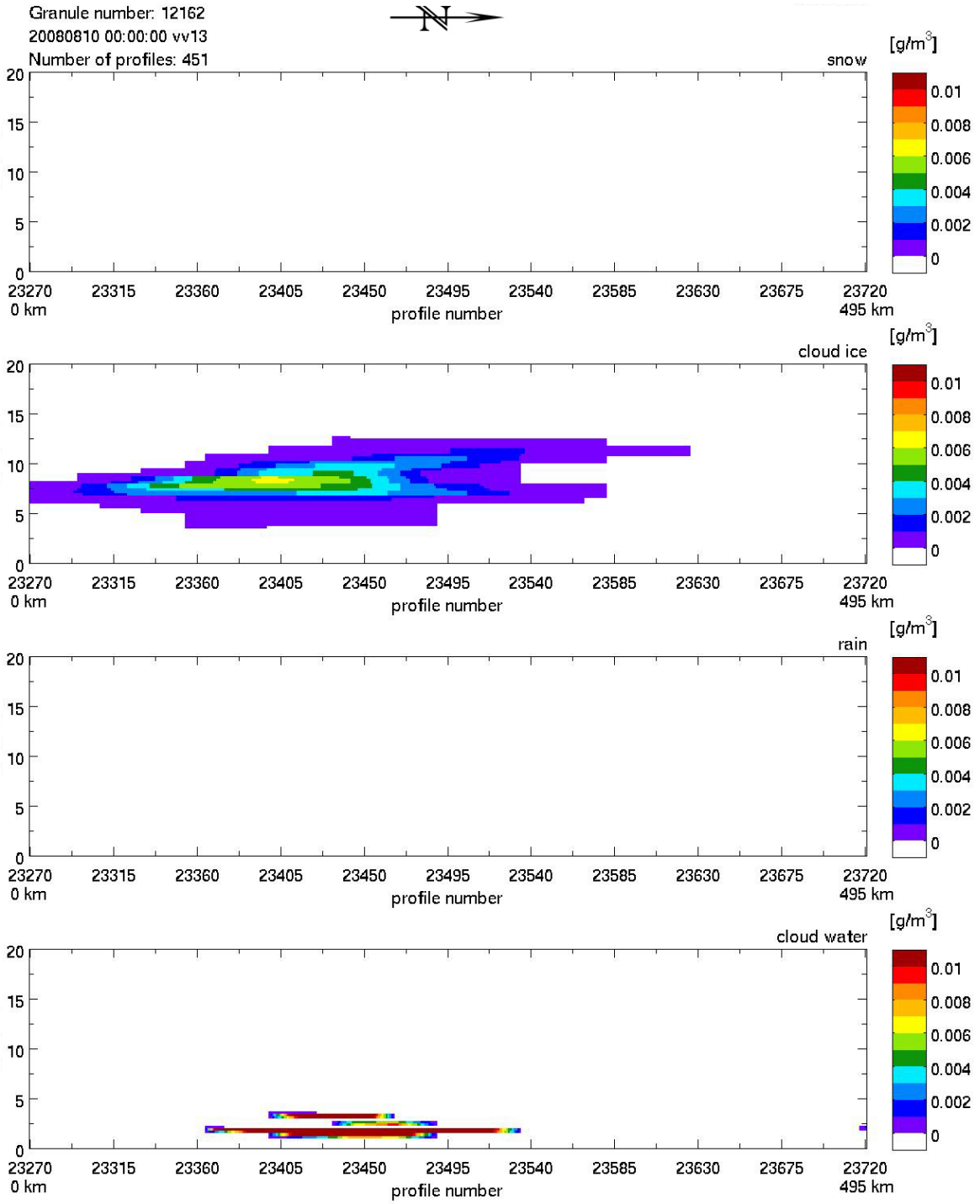

Figure 6.7: Along-track cross sections of GMEdiag (GME6864) specific hydrometeor contents for a part of granule 12162 on 10 August 2008 around 1310 UTC. Values of zero are displayed in white.

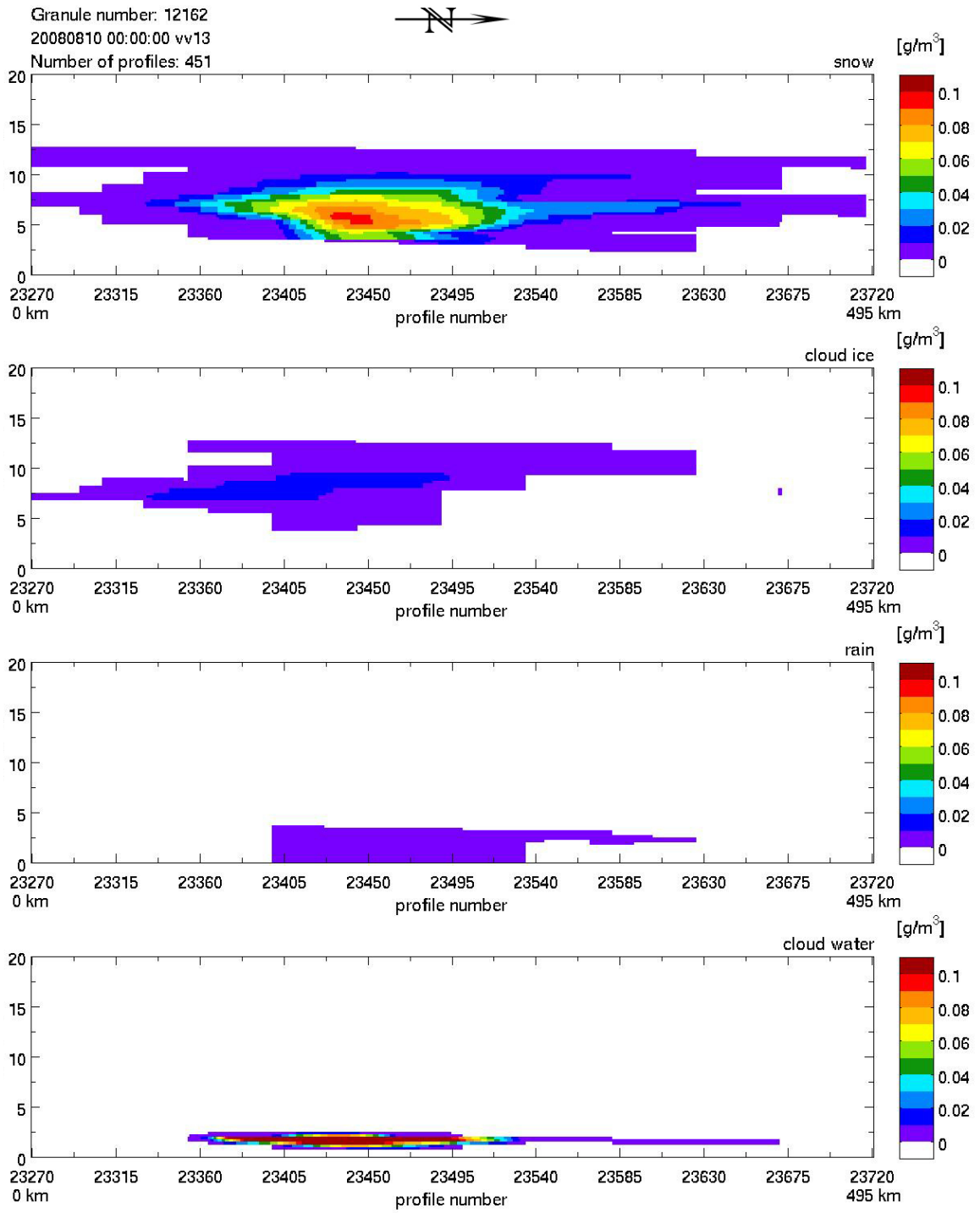

Figure 6.8: Along-track cross sections of GMEprog (GME6831) specific hydrometeor contents for a part of granule 12162 on 10 August 2008 around 1310 UTC. Values of zero are displayed in white.

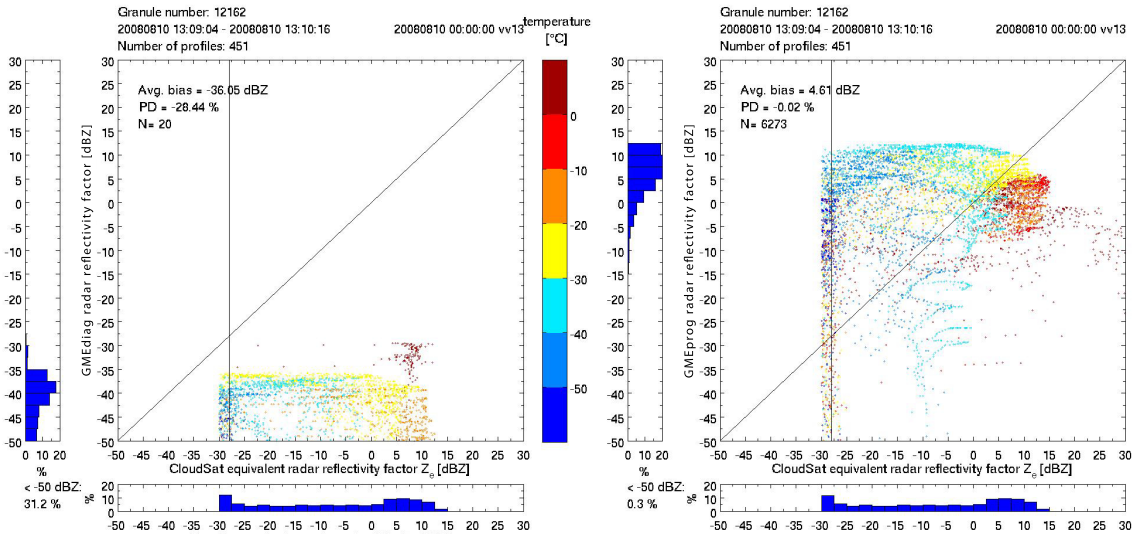

Figure 6.9: Scatterplots of observed CloudSat versus simulated GME attenuated radar reflectivities as a function of GME temperature for a part of granule 12162 on 10 August 2008 around 1310 UTC. Left: GMEdiag (GME6864), right: GMEprog (GME6831). Note that cool colours may overlap warmer colours. The vertical black line denotes the CloudSat detection limit. The narrow plots below and to the left of the scatterplots depict the frequency distributions. Note that the CloudSat noise below -30 dBz is cut off. Average bias and PD are calculated for reflectivity factors ≥ -30 dBz only, according to Eqs. 6.3 and 6.4. The amount of data with GME radar reflectivity factor < -50 dBz is given in the lower left corner of the respective plot.

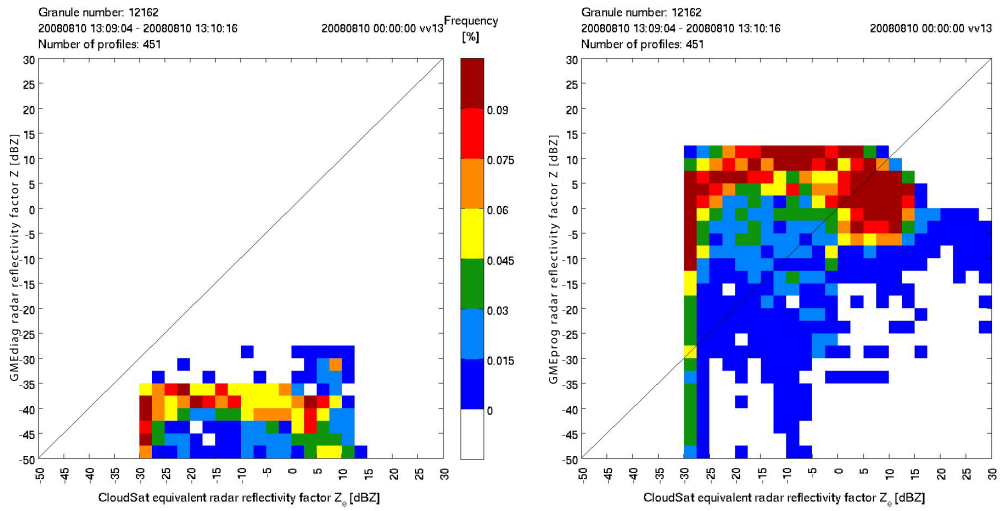

Figure 6.10: Same as in Fig. 6.9 but as frequency density plots. Values of 0 % are displayed in white.

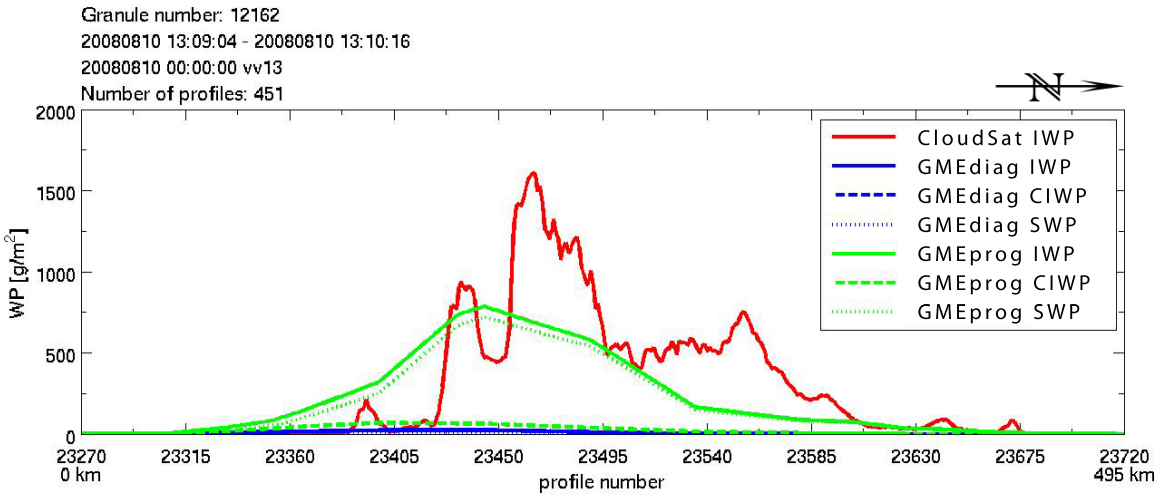

Figure 6.11: Water paths for a part of granule 12162 on 10 August 2008 around 1310 UTC. Here, GMEdiag is GME6864 and GMEprog is GME6831.

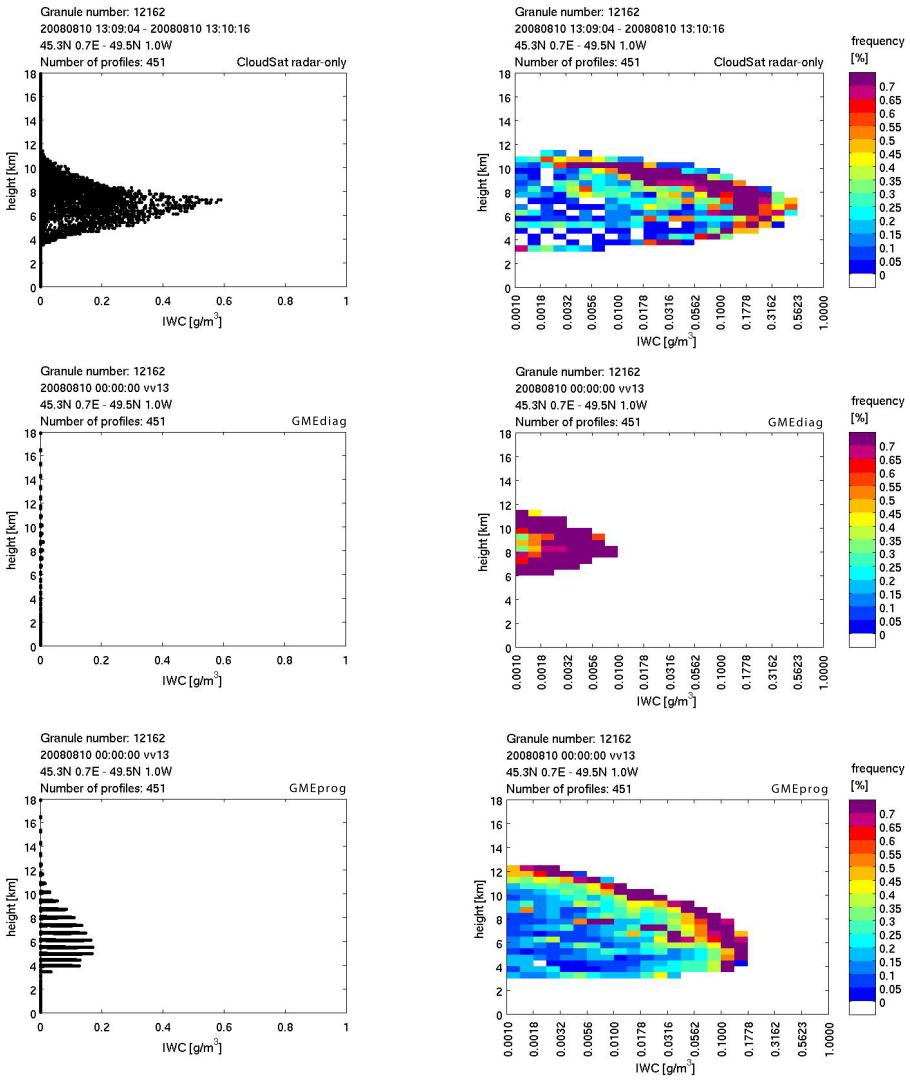

Figure 6.12: Height-IWC plots for a part of granule 12162 on 10 August 2008 around 1310 UTC. Left column: scatterplots with IWC scaled linearly. Right column: Logarithmic frequency distribution of IWC. Here, GMEdiag is GME6864 and GMEprog is GME6831.

6.4 Statistical approach

Though a case study such as the one presented in the previous chapter can improve the understanding of the models' microphysics and the applied methodologies, a statistical approach is required in order to enable conclusive statements on the performance of the two model versions. This is done in the following chapter for a period of four months (see Chap.3.1.4). Since the result of a statistical approach is chiefly dependent on the choice of data pairs included in the comparison, both resolution and cloud scene issues are addressed (Chap. 6.4.1) before the results are presented (Chap. 6.4.2). The results presented in this chapter have been published in *Reitter et al. (2011)*.

6.4.1 Matching GME and CloudSat CPR - Part II

In addition to the matching described in Chap. 6.2 for the case study, an along-track 37-profile moving average is applied to the CloudSat data, to take the coarser model resolution into consideration. The original horizontal resolution of the CloudSat data is maintained, but by applying this running mean, clouds in the observations become broader and in-cloud radar reflectivity factor maxima are attenuated. This is important, since the model with its coarser resolution is technically not able to resolve such maxima.

After this preprocessing, in order to account for instrument and retrieval algorithm sensitivities, only data (from model and observation) which are firstly within the CloudSat CPR's sensitivity range and secondly deemed trustworthy are included in the investigations. That is, only radar reflectivity factors between $-26\,\mathrm{dBz}$ and $29\,\mathrm{dBz}$ and IWCs between $0.001\,\mathrm{g\,m^{-3}}$ and $1\,\mathrm{g\,m^{-3}}$ are considered. No radar reflectivity factors below $-26\,\mathrm{dBz}$ are used due to increased influence of noise and no IWCs above $1\,\mathrm{g\,m^{-3}}$ are used since they are deemed untrustworthy by *Austin et al. (2009)*.

Since the model is not capable of assessing all regimes equally well, an effort is made to improve the comparability of model and observations by excluding those regimes, which the model can not sufficiently assess. Four criteria, based on model and/or observational parameters, are applied as a filter to all three data sets, models and observations. If a threshold is not met, both models and observations of a matching pixel are discarded. The four criteria are:

(1) only temperatures lower than $-10\,^{\circ}\mathrm{C}$ to avoid liquid and most mixed phase clouds,

(2) top of convection below 1 km height to reduce subgrid and mixed phase effects associated with convection,

(3) cloud cover larger than 50 % to ensure homogeneous conditions, and

(4) total column attenuation not larger than 3 dBz to avoid large particles and the large attenuation associated with these.

Criterion (4) is only applicable in the model-to-observation approach, which offers a better control. Criteria (1) and (4) are diagnosed from both observations and model and applied to the respective data set. Criteria (2) and (3), though diagnosed from model output, are assumed to be true for the observations. This is feasible for a NWP model analysis, because with a forecast age of less than or equal to 24 h (see Chap. 6.2), the model is — in most cases — able to predict the large-scale environment in a deterministic sense. For example, the model is able to predict the large-scale occurrence of deep convection well on this time scale (possibly overestimating the convective area), though its ability to predict the related IWC correctly may be poor. Note that this conditional sampling approach, though applicable in the evaluation of a short-range NWP model, can not be applied to a climate model.

Depending on the investigated parameter, these four criteria reduce the number of included pixels to approximately 20–25 % of the total amount. Especially concerning the warmer temperature regime, these criteria improve the comparability of model and satellite data distinctly.

6.4.2 Results

In a first evaluation step, global frequency distributions are investigated as a function of temperature (cf. Fig. 6.13). For both CloudSat (cf. Fig. 6.13a) and GMEprog (cf. Fig. 6.13b) the occurring IWCs cover the full range of values up to the upper sensitivity threshold of the CloudSat CPR. Contrary, the largest IWCs for GMEdiag (cf. Fig. 6.13c) are merely $0.06\,\mathrm{g\,m^{-3}}$ (-1.2 in $\log_{10}$(IWC)). This is primarily due to the missing snow which — being diagnosed — falls out instantaneously after generation. Note that the diagnostic scheme of GMEdiag does assume an equilibrium precipitation profile, enabling the estimation of SWC for that profile. Though this might be considered the more consistent evaluation strategy of the diagnostic scheme, this route is not pursued because the hydrological cycle of the model can not store mass in this profile. When considering GMEprog CIWC (cf. Fig. 6.13d) a similiar shape of the frequency distribution as for GMEdiag IWC (cf. Fig. 6.13c), but with a shift towards larger values, is notable. In general, GMEprog (cf. Fig. 6.13b) captures the enhanced occurrence of smaller IWCs with decreasing temperatures which CloudSat (cf. Fig. 6.13a) features well. However, the observation-to-model approach also reveals a distinct difference between CloudSat and GMEprog: the GMEprog maximum of the frequency of occurrence of IWCs reaches up to lower temperature regimes than for CloudSat ($-54\,^{\circ}\mathrm{C}$ versus $-50\,^{\circ}\mathrm{C}$), most likely because the CloudSat retrieval does not produce a clear IWC maximum from the measured reflectivity factors in these heights, but rather produces a broad range of IWC values.

The model-to-observation approach (cf. Fig. 6.13e and f), too, shows how well GMEprog

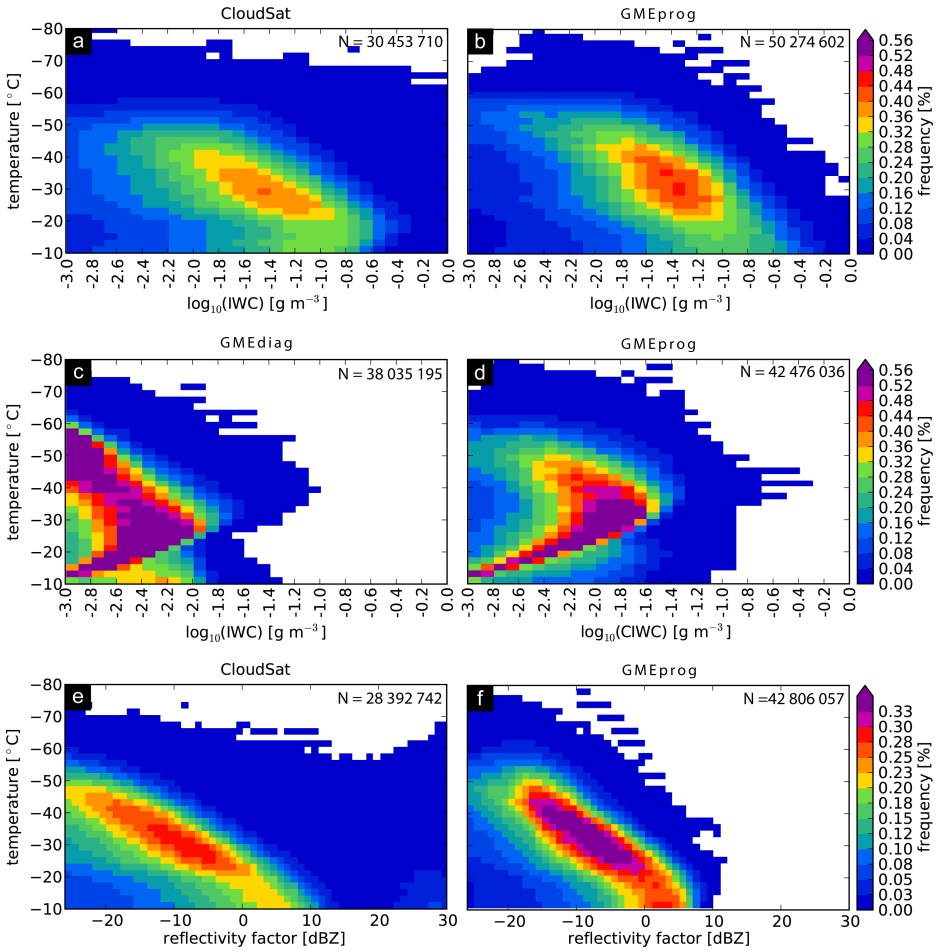

Figure 6.13: Global frequency distributions for 1 July 2009 to 31 October 2009. (a) CloudSat IWC, (b) GMEprog IWC, (c) GMEdiag IWC, (d) GMEprog CIWC, (e) CloudSat CPR reflectivity factor, and (f) GMEprog radar reflectivity factor. Each data set is normalized with its number N of included pixels. Here, GMEdiag is the operational GME of that time and GMEprog is GME1007.

reproduces the frequency distribution of CloudSat. Here, another difference between CloudSat and GMEprog is revealed: The frequency distribution is more narrow for GMEprog than for CloudSat; it spans a smaller reflectivity factor range at a given temperature level (e. g. -20–2 dBz versus -26–0 dBz at -30 °C), indicating a tighter temperature-reflectivity factor relationship (and therewith tighter temperature-IWC relationship) in the model parameterizations. Also, the slope of the maximum is steeper for GMEprog. Contrary to GMEprog, GMEdiag hardly shows any reflectivity factors above -26 dBz (not shown).

In a next step, analyses are refined to resolve meridional variation in IWP (cf. Fig. 6.14). At this point, it is appropriate to demonstrate the individual influence of the applied criteria on IWP. The temperature criterion (1) alone (cf. Fig. 6.14c) slightly reduces the IWP of all data sets at all latitudes, but does not change the general meridional variation in comparison to without any criteria (cf. Fig. 6.14a). The convection criterion (2) alone (cf. Fig. 6.14d) reduces IWP distinctly in the tropics, underlining the importance of convectively induced

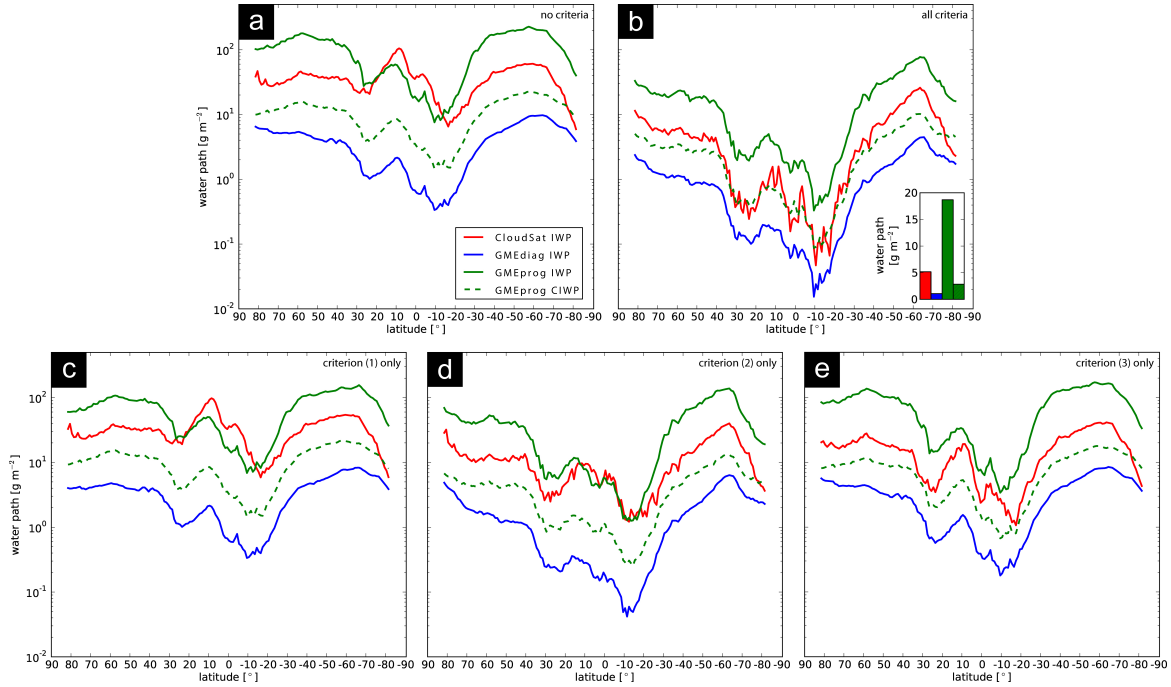

Figure 6.14: Zonally averaged water paths for 1 July 2009 to 31 October 2009. Red: CloudSat; blue: GMEdiag; green: GMEprog. Solid: IWP; dashed: CIWP. a) no criteria, b) all criteria, c) temperature criterion only, d) convection criterion only, e) cloud cover criterion only. Inset in b): globally averaged IWP on linear scale. Averaged over total number of pixels and profiles, respectively. Here, GMEdiag is the operational GME of that time and GMEprog is GME1007.

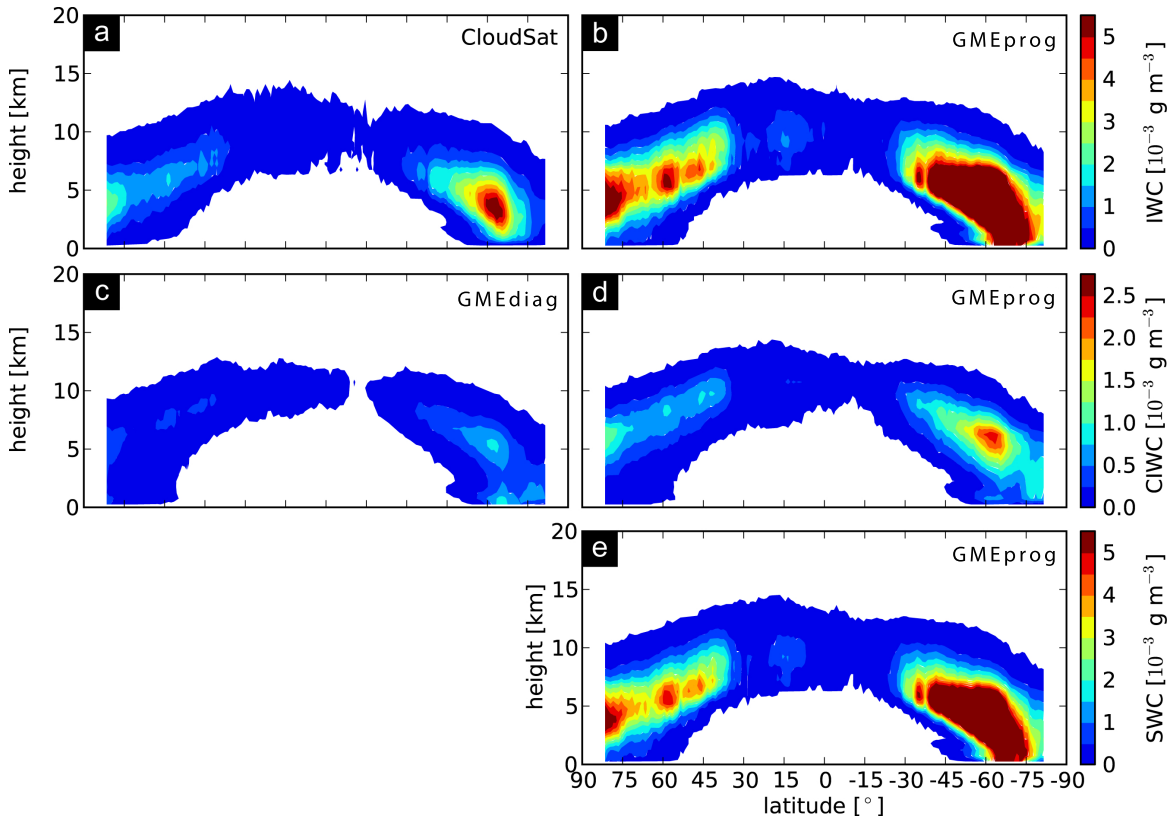

Figure 6.15: Zonally averaged water contents for 1 July 2009 to 31 October 2009: (a) CloudSat IWC, (b) GMEprog IWC, (c) GMEdiag IWC, (d) GMEprog CIWC, and (e) GMEprog SWC. Averaged over total number of pixels and profiles, respectively. Here, GMEdiag is the operational GME of that time and GMEprog is GME1007.

IWC in this region, but IWP is also reduced in the mid-latitudes. The cloud cover criterion (3) alone (cf. Fig. 6.14e) appears to affect only the tropics; IWP in mid-latitudinal and polar regions remains overall the same. This emphasizes the fact that IWC in the tropics is largely connected to small scale events, which the microphysical scheme is not able to capture due to the model's resolution; subgrid-scale processes are not represented in the hydrometeor output. When applying all criteria (cf. Fig. 6.14b), GMEprog captures the zonally averaged IWP pattern of CloudSat rather well. CIWP in GMEprog is small in comparison to its IWP, underlining again the importance of SWP as a contribution to IWP. Yet CIWP of GMEprog remains distinctly larger than GMEdiag IWP, as shown in Fig. 6.13. However, GMEprog consequently overestimates IWP and considerably overestimates mid-latitudinal IWP by a factor of 4. This strong overestimation is not discernible in the frequency distributions shown in Fig. 6.14, because they are normalized for each data set separately with the number of included pixels. Checks with mass distributions instead of frequency distributions (not shown) confirm the overestimation of IWP in GMEprog as revealed by Fig. 6.14b.

The zonally averaged IWC (cf. Fig. 6.15) shows that the meridional position of the IWC peaks of CloudSat is captured well by GMEprog (cf. Fig. 6.15b), though these peaks are positioned at lower heights in GMEprog than in CloudSat (cf. Fig. 6.15a). GMEdiag IWC and GMEprog CIWC are positioned at exactly the same heights, but the peaks are larger in GMEprog than in GMEdiag (0.75 versus $2.25\,10^{-3}\,\mathrm{g\,m^{-3}}$), which fits to the global frequency distributions in Fig. 6.13.

Further refinement — separation into three temperature regimes for three zonal regions — is applied to specify the differences in zonally averaged IWP between GMEprog and CloudSat. Contrary to the frequency distributions above, the histograms in Fig. 6.16 do reflect the above mentioned over-/underestimation of IWC, because they are normalized with the total number of pixels, whether cloudy or not. GMEdiag consequently underestimates the higher IWC values, as discussed above. In general, GMEprog reproduces the shape of the distribution of CloudSat better than GMEdiag, especially in the mid-latitudes and polar regions. Here, the peak of maximum frequency of occurrence is located at roughly the same IWC, shifted by 2 bins (i. e. $0.02\,\mathrm{g\,m^{-3}}$) at the most. Yet, the peak is highly overestimated; in the warmest temperature regime by a factor of 3 in the tropics, by a factor of 1.5 in the mid-latitudes, and by a factor of 2 in the polar regions. With decreasing temperature the overestimation increases. This points to an overlong residence time of snow in the air, i. e. an underestimation of the fall speed of snow, leading to the overestimation of zonally averaged IWC and IWP seen in Fig 6.14 and Fig 6.15. As for the upper IWC range, this is not reproduced (or underrepresented) in the tropics in GMEprog, partly compensating the overestimation of IWP in this region (Fig 6.14). This might be attributed to the fact that deep convective events which produce the largest particles in the tropics are not resolved by the model and are eliminated by the criteria. Finally, small IWCs are underrepresented in GMEprog in comparison to CloudSat, which might be due to several reasons, e. g. a too fast depositional growth or the missing homogeneous nucleation of aerosols.

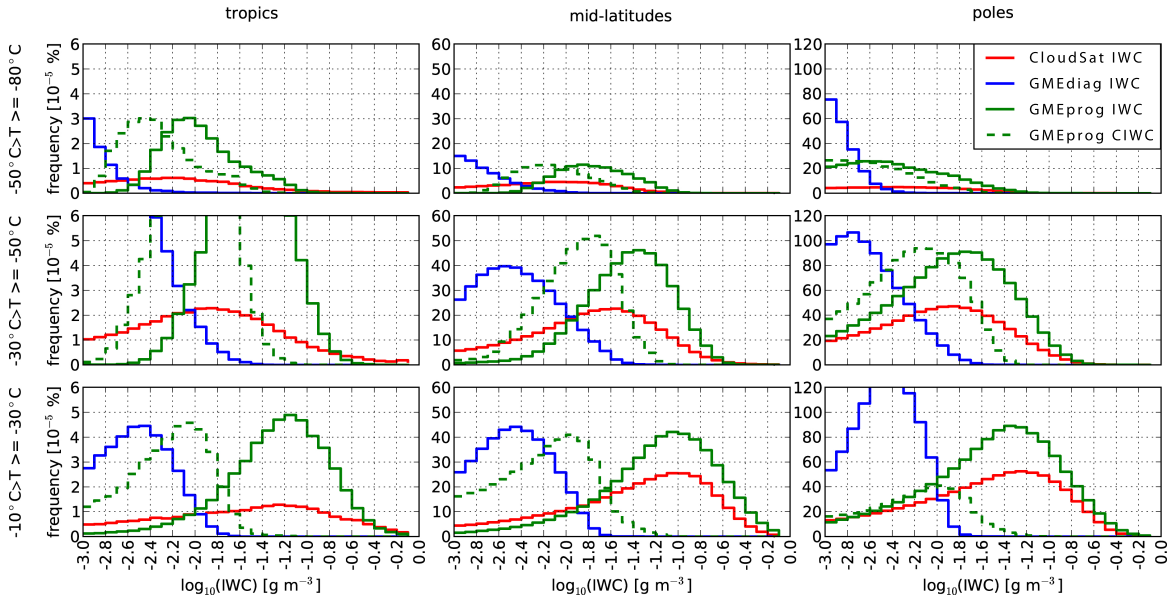

Figure 6.16: Histograms of frequency distributions of IWC for 1 July 2009 to 31 October 2009 for three temperature (−10 to −30 °C (bottom), −30 to −50 °C (middle), −50 to −80 °C (top)) and three latitudinal (tropics (left), mid-latitudes (middle), polar regions (right)) regimes. Normalized with total number of pixels. Here, GMEdiag is the operational GME of that time and GMEprog is GME1007.

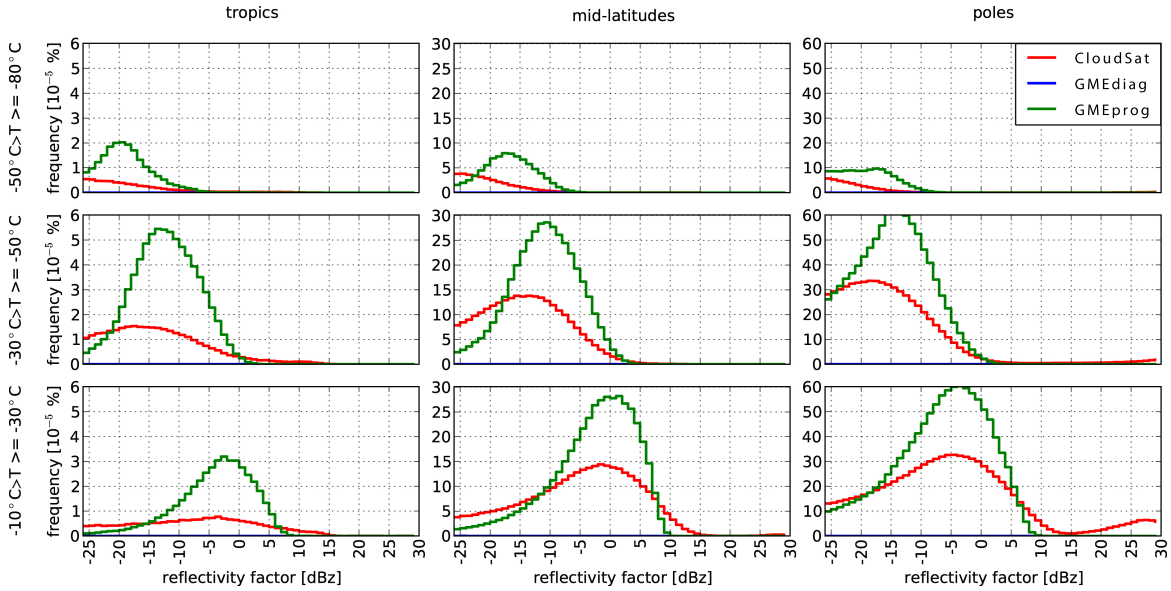

Figure 6.17: Histograms of frequency distributions of radar reflectivity factor for 1 July 2009 to 31 October 2009 for three temperature (−10 to −30 °C (bottom), −30 to −50 °C (middle), −50 to −80 °C (top)) and three latitudinal (tropics (left), mid-latitudes (middle), polar regions (right)) regimes. Normalized with total number of pixels. Here, GMEdiag is the operational GME of that time and GMEprog is GME1007.

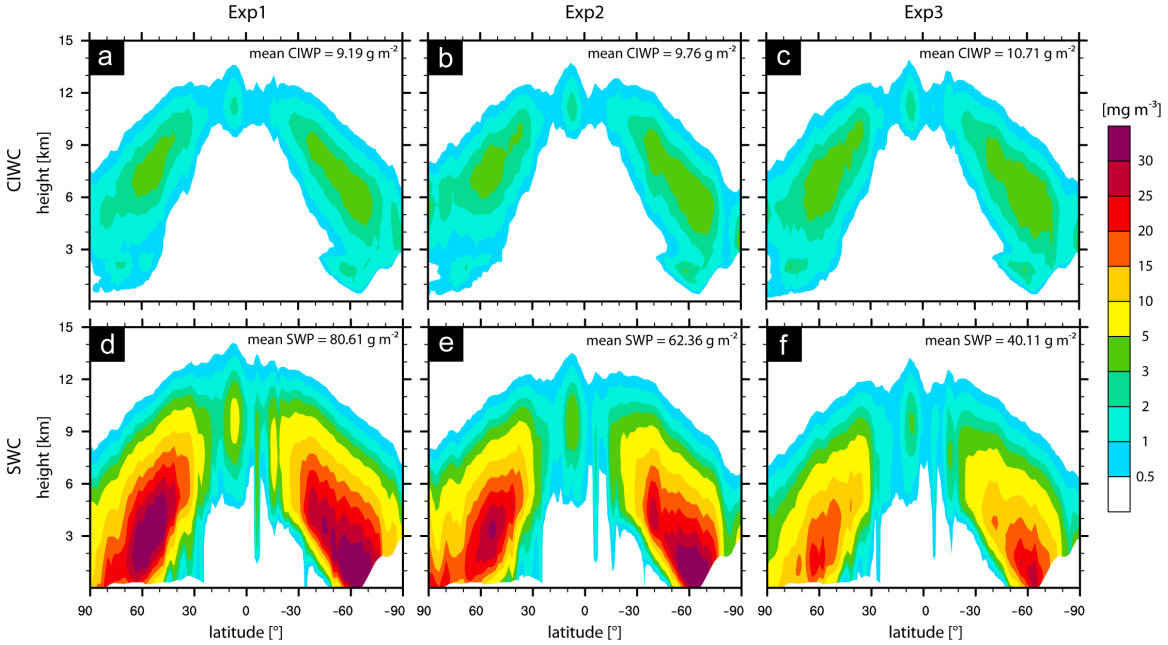

Figure 6.18: Zonal averages of GMEprog (GME1007) for a 25 day period. Top row: Zonally averaged CIWC, bottom row: Zonally averaged SWC. Left column: Exp1, middle column: Exp2, right column: Exp3.

The features discernible in the IWC frequency distributions are robust, also in reflectivity factor (cf. Fig. 6.17). Additionally, two further features are discernible. First, with decreasing temperature, the peak of maximum frequency of occurrence of GMEprog is shifted more and more to higher reflectivity factors than for CloudSat. Second, the frequency distribution is more narrow for GMEprog than for CloudSat. These findings agree with the steeper and narrower global frequency distribution for GMEprog seen before in Fig. 6.13. As in Fig. 6.13, GMEdiag produces small reflectivity factors which are outside the displayed range and therewith outside the detection limit of CloudSat. The same applies for GMEprog reflectivity factors calculated from CIWC only.

In order to test the hypothesis of a too small fall speed of snow being responsible for the IWC/IWP overestimation, a sensitivity study is conducted (cf. Fig. 6.18); three experiments are set up:

Exp1: Control run with the same configuration as GMEprog.

Exp2: Introduction of a density correction for the fall speed of precipitating hydrometeors. Consequently, the fall speed of precipitating hydrometeors is no longer constant with height. Rather, in higher altitudes where air density is lower, particles fall faster than in lower altitudes with higher air density.

Exp3: Additional introduction of an increased and more realistic fall speed of snow, compared to a reference fall speed based on *Khvorostyanov and Curry (2005)*, with $v = 25 \cdot D^{0.5}$.

For each experiment, a 30-day simulation is performed, and only the last 25 days are analysed to exclude effects of model spin-up. As expected, the faster falling snow leads to a reduction of SWC (cf. Fig. 6.18) while large-scale surface precipitation is only marginally affected (not shown). Globally averaged, this amounts to a reduction of mean SWP from $81\,\mathrm{g\,m^{-2}}$ to $62\,\mathrm{g\,m^{-2}}$ for Exp2 and a further reduction to $40\,\mathrm{g\,m^{-2}}$ for Exp3. CIWC and CIWP, respectively, increase negligibly with increased snow fall speed. Therefore, the unrealistically small fall speed of snow in GMEprog can explain most of the positive bias in IWC and IWP, respectively, which is found compared to CloudSat.

To explain the remaining IWC bias, note that a further increase of snow fall speeds might occur in regions of heavy riming or graupel formation, however, both are currently not taken into account for grid-scale clouds in GME. Furthermore, other model errors than cloud microphysics might also contribute to the remaining unexplained IWC bias.

6.5 Summary and conclusions

This part of the present study evaluates the global NWP model GME with respect to frozen particles, and in doing so focuses on the performance of a prognostic versus a diagnostic precipitation scheme. As a reference, CloudSat CPR observations are utilized, which offer the so far unique opportunity to vertically resolve clouds at a near-global scale.

The prognostic scheme is found to capture the shape and magnitude of the CloudSat CPR frequency distributions of IWC and radar reflectivity factor well. In contrast, the diagnostic scheme considerably underestimates the larger IWC and radar reflectivity factor values, a result of the fact that snow falls out instantaneously. As a consequence of the improved overall performance, the prognostic scheme presented here went operational on 2 February 2010.

Furthermore, the height-resolving CloudSat CPR enables the continuous assessment of processes within clouds. It is shown that the prognostic scheme still requires improvements, especially concerning the overestimation of IWP. One source of error, the too small fall speed of snow, is identified: With the introduction of a — so far neglected — density-dependency, the fall speed increases with height, thereby reducing IWP. Due to this further improvement in performance, the microphysical choices of Exp2 went operational on 1 December 2010.

The presented multi-parameter validation enables the comparison of the two approaches: The general features are robust and captured by both approaches. However, details are captured by merely one or the other approach, in which case both approaches together deliver the largest informational content. But, the model-to-observation approach ensures a better control over the comparison, notably through the attenuation criterion, which filters

out grid cells with higher attenuation and therefore uncertainty. The developed criteria successfully filter out situations the model is not able to capture (e. g. subgrid-scale processes contributing to IWC) and thereby improve the comparability between model and observations distinctly.

Finally, the evaluation presented in this chapter shows that in GME snow is the dominant contributor to IWC and IWP. This finding agrees well with the aircraft measurements of *Field et al. (2005)*, which reveal that snow (aggregates) contributes up to 90 % to IWC in frontal clouds. This might help to explain why most climate models, which do not resolve snow and rain explicitly, tend to underestimate IWC (*Waliser et al., 2009*).

7 Evaluation of COSMO-DE

In the following chapter, the performance of a novel two-moment cloud ice scheme in COSMO-DE (COSMO-DE8822, Chap. 3.2.5) is compared to that of two standard microphysical schemes (COSMO-DE8819, see Chap. 3.2.4 and COSMO-DE9009, see Chap. 3.2.3) and evaluated with satellite observations (Chap. 4). The comparison is undertaken with respect to a specific long-known bias in COSMO-DE, which is introduced in Chap. 7.1. After this introduction, results from a statistical approach are presented first (Chap. 7.2). Second, in a case study, the reason for the observed behaviour is investigated in detail (Chap. 7.3.2). For this case, a set of sensitivity experiments is finally undertaken (Chap. 7.3.3) before at the end of this chapter a summary of the findings is given and the COSMO-DE-specific conclusions are presented (Chap. 7.4). More general conclusions are left for the overall conclusions and outlook in Chap. 8.

7.1 Posing the question

With the long-term goal of eventually assimilating MSG SEVIRI brightness temperatures operationally in COSMO-DE, DWD coupled the radiative transfer model RTTOV to COSMO-DE via the diagnostic tool SynSat (see Chap. 5.3). This enables the operational simulation of observed brightness temperatures from COSMO-DE output. Within their evaluation of COSMO-DE's forecasting performance during the General Observation Period (GOP; *Crewell et al., 2008*) of the German Priority Programme on Quantitative Precipitation Forecasting (Praecipitationis Quantitativae Praedictio, PQP), *Böhme et al. (2011)* find a distinct bias between simluated COSMO-DE and observed MSG SEVIRI brightness temperatures in the 10.8 μm channel: In this channel, COSMO-DE distinctly overestimates the

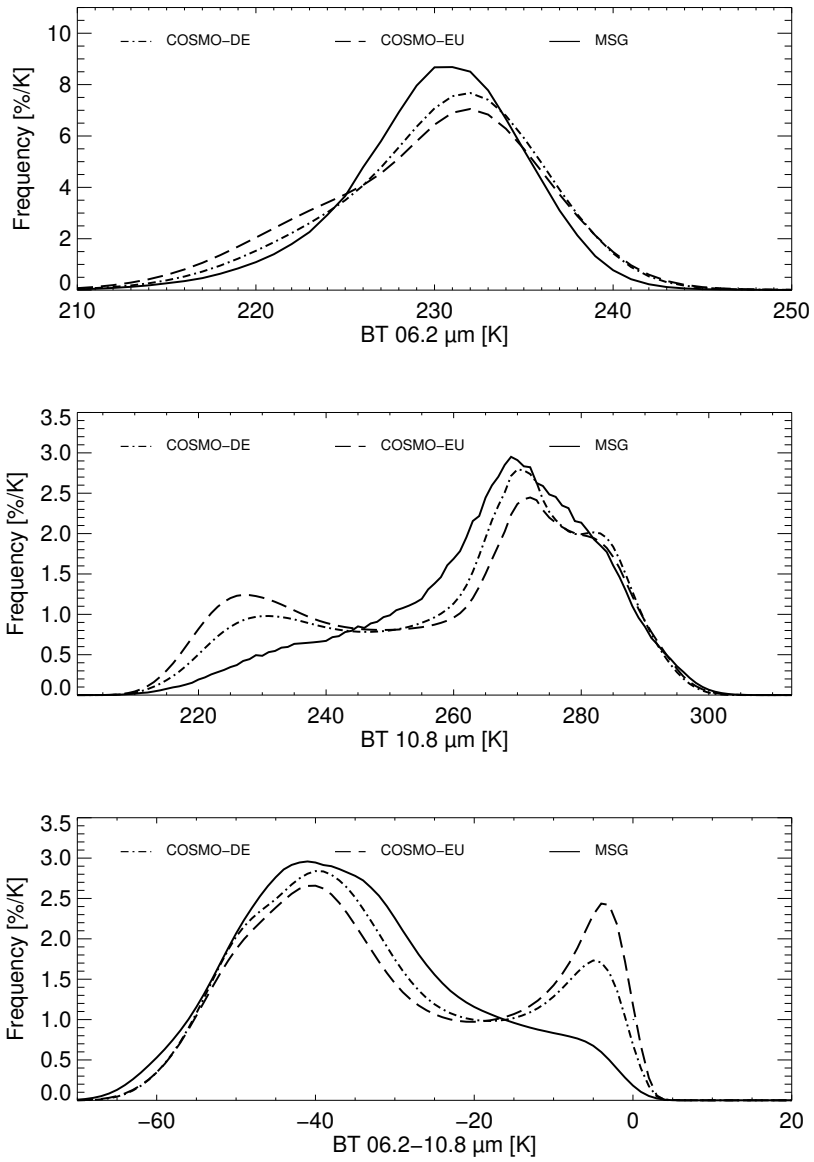

Figure 7.1: Histograms of brightness temperatures at 6.2 μm (top) and at 10.8 μm (center), and of the difference between brightness temperatures at 6.2 μm minus at 10.8 μm (bottom) for the GOP period (1 January 2007 to 31 December 2008). From *Böhme et al. (2011)*.

occurrence of low brightness temperatures resulting in a secondary peak at approximately 230 K in the frequency distribution, in addition to the main peak at 270 K (cf. middle panel in Fig. 7.1). This secondary peak is non-existent in the MSG SEVIRI observations. In the frequency distributions of the brightness temperature differences between the 6.2 μm and the 10.8 μm channel (cf. lower panel in Fig. 7.1), this becomes even more apparent: Here, values around 0 K indicate that water vapour emission above cloud top is negligible and therefore both channels sense the top of the cloud. Since the 10.8 μm channel is a good indicator for CTH (see Chap. 4.3), this suggests that COSMO-DE either overestimates the occurrence of high clouds in general (too frequent or horizontally too extended) as proposed by *Pfeiffer et al. (2010)*, overestimates CTH when high clouds are present, overestimates

cloud optical thickness, or a combination of these biases. The goal of this second part of the present study is to determine firstly, whether more recent versions of COSMO-DE still exhibit the same behaviour, secondly, whether the novel two-moment cloud ice microphysical parameterization developed by *Köhler (2013)* performs better than the standard three-category ice scheme (see Chap. 3.2.3) with respect to this secondary peak, and thirdly, if yes, why.

7.2 Statistical approach

First of all it is to be determined whether the feature *Böhme et al. (2011)* describe is actually robust. Does it still occur, with the more recent model version the new two-moment cloud ice scheme is based on? Secondly, the model runs performed within the present study cover merely one month, June 2010. Is the feature reproducible with this much shorter sampling period as opposed to the two years of *Böhme et al. (2011)*? After the sampling of the data is described in Chap. 7.2.1, the results of the statistical approach are presented in Chap. 7.2.2.

7.2.1 Matching COSMO-DE and satellite data - Part I

Firstly, in order to avoid regions where either MSG SEVIRI or COSMO-DE are known to have difficulties (over ocean and over highly structured terrain), the frequency distributions are computed for a reduced model domain ranging from 5 to 18.15 °E and 48 to 53.8 °N (cf. Fig. 7.2). Thereby, potential differences between model and observations can be clearly

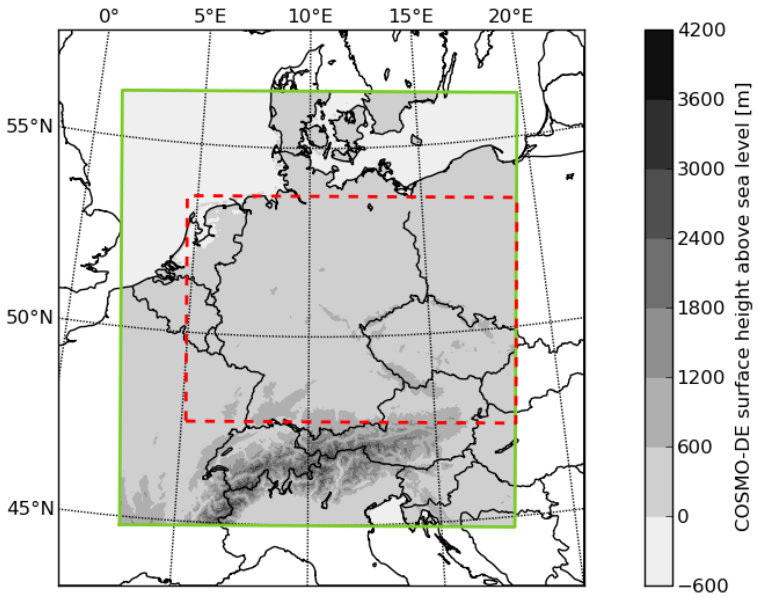

Figure 7.2: COSMO-DE domain (solid green) and reduced COSMO-DE domain (dashed red).

assigned to the model parameterizations. This COSMO-DE model domain reduction results in a pixel* reduction from 98,345 to 29,382 for MSG SEVIRI data and from 194,081 to 76,967 for COSMO-DE data.

Secondly, to avoid effects introduced by varying forecast age, of the three model runs initialized per day (see Chap. 3.2.3), only the 12-h old forecasts are considered. For each forecast target date, the corresponding MSG SEVIRI observation is chosen. No interpolation from one grid to the other is done, since this would decrease the information content. Given the size of the domain and the length of the time series, this is feasible. Note that the frequency distributions are normalized with the number of included gridpoints of MSG SEVIRI and COSMO-DE, respectively.

7.2.2 Results

In the 10.8 μm channel, COSMO-DE9009 with the currently operational three-category ice scheme (Chap. 3.2.3) distinctly overestimates the occurrence of low brightness temperatures in comparison to MSG SEVIRI observations, leading to a secondary maximum at approximately 225 K (cf. top panel in Fig. 7.3). This is in good agreement with the findings of *Böhme et al. (2011)*, in spite of the use of a more recent model version, a smaller domain, and a much shorter time period. The occurrence of mid-range brightness temperatures (250 K to 280 K) in the same channel is underestimated by COSMO-DE9009 whereas the peak at approximately 280 K is captured well: it is only shifted slightly towards higher brightness temperatures. In the 6.2 μm channel, COSMO-DE9009 underestimates the peak at 234 K and overestimates the occurrence of low brightness temperatures between 220 K and 225 K (cf. middle panel in Fig. 7.3). These features are reflected in the difference between these two channels (cf. bottom panel in Fig. 7.3). In total, the behaviour of COSMO-DE9009 with the three-category ice scheme agrees well with that found by *Böhme et al. (2011)*.

COSMO-DE8819 with the two-category ice scheme (Chap. 3.2.4), in comparison to COSMO-DE9009 with the three-category ice scheme, exhibits very similar frequency distributions for both channels and the difference between the two channels. In the presented monthly frequency distribution, the results of the two schemes hardly differ. This implies that COSMO-DE8819 is well suitable as a control run for COSMO-DE8822 and that the conclusions drawn from it can be transferred to the operational three-category ice scheme used in COSMO-DE9009.

In contrast, COSMO-DE8822 with the two-moment cloud ice scheme (Chap. 3.2.5), shows a distinct reduction of the bias in the occurrence of low brightness temperatures in the 10.8 μm channel. In fact, it is quite similar to the MSG SEVIRI observations though the

*The spatial resolution of satellite images is defined via the pixel size of the image measured on the Earth's surface.

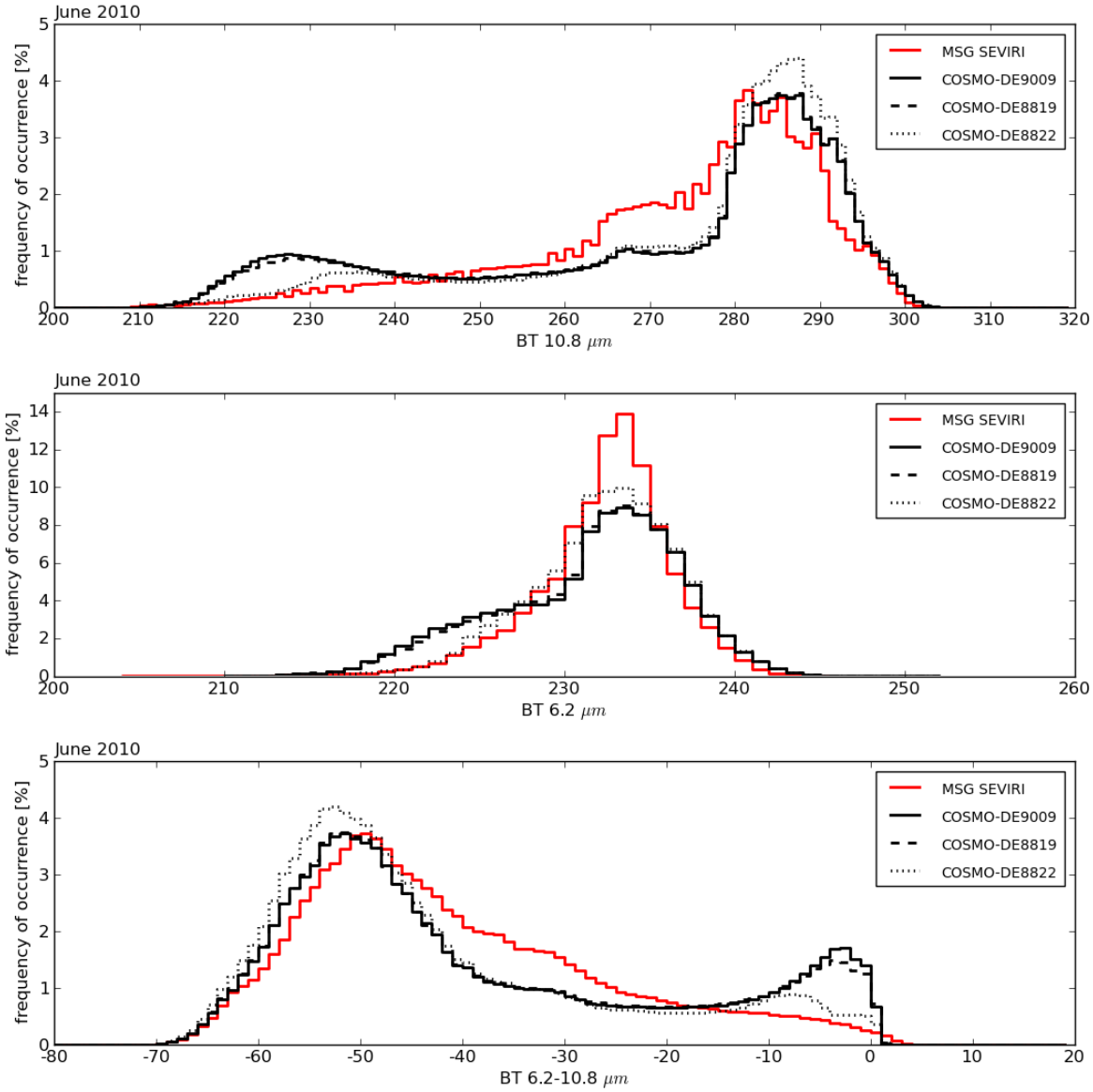

Figure 7.3: Histograms of brightness temperatures at 10.8 μm (top), of brightness temperatures at 6.2 μm (center), and of the difference between brightness temperatures at 6.2 μm minus those at 10.8 μm (bottom) for 0, 12, and 18 UTC June 2010.

underestimation in the mid-range of 10.8 μm brightness temperatures remains. In contrast to the three-category ice scheme in COSMO-DE9009 and the two-category ice scheme in COSMO-DE8819, the peak around 280 K is slightly overestimated. The changes in the 6.2 μm channel are less obvious than those in the 10.8 μm channel, but still notable: The peak at approximately 235 K is slightly less underestimated in comparison to the three-category ice scheme in COSMO-DE9009 and the two-category ice scheme in COSMO-DE8819. The underestimation of low brightness temperatures disappears.

Qualitatively, the differences between the observations and the three model versions become even more apparent in in Fig. 7.4. The joint 10.8 μm-6.2 μm frequency distributions

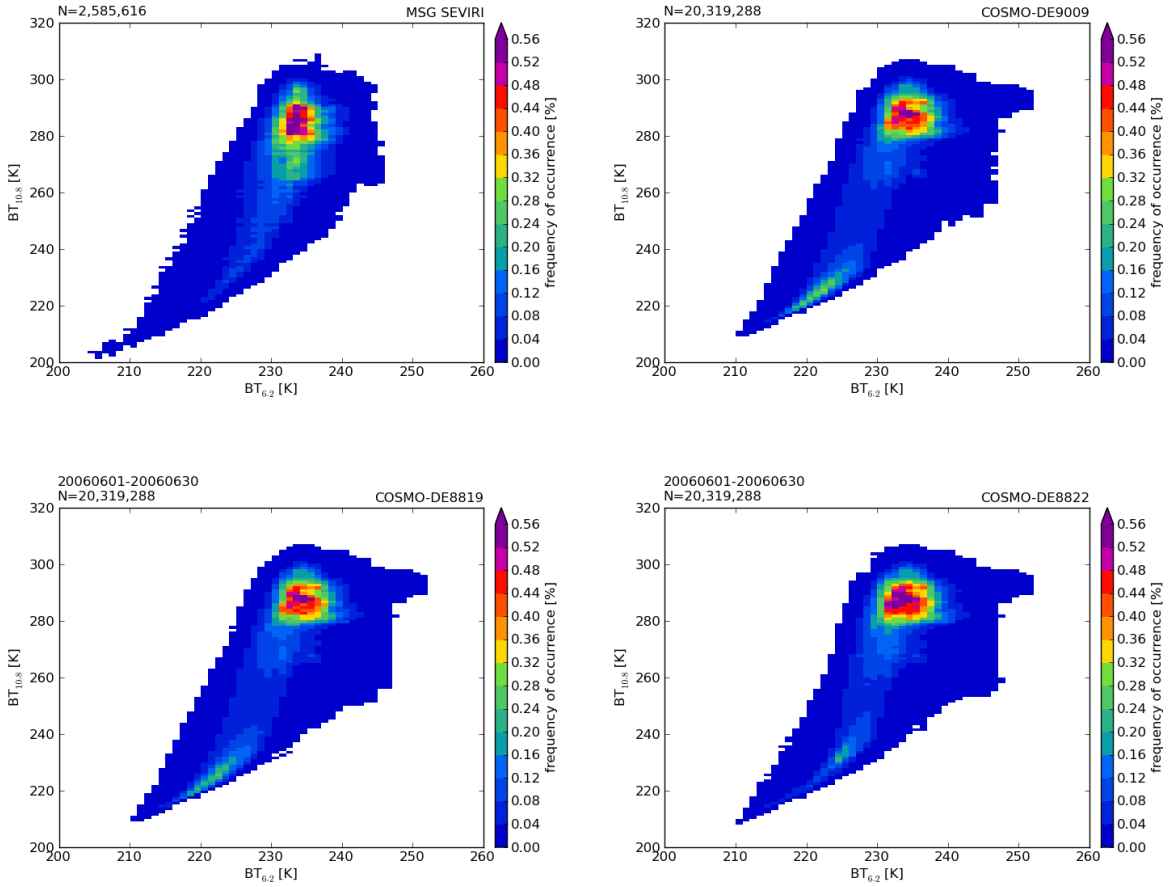

Figure 7.4: Histograms of brightness temperatures at 10.8 μm versus 6.2 μm for 0, 12, and 18 UTC June 2010 over the reduced model domain. Upper left: MSG SEVIRI; upper right: three-category ice COSMO-DE9009; lower left: two-category ice COSMO-DE8819; lower right: two-moment cloud ice COSMO-DE8822.

enable to relate biases in one channel to those in the other channel. The reduction of the secondary maximum in the 10.8 μm channel for the two-moment cloud ice COSMO-DE8822 in comparison to the other two COSMO-DE versions is very prominent. This peak corresponds to the underestimation of mid-range brightness temperatures in the 10.8 μm channel. The secondary maximum in the 10.8 μm corresponds to the overestimation of the lower brightness temperatures in the 6.2 μm channel. Also discernable is the overestimation of the frequency of occurrence of high brightness temperatures in the 6.2 μm channel, accompanied by high brightness temperatures in the 10.8 μm channel.

For a more objective comparison of the model performances, the so-called Shannon Entropy H (*Rodgers, 1976*) of the frequency distributions is calculated:

$$H = -\sum_{i}^{n} p_i \cdot log_e(p_i), \tag{7.1}$$

with number of bins n and frequency of bin occurrence p_i (normalized with total number

of included pixels). The Shannon entropy describes the information content of a frequency distribution through a single number. These numbers are then more easily compared to each other and enable a more quantitative assessment of model performance than sheer subjective "blob-analyses". A change of the shape of the frequency distribution would (through the logarithm) induce a change of the Shannon entropy. In contrast, other measures such as the mean value of a frequency distribution may be the same for completely different distribution shapes. Note that a frequency distribution of same shape which is simply shifted or flipped left/right results in the same Shannon entropy. Therefore, though being a helpful objective measure, it cannot replace a subjective assessment of the frequency distributions.

The Shannon entropies for MSG SEVIRI and the three COSMO-DE versions are listed in Table 7.1. For all three frequency distributions (the two channels and the difference between the two channels), the Shannon entropy of the two-moment cloud ice COSMO-DE8822 is closest to that of MSG SEVIRI. This confirms the subjective impression, that the two-moment cloud ice COSMO-DE8822 is more similar to the observations from MSG SEVIRI than the other two model versions.

Table 7.1: Shanon entropys of frequency distributions of brightness temperatures for June 2010 over the reduced model domain.

	10.8 μm	6.2 μm	6.2 μm − 10.8 μm
MSG SEVIRI	4.089	2.747	3.995
COSMO-DE9009	4.187	3.062	4.038
COSMO-DE8819	4.182	3.049	4.040
COSMO-DE8822	4.034	2.897	3.956

7.3 Case study

The statistical approach presented in the previous chapter answers questions 1 and 2: The more recent version of COSMO-DE underlying the investigated model runs does still have the same deficits in representing the occurrence of low brightness temperatures in the 10.8 μm channel as the COSMO-DE version used by *Böhme et al. (2011)*. And the two-moment cloud ice scheme of COSMO-DE8822 does perform better in this respect than two standard microphysical schemes. As for question 3, what exactly makes the new microphysical scheme better, this can only be answered on a case study basis, which enables to look into the details. Five cases were investigated so far, one of which, CloudSat granule 21970 on 15 June 2010 at approximately 2 UTC, is presented in the following chapter.

7.3.1 Matching COSMO-DE and satellite data - Part II

The matching procedure for COSMO-DE is quite similar to that of GME described in Chap. 6.2. Temporally, all model runs with forecasts for the full hour closest to the mean time of the CloudSat orbit are chosen. For the presented case study on 15 June 2010, 01:46:52 UTC is the mean CloudSat time. Since only three model runs per day were performed in the present study (see Chap. 3.2), two differently aged forecasts are available for 2 UTC: the ones initialized at 6 and 12 UTC of the previous day.

To match the spatial domain of COSMO-DE, MSG SEVIRI, and CloudSat CPR, the data of the first two are horizontally interpolated onto the CloudSat track with the nearest neighbour technique. Due to the coarser resolution of the model (see Chap. 3.2), one model profile is assigned to several adjacent CloudSat profiles. This way, no information contained in the high-resolution CloudSat data is lost. However, since model resolution (2.8 km) is close to CloudSat resolution (1.09 ± 0.01 km), this is of not much consequence. The CALIPSO CALIOP data are not interpolated in any way, since they are already on the same track as the CloudSat CPR data (though available in a higher resolution) and only qualitatively used in the present study.

7.3.2 Results

On 15 June 2010, CloudSat overpassed Germany at approximately 2 UTC. On this day, a longwave trough was situated over Scandinavia and reached as far south as northern Spain (cf. Fig. 7.6). Several minor disturbances were embedded in this longwave trough, but the most prominent feature was a low over the Bay of Biscay which was in the process of disconnecting from the upper-level flow. In the following hours, this cut-off process was ongoing until eventually a cut-off low developed. According to the surface analysis chart (cf. Fig. 7.5), the warm front of the corresponding surface low stretched zonally along the Alps. As for the COSMO-DE domain, Germany was influenced by weak high pressure, it was no yet affected by the eastward-propagating trough and the associated lifting (cf. Fig. 7.6). Very small to zero convective available potential energy (CAPE) values and positive Lifted Index values (cf. Fig. 7.7) indicate that the atmosphere was stable and there was no convective activity over the COSMO-DE domain on this date. This makes this case especially suitable for evaluating the cloud ice microphysical parameterizations, since the convection scheme is not expected to be called in COSMO-DE.

The observed MSG SEVIRI brightness temperatures at the 10.8 μm channel are displayed in Fig. 7.8.1. The low brightness temperatures in the south and south-western part of the COSMO-DE model domain indicate high CTHs. COSMO-DE9009 with the standard three-category ice scheme (cf. Fig. 7.8.2) simulates cold brightness temperatures over a larger region than observed; on the one hand in the southern parts of the domain, on the other hand

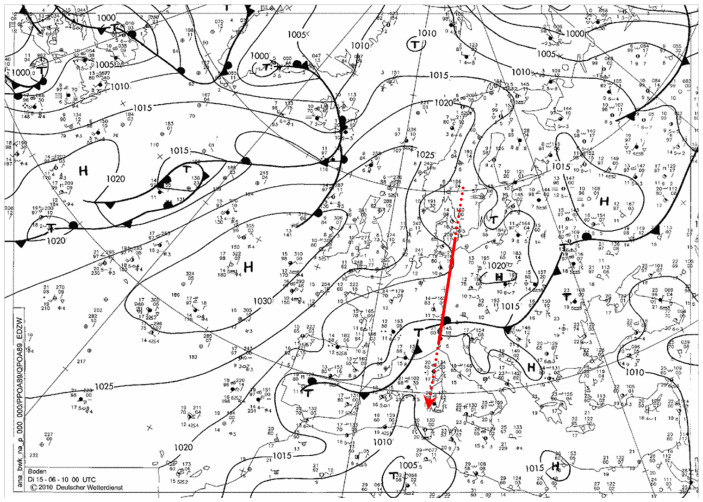

Figure 7.5: DWD surface analysis for 15 June 2010 0 UTC (source: `www.wetter3.de`). The red-dotted line denotes the approximate CloudSat track and direction of overpass; the solid red part of the line corresponds to the investigated cross section.

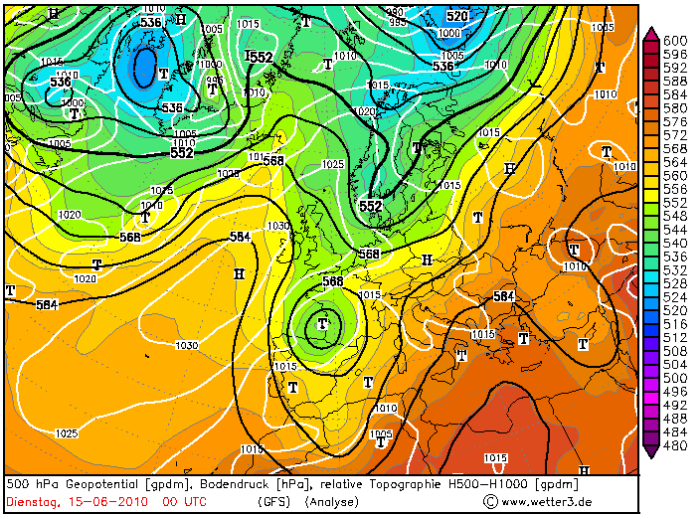

Figure 7.6: GFS analyses 500 hPa geopotential height (black contour lines), surface pressure (white contour lines), and relative topography (coloured) for 15 June 2010 0 UTC (source: `www.wetter3.de`).

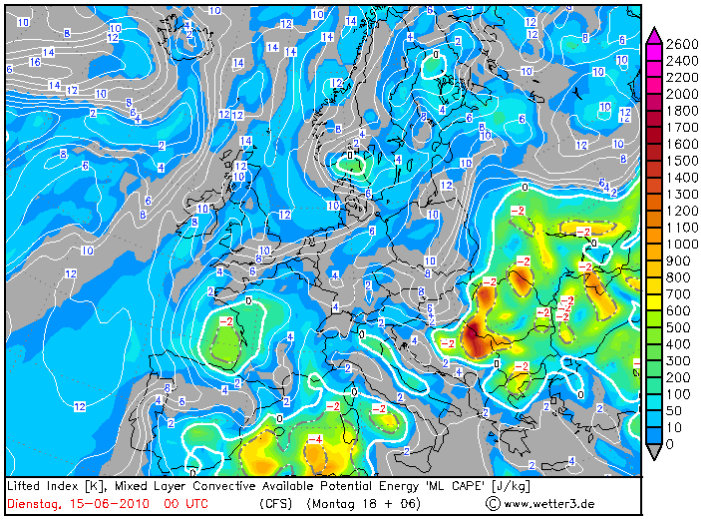

Figure 7.7: GFS analyses Lifted Index (contour lines) and CAPE (coloured) for 15 June 2010 0 UTC (source: `www.wetter3.de`).

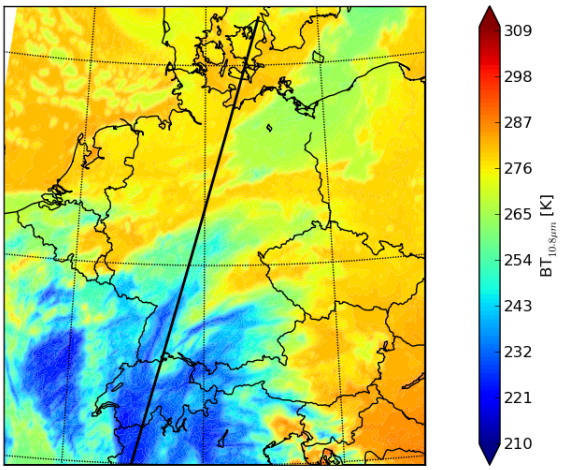

7.8.1: MSG SEVIRI.

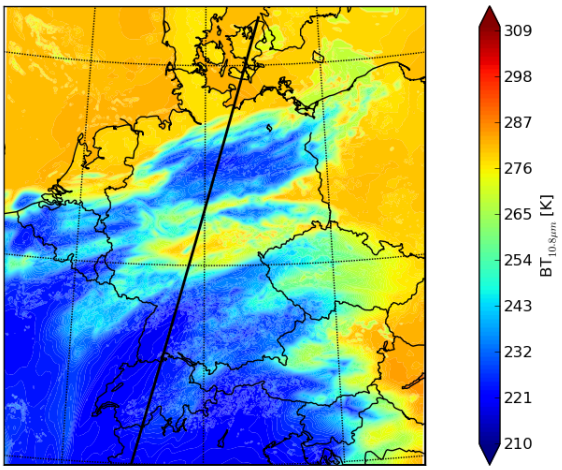

7.8.2: COSMO-DE9009 (three-category ice scheme).

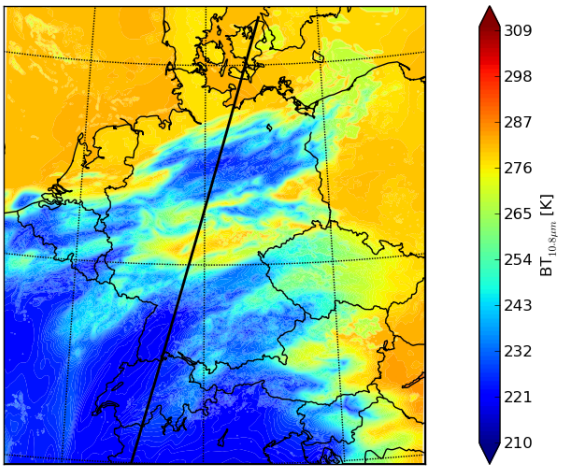

7.8.3: COSMO-DE8819 (two-category ice scheme).

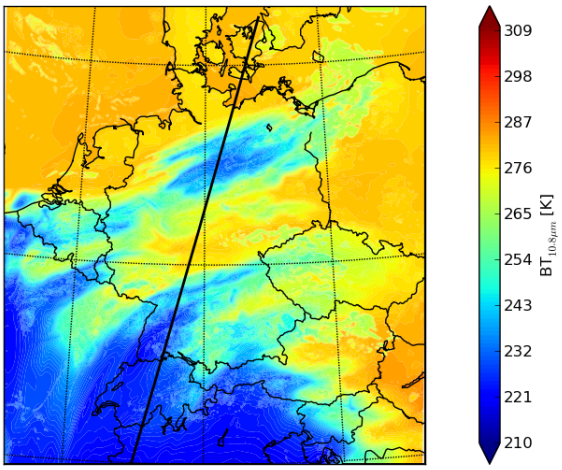

7.8.4: COSMO-DE8822 (two-moment cloud ice scheme).

Figure 7.8: Observed and simulated brightness temperatures at 10.8 μm on 15 June 2010 at 2 UTC. Forecast age of model runs: 14 h. Solid black line: CloudSat overpass for 01:45:21–01:48:53 UTC of same day.

over northern Germany. COSMO-DE8819 with the two-category ice scheme (cf. Fig. 7.8.3) simulates only very slightly different brightness temperatures; they are marginally less low than for COSMO-DE9009 with the three-category ice scheme. COSMO-DE8822 with the two-moment cloud ice scheme (cf. Fig. 7.8.4), though still not perfectly matching the observations, does simulate distinctly less low brightness temperatures than COSMO-DE8819 with the two-category ice scheme.

In the 6.2 μm channel (cf. Fig. 7.9), the improvement is similar: The overestimation of low simulated brightness temperatures in COSMO-DE9009 with the three-category ice scheme and COSMO-DE8819 with the two-category ice scheme is distinctly reduced in COSMO-DE8822 with the two-moment cloud ice. Hence, the picture this case study gives

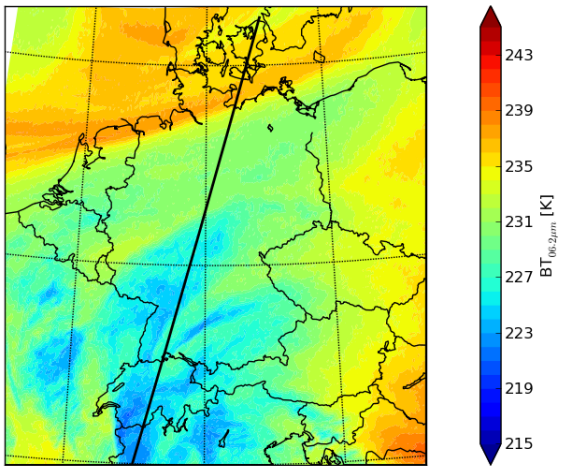

7.9.1: MSG SEVIRI.

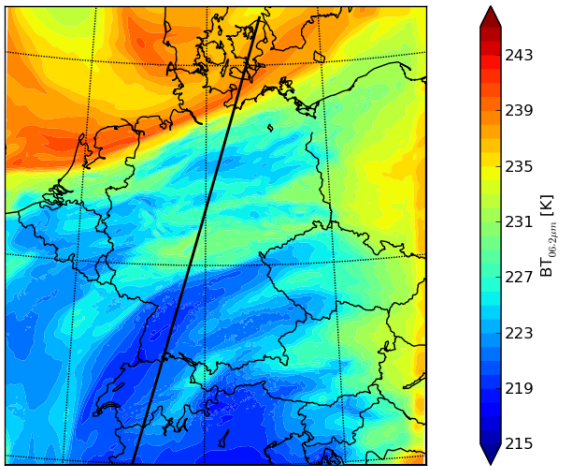

7.9.2: COSMO-DE9009 (three-category ice scheme).

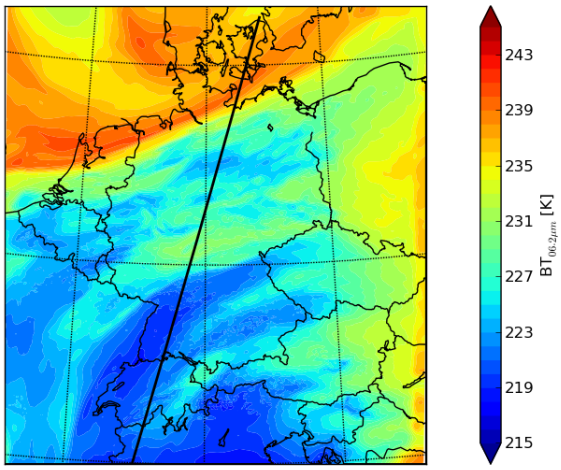

7.9.3: COSMO-DE8819 (two-category ice scheme).

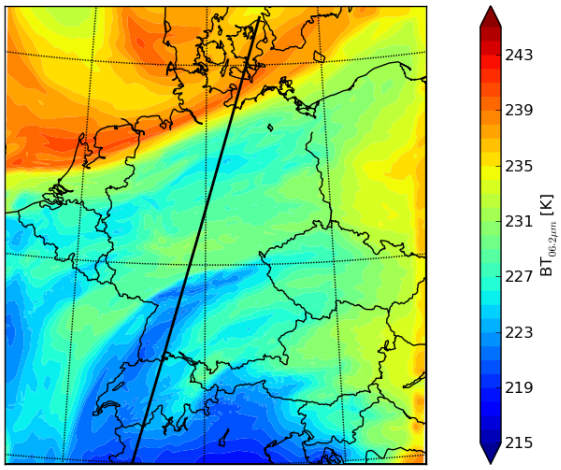

7.9.4: COSMO-DE8822 (two-moment cloud ice scheme).

Figure 7.9: Observed and simulated brightness temperatures at 6.2 μm on 15 June 2010 at 2 UTC. Forecast age of model runs: 14 h. Solid black line: CloudSat overpass for 01:45:21–01:48:53 UTC of same day.

matches exactly what is reflected in the frequency distribution for June 2010 presented in Chap. 6.4.2. Note that the boundary effects on the eastern border should be disregarded.

The question is now, what exactly is different in the two-moment cloud ice scheme of COSMO-DE8822, that the simulated brightness temperatures match the observed ones better than in the other cloud microphysical schemes? The maps of cloud water path (CWP), rain water path (RWP), and SWP of the three model versions reveal no major differences between the three model versions (cf. Figs. A-C in appendix). For CIWP this is different: COSMO-DE8822 with the two-moment cloud ice scheme (cf. Fig. 7.10.2) produces more concentrated regions of CIWP than COSMO-DE8819 with the two-category ice scheme (cf. Fig. 7.10.1), but generally smaller values in the surrounding area. Note firstly the colour

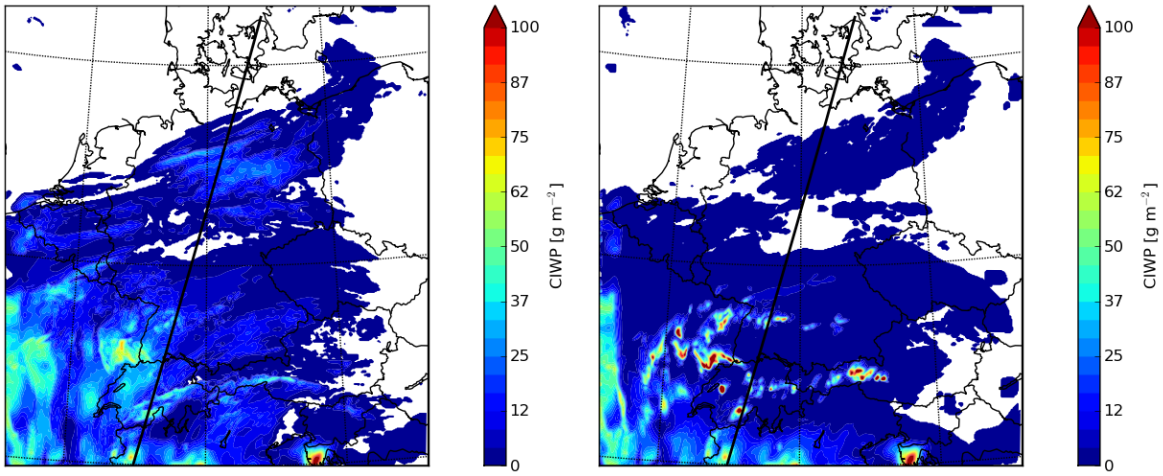

7.10.1: COSMO-DE8819 (two-category ice scheme).

7.10.2: COSMO-DE8822 (two-moment cloud ice scheme).

Figure 7.10: CIWPs on 15 June 2010 at 2 UTC. Forecast age of model runs: 14 h. Solid black line: CloudSat overpass for 01:45:21–01:48:53 UTC of same day.

bar: values unequal zero are already displayed in blue, no matter how small they are. Note secondly that the boundary effects discernible on the eastern and western border of the CIWP maps should be disregarded. CIWP from COSMO-DE9009 with the three-category ice scheme looks very similar to COSMO-DE8819 with the two-category ice scheme and is therefore not shown.

In order to investigate the chosen case more closely, information from within the cloud is required. To this end, the cross sections along an A-Train overflight are analysed. The observed MSG SEVIRI brightness temperatures in both channels along this A-Train track are predominantly higher than those simulated from COSMO-DE (cf. Fig. 7.11). As shown before, the control runs COSMO-DE9009 with the three-category ice scheme and COSMO-DE8819 with the two-category ice scheme do not differ much from each other. The new two-moment cloud ice scheme in COSMO-DE8822 is comparably closer to the observations: The underestimation of brightness temperatures is decreased by up to 25 K (i. e. 50 % at 51.5 °N) for the 10.8 μm channel and up to 2.5 K (i. e. 50 % at 48 °N) for the 6.2 μm channel. The CloudSat CPR radar reflectivity factors (cf. Fig. 7.12, top panel) reveal a cloud system typical for a warm front: Ahead of the front the upgliding airmasses form cirrus, cirrostratus, and eventually deep nimbostratus clouds in the southern part of the CloudSat track. Over the Alps, orographical uplifting may add to deep cloud formation. CTH is just below 12 km. At 53 °N a weak signature from a cloud at approximately 8 km height is observed. Since the difference between the three model versions is their ice microphysical parameterization, for this case the CALIPSO CALIOP backscatter is also regarded because it is more sensitive to small particles than the CloudSat CPR. The lidar reveals the same overall cloud structure (cf. Fig. 7.12, lower panel). CTH estimated from CALIPSO CALIOP is approximately 12 km and thus agrees well with that estimated from CloudSat

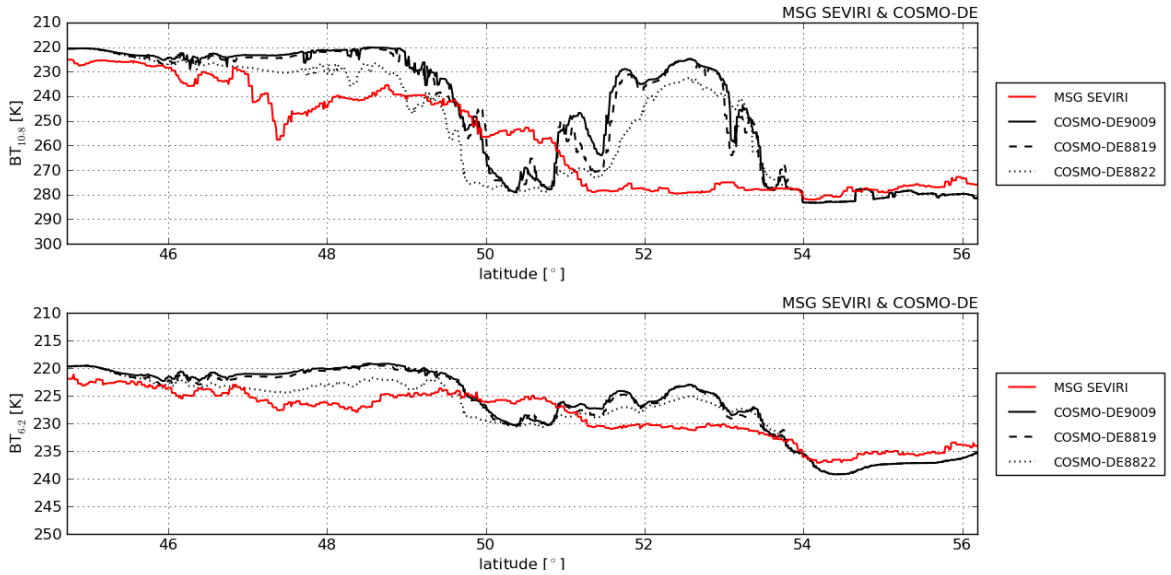

Figure 7.11: Cross section along A-Train overflight on 15 June 2010 at 2 UTC. **Top**: MSG SEVIRI observed (red) and COSMO-DE simulated (black) brightness temperatures at 10.8 μm. **Bottom**: The same but at 6.2 μm. Forecast age of model runs: 14 h.

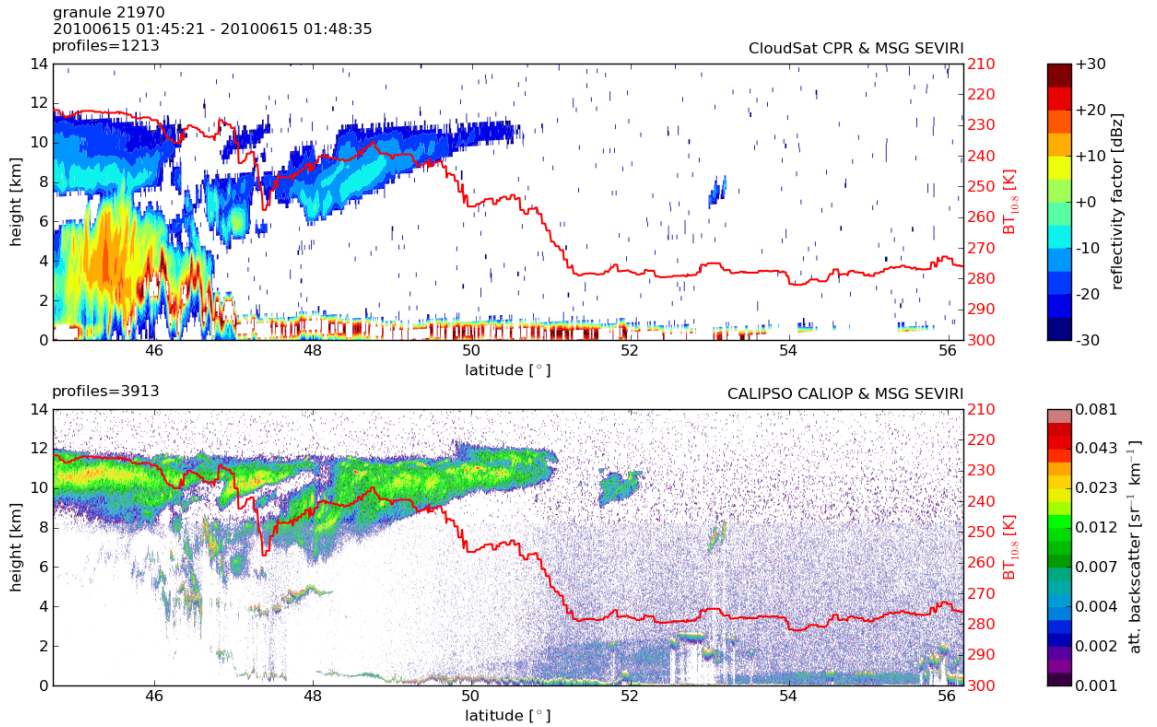

Figure 7.12: Cross section along A-Train overflight on 15 June 2010 at approximately 2 UTC. **Top**: CloudSat CPR radar reflectivity factor with MSG SEVIRI brightness temperatures at 10.8 μm in red. **Bottom**: CALIPSO CALIOP attenuated backscatter with MSG SEVIRI brightness temperatures at 10.8 μm in red.

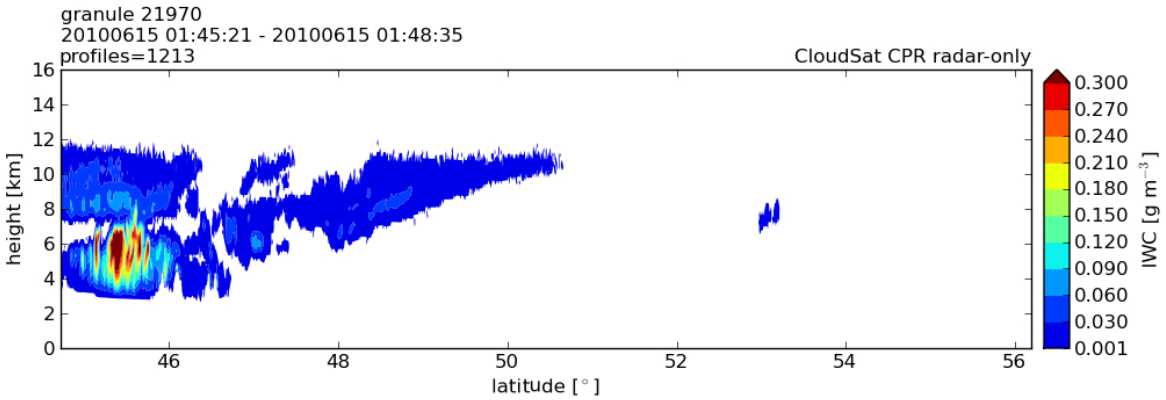

Figure 7.13: Cross section of retrieved CloudSat CPR radar-only IWC on 15 June 2010 between 01:45:21 and 01:48:35 UTC.

for the chosen case. This implies that the CloudSat CPR does not miss too many small particles which would be expected to prevail at cloud top. The lower parts of the large cloud system are not observed by the lidar in contrast to the radar, since its signal is attenuated completely. Concerning the feature observed at 53 °N in 8 km height, the lidar also detects it, but not much larger than CloudSat already does, implying again, that the radar does not miss too much of the cloud. There are merely two features, which the radar actualy does miss but the lidar still detects: At the 53 °N in 2 km height and at 52 °N in 10 km height. In both cases, the clouds are very small. It can be concluded, that in the chosen case study, the CloudSat CPR performs quite well. The IWCs retrieved from the CloudSat CPR (cf. Fig. 7.13) show maximum values at approximately 45.5 °N between 4 and 6 km height. The three COSMO-DE versions capture the basic distribution of the cloud well (cf. Fig. D in appendix). But they overestimate its general vertical extent, overestimate the vertical extent of the maximum IWCs in the core, and underestimate the maximum IWC values. The latter may be attributed to the lower horizontal resolution of COSMO-DE compared to the observations. The feature at 53 °N, which is hardly discernible in the observations, is well pronounced in all COSMO-DE versions, though only with small IWC values. In general, the three model versions do not differ greatly in IWC. Viewing all four hydrometeor contents separately shows that the model versions differ only marginally in CWC, RWC, and SWC (cf. Figs. E–G in appendix). Therefore, the differences in the simulated brightness temperatures must stem from CIWC differences alone.

The cross sections of CIWC are depicted in Fig. 7.14 and reveal that the new two-moment cloud ice scheme in COSMO-DE8822 predicts a very different CIWC distribution than the other two model versions. Most obvious is the shift of cloud ice down to lower altitudes than in the two control runs. The CIWC values at 53 °N are distinctly reduced. CTH actually increases, though the CIWCs at cloud top are very small. Note the different scaling of the colour bar than for the IWCs in Fig. D in appendix. Hence it can be concluded, that the reduction of cloud ice in upper layers leads to an optical thinning of the cloud ultimately resulting in less low simulated brightness temperatures for COSMO-DE8822. The question

remains, which of the introduced changes in COSMO-DE8822 with its two-moment cloud ice scheme is responsible for this remarkable change in CIWC distribution?

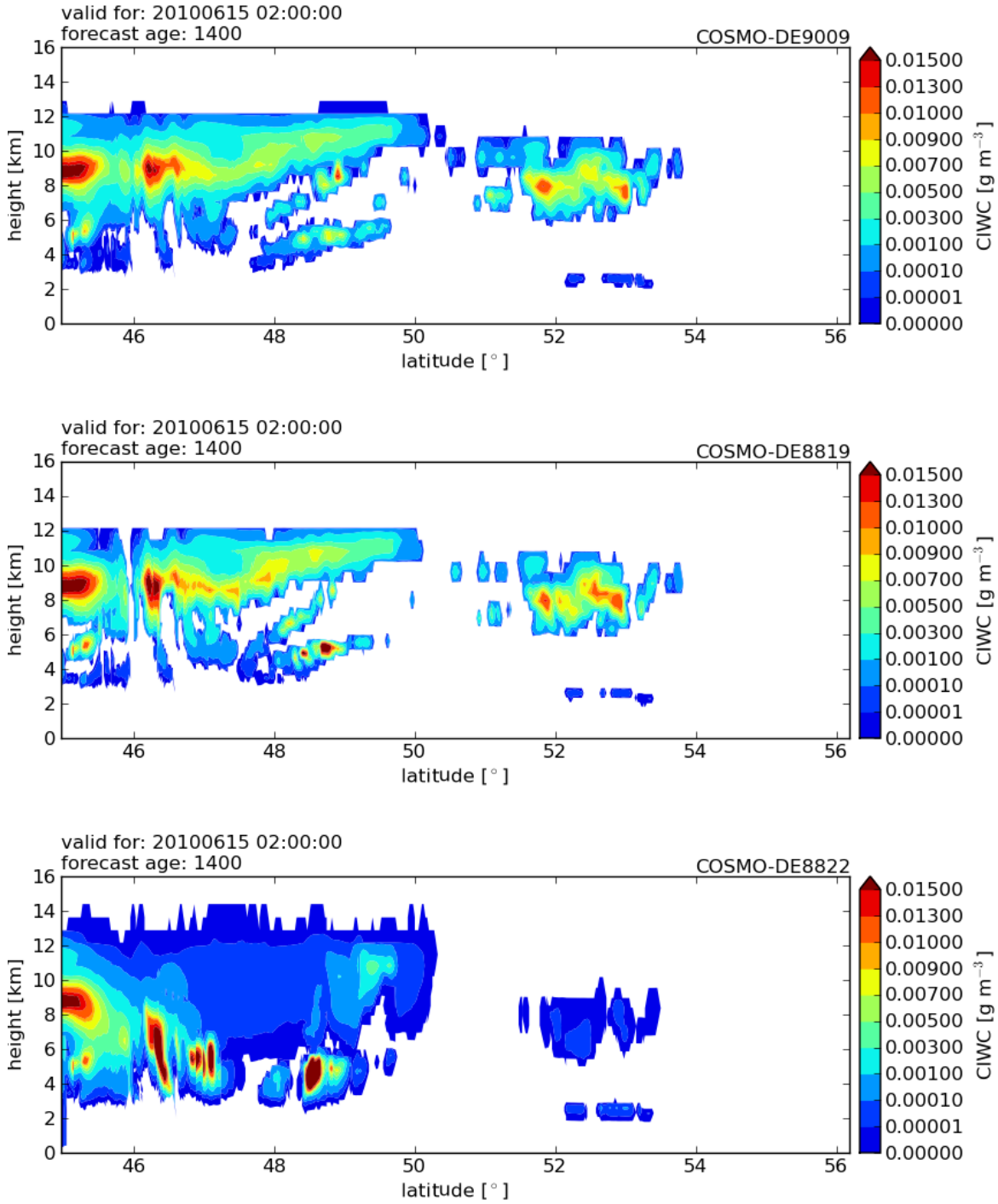

Figure 7.14: Cross sections of COSMO-DE CIWC along CloudSat track on 15 June 2010 at 2 UTC. Forecast age of model runs: 14 h. Note that CIWC values unequal zero are already depicted in blue.

7.3.3 Sensitivity experiments

In order to verify exactly which of the changes introduced in the two-moment cloud ice scheme in COSMO-DE8822 is responsible for its improved behaviour with respect to the simulated brightness temperatures, a series of sensitivity experiments is performed for the investigated case.

Since the three-category ice scheme in COSMO-DE9009 and the two-category ice scheme in COSMO-DE8819 exhibit hardly any differences for the investigated case, from now on the latter is used as single control run for COSMO-DE8822 with the novel two-moment cloud ice scheme. It is presumed that the results obtained from comparing these two model versions can be tranferred to the operational three-category ice scheme of COSMO-DE9009.

Switches

Within the two-moment cloud ice scheme of COSMO-DE8822 a number of changes is introduced into the cloud ice microphysical scheme (see Chap. 3.2.5 for details). Beginning with the switch from the two-category ice scheme (COSMO-DEse0, corresponding

Table 7.2: Overview of sensitivity experiments perfomed with COSMO-DE. Heterogeneous ice nucleation scheme "F" and "P" refer to the old modified *Fletcher (1962)* and the new *Phillips et al. (2008)* formulations. Microphysics scheme "3" and "32" refer to the two-category ice scheme and the two-moment cloud ice scheme. "y" and "n" refer to whether the respective switch is set in COSMO-DE or not (see Chap. 3.2.5 for a comprehensive overview of the switches).

COSMO-DE experiment	microphys. scheme	hetero. ice nuc. scheme	cloud ice sediment.	IN track.	depos. adjust.	level number	aerosol num. conc.
se0	3	F	n	n	y	50	–
se1	32	F	n	n	y	50	–
se2	32	P	n	n	y	50	–
se22	32	F	y	n	y	50	–
se3	32	P	y	n	y	50	–
se4	32	P	y	y	y	50	–
se5	32	P	y	y	n	50	–
se5a	32	P	y	y	y	50	$N_{a,dust} \times 10$
se5b	32	P	y	y	y	50	$N_{a,dust} \times 10^{-1}$
se5c	32	P	y	y	y	50	$N_{a,homo} = 0$
se5d	32	P	y	y	y	50	$N_{a,soot} = 0$
c50	32	P	y	y	n	50	–
c85	32	P	y	y	n	84	–
c150	32	P	y	y	n	150	–

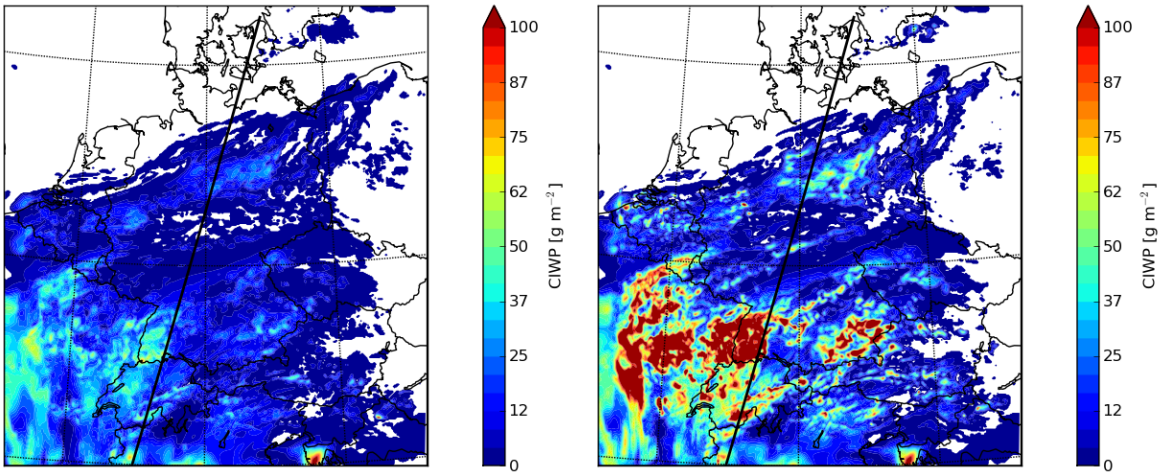

7.15.1: COSMO-DEse0. **7.15.2:** COSMO-DEse1.

Figure 7.15: CIWPs on 15 June 2010 at 2 UTC. Forecast age of model runs: 14 h. Solid black line: CloudSat overpass for 01:45:21–01:48:53 UTC of same day. See Table 7.2 for details on the settings in the individual experiments.

to COSMO-DE8819) to the two-moment cloud ice scheme (COSMO-DEse1), the additional changes are in the following switched on sequentially to observe their immediate effect on CIWC. In COSMO-DEse2, the ice nucleation scheme is changed from the former modified *Fletcher (1962)* formulation to the new *Phillips et al. (2008)* formulation. In COSMO-DEse3, cloud ice sedimentation is added. In COSMO-DEse4, the tracking of activated IN is included. Finally in COSMO-DEse5, the treatment of the deposition adjustment is changed. With this, COSMO-DEse5 corresponds to the full COSMO-DE8822. An overview of the settings in the sensitivity experiments is given in Table 7.2.

Note that, though one might think COSMO-DE8819 with its two-category ice scheme could serve as a control run for the sensitivity experiments, this is not the case. COSMO-DE8819 was run within DWD's experimental sytem NUMEX, which ensures full equivalence to the routine runs at that time through assimilating the same observational data (nudgecast mode). The sensitivity experiments however are run stand-alone, that is without assimilation (forecast mode). Therefore, the results of COSMO-DE8819 and COSMO-DEse0 do differ, though not substantially. The same applies for COSMO-DE8822 and COSMO-DEse5.

As a first step, the cloud microphysics scheme is switched from the two-category ice scheme (COSMO-DEse0) to the two-moment cloud ice scheme (COSMO-DEse1). The middle panel in Fig. 7.16 shows that COSMO-DEse1 produces far more CIWC than COSMO-DEse0, though the vertical distribution hardly changes. This is because in COSMO-DEse1, together with the change from one- to two-moment cloud ice, three other changes are introduced. Firstly, the numerical solution for the treatment of diffusional growth is changed: The two-category ice scheme applies the forward Euler method as numerical procedure for solving the differential equations, whereas the two-moment cloud ice scheme performs a

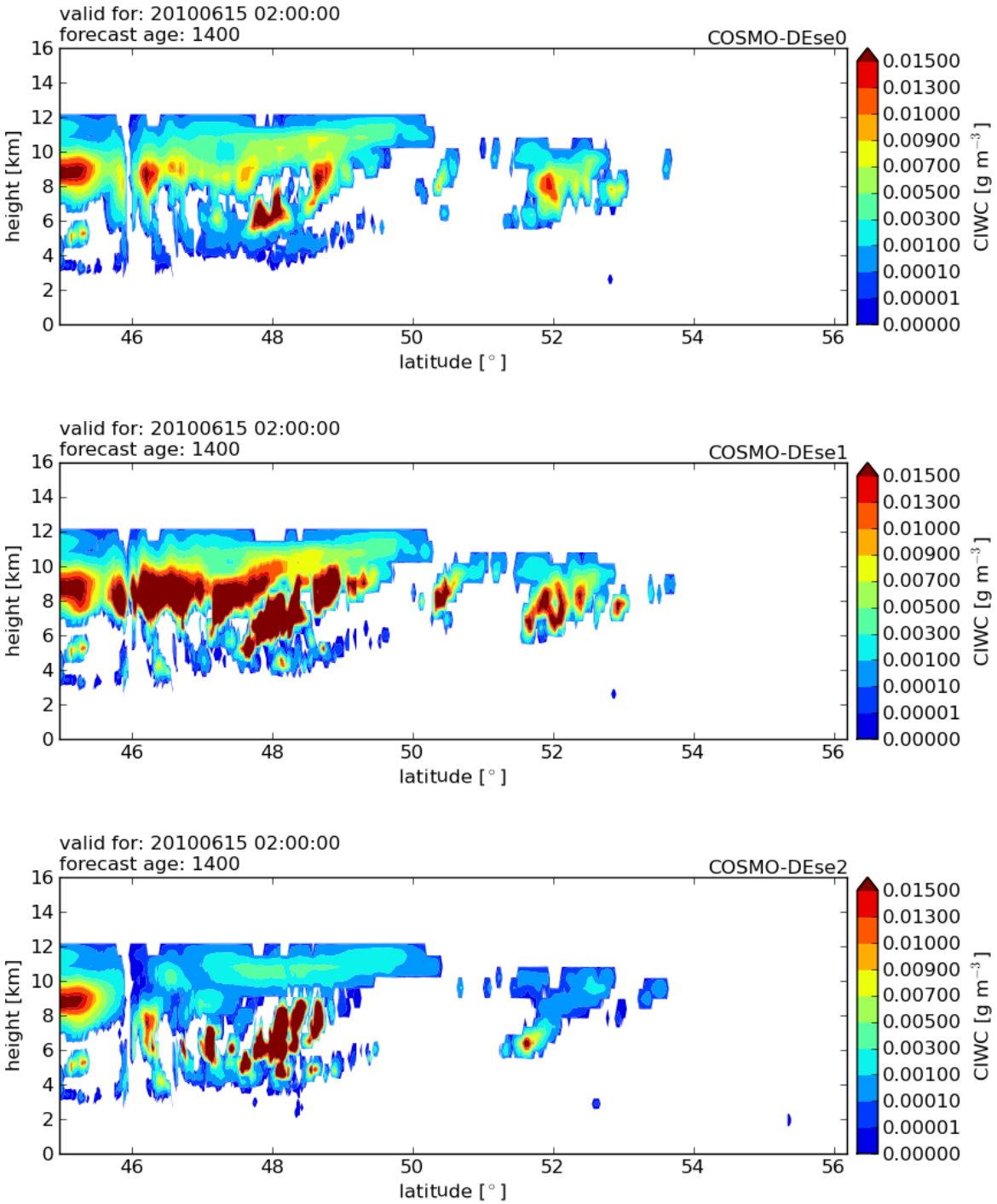

Figure 7.16: Cross sections of COSMO-DEse0-2 CIWC along CloudSat track on 15 June 2010 at 2 UTC. Forecast age of model runs: 14 h. Note that CIWC values unequal zero are already depicted in blue. See Table 7.2 for details on the settings in the individual experiments.

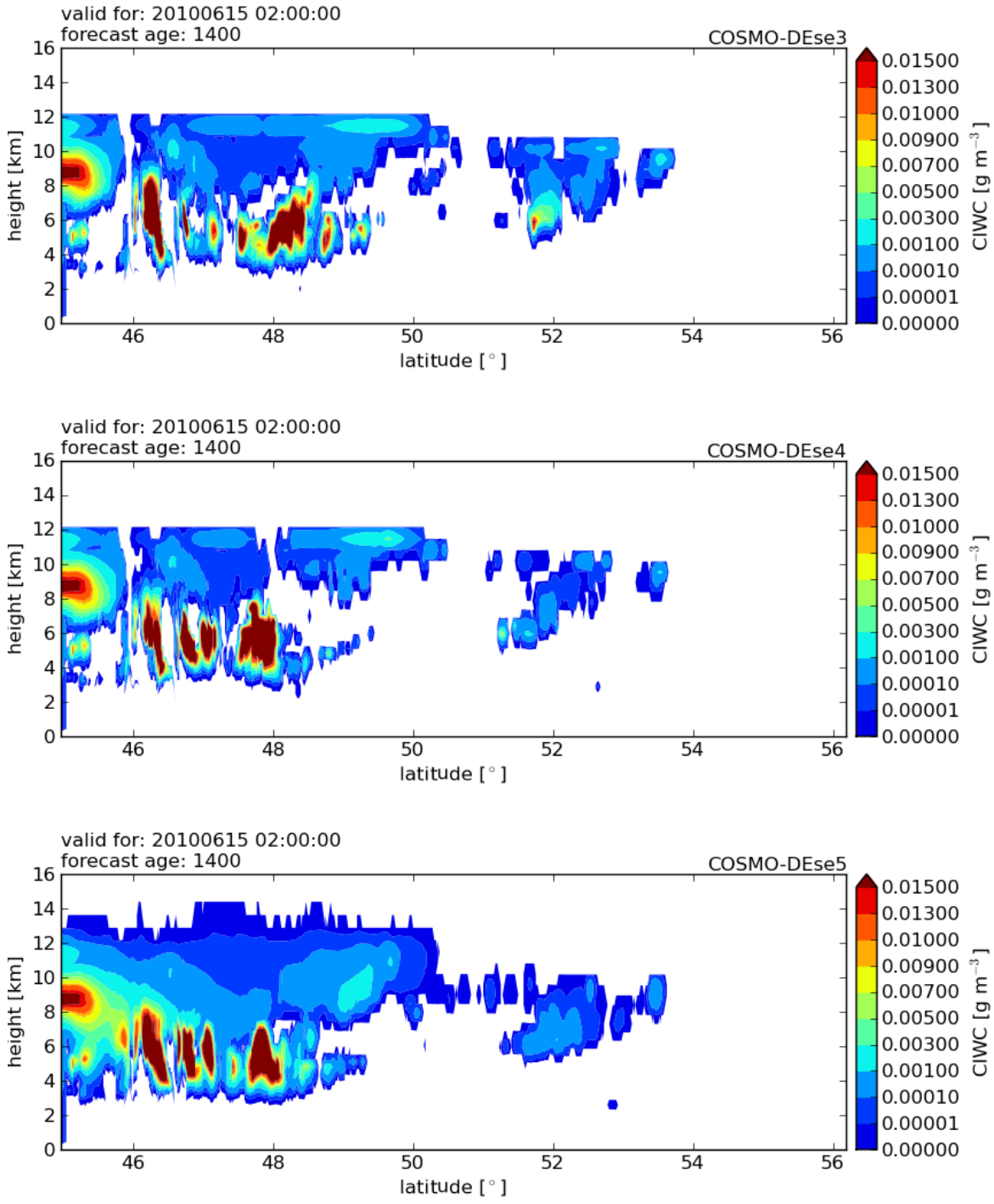

Figure 7.17: Cross sections of COSMO-DEse3-5 CIWC along CloudSat track on 15 June 2010 at 2 UTC. Forecast age of model runs: 14 h. Note that CIWC values unequal zero are already depicted in blue. See Table 7.2 for details on the settings in the individual experiments.

relaxation approach. This is of no consequence for the microphysical result. Secondly, the treatment of homogeneous ice nucleation of liquid aerosols is considered in contrast to before. This too, is of no consequence in the presented case study, as shown later. Finally, a further change concerning the treatment of the depositional growth in general is introduced. Now, all particles compete for the available water vapour. Smaller particles grow faster through depositional growth than larger ones, because of their larger surface. Therefore, more water vapour is at disposal for depositional growth of cloud ice than before, resulting in the production of more CIWC. This leads to higher CIWPs over the whole model domain (cf. Fig. 7.15). The frequency distribution of CIWCs in Fig. 7.21 confirms this (note that each temperature bin is normalized individually).

Secondly, instead of the modified *Fletcher (1962)* scheme for heterogeneous ice nucleation used in the two-category ice scheme, the *Phillips et al. (2008)* scheme with its three classes of background aerosol is used (COSMO-DEse2; bottom panel in Fig. 7.16). A substantial

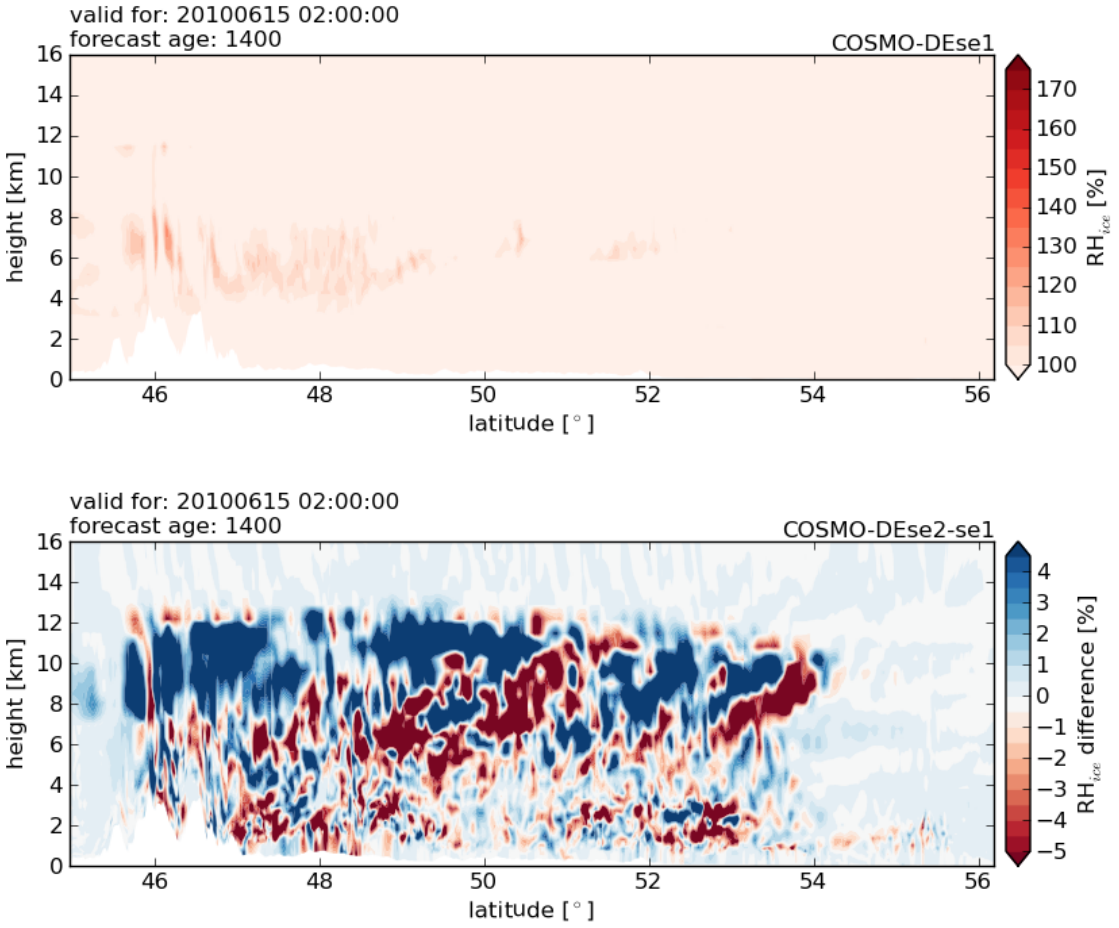

Figure 7.18: Cross sections of supersaturation with respect to frozen phase for COSMO-DEse1 (top) and difference of COSMO-DEse2 to COSMO-DEse1 (bottom) along CloudSat track on 15 June 2010 at 2 UTC. Forecast age of model runs: 14 h. The settings of the sensitivity experiments are given in Table 7.2. Note that in the bottom panel not the percent difference, but the difference between COSMO-DEse2 and COSMO-DEse1 is depicted.

change is observed: CIWC is reduced throughout the cloud, by up to one order of magnitude. The CIWCs of the small cloud at 53 °N are distinctly reduced. The effect is most pronounced at cloud top. This is due to the change in the supersaturation with respect to frozen phase. In comparison to the modified *Fletcher (1962)* scheme, the *Phillips et al. (2008)* scheme produces oversaturations with respect to frozen phase which are up to 5% larger in the upper troposphere and up to 5% smaller in the middle troposphere (cf. Fig. 7.18). Between 9–12 km height the temperatures are below −35 °C (cf. Fig. 7.19). In this temperature range, the modified *Fletcher (1962)* scheme provides more activated IN than the *Phillips et al. (2008)* scheme (cf. Fig. 7.20). A larger number of IN can deplete more water vapour resulting in less supersaturation with respect to frozen phase and more CIWC. In general, the *Phillips et al. (2008)* scheme has strickter criteria for activating IN; it produces less and not so many at once as the modified *Fletcher (1962)* scheme, which basically provides an infinite number of IN at once. Note that, though homogeneous ice nucleation sets in at −37 °C, this ice nucleation process is untouched by the choice of heterogeneous ice nucleation scheme. The observed changes are therefore due to the new heterogeneous ice

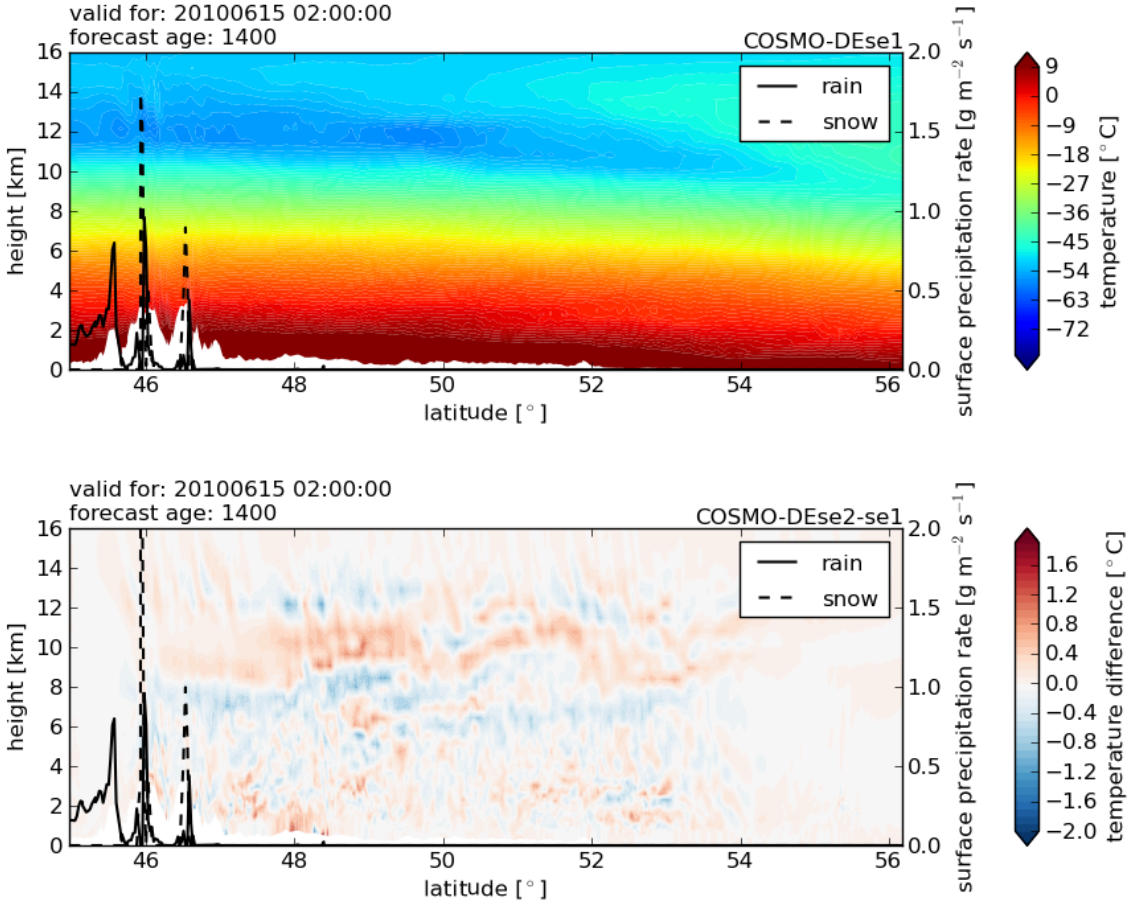

Figure 7.19: Cross sections of temperature for COSMO-DEse1 (top) and difference of COSMO-DEse2 to COSMO-DEse1 (bottom) along CloudSat track on 15 June 2010 at 2 UTC. Forecast age of model runs: 14 h. Surface precipitation rates are added in solid (rain) and dashed (snow) lines. The settings of the sensitivity experiments are given in Table 7.2.

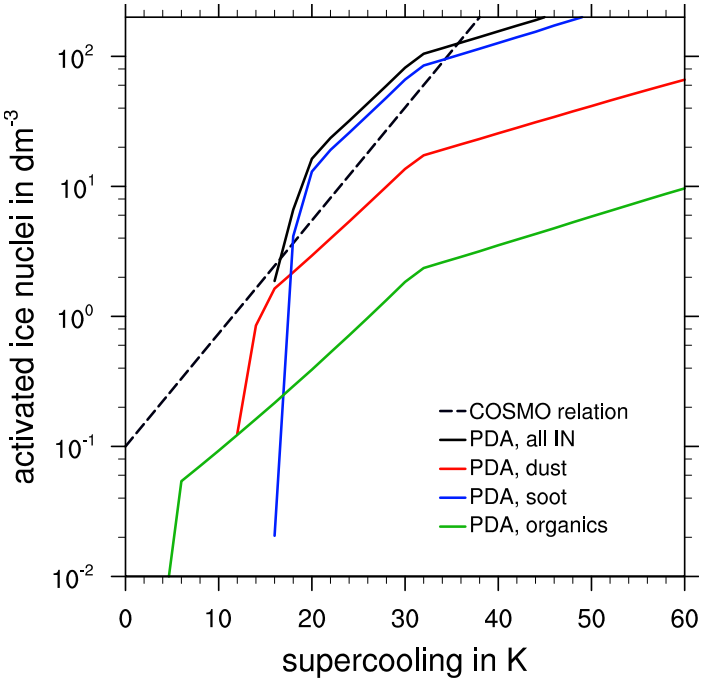

Figure 7.20: Number of activated IN as a function of supercooling for the three classes of background aerosol of the *Phillips et al. (2008)* scheme for condensation/immersion mode[†]. The dashed black line denotes the operational COSMO scheme, that is the modified *Fletcher (1962)* scheme.

nucleation scheme alone.

In a third step, cloud ice sedimentation is switched on (COSMO-DEse3; cf. top panel in Fig. 7.17). As expected, CIWC is shifted to lower altitudes, thereby being reduced even more at cloud top. The effect is similar to that observed in Chap. 6.4.2 for GME. In fact, CIWC is reduced by a further order of magnitude (cf. top right panel in Fig. 7.21). The effect of cloud ice sedimentation on the vertical CIWC distribution is expected to be even stronger, when the density correction to the fall speed of cloud ice is introduced, as described in Chap. 6.4.2 for GME. However, in the COSMO-DE runs peformed in the present study, this density correction was not switched on. Interestingly, if cloud ice sedimentation is switched on before switching from the modified *Fletcher (1962)* to the new *Phillips et al. (2008)* heterogeneous ice nucleation scheme (COSMO-DEse22), it does not have that great an effect (cf. Fig. H in appendix). An effect is only notable for temperatures warmer than $-20\,°C$. Here, the CIWC frequency distributions (cf. Fig. I in appendix) show that larger CIWCs occur less often than in COSMO-DEse1. At colder temperatures, no change is observable. Viewing only these figures, with cloud ice sedimentation switched on before changing the heterogeneous ice nucleation scheme, one might have assumed that the introduction of cloud ice sedimentation had negligible effects and that the change in heterogeneous ice nucleation scheme alone was strong.

[†]Within COSMO-DE's heterogeneous ice cnucleation scheme, it is distinguished between two freezing modes: Deposition and condensation/immersion freezing. It is switched to the latter, when the specific content of cloud water exheeds a threshold value and when supersaturation with respect to liquid phase is given.

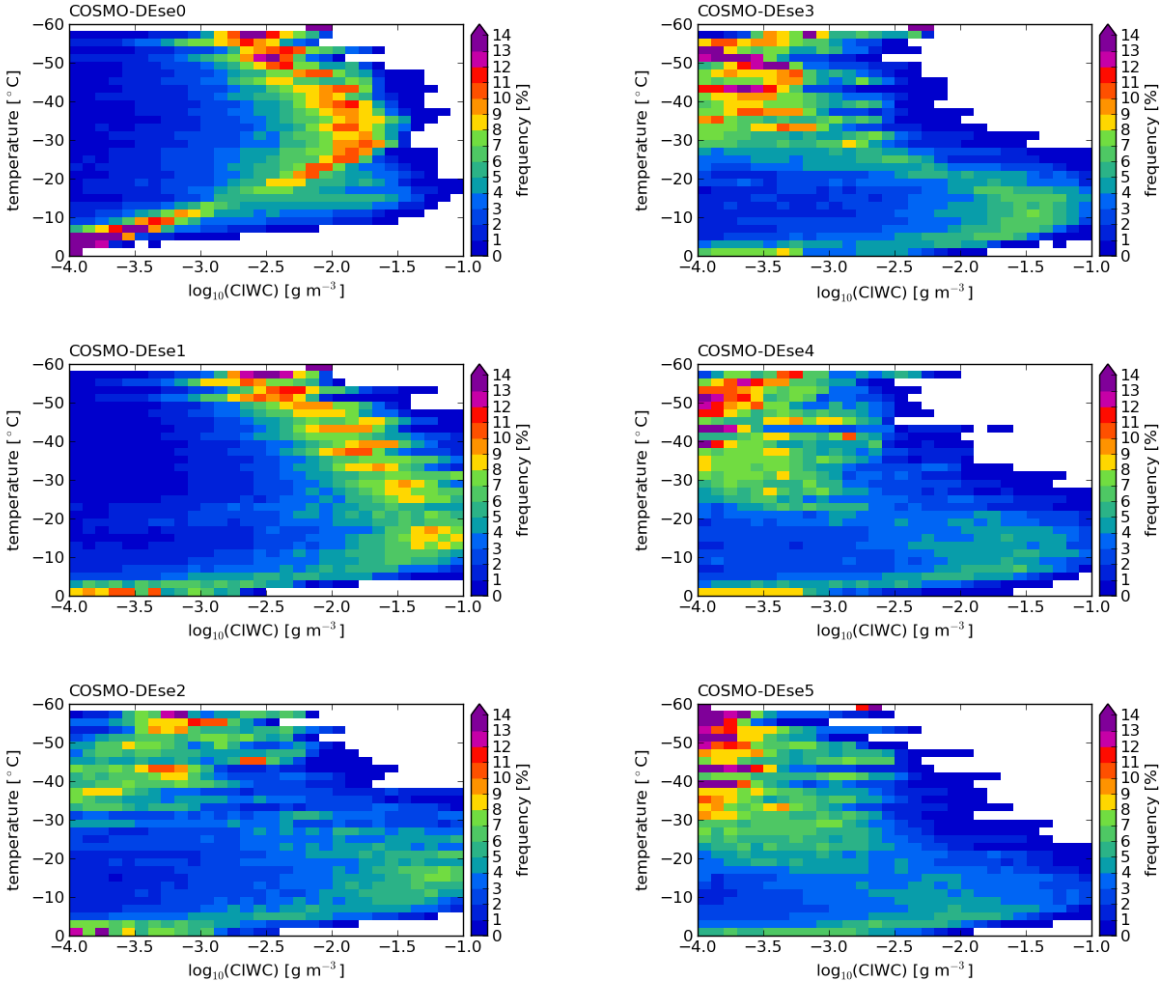

Figure 7.21: Frequency distributions of CIWCs for sensitivity experiments with varying model switches over the reduced model domain as depicted in Fig. 7.2 on 15 June 2010 at 2 UTC. Forecast age of model run: 14 h. Note that each temperature bin is normalized individually. See Table 7.2 for details on the settings in the individual experiments.

Fourthly, the additional prognostic tracking of activated IN is introduced (COSMO-DEse4). Little effect is discernible in the cross sections of CIWC (cf. middle panel in Fig. 7.17) except for a slight increase in CIWC in the lower parts of the cloud at 48 °N but a decrease of CIWC in the small cloud at 52 °N. This gives no concise picture. The frequency distribution of CIWC for the whole reduced model domain (cf. middle right panel in Fig. 7.21) reveals no change for temperatures below −30 °C. At warmer temperatures however, large CIWCs occur slightly less frequently (approximately 1 %), just as large SWCs occur slightly less frequently (not shown). All in all, in comparison to the effect that the choice of heterogeneous ice nucleation scheme and introduction of cloud ice sedimentation have, this effect is negligable in the presented case study. This might be contributed to the choice of case; firstly, it could well be possible, that in the investigated case, more IN would anyhow not be available without tracking and secondly, the effect of the introduction of a tracking variable is expected to increase with cloud age (*Köhler, 2013*).

Finally, the adjustment of depositional growth of cloud ice is changed (COSMO-DEse5). In the first place this adjustment is intended to prevent overshooting during depositional growth/sublimation: With the forward Euler method of the two-category ice scheme, within one time step, water vapour can be depleted so far that saturation with respect to frozen phase is lower than 100 %. The saturation adjustment was designed to correct for this overshooting by adding the water vapour difference needed to maintain saturation with respect to frozen phase. With the new relaxation approach, overshooting does not occur, making this adjustment obsolete. However, within COSMO-DE, this saturation adjustment switch is coupled to another fundamental assumption: It is assumed that cloud ice sublimates completely as soon as undersaturation with respect to frozen phase occurs. In the two-moment cloud ice scheme this switch is turned off, enabling slow sublimation of cloud ice once more. The effect on the cross section of CIWC (cf. bottom panel in Fig. 7.17) is as follows: At cloud top CIWC is further reduced. Also, CTH — if defined through $CIWC > 0$ — changes: it rises. However, as with the introduction of the tracking variable one step earlier, the effect is negligible in comparison to the effects that the changes in heterogeneous ice nucleation and cloud ice sedimentation have.

Levels

As described in Chap. 3.2, the operational COSMO-DE currently has 50 vertical levels. Generally, CIWC distribution is expected to be sensitive to vertical level number. *Barrett et al. (2012)* find several GCMs to produce too much cloud ice at cloud top, just as the standard two-category ice scheme in COSMO-DE8819. They perform sensitivity tests with a single column model to determine the reason for this behaviour, one model run is with a vertical resolution of 50 m, another with 500 m. With decreasing resolution, information on the vertical structure of a cloud is lost. In the high resolution version, the cloud ice growth rate peaks at 200 m below cloud top. It is dependent firstly on cloud ice mixing ratio, which increases linearly with distance from cloud top due to cloud ice sedimentation and secondly on saturation ratio with respect to frozen phase, which first remains constant in the top most layers of the cloud but then decreases linearly with increasing distance form cloud top. Cloud ice growth rate is largest at intermediate values of the two. The maximum cloud ice growth rate is reached at approximately 200 m below cloud top. In the low resolution version, the layer mean cloud ice mixing ratio and the supersaturation with respect to frozen phase are such that they result in exactly this maximum cloud ice growth rate. But now not only in a specific height, as in the high resolution version, but over the entire layer. Therefore, glaciation occurs much more rapidly, in fact it increases with time, LWC is reduced, and even completely depleted at cloud top. Contrary, in the high resolution version, cloud ice growth rate and sedimentation rate reach an equilibrium state at cloud top, enabling the liquid layer on top to prevail, which is a much more realistic scenario.

To test the sensitivity of the new two-moment cloud ice scheme to the number of vertical levels, further sensitivity tests are performed. The number of vertical layers is firstly multiplied by 1.5, then by 3, resulting in a 84- and a 150-layer version of COSMO-DE8822 with

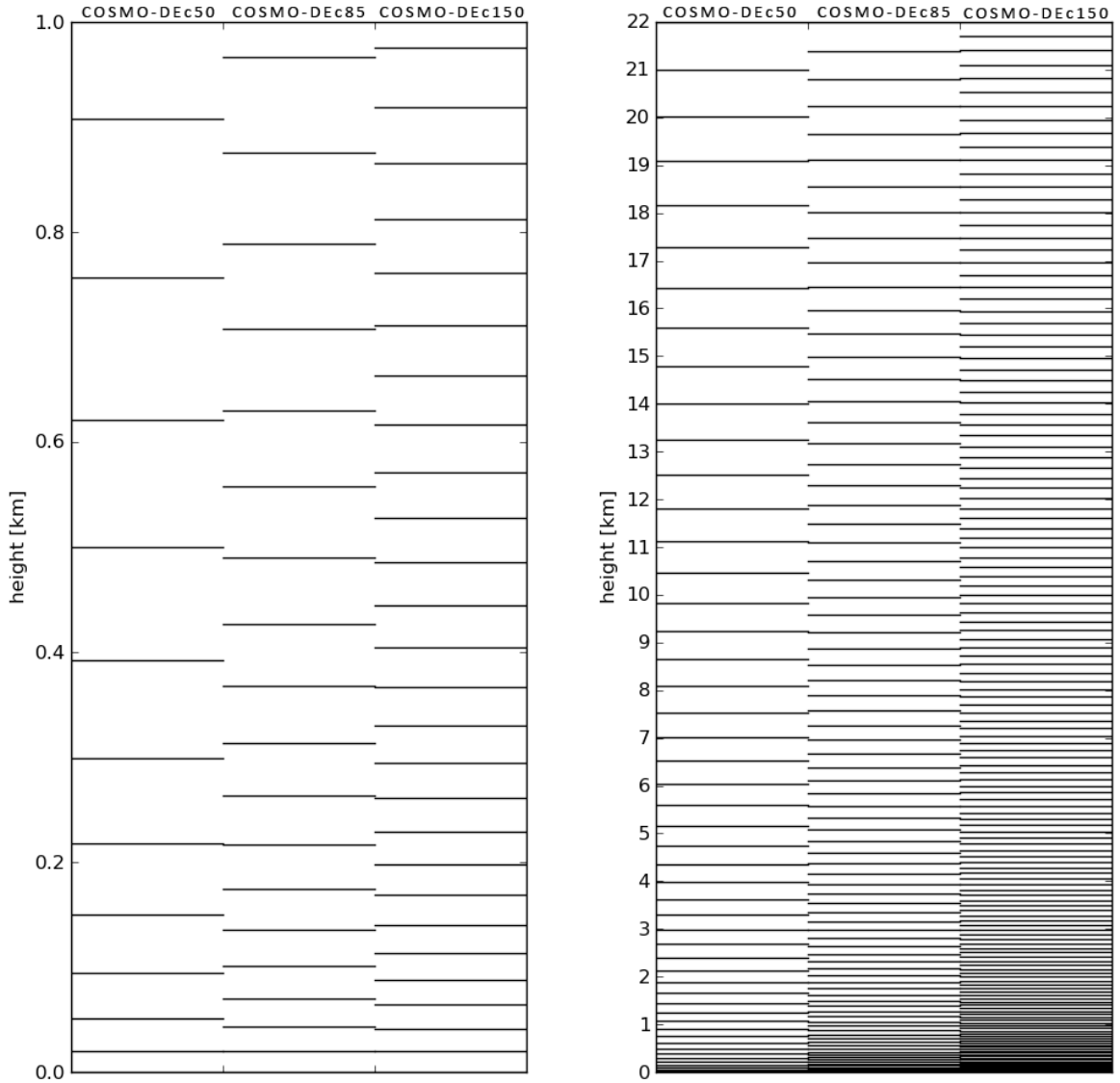

7.22.1: Lowest 1 km.

7.22.2: Whole profile.

Figure 7.22: Vertical distribution of vertical levels in enhanced level number experiments.

its two-moment cloud ice scheme. These and the control run with the standard 50 layers are in the following termed COSMO-DEc50, COSMO-DEc85, and COSMO-DEc150 and are listed together with the other sensitivity experiments in Table 7.2. Figure 7.22 shows how the new levels are vertically distributed.

The CIWC cross sections reveal little difference between the model versions with the different number of levels (cf. Fig. 7.24). The overschooting above 13 km height is diminished because the layers in this height are now less thick, but in this part of the cloud, CIWC is anyhow very small: less than $10^{-5}\,\mathrm{g\,m^{-3}}$. The CIWC maxima are somewhat reduced in 4–6 km height. The expected effect of cloud ice being shifted to lower layers is not recognizable, in contrast to when cloud ice sedimentation was switched on. The frequency distri-

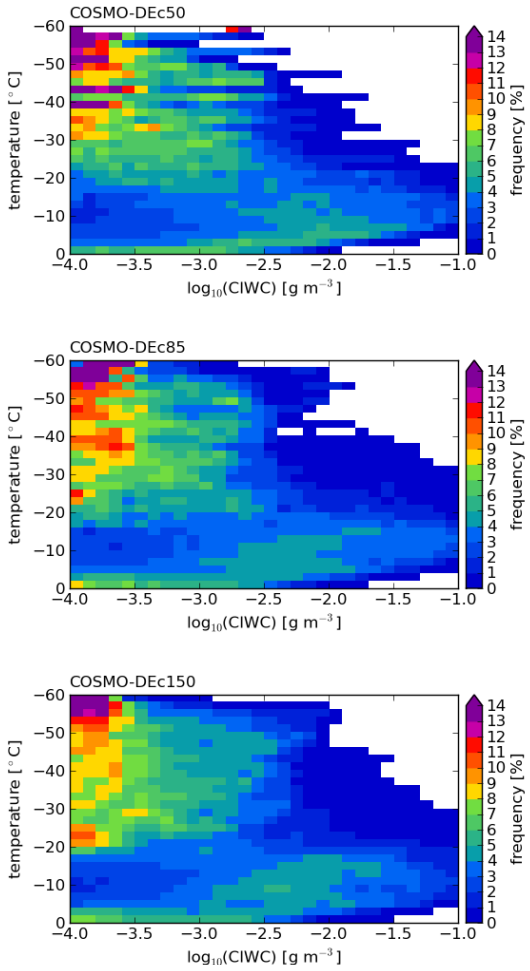

Figure 7.23: Frequency distributions of CIWCs for sensitivity experiments with varying level numbers over the reduced model domain as depicted in Fig. 7.2 on 15 June 2010 at 2 UTC. Forecast age of model run: 14 h. Note that each temperature bin is normalized individually. See Table 7.2 for details on the settings in the individual experiments.

butions of CIWC (cf. Fig. 7.23) do not indicate any vertical redistribution either, except for a higher occurrence of low CIWC at −20 °C for higher vertical resolutions. However, the frequency distributions do show, that with increasing vertical level number, the frequency distributions become smoother at the top of the troposphere. Due to the thinner levels cloud top is resolved better. Concerning the number of vertical cloud layers, Fig. 7.25 shows that their number changes with changing number of vertical model levels. As expected, the frequency of occurrence of profiles with many cloud layers (that is three and four) increases with increasing number of vertical model levels; in fact, by over 100 % for four layers in COSMO-DEc150. The more numerous model layers are thinner and therefore capture more detailed cloud structures. As a consequence, the number of profiles with less cloud layers (that is one and two) is reduced; for example by approximately 11 % for one cloud layer and COSMO-DEc150. However, the number of clear-sky profiles is slightly increased. The reason for this behaviour might be interesting for future studies to investigate. Concluding, the increased computational cost connected with the increase in vertical level number is not

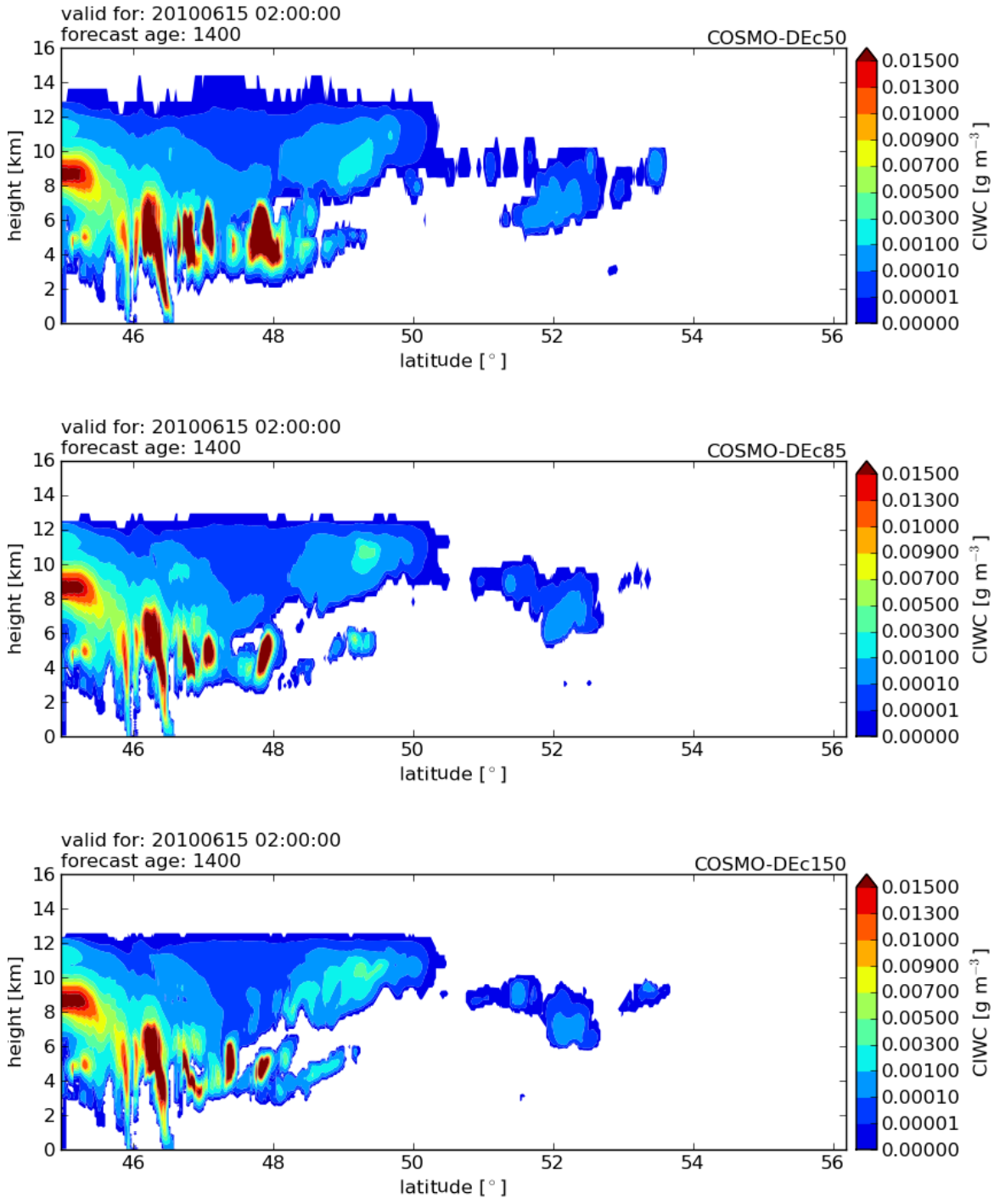

Figure 7.24: Cross sections of COSMO-DEc50-c150 CIWC along CloudSat track on 15 June 2010 at 2 UTC. Forecast age of model runs: 14 h. Note that CIWC values unequal zero are already depicted in blue. The settings of the sensitivity experiments are given in Table 7.2.

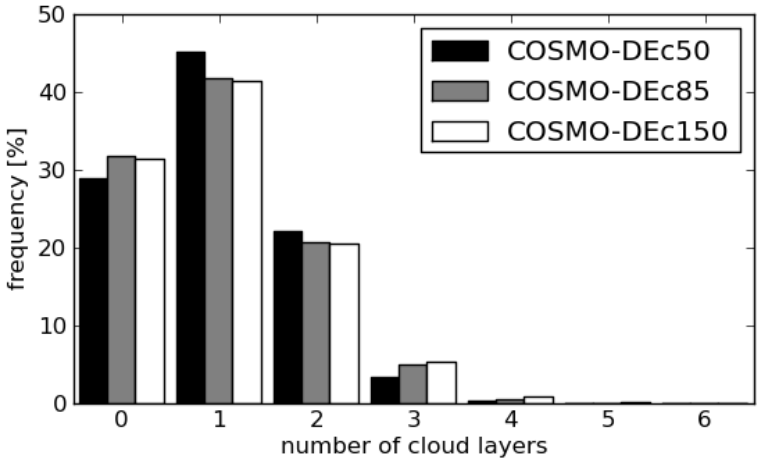

Figure 7.25: Frequency distributions of number of cloud layers for sensitivity experiments with varying level numbers over the reduced model domain as depicted in Fig. 7.2 on 15 June 2010 at 2 UTC. Forecast age of model run: 14 h. Note that a model layer is identified as cloudy if either QC or QI is unequal zero. See Table 7.2 for details on the settings in the individual experiments.

justified by an improved representation of CIWC within the two-moment cloud ice scheme.

Number concentrations

Changes in IN concentrations are expected to translate into cloud microphysical property and cloud forcing differences (*DeMott et al., 2010*). This emphasizes the need for a realistic aerosol climatology. In COSMO-DE, both the number of CCN and IN are dependent on their respective predefined aerosol load (*Seifert et al., 2012*). And the development of a cloud in turn is dependent on the number of activated CCN and IN. The more IN are activated, the more cloud ice crystals develop and glaciation is expected to occur more rapidly. The more CCN are activated, the more but smaller cloud droplets develop and glaciation is expected to be slower. Less but larger cloud droplets would result in a more rapid glaciation of a cloud, because of the droplet volume-dependency of condensation/immersion freezing.

The sensitivity of the novel two-moment cloud ice scheme to aerosol number concentrations which serve as IN is therefore investigated in the following. Four sensitivity experiments are performed. The changes in aerosol number concentrations are listed in Table 7.2 together with the other sensitivity experiments. Note that aerosol number concentration is not a prognostic variable in COSMO-DE, it does not change with time but is implemented as constant background aerosol. Note also, that the number of IN actually activated from available total aerosol number is temperature dependent in the *Phillips et al. (2008)* formulation.

In the first two experiments (COSMO-DE5a, and 5b), dust number concentration is multiplied and divided by ten, as in *Seifert et al. (2012)*. In a third experiment (COSMO-DE5c), the number concentration of liquid aerosols serving as IN for homogeneous ice nucleation is set to zero, to observe how much influence it actually has, or whether heterogeneous ice

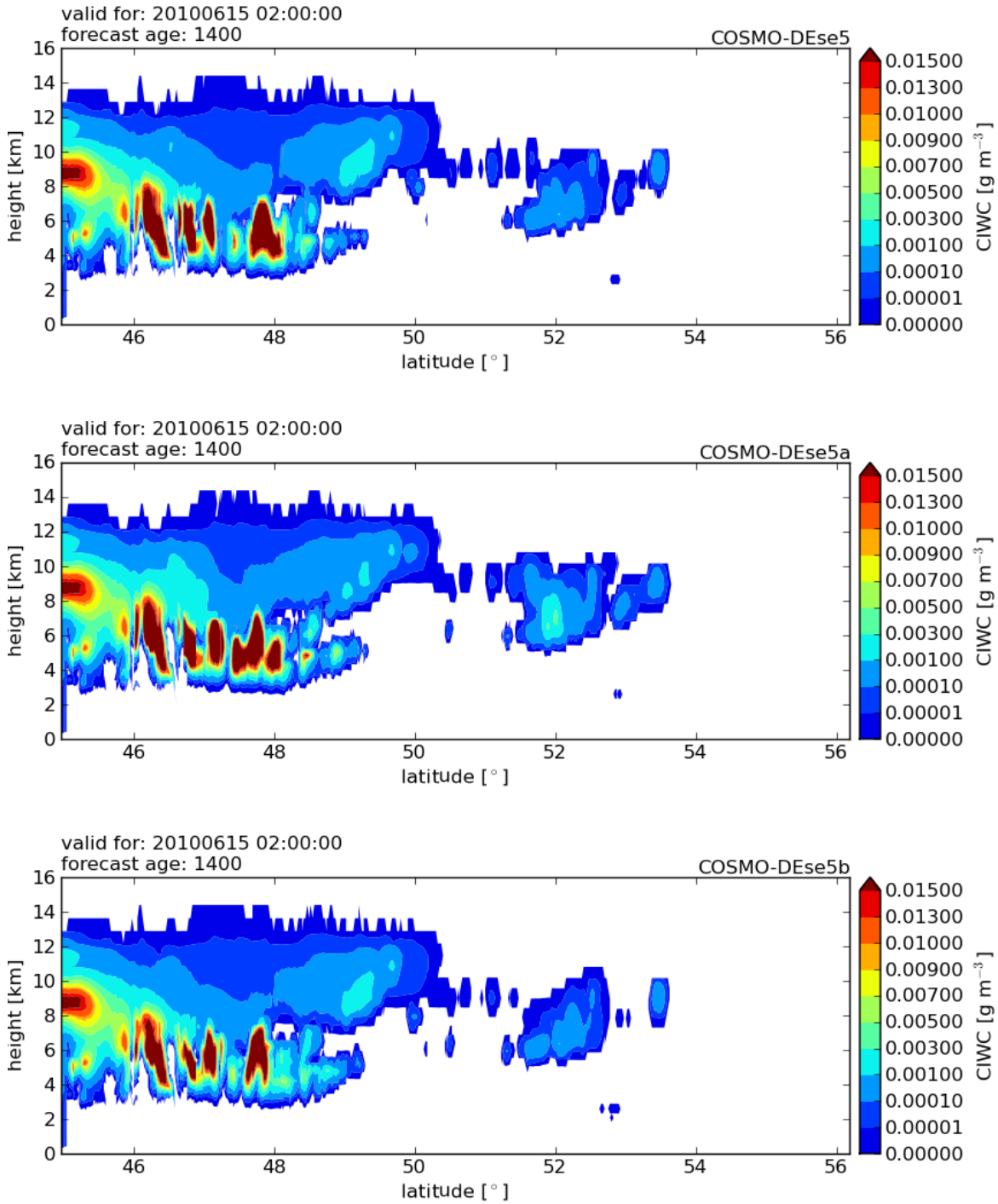

Figure 7.26: Cross sections of COSMO-DEse5, 5a, and 5b CIWC along CloudSat track on 15 June 2010 at 2 UTC. Forecast age of model runs: 14 h. Note that CIWC values unequal zero are already depicted in blue. The settings of the sensitivity experiments are given in Table 7.2.

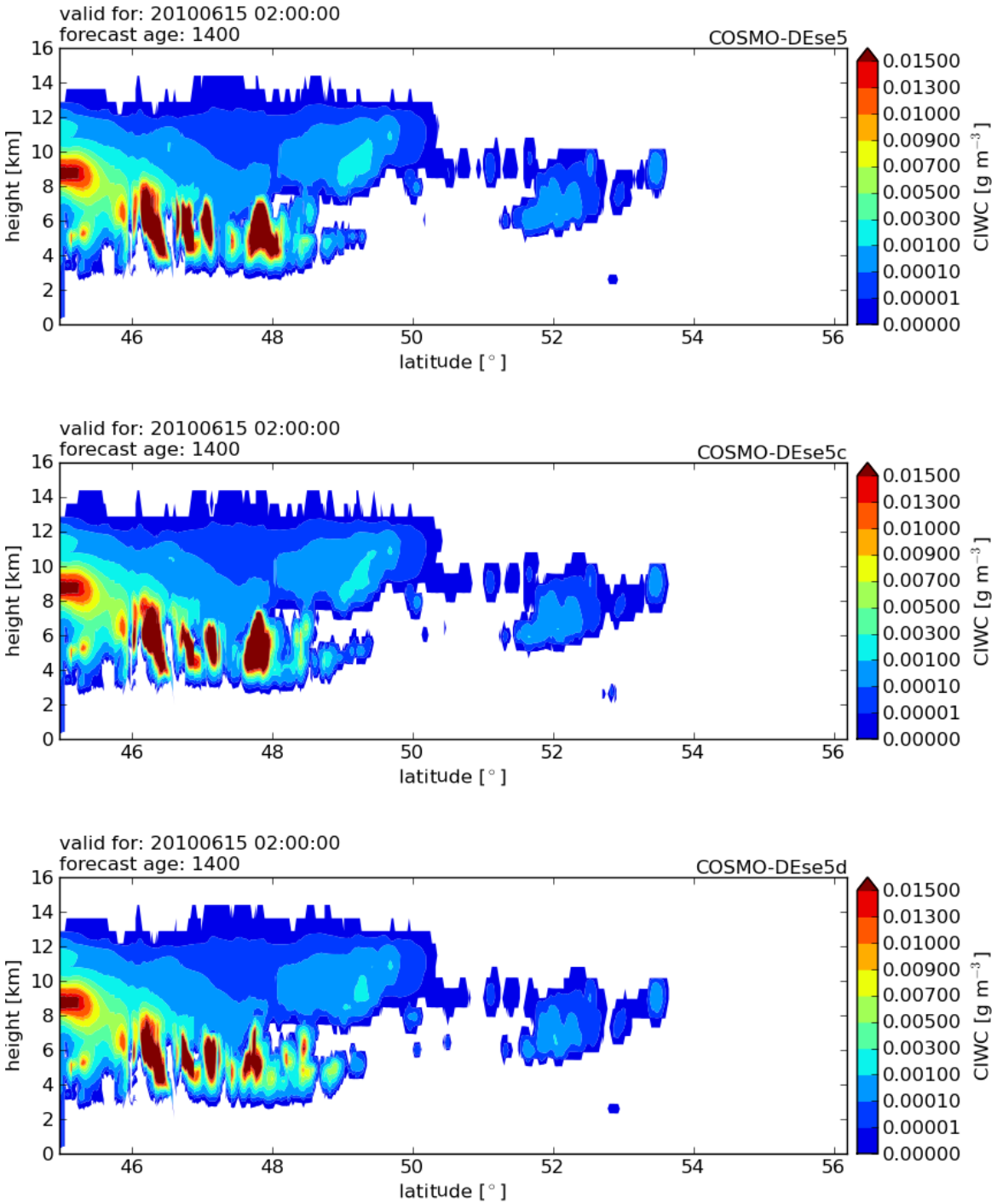

Figure 7.27: Cross sections of COSMO-DEse5, 5c, and 5d CIWC along CloudSat track on 15 June 2010 at 2 UTC. Forecast age of model runs: 14 h. Note that CIWC values unequal zero are already depicted in blue. The settings of the sensitivity experiments are given in Table 7.2.

nucleation and (pure) homogeneous ice nucleation are the more dominant processes anyhow. In a fourth experiment (COSMO-DE5d), the number concentration of soot is set to zero, since its suitability as IN is still a topic of ongoing discussions.

From the cross sections of CIWC (cf. Figs. 7.26 and 7.27), both the increase and the decrease in dust number concentrations exhibit little effect on CIWC. A slight reduction in maximum CIWC might be seen for the reduced dust number concentration in COSMO-DE5b (cf. bottom panel in Fig. 7.26). The sensitivity to soot is larger: In setting the number concentration of soot to zero the CIWC maxima are reduced in the lower part of the cloud at 48 °N (cf. bottom panel in Fig. 7.27). Setting the number of liquid aerosols to zero has negligible effect on CIWC (cf. middle panel in Fig. 7.27), indicating that homogeneous ice nucleation of liquid aerosol does not play a major role in the presented case. At CTH, no effect is to be seen for either of the four changes. In the CIWC frequency distributions, too,

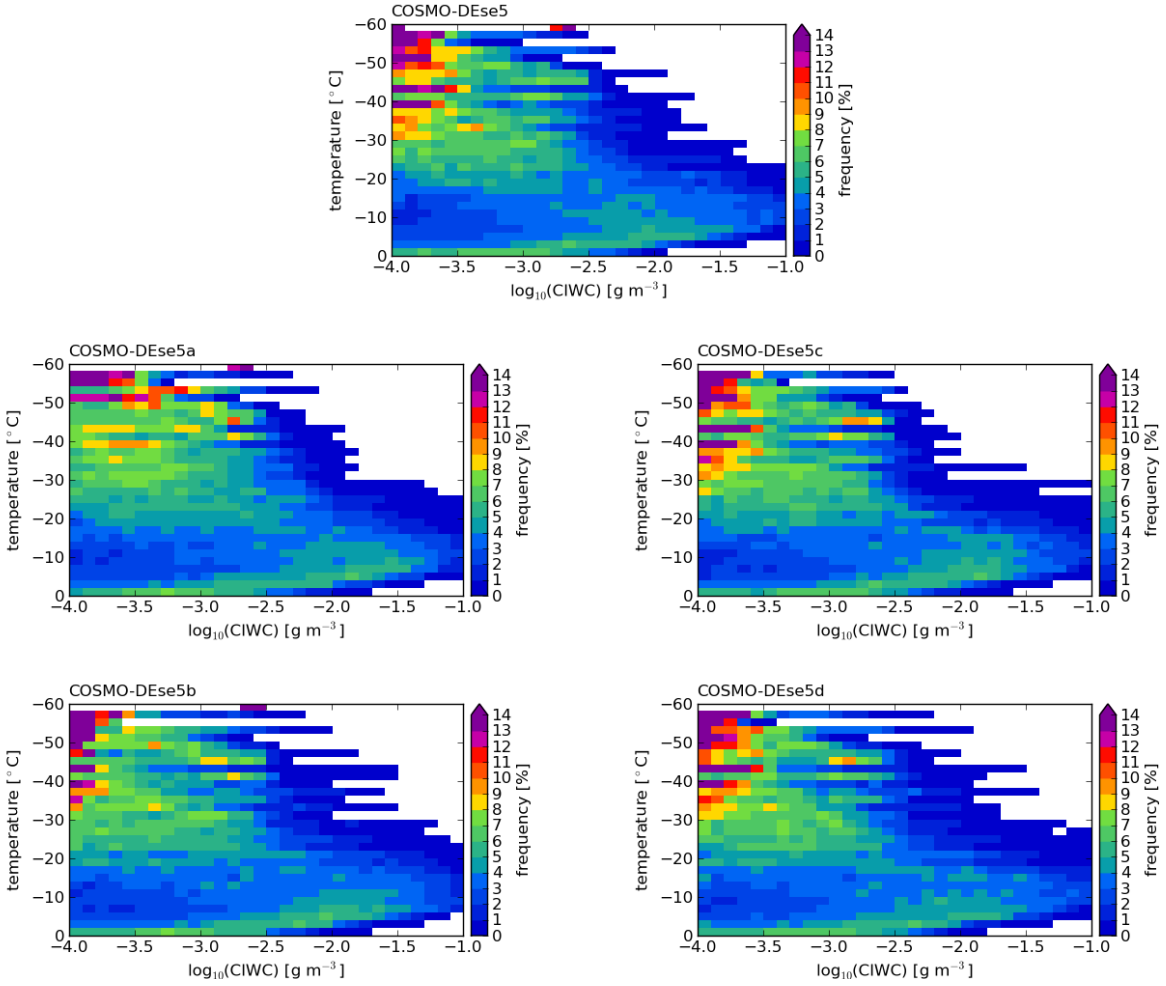

Figure 7.28: Frequency distributions of CIWCs for sensitivity experiments with varying aerosol concentration numbers over the reduced model domain as depicted in Fig. 7.2 on 15 June 2010 at 2 UTC. Forecast age of model run: 14 h. Note that each temperature bin is normalized individually. See Table 7.2 for details on the settings in the individual experiments.

hardly any effect is discernible (cf. Fig. 7.28). That homogeneous ice nucleation of liquid aerosols does not play a role in the presented case is because no supersaturations with respect to frozen phase of more than 160 % occur (cf. Fig. 7.18). Given this, homogeneous ice nucleation of liquid aerosols is per definition not initialized. A different case than the one investigated in the present study, where homogeneous ice nucleation actually does play a role, might give further insight as to how much change the consideration of homogeneous ice nucleation actually makes. This could, for example, be a convective case where high updraft velocities generate high supersaturations with respect to frozen phase fast enough, that heterogeneous ice nucleation does not have the time to deplete the excess water vapour, before homogeneous ice nucleation of liquid aerosols sets in.

7.4 Summary and conclusions

This part of the present study evaluates the regional NWP model COSMO-DE with respect to its ability to simulate MSG SEVIRI observed brightness temperatures at 10.8 μm. The performance of a new two-moment cloud ice scheme is compared to that of two standard schemes, a two- and a three-category ice scheme. As a reference, MSG SEVIRI, CloudSat CPR, and CALIPSO CALIOP data are used.

The two-category ice scheme is found to overestimate the occurrence of low brightness temperatures at 10.8 μm. In contrast, the two-moment cloud ice scheme captures the frequency distribution of brightness temperatures at 10.8 μm well. A case study is performed to determine the reason for this improved performance: It lies in the distribution of cloud ice. The two-moment cloud ice scheme produces smaller IWPs and even more important, it shifts cloud ice to lower altitudes.

Furthermore, a series of sensitivity studies is performed with the new two-moment cloud ice scheme to determine which part of the new scheme is responsible for the observed improvement. The changes introduced in this scheme are switched on individually. The change from the former modified *Fletcher (1962)* to the *Phillips et al. (2008)* ice nucleation scheme and the introduction of the sedimentation of cloud ice account for the largest change. The effect of the latter is expected to be even more pronounced, with the implementation of the density correction of the fall speed of cloud ice, similar to that described for GME in Chap. 6.4.2[‡]. For this reason, the sedimentation of cloud ice is per se implemented into the new NWP model ICON (Icosahedral nonhydrostatic; `http://www.mpimet.mpg.de/en/science/models/icon.html`), which is currently being developed by Max-Planck-Institute (MPI) for Meteorology and DWD in a joint effort; the two-moment cloud ice scheme itself is for research application only.

Finally, a further set of sensitivity experiments with the two-moment cloud ice scheme is

[‡]In the model versions utilized in the present study, this was switched off.

performed, with the goal of testing its sensitivity firstly to the number of vertical levels, and secondly to changes in the aerosol number concentrations, which serve as IN. The increase in vertical level number does not lead to such a distinct reduction of CIWC at cloud top and displacement of CIWC to lower layers as presumed. Therefore, the increase in computational cost caused by the increase in vertical level number is not justifiable and thus not recommended. The sensitivity of COSMO-DE CIWC to changes in aerosol number concentration is given, but small in comparison to the differences the other parts of the new two-moment cloud ice scheme cause. It can be concluded that the exact aerosol number concentrations implemented in the model play a minor role.

The evaluation presented in this chapter shows that, though IWC is dominated by SWC, the COSMO-DE simulated brightness temperatures are mainly dependent on the magnitude and vertical distribution of cloud ice alone. This emphasizes the importance of a realistic description of cloud ice in NWP models and the need for good parameterization schemes. Though the presented case study shows no noteworthy sensitivity to the underlying aerosol PSDs, investigations should be extended to other cases and longer time series, before a robust conclusion can be drawn.

8 General summary, conclusions, and outlook

The present study evaluates the performance of two NWP models with respect to specific questions concerning their ice microphysical parameterizations. To this end, data from various satellite instruments are utilized. The two possible approaches available when comparing model to satellite data — observation-to-model and model-to-observation — are compared and their advantages and disadvantages discussed.

The first part of the study is concerned with the global NWP model GME and compares the performance of a diagnostic to that of a prognostic precipitation scheme. The prognostic scheme was introduced at DWD to meet the demands of increasingly higher horizontal grid resolution and to adjust the microphysical parameterizations of the models in DWD's operational model chain. CloudSat CPR data are used as a reference. In comparison to the diagnostic scheme, the prognostic scheme exhibits improved performance with respect to IWC. For this reason the prognostic scheme went operational on 2 February 2010. Furthermore, one reason for the remaining difference between prognostic scheme and observations — the unrealistic fall speed of snow — is identified. Consequently, this new fall speed was implemented into the microphysical scheme and went operational on 1 December 2010. Finally, the evaluation reveals that in GME snow is the dominant contributor to frozen phase hydrometeor content. This is a common problem in GCMs still posing a challenge (*Inoue et al. (2010)* state the same problem for the NICAM model). Or rather, it poses the challenge of determining what exactly is cloud ice and what is snow. This is merely a question of definition, as the introduction of sedimentation of cloud ice in COSMO-DE shows.

The second part of the study deals with the regional NWP model COSMO-DE and investigates the performance of a two-moment cloud ice microphysical scheme (*Köhler, 2013*) in comparison to the standard two-category ice scheme with respect to a long-known bias between simulated and observed MSG SEVIRI brightness temperatures. The two-moment

cloud ice scheme was originally developed to improve the representation of ice nucleation processes in the model. MSG SEVIRI, CloudSat CPR, and CALIPSO CALIOP data are used as a reference. The simulated brightness temperatures of the two-moment cloud ice scheme match those observed by MSG SEVIRI distinctly better. This improved performance is robust on a monthly basis and even discernible on a case study basis. The reason lies in the predicted cloud ice. The two-moment cloud ice scheme reduces CIWP and shifts CIWC to lower altitudes. A series of sensitivity studies is performed to determine which part of the new scheme is responsible for the observed improvement. Two novelties, the change towards the *Phillips et al. (2008)* heterogeneous ice nucleation scheme and the introduction of the sedimentation of cloud ice are shown to account for the largest change. Though this two-moment cloud ice scheme is yet for research use only, the results still find application in operational NWP models: in the ICON model, currently still under development by the MPI for Meteorology and DWD as a joint effort, cloud ice sedimentation is built in per se. To test the sensitivity of the two-moment cloud ice scheme to other changes, further experiments are conducted. They reveal firstly, that an increase of number of model levels does not lead to a distinct change in vertical CIWC distribution, and secondly, that the sensitivity to aerosol number concentrations is smaller than that to other changes in the cloud ice microphysical parameterizations. Finally it is shown, that although IWC is dominated by SWC, the COSMO-DE simulated brightness temperatures are mainly dependent on CIWC alone.

Within the two model evaluations performed in the present study, both possible approaches — observation-to-model and model-to-observation — are pursued. In doing so it is possible to compare them directly and expose their respective advantages and disadvantages. The observation-to-model approach has the advantage of its easy computation, and the actual model parameters are compared. However, the CloudSat IWC-retrieval introduces additional uncertainties which are not easily assessed: Within the optimal estimation technique, the radar reflectivity factor (one value) is composed of three unknowns, namely ice particle number concentration, geometric mean diameter, and width parameter. Additionally, other assumptions are made. Firstly, the ill-determined problem is constrained via a priori information consisting of ECMWF temperatures as well as the CloudSat CPR radar reflectivity factors themselves. The latter is questionable since in the formal optimal estimation approach the a priori information needs to be independent of the measurement vector. Secondly, phase-discrimination is achieved by a simple linear scaling between -20 and $0\,^{\circ}\mathrm{C}$. This might artificially change the height of the peak radar reflectivity factors (*Waliser et al., 2009*). Finally, functions for the PSDs need to be assumed, which are not necessarily representative of the actual PSDs. In contrast to this, the model-to-observation approach avoids these retrieval uncertainties and is closer to the actual physics by simulating the radar reflectivity factor the radar would have measured in the presence of a given amount of hydrometeors. But this approach, too, relies on assumptions. Firstly, in QuickBeam (*Haynes et al., 2007*), ice crystals are modelled as soft spheres which *Liu (2004)* finds to be a questionable approximation for the actual particle habit, in this case of the model. Secondly, this version of QuickBeam does not account for multiple scattering effects. And thirdly, neither

does it simulate the bright band. This limits the use of QuickBeam to cloud situations, in which neither of the two occur. As for the direct comparison of the two approaches: The present study finds the general features to be captured by both approaches. Some details are captured merely by the one or the other approach, in which case both approaches together give the more complete picture. However, the model-to-observation approach appears to be easier to interpret. Its uncertainties are easier to assess than those of the observation-to-model approach and it ensures a better control over the comparison, notably through the attenuation criterion; grid cells affected by attenuation (and therefore uncertainty) can be filtered out. Concluding, though retrieval development is ongoing, the observation-to-model approach is considered to be more error prone than the model-to-observation approach.

Model evaluation is a constantly ongoing and absolutely essential process; for assessing models as well as for improving the understanding of models. The present study contributes to both. However, further research is desirable to further reinforce the presented results. The discussed COSMO-DE case study delivers valuable insight into the model's ice microphysics and how it works. But further case studies and long-term evaluations are required, to corroborate this knowledge and obtain robust results. Further case studies might be able to identify cases in which other switches have more influence in CIWC than in the presented case. Specifically, homogeneous ice nucleation of liquid aerosols, calls for a synoptic situation with high supersaturations with respect to frozen phase. The tracking of activated IN calls for a synoptic situation, where either a large number of IN is available without the tracking or, where cloud age is old. As for the need for long-term evaluations, these are especially valuable since only a large-enough data volume enables to automatically identify specific cloud situations and analyse them statistically; each type of cloud situation has a recognizable frequency distribution and it is challenging for models to perform equally well in all. Specifically for the glaciation of a cloud in dependence on aerosol load, frequency distributions of ice fraction might be advantageous to look at. The case study presented here unfortunately did not include enough grid-points with both liquid and frozen phase to come to a conclusive result with this respect. Another interesting point of research might be to test the sensitivity of the presented results to varying forecast age. Also, the sensitivity to horizontal resolution effects (sampling) needs to be assessed in more detail in the future. Finally, the new scheme ought to be included in the currently operational three-category ice scheme, to improve its representation of ice clouds. As for the methodologies applied, given the crudeness of how RTTOV is coupled to COSMO-DE, it could be validated against other radiative transfer models to determine how much error in the simulated brightness temperatures stems from RTTOV and how much from COSMO-DE. Another interesting point might be to further exploit the CloudSat CPR. It provides more information than the utilized microphysical properties such as magnitude and distribution of IWC alone. It also gives information on cloud macrophysics, such as cloud base and top and vertical overlap. It is advisable for future studies to include these variables in their model evaluations. Concerning the uncertainty introduced by the soft sphere assumption of the forward operator QuickBeam, at a frequency of 94 GHz this is particular important for snow particles. Observations at the mid-latitude site Schneefernerhaus in the Alps indicate

that the dominating snow habit is aggregates without any preferred direction. Therefore, it is desirable in the future to include the scattering characteristics of such aggregates into a radar simulator and analyse the impact of this factor on simulated radar reflectivity factors. At the Institut für Geophysik und Meteorologie, Universität zu Köln (IGMK), a new Passive and Active Microwave TRAnsfer (PAMTRA) model is currently under development and should give new insights. Finally, it would be desirable to extend this work to the new ICON model which is currently still under development. To this end, it is important that the necessary auxiliary information is stored to allow for coupling to forward operators.

The CloudSat mission — originally funded for a 22 month lifetime — has up to now extended to seven years. The need for a successor has been acknowledged: As a part of the Earth Clouds, Aerosols, and Radiation Explorer (EarthCARE) mission (*Battaglia et al., 2011*) a new cloud radar is scheduled for launch in 2016. It will operate at the same frequency as the CloudSat CPR, but with a higher resolution and sensitivity. Additionally, it will measure Doppler velocities. For the atmospheric science community, EarthCARE will firstly mean a continuation and further refinement of the long-term evaluation of modelled cloud microphysics with satellite data. Secondly, for the first time ever, EarthCARE will deliver information on particle fall speed from space through its Doppler capability. This will enable two things: On the one hand, the first time ever application of radar reflectivity factor-Doppler velocity retrievals (*Mace et al., 2002*) to spaceborne data. These retrievals exhibit approximately the same accuracy as radar-lidar retrievals, but are not limited by restriction in optical depth. On the other hand, the Doppler velocity enables to distinguish between suspended and precipitating particles, a much needed information from a modelling perspective for improving precipitation understanding and prediction.

References

AUSTIN, R. T. 2007. Level 2B Radar-only Cloud Water Content (2B-CWC-RO) Process Description Document Version 5.1. *CloudSat Project*, 24 pp.

AUSTIN, R. T., HEYMSFIELD, A. J., AND STEPHENS, G. L. 2009. Retrieval of ice cloud microphysical parameters using the CloudSat millimeter-wave radar and temperature. *J. Geophys. Res.*, **114**, 19 pp.

AVRAMOV, A., AND HARRINGTON, J. Y. 2010. Influence of Parameterized Ice habit on Simulated Mixed Phase Arctic Clouds. *J. Geophys. Res.*, **115**, 14 pp.

BALDAUF, M., FÖRSTNER, J., KLINK, S., REINHARDT, T., SCHRAFF, C., SEIFERT, A., AND STEPHAN, K. 2011. Kurze Beschreibung des Lokal-Modells Kürzestfrist COSMO-DE LMK und seiner Datenbanken auf dem Datenserver des DWD. *Tech. Rep., Deutscher Wetterdienst, Offenbach, Germany*, 81 pp.

BARRETT, A., HOGAN, R., AND FORBES, R. 2012. Evaluation and improvement of mixed-phase cloud schemes using radar and lidar observations. *ECMWF Workshop on Parametrization of Clouds and Precipitation, 5 - 8 November 2012*, 12 pp.

BATTAGLIA, A., AJEWOLE, M. O., AND SIMMER, C. 2007. Evaluation of radar multiple scattering effects in CloudSat configuration. *Atmos. Chem. Phys.*, **7**, 1719–1730.

BATTAGLIA, A., HAYNES, J. M., L'ECUYER, T., AND SIMMER, C. 2008a. Identifying multiple-scattering-affected profiles in CloudSat over the ocean. *J. Geophys. Res.*, **113**, 13 pp.

BATTAGLIA, A., KOBAYASHI, S., TANELLI, S., IM, E., AND SIMMER, C. 2008b. Multiple scattering effects in pulsed radar systems: An intercomparison study. *J. Atmos. Ocean. Technol.*, **25**, 1556–1567.

BATTAGLIA, A., AUGUSTYNEK, T., TANELLI, S., AND KOLLIAS, P. 2011. Multiple scattering identification in spaceborne W-band radar measurements of deep convective cores. *J. Geophys. Res.*, **116**, 12 pp.

BENEDETTI, A., STEPHENS, G. L., AND HAYNES, J. M. 2003. Ice Cloud Microphysical Retrievals from Millimeter Radar and Visible Optical Depth Using an Estimation Theory Approach. *J. Geophys. Res.*, **108**, 23 pp.

BODAS-SALCEDO, A., WEBB, M. J., BROOKS, M. E., RINGER, M. A., WILLIAM, K. D., MILTON, S. F., AND WILSON, D. R. 2008. Evaluating cloud systems in the Met Office global forecast model using simulated CloudSat radar reflectivities. *J. Geophys. Res.*, **113**, 18 pp.

BODAS-SALCEDO, A., WEBB, M. J., BONY, S., CHEPFER, H., DURESNIE, J.-L., KLEIN, S. A., ZHANG, Y., MARCHAND, R., HAYNES, J. M., PINCUS, R., AND JOHN, V. O. 2011. COSP. Satellite simulation software for model assessment. *Bull. Am. Met. Soc.*, **92**(8), 1023–1043.

BROWN, P. R. A., AND FRANCIS, P. N. 1995. Improved measurements of the ice water content in cirrus using a total-water probe. *J. Atmos. Ocean. Technol.*, **12**, 410–414.

BÖHME, T., STAPELBERG, S., AKKERMANS, T., CREWELL, S., FISCHER, J., REINHARDT, T., SEIFERT, A., SELBACH, C., AND LIPZIG, N. VAN. 2011. Long-term evaluation of COSMO forecasting using combined observational data of the GOP period. **20 (2)**, 119–132.

CANTRELL, W., AND HEYMSFIELD, A. J. 2005. Production of Ice in Tropospheric Clouds: A Review. *Bull. Am. Met. Soc.*, **86**, 795–807.

CHEN, W.-T., WOODS, C. P., LI, J.-L. F., WALISER, D. E., CHERN, J.-D., TAO, W.-K., JIANG, J. H., AND TOMPKINS, A. M. 2011. Partitioning CloudSat ice water content for comparison with upper tropospheric ice in global atmospheric models. *J. Geophys. Res.*, **116**, 16 pp.

CIRA. 2008. CloudSat Standard Data Products Handbook. *Tech. Rep., Cooperative Institute for Research in the Atmosphere, Colorado State University, Fort Collins, USA*, 18 pp.

CLOUGH, S. A., SHEPHARD, M. W., MLAWER, E. J., DELAMERE, J. S., IACAONO, M. J., CADY-PEREIRA, K., BOUKABARA, S., AND BROWN, P. D. 2005. Atmospheric radiative transfer modeling: a summary of the AER codes, Short Communication. *J. Quant. Spectrosc. Radiat. Transfer*, **91**, 233–244.

CREWELL, S., MECH, M., REINHARDT, T., SELBACH, C., BETZ, H.-D., BROCARD, E., DOCK, G., O'CONNOR, E., FISCHER, J., HANISCH, T., HAUF, T., HÜHNERBEIN, A., DELOBBE, L., MATHES, A., PETERS, G., WERNLI, H., WIEGNER, M., AND

WULFMEYER, V. 2008. The General Observation Period 2007 within the Priority Program on Quantitative Precipitation Forecasting: Concept and first reults. **17**, 849–866.

DELANOË, J., AND HOGAN, R. J. 2008. A variational method for retrieving ice cloud properties from combined radar, lidar, and infrared radiometer. *J. Geophys. Res.*, **118**(7), 21 pp.

DELANOË, J., AND HOGAN, R. J. 2010. Combined CloudSat-CALIPSO-MODIS retrievals of the properties of ice clouds. *J. Geophys. Res.*, **115**, 17 pp.

DELANOË, J., HOGAN, R. J., FORBES, R. M., BOSA-SALCEDO, A., AND STEIN, T. H. M. 2011. Evaluation of ice cloud representation in the ECMWF and UK Met Office models using CloudSat and CALIPSO data. *Quart. J. Roy. Met. Soc.*, **137 (661)**, 15 pp.

DEMOTT, P. J., CZICZO, D. J., PRENNI, A. J., MURPHY, D. M., KREIDENWEIS, S. M., THOMSON, D. S., BORYS, R., AND ROGERS, D. C. 2003. Measurements of the Concentration and Composition of Nuclei for Cirrus Formation. *Proc. Natl. Acad. Sci. USA*, **100**(25), 14655–14660.

DEMOTT, P. J., PRENNI, A. J., LIU, X., KREIDENWEIS, S. M., PETTERS, M. D., TWOHY, C. H., RICHARDSON, M. S., EIDHAMMER, T., AND ROGERS, D. C. 2010. Predicting global atmospheric ice nuclei distributions and their impacts on climate. *Proc. Natl. Acad. Sci. USA*, **107**, 6 pp.

DOMS, G., FÖRSTNER, J., HEISE, E., HERZOG, H.-J., RASCHENDORFER, M., SCHRODIN, R., REINHARDT, T., AND VOGEL, G. 2004. A Description of the Nonhydrostatic Regional Model LM, Part II: Physical Parameterization. LM_F90 3.11. *Tech. Rep., Deutscher Wetterdienst, Offenbach, Germany*, 134 pp.

DOMS, G., FÖRSTNER, J., HEISE, E., HERZOG, H.-J., MIRONOV, D., RASCHENDORFER, M., REINHARDT, T., RITTER, B., SCHRODIN, R., SCHULZ, J.-P., AND VOGEL, G. 2011. A Description of the Nonhydrostatic Regional COSMO Model, Part II: Physical Parameterization. LM_F90 4.20. *Tech. Rep., Deutscher Wetterdienst, Offenbach, Germany*, 154 pp.

DONOVAN, D. P., AND VAN LAMMEREN, A. C. A. P. 2001. Cloud effective particle size and water content profile retrievals using combined lidar and radar observations 1. Theory and examples. *J. Geophys. Res.*, **106**, 27425–27448.

EDWARDS, D. P. 1992. GENLN2. A General Line-by-Line Atmospheric Transmittance and Radiance Model. Version 3.0 Description and Users Guide. NCAR/TN-367+STR. *Tech. Rep., National Center for Atmospheric Research, Boulder, Colorado, USA*, 157 pp.

EUMETSAT. 2007. A Planned Change to the MSG Level 1.5 Image Product Radiance Definition. Doc.No. EUM/OPS-MSG/TEN/06/-519. *Tech. Rep., European Organisation for the Exploitation of Meterological Satellite Observations, Darmstadt, Germany*, 9 pp.

EYRE, J. R. 1991. A fast radiative transfer model for satellite sounding systems. *ECMWF, Technical Memorandum*, **176**, 30 pp.

FIELD, P. R., HOGAN, R. J., BROWN, P. R. A., ILLINGWORTH, A. J., CHOULARTON, T. W., AND COTTON, R. J. 2005. Parameterization of Ice-particle Size Distributions for Mid-latitude Stratiform Clouds. *Quart. J. Roy. Met. Soc.*, **131**, 1997–2017.

FLETCHER, N. H. 1962. Physics of Rain Clouds. *Cambridge University Press*, 386 pp.

FORNEA, A. P., BROOKS, S. D., DOOLEY, J. B., AND SAHA, A. 2009. Heterogeneous Freezing of Ice on Atmospheric Aerosols Containing Ash, Soot, and Soil. *J. Geophys. Res.*, **114**, 12 pp.

FRIDLIND, A. M., ACKERMAN, A. S., MCFARQUHAR, G., ZHANG, G., POELLOT, M. R., DEMOTT, P. J., PRENNI, A. J., AND HEYMSFIELD, A. J. 2007. Ice Properties of Single-layer Stratocumulus During the Mixed-Phase Arctic Cloud Experiment: 2. Model Results. *J. Geophys. Res.*, **112**, 25 pp.

GIERENS, K. M. 2003. On the transition between heterogeneous and homogeneous freezing. *Atmos. Chem. Phys.*, **3**, 437–446.

GLICKMAN, T. S., AND AMERICAN METEOROLOGICAL SOCIETY. 2000. Glossary of Meteorology. *American Meteorological Society*, 855 pp.

GRODY, N. C. 1993. Remote Sensing of the Atmosphere from Satellites Using Microwave Radiometry. *Wiley Series in Remote Sensing. Atmospheric Remote Sensing by Microwave Radiometry. Edited by Michael E. Janssen*, 259–314.

HALLETT, J., AND MOSSOP, S. 1974. Production of Secondary Ice Particles During the Riming Process. *Nature*, **249**, 26–28.

HAYNES, J. M., MARCHAND, R. T., BODAS-SALCEDO, L. A., AND STEPHENS, G. L. 2007. A Multipurpose Radar Simulation Package: QuickBeam. *Bull. Am. Met. Soc.*, **88 (11)**, 1723–1727.

HEINTZENBERG, J., AND CARLSON, R. J. 2009. Clouds in the Perturbed Climate System. *MIT Press*, 597 pp.

HEWISON, T. J., AND MÜLLER, J. 2013. Ice Contamination of Meteosat/SEVIRI Implied by Intercalibration Against Metop/ISAI. *Geoscience and Remote Sensing, IEEE Transactions on*, **51**(3), 1182–1186.

HEYMSFIELD, A., SCHMITT, C., AND BANSEMER, A. 2013. Ice Cloud Particle Size Distributions and Pressure-Dependent Terminal Velocities from In Situ Measurements from 0 to -86C. *J. Atmos. Sci.*, **in press**.

HILEY, M. J., KULIE, M. S., AND BENNARTZ, R. 2011. Uncertainty Analysis for CloudSat Snowfall Retrievals. **50**, 399–418.

HOGAN, R. J., MITTERMAIER, M. P., AND ILLINGWORTH, A. J. 2006. The Retrieval of Ice Water Content from Radar Reflectivity Factor and Temperature and Its Use in Evaluating a Mesoscale Model. **45**, 301–317.

HOOSE, C., AND MÖHLER, O. 2012. Heterogeneous Ice Nucleation on Atmospheric Aerosols: A Review of Results From Laboratory Experiments. *Atmos. Chem. Phys.*, **12**, 9817–9854.

HOSTETLER, C., LIU, Z., REAGAN, J., VAUGHAN, M., OSBORN, M., HUNT, W. H., POWELL, K. A., AND TREPTE, C. 2006. CALIOP Algorithm Theoretical Basis Document: Calibration and Level 1 Data Products. *Tech. Rep.*, 66 pp.

HUNT, W. H., WINKER, D. M., VAUGHAN, M. A., POWELL, K., LUCKER, P. L., AND WEIMER, C. 2009. CALIPSO Lidar Description and Performance Assessment. *J. Atmos. Ocean. Technol.*, **26**, 1214–1228.

INOUE, T., SATOH, M., HAGIHARA, Y., MIURA, H., AND SCHMETZ, J. 2010. Comparison of High-Level Clouds Represented in a Global Cloud System-Resolving Model with CALIPSO/CloudSat and Geostationary Satellite Observations. *J. Geophys. Res.*, **115**, 15 pp.

IPCC. 2007. Climate Change 2007: The physical science basis. Contribution of working group I to the Fourth Assessment Report of the Intergovernmental Panel on Climate Change. *Cambridge University Press, Cambridge, United Kingdom and New York, NY, USA*, 1007 pp.

JOSEPH, J. H., WISCOMBE, W. J., AND WEINMAN, J. A. 1976. The Delta-Eddington Approximation for Radiative Flux Transfer. *J. Atmos. Sci.*, **33**, 2452–2459.

KEIL, C., TAFFERNER, A., AND REINHARDT, T. 2006. Synthetic satellite imagery in the Lokal-Modell. *Atmos. Res.*, **82**, 19–25.

KHVOROSTYANOV, V. I., AND CURRY, J. A. 2005. Fall Velocities of Hydrometeors in the Atmosphere: Refinement to a Continuous Analytical Power Law. *J. Atmos. Sci.*, **62**, 4343–4357.

KHVOROSTYANOW, V. I., AND CURRY, J. A. 2001. Terminal Velocities of Droplets and Crystals: Power Laws with Continuous Parameters over the Size Spectrum. *J. Atmos. Sci.*, **59**, 1872–1884.

KIDDER, S. Q., AND VONDER HAAR, T. H.. 1995. Satellite Meteorology. *Academic Press*, 466 pp.

KIM, S.-W., BERTHIER, S., RAUT, J.-C., CHAZETTE, P., DULAC, F., AND YOON, S.-C. 2008. Validation of areosol and cloud layer structure from the space-borne lidar CALIOP using a ground-based lidar in Seoul, Korea. *Atmos. Chem. Phys.*, **8**, 3705–3720.

KOROLEV, A. 2006. Limitations of the Wegener-Bergeron-Findeisen Mechanism in the Evolution of Mixed-Phase Clouds. *J. Atmos. Sci.*, **64**, 4 pp.

KÄRCHER, B., AND KOOP, T. 2005. The Role of Organic Aerosols in Homogeneous Ice Formation. *Atmos. Chem. Phys.*, **5**, 703–714.

KÄRCHER, B., HENDRICKS, J., AND LOHMANN, U. 2006. Physically based parameterizations of cirrus cloud formation for use in global atmospheric models. *J. Geophys. Res.*, **111**, 11 pp.

KÖHLER, C. 2013. Cloud Ice Particle Nucleation and Atmospheric Ice Supersaturation in Numerical Weather Prediction Models. *Dissertation at Ludwig-Maximilians-Universität München*, 128 pp.

LAMB, D., AND VERLINDE, J. 2012. Physics and chemistry of clouds. *Cambridge University Press*, 584 pp.

LI, J.-L. F., WALISER, D. E., CHEN, W.-T., GUAN, B., KUBAR, T. L., STEPHENS, G. L., MA, H.-Y., MIN, D., DONNER, L. J., SEMAN, C. J., AND HOROWITZ, L. W. 2012. An observationally-based evaluation of cloud ice water in CMIP3 and CMIP5 GCMs and contemporary reanalyses using contemporary satellite data. *J. Geophys. Res.*, **117**, 26 pp.

LI, J.-L. F., WALISER, D. E., STEPHENS, G., LEE, SEUNGWON, L'ECUYER, T., KATO, SEJI, LOEB, NORMAN, AND MA, HSI-YEN. 2013. Characterizing and understanding radiation budget biases in CMIP3/CMIP5 GCMs, contemporary GCM, and reanalysis. *J. Geophys. Res.*, **118**, 1–19.

LIEBE, H. J. 1989. MPM - An Atmospheric MM-Wave Propagation Model. *Int. J. Infrared Millimeter Waves*, **10**, 631–650.

LIM, K.-S. S., AND HONG, S.-Y. 2010. Development of an Effective Double-Moment Cloud Microphysics Scheme with Prognostic Cloud Condensation Nuclei (CCN) for Weather and Climate Models. *Mon. Wea. Rev.*, **138**, 1587–1612.

LIN, Y.-L., FARLEY, R. D., AND ORVILLE, H. D. 1983. Bulk Parameterization of the Snow Field in a Cloud Model. *J. Clim. Appl. Meteorol.*, **22**, 1065–1092.

LIU, C.-L., AND ILLINGWORTH, A. J. 2000. Toward more accurate retrievals of ice water content from radar measurements of clouds. *J. Appl. Meteorol.*, **39**, 1130–1146.

LIU, G. 2004. Approximation of Single Scattering Properties of Ice and Snow Particles for High Microwave Frequencies. *J. Atmos. Sci.*, **61**, 2441–2456.

LIU, G. 2008. Deriving snow cloud characteristics from CloudSat observations. *J. Geophys. Res.*, **113**, 13 pp.

LÖHNERT, U., CREWELL, S., KRASNOV, O., O'CONNOR, E., AND RUSSCHENBERG, H. 2008. Advances in Continuously Profiling the Thermodynamic State of the Boundary Layer: Integration of Measurements and Methods. *J. Atmos. Ocean. Technol.*, **25**, 1251–1266.

MACE, G. G., HEYMSFIELD, A. J., AND POELLOT, M. R. 2002. On retrieving the microphysical properties of cirrus clouds using the moments of the millimetre-wavelength Doppler spectrum. *J. Geophys. Res.*, **107**, 26 pp.

MACE, G. G., ZHANG, Q., VAUGHAN, M., MARCHAND, R., STEPHENS, G. L., TREPTE, C., AND WINKER, D. 2009. A description of hydrometeor layer occurrence statistics derived from the first year of merged CloudSat and CALIPSO data. *J. Geophys. Res.*, **114**, 17 pp.

MAJEWSKI, D., LIERMANN, D., PROHL, P., RITTER, B., BUCHHOLD, M., HANISCH, T., PAUL, G., WERGEN, W., AND BAUMGARDNER, J. 2002. The Operational Global Icosahedral-Hexagonal Gridpoint Model GME: Description and High-Resolution Tests. *Mon. Wea. Rev.*, **139**, 319–338.

MAJEWSKI, D., FRANK, H., LIERMANN, D., AND RITTER, B. 2004. Kurze Beschreibung des Global-Modells GME (40 km/L 40) und seiner Datenbanken auf dem Datenserver (DAS2/4) des DWD. *Tech. Rep., Deutscher Wetterdienst, Offenbach, Germany*, 76 pp.

MAMOURI, R. E., AMIRIDIS, V., PAPAYANNIS, A., GIANNAKAKI, E., TSAKNAKIS, G., AND BALIS, D. S. 2009. Validation of CALIPSO space-borne-derived attenuated backscatter coefficient profiles using a ground-based lidar in Athens, Greece. **2**, 513–522.

MARCHAND, R., HAYNES, J., MACE, G. M., ACKERMAN, T., AND STEPHENS, G. 2009. A comparison of simulated cloud radar output from the multiscale modeling framework global climate model with CloudSat cloud radar observations. *J. Geophys. Res.*, **114**, 18 pp.

MARKS, C., AND RODGERS, C. D. 1993. A Retrieval Method for Atmospheric Composition From Limb Emission Measurements. *J. Geophys. Res.*, **98**, 14939–14953.

MAY, P. T., MATHER, J. H., VAUGHAN, G., AND JAKOB, C. 2008. Characterizing Oceanic Convective Cloud Systems. The Tropical Warm Pool International Cloud Experiment. *Bull. Am. Met. Soc.*, **89 (2)**, 153–155.

MCFARQUHAR, G. M., IACOBELLIS, S., AND SOMERVILLE, R. C. J. 2003. SCM simulations of tropical ice clouds using observationally based parameterizations of microphysics. **16**, 1643–1664.

MCFARQUHAR, G. M., ZHANG, G., POELLOT, M. R., KOK, G. L., MCCOY, R., TOOMAN, T., FRIEDLAND, A., AND HEYMSFIELD, A. J. 2007. Ice properties of single-layer stratocumulus during the Mixed-Phase Arctic Cloud Experiment. *J. Geophys. Res.*, **112**, 19 pp.

MCGILL, M. J., VAUGHAN, M. A., TREPTE, C. R., HART, W. D., HLAVKA, D. L., WINKER, D. M., AND KUEHN, R. 2007. Airborne Validation of Spatial Properties Measured by the CALIPSO Lidar. *J. Geophys. Res.*, **112**, 8 pp.

MONA, L., PAPPALARDO, G., AMODEO, A., D'AMICO, G., MADONNA, F., BOSELLI, A., GUINTA, A., RUSSO, F., AND CUOMO, V. 2009. One year of CNR-IMAA multi-wavelength Raman lidar measurements in coincidence with CALIPSO overpasses: Level 1 products comparison. *Atmos. Chem. Phys.*, **9**, 7213–7228.

NAM, C. C. W., AND QUAAS, J. 2012. Evaluation of Clouds and Precipitation in the ECHAM5 General Circulation Model Using CALIPSO and CloudSat Satellite Data. **25**(14), 4975–4992.

NAUD, C., MULLER, J.-P., AND DE VALK, P. 2005. On the use of ICESAT-GLAS measurements for MODIS and SEVIRI cloud-top height accuracy measurements. *Geophys. Res. Lett.*, **32**, 4 pp.

NOH, Y.-J., SEAMAN, C. J., VONDER HAAR, T. H., HUDAK, D. R., AND RODRIGUEZ, P. 2011. Comparisons and analyses of aircraft and satellite observations for wintertime mixed-phase clouds. *J. Geophys. Res.*, **116**, 32 pp.

PETTY, G. W. 2006. A First Course in Atmospheric Radiation. *Sundog Publishing*, 458 pp.

PFEIFFER, M., YEN, W., BALDAUF, M., CRAIG, G., CREWELL, S., FISCHER, J., HAGEN, M., HÜHNERBEIN, A., MECH, M., REINHARDT, T., SCHRÖDER, M., AND SEIFERT, A. 2010. Validating precipitation forecasts using remote sensor synergy: A case study approach. **19 (6)**, 601–617.

PHILLIPS, V., DEMOTT, P., AND ANDRONACHE, C. 2008. An Empirical Parameterization of Heterogeneous Ice Nucleation for Multiple Chemical Species of Aerosols. *J. Atmos. Sci.*, **65**, 2757–2783.

PROTAT, A., BOUNIOL, D., DELANOË, J., MAY, P. T., PLANA-FATTORI, A., HASSON, A., O'CONNOR, E., GÖRSDORF, U., AND HEYMSFIELD, A. J. 2009. Assessment of CloudSat Reflectivity Measurements and Ice Cloud Properties Using Ground-Based and Airborne Cloud Radar Observations. *J. Atmos. Ocean. Technol.*, **26**, 1717–1741.

PRUPPACHER, H. R., AND KLETT, J. D. 1997. Microphysics of Clouds and Precipitation. Second revised and Enlarged Edition with an Introduction to Cloud Chemistry and Cloud Electricity. *Kluwer Academiv Publishers*, 954 pp.

REINHARDT, T., AND SEIFERT, AXEL. 2006. A three-category ice scheme for LMK. *COSMO-Newsletter, Deutscher Wetterdienst, Offenbach, Germany*, **6**, 115–120.

REITTER, S., FRÖHLICH, K., SEIFERT, A., CREWELL, S., AND MECH, M. 2011. Evaluation of ice and snow content in the numerical weather prediction model GME with CloudSat. **4**, 579–589.

REN, C., AND MACKENZIE, A. R. 2005. Cirrus parameterization and the role of ice nuclei. *Quart. J. Roy. Met. Soc.*, **131**, 1585–1605.

RINEHART, R. E. 1991. Radar for Meteorologists. *Knight Printing Company*, 334 pp.

RODGERS, C. D. 1976. Retrieval of Atmospheric Temperature and Composition from Remote Measurements of Thermal Radiation. *Rev. Geophys.*, **14**(4), 609–624.

ROEBELING, D. R., MINNIS, P., AND NGUYEN, L. 2004. Calibration Compasiron Between SEVIRI, MODIS and GOES Data. *Proc. Second MSG RAO Workshop, Salzburg, Austria, 9–10 September 2004*, **ESA SP-582 November 2004**, 5 pp.

ROEBELING, D. R., FEIJT, A. J., AND STAMMES, P. 2006. Cloud property retrievals for climate monitoring: Implications of differences between Spinning Enhanced Visible and Infrared Imager (SEVIRI) on METEOSAT-8 and Advanced Very High Resolution Radiometer (AVHRR) on NOAA-17. *J. Geophys. Res.*, **111**, 16 pp.

ROGERS, D. C., DEMOTT, P. J., KREIDENWEIS, S. M., AND CHEN, Y. 1998. Measurement of ice nucleating aerosols during SUCCESS. *Geophys. Res. Lett.*, **25**, 1383–1386.

ROGERS, R. R., AND YAU, M. K. 1989. A Short Course in Cloud Physics. *Butterworth-Heinemann*, 290 pp.

ROGERS, R. R., HOSTETLER, C. A., HAIR, J. W., FERRARE, R. A., LIU, Z., OBLAND, M. D., HAROER, D. B., COOK, A. L., POWELL, K. A., VAUGHAN, M. A., AND WINKER, D. M. 2011. Assessment of the CALIPSO Lidar 532 nm attenuated backscatter calibration usind NASA LaRC airborne High Spectral Resolution Lidar. *Atmos. Chem. Phys.*, **11**, 1295–1311.

RUTLEDGE, S. A., AND HOBBS, P. V. 1983. The Mesoscale and Microscale Structure and Organization of Clouds and Precipitation in Midlatitude Cyclones. VIII: A Model for the 'Seeder-Feeder' Process in Warm-Frontal Rainbands. *J. Atmos. Sci.*, **40**, 1185–1206.

SATO, K., AND OKAMOTO, H. 2006. Characterization of Z_e and LDR of nonspherical and inhomogeneous ice particles for 95-GHz cloud radar: Its implication to microphysical retrievals. *J. Geophys. Res.*, **111**, 15 pp.

SATOH, M., INOUE, T., AND MIURA, H. 2010. Evaluations of cloud properties of global and local cloud system resolving models using CALIPSO and CloudSat simulators. *J. Geophys. Res.*, **115**, 18 pp.

SAUNDERS, C. P. R., AND HOSSEINI, A. S. 2001. A Laboratory Study of the Effect of Velocity on Hallett-Mossop Ice Crystal Multiplication. *Atmos. Res.*, **59**, 3–14.

SAUNDERS, R., MATRICARDI, M., AND BRUNEL, P. 1999. An improved fast radiative transfer model for assimilation of satellite radiance observations. *Quart. J. Roy. Met. Soc.*, **125**, 1407–1425.

SAUNDERS, R., MATRICARDI, M., AND GEER, A. 2010. RTTOV-9 User Guide Version 1.7. Doc ID: NWPSAF-MO-UD-016. *Tech. Rep., NWP-SAF*, 57 pp.

SCHMETZ, J., PILI, P., TJEMKES, S., JUST, D., KERKMANN, J., ROTA, S., AND RATIER, A. 2002a. An Introduction to Meteosat Second Generation (MSG). *Bull. Am. Met. Soc.*, **83**(7), 977–992.

SCHMETZ, J., PILI, P., TJEMKES, S., JUST, D., KERKMANN, J., ROTA, S., AND RATIER, A. 2002b. Supplement to An introduction to Meteosat Second Generation (MSG): SEVIRI Calibration. *Bull. Am. Met. Soc.*, **83**(7), 992–992.

SCHRAFF, C., AND HESS, R. 2012. A Description of the Nonhydrostatic Regional COSMO Model, Part III: Data Assimilation. *Tech. Rep., Deutscher Wetterdienst, Offenbach, Germany*, 93 pp.

SCHULZ, J.-P., AND SCHÄTTLER, U. 2011. Kurze Beschreibung des Lokal-Modells Europa COSMO-EU (LME) und seiner Datenbanken auf dem Datenserver des DWD. *Tech. Rep., Deutscher Wetterdienst, Offenbach, Germany*, 71 pp.

SCHÄTTLER, U. 2012. A Description of the Nonhydrostatic Regional COSMO Model, Part V: Preprocessing: Initial and Boundary Data for the COSMO-Modell. *Tech. Rep., Deutscher Wetterdienst, Offenbach, Germany*, 48 pp.

SEIFERT, A., AND BEHENG, K. D. 2006. A Two-moment Cloud Microphysics Parameterization for Mixed-phase Clouds. Part 1: Model description. *Meteorol. Atmos. Phys.*, **92**, 45–66.

SEIFERT, A., KÖHLER, C., AND BEHENG, K. D. 2012. Aerosol-cloud-precipitation effects over Germany as simulated by a convective-scale numerical weather model. *Atmos. Chem. Phys.*, **12**, 709–725.

STEPHENS, G. L., VANE, D. G., BOAIN, R. J., MACE, G. G., SASSEN, K., WANG, Z., ILLINGWORTH, A. J., O'CONNOR, E. J., ROSSOW, W. B., DURDEN, S. L., MILLER, S. D., AUSTIN, R. T., BENESETTI, A., MITRESCU, C., AND THE CLOUDSAT SCIENCE TEAM. 2002. The CloudSat Mission and the A-Train. A New Dimension of Space-based Observations of Clouds and Precipitation. *Bull. Am. Met. Soc.*, **83**, 1771–1790.

STROW, L. LARRABEE, MOTTELER, HOWARD E., BENSON, ROBERT G., HANNON, SCOTT E., AND SOUZA-MACHADO, SERGIO DE. 1998. Fast Computation of

Monochromatic Infrared Atmospheric Transmittances using Compressed Look-up Tables. *J. Quant. Spectrosc. Radiat. Transfer*, **59**, 481–493.

TANELLI, S., DURDEN, S. L., IM, E., PAK, K. S., REINKE, D. G., PARTAIN, P., HAYNES, J. M., AND MARCHAND, R. T. 2008. CloudSat's Cloud Profiling Radar after Two Years in Orbit: Performance, Calibration, and Processing. *IEEE Transactions on Geoscience and Remote Sensing*, **46**(11), 3560–3573.

THOMPSON, G., FIELD, P. R., RASMUSSEN, R. M., AND HALL, W. D. 2008. Explicit Forecasts of Winter Precipitation Using an Improved Bulk Microphysics Scheme. Part II: Implementation of a New Snow Parameterization. *Mon. Wea. Rev.*, **132**, 519–542.

TIAN, L., HEYMSFIELD, G. M., HEYMSFIELD, A. J., BANSEMER, A., LI, L., TWOHY, C. H., AND SRIVASTAVA, R. C. 2010. A Study of Cirrus Ice Particle Size Distribution Using TC4 Observations. *J. Atmos. Sci.*, **67**, 195–216.

VAUGHAN, M., YOUNG, S., WINKER, D., POWELL, K., OMAR, A., LIU, Z., HU, Y., AND HOSTETLER, C. 2004. Fully Automated Analysis of Space-based Lidar Data: An Overview of the CALIPSO Retrieval Algorithms and Data Products. *Lidar Radar Techniques for Atmospheric Sensing, Proceedings of SPIE*, **5575**, 16–30.

WALISER, D. E., LI, J.-L. F., WOODS, C., AUSTIN, R. T., BACMEISTER, J., CHERN, J., GENIO, A. D., JIANG, J. H., KUANG, Z., MENG, H., MINNIS, P., PLATNICK, S., ROSSOW, W. B., STEPHENS, G. L., SUN-MACK, S., TAO, W.-K., TOMPKINS, A. M., VANE, D. G., WALKER, C., AND WU, D. 2009. Cloud ice: A climate model challenge with its signs and expectations of progress. *J. Geophys. Res.*, **114**, 27 pp.

WALISER, D. E., LI, J.-L. F., L'ECUYER, T. S., AND CHEN, W.-T. 2011. The impact of precipitating ice and snow on the radiation balance in global climate models. *Geophys. Res. Lett.*, **38**, 6 pp.

WALLACE, J. M., AND HOBBS, P. V. 1977. Atmospheric Science. An Introductory Survey. *Academic Press*, 467 pp.

WEITKAMP, C. 2005. Lidar: Range-Resolved Optical Remote Sensing of the Atmosphere. *Springer*, 455 pp.

WERGEN, W., AND BUCHHOLD, M. 2002. Datenassimilation für das Globalmodell GME. *Promet*, **27**, 150–155.

WINKER, D. M., HUNT, W. H., AND MCGILL, M. J. 2007. Initial Performance Assessment of CALIOP. *Geophys. Res. Lett.*, **34**, 5 pp.

WINKER, D. M., VAUGHAN, M. A., OMAR, A., HU, Y., POWELL, K. A., YU, Z., HUNT, W. H., AND YOUNG, S. A. 2009. Overview of the CALIPSO Mission and the CALIOP Data Processing Algorithms. *J. Atmos. Ocean. Technol.*, **26**, 2310–2323.

WOODS, C. P., WALISER, D. E., LI, J.-L., AUSTIN, R. T., STEPHENS, G. L., AND VANE, D. G. 2008. Evaluating CloudSat ice water content retrievals using a cloud-resolving model: Sensitivities to frozen particle properties. *J. Geophys. Res.*, **113**, 16 pp.

YORK, J. E., HLAVKA, D. L., VAUGHAN, M. A., MCGILL, M. J., HART, W. D., RODIER, S., AND KUEHN, R. 2011. Airborne validation of cirrus cloud properties derived from CALIPSO lidar measurements: Spatial properties. *J. Geophys. Res.*, **116**, 19 pp.

ZHANG, K., LIU, X., WANG, M., COMSTOCK, J. M., MITCHELL, D. L., MISHRA, S., AND MACE, G. G. 2013. Evaluating and Constraining Ice Cloud Parameterizations in CAM5 using aircraft Measurements from the SPARTICUS Campaign. *Atmos. Chem. Phys.*, **13**, 4963–4982.

Appendices

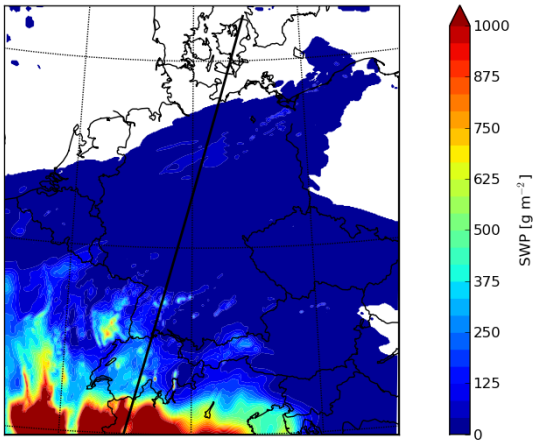

A.1: COSMO-DE8819 (two-category ice scheme).

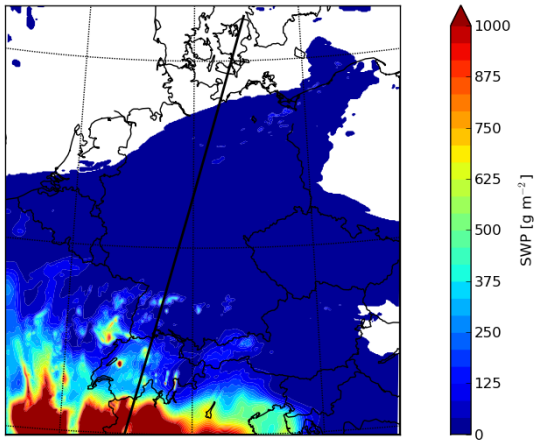

A.2: COSMO-DE8822 (two-moment cloud ice scheme).

Abbildung A: SWPs on 15 June 2010 at 2 UTC. Forecast age of model runs: 14 h. Solid black line: CloudSat overpass for 01:45:21–01:48:53 UTC of same day.

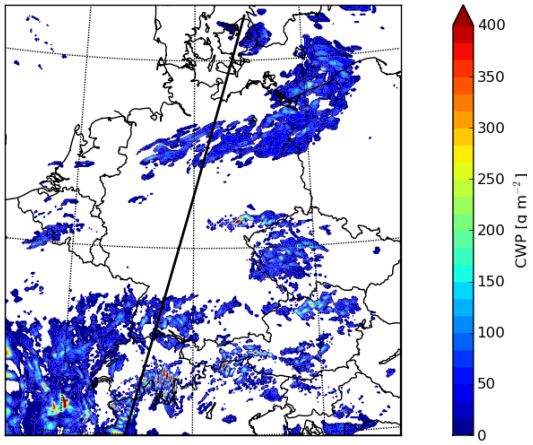

B.1: COSMO-DE8819 (two-category ice scheme).

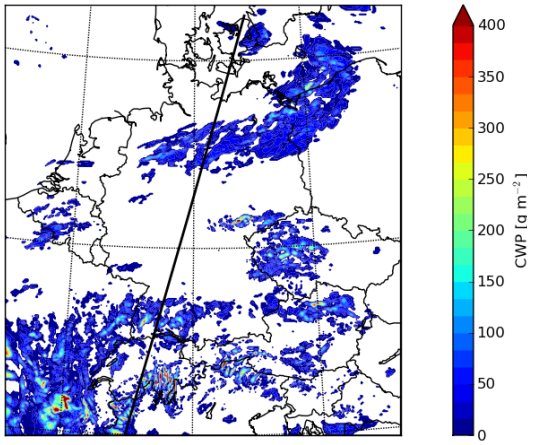

B.2: COSMO-DE8822 (two-moment cloud ice scheme).

Abbildung B: CWPs on 15 June 2010 at 2 UTC. Forecast age of model runs: 14 h. Solid black line: CloudSat overpass for 01:45:21–01:48:53 UTC of same day.

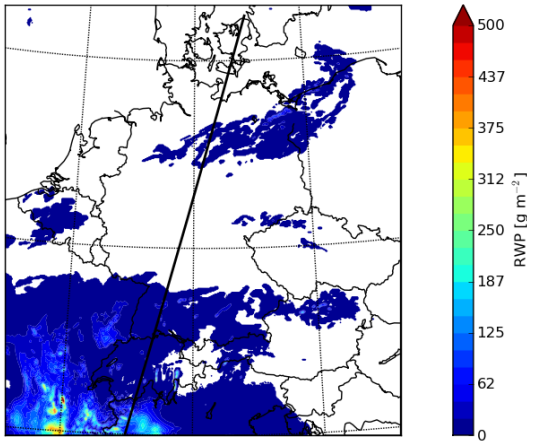

C.1: COSMO-DE8819 (two-category ice scheme).

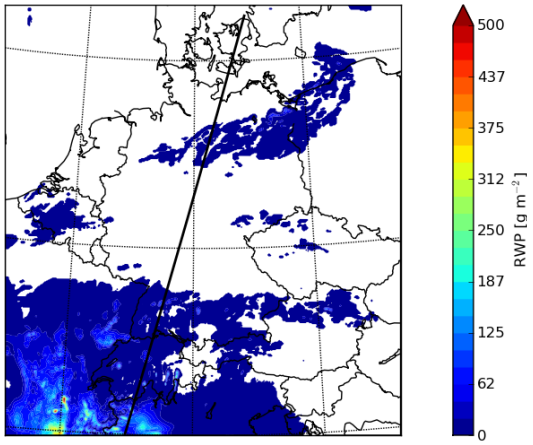

C.2: COSMO-DE8822 (two-moment cloud ice scheme).

Abbildung C: RWPs on 15 June 2010 at 2 UTC. Forecast age of model runs: 14 h. Solid black line: CloudSat overpass for 01:45:21–01:48:53 UTC of same day.

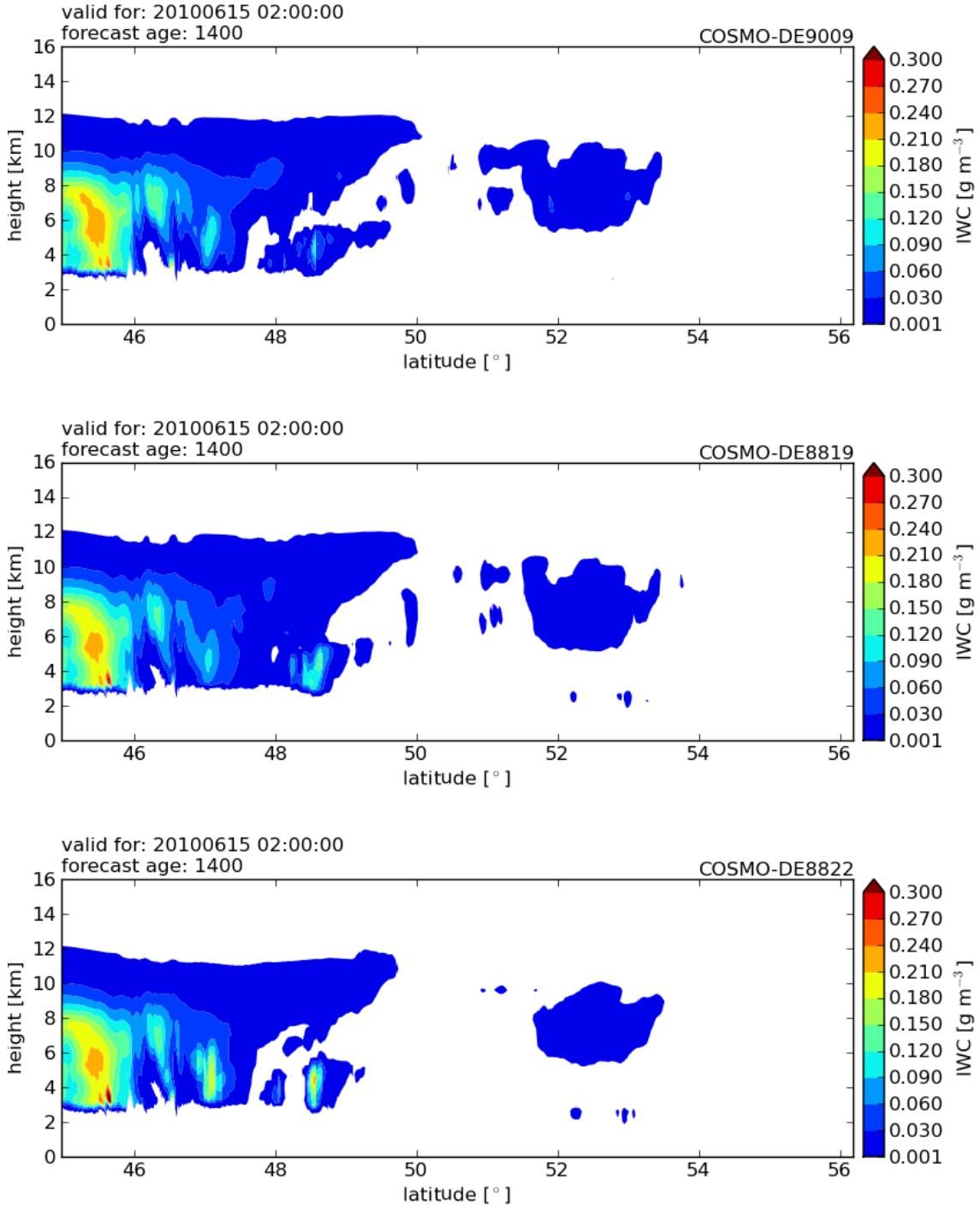

Abbildung D: Cross sections of IWC along CloudSat track on 15 June 2010 at 2 UTC. Forecast age of model runs: 14 h. See Table 7.2 for details on the settings in the individual experiments.

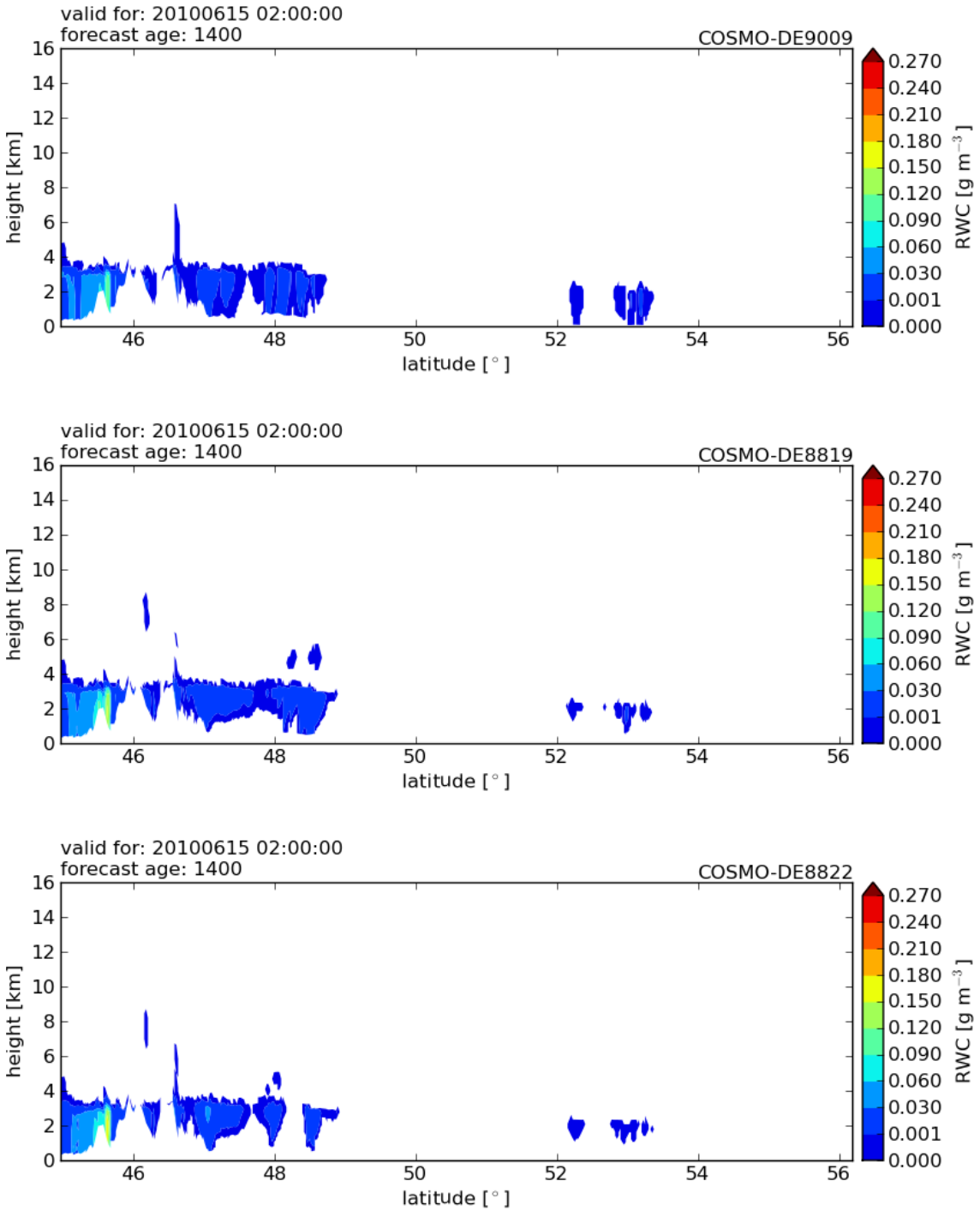

Abbildung E: Cross sections of RWC along CloudSat track on 15 June 2010 at 2 UTC. Forecast age of model runs: 14 h. Note that RWC values unequal zero are already depicted in blue. See Table 7.2 for details on the settings in the individual experiments.

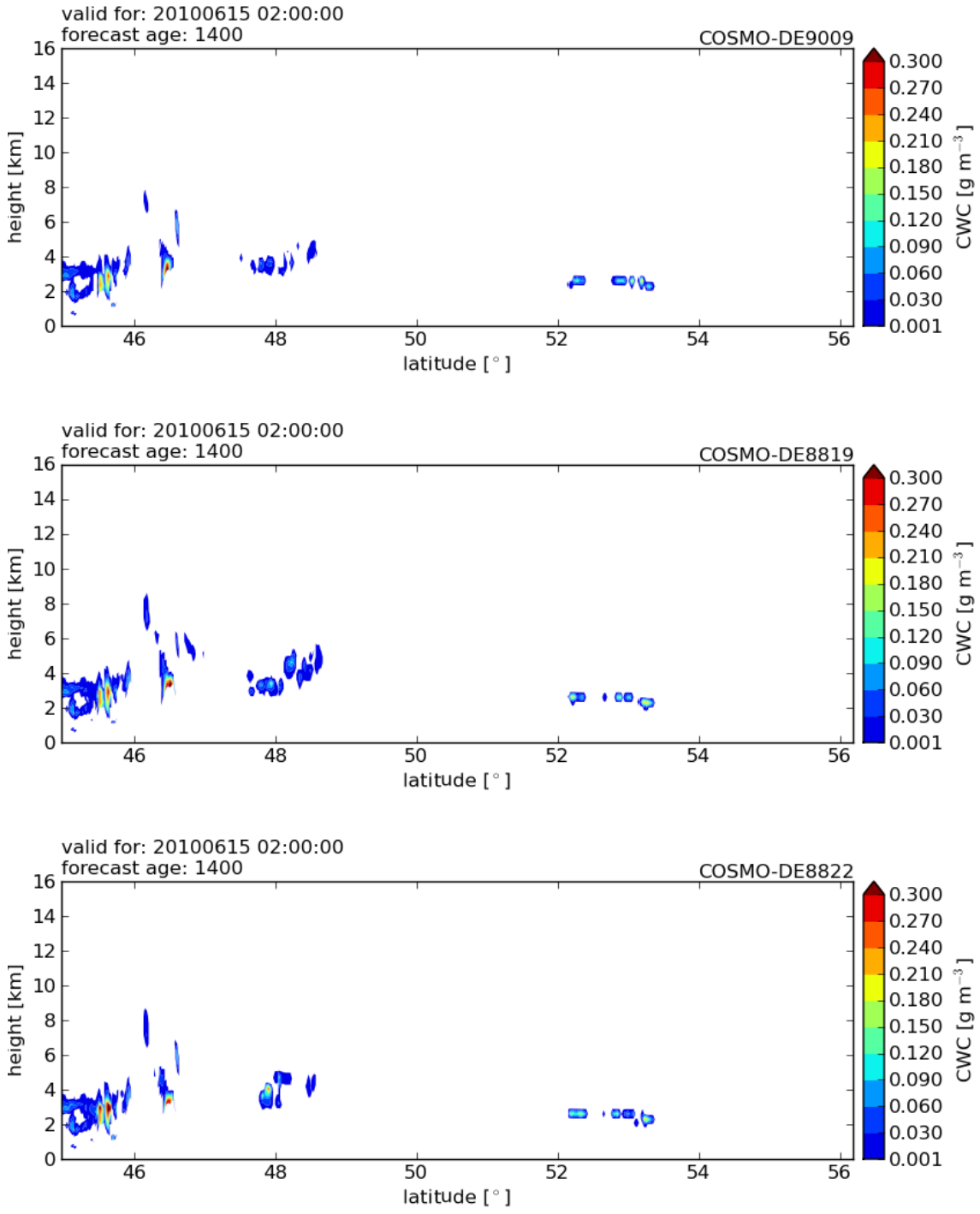

Abbildung F: Cross sections of CWC along CloudSat track on 15 June 2010 at 2 UTC. Forecast age of model runs: 14 h. Note that CWC values unequal zero are already depicted in blue. See Table 7.2 for details on the settings in the individual experiments.

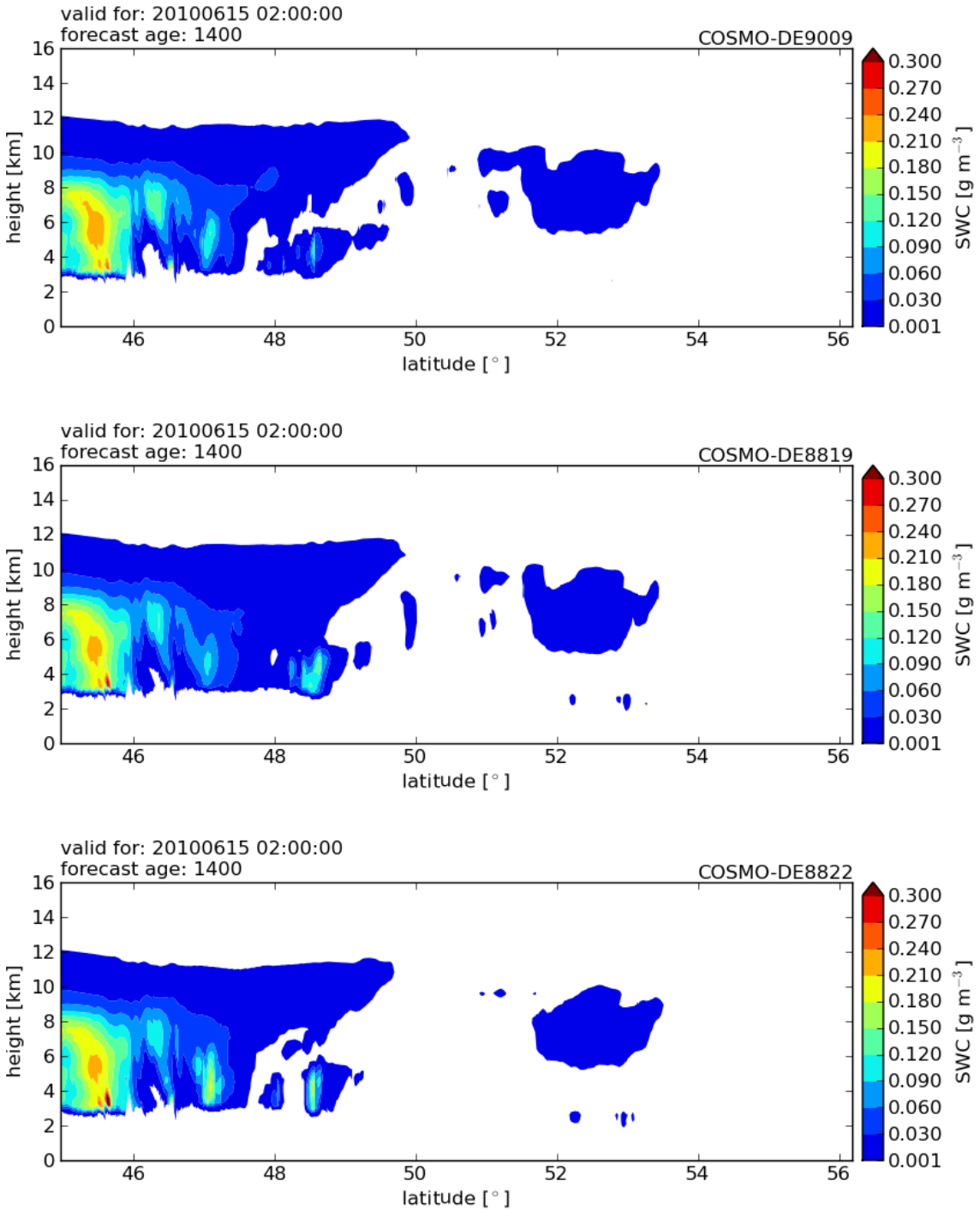

Abbildung G: Cross sections of SWC along CloudSat track on 15 June 2010 at 2 UTC. Forecast age of model runs: 14 h. Note that SWC values unequal zero are already depicted in blue. See Table 7.2 for details on the settings in the individual experiments.

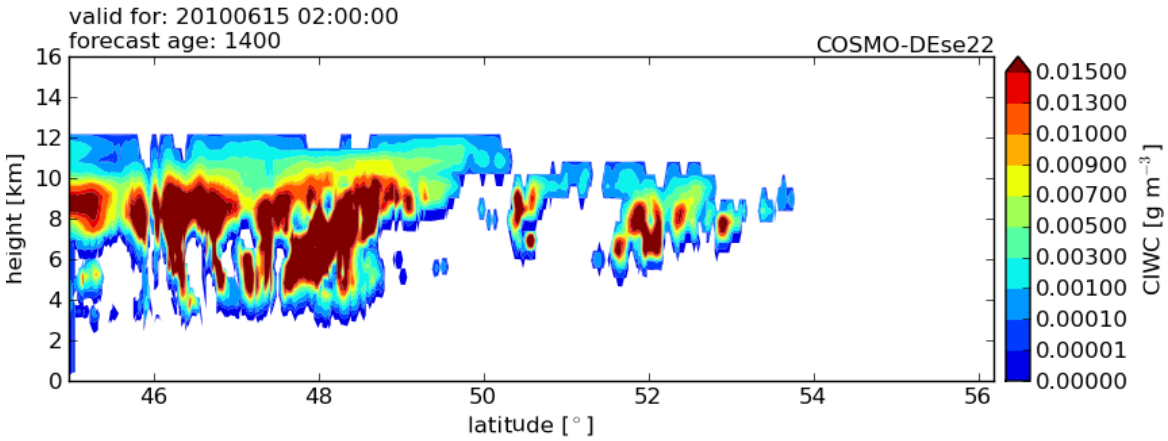

Abbildung H: Cross sections of CIWC along CloudSat track on 15 June 2010 at 2 UTC. Forecast age of model runs: 14 h. Note that CIWC values unequal zero are already depicted in blue. See Table 7.2 for details on the settings in the individual experiment.

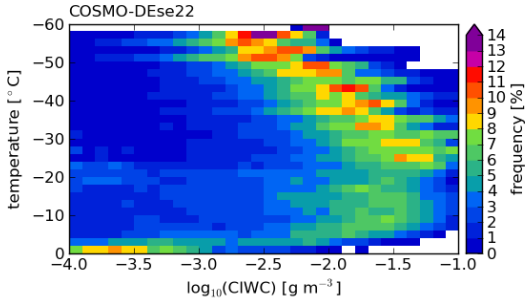

Abbildung I: Frequency distributions of CIWCs for sensitivity experiment COSMO-DEse22 over the reduced model domain as depicted in Fig. 7.2 on 15 June 2010 at 2 UTC. Forecast age of model run: 14 h. Note that each temperature bin is normalized individually. See Table 7.2 for details on the settings in experiment COSMO-DEse22.

Danksagung

Ein Teil dieser Arbeit wurde unterstützt von der Deutsche Forschungsgemeinschaft unter der Bewilligungsnummer QUEST CR 111/5-3.

Danke Susanne. Für die Begutachtung und Betreuung der Arbeit, für deinen unermüdlichen Einsatz und für den Freiraum den du mir eingeräumt hast. Ich habe mich immer sehr gut aufgehoben gefühlt.

Danke Roel. Dass du dich bereit erklärt hast die Zweitbegutachtung dieser Arbeit zu übernehmen.

Danke Axel. Für die Zeit und Geduld die du investiert hast um mich in die Welt der Modelle und ihrer Parametrisierungen einzuführen. Für die Hilfe bei der immer wiederkehrenden Fehlersuche. Und vor allem für die erhellenden Diskussionen rund um die Ergebnisse. Die Zusammenarbeit war immer angenehm und hat mir sehr viel Freude bereitet. Man muss es ganz klar sagen: Ohne dich wäre diese Arbeit nicht zu realisieren gewesen!

Danke Carmen. Dass ich dein Schema benutzen durfte und für deine unendliche Geduld, auch wenn ich zum x-ten Mal nachgefragt habe. Jetzt haben wir es geschafft!

Danke FE-13, insbesondere Jochen, Thomas, Uli und Robin. Für den Rat und Tat bei allen technischen Problemen.

Danke Kerstin. Nicht nur für die weitaus größte Mühe beim Korrekturlesen, sondern noch viel wichtiger, für's da sein, wenn die Not am größten war. Aber nun zu erfreulicheren Dingen: Wann und wo gehen wir den nächsten Cocktail trinken? Alles weitere siehe unten.

Thank you Uli. For your thorough proofreading, your encouragement, the occasional tissue,

and the laughs. Now repeat after me: The launched series of airborne experiments investigates how soot determines...

Danke Mario. Ebenso nicht nur für das Korrekturlesen. Afraid of everyone – das war einmal.

Danke Andreas. Für den Versuch mir doch noch ein wenig wahre Synoptik beizubringen :) Und siehe unten.

Danke Stefan und Jennifer. Für das Bereitstellen der MSG SEVIRI Daten.

Danke Infernos. Für den Spaß mit euch. Insbesondere: Danke Gerrit. Einen netteren Mitstreiter und geduldigeren Büromitbewohner kann es kaum geben. Mit keinem füßelt es sich so schön wie mit dir! Danke Max. Was ein Glück, dass wir vorerst weiter Büromitbewohner bleiben. Mit keinem kloppt es sich so schön wie mit dir! Danke Sandra. Dass du mich in der schlimmsten Woche ertragen und verpflegt hast, dafür verdienst du einen Extrapreis!

Und schließlich: Danke meine lieben Freunde. Ihr seid mit mir durch alle Höhen und Tiefen gegangen. Ihr habt mich ertragen und getragen. Mehr brauch ich wohl nicht zu sagen. Ihr wisst schon.

Erklärung

Ich versichere, dass ich die von mir vorgelegte Dissertation selbständig angefertigt, die benutzten Quellen und Hilfsmittel vollständig angegeben und die Stellen der Arbeit – einschließlich Tabellen, Karten und Abbildungen –, die anderen Werken im Wortlaut oder dem Sinn nach entnommen sind, in jedem Einzelfall als Entlehnung kenntlich gemacht habe; dass diese Dissertation noch keiner anderen Fakultät oder Universität zur Prüfung vorlgelegt wurde; dass sie – abgesehen von unten angebenen Teilpublikationen – noch nicht veröffentlicht worden ist sowie, dass ich eine solche Veröffentlichung vor Abschluß des Promotionsverfahrens nicht vornehmen werde. Die Bestimmungen dieser Promotionsordnung sind mir bekannt. Die von mir vorgelegte Dissertation ist von Prof. Dr. Susanne Crewell betreut worden.

Köln, den 4. November 2013

(Sonja Reitter)

Teilveröffentlichung

Reitter, S., K. Fröhlich, A. Seifert, S. Crewell, and M. Mech (2011) Evaluation of ice and snow content in the global numerical weather predicition model GME with CloudSat, *Geosci. Model Dev., 4*, 579-589.